Electronic Structure and Magnetism of EuO Films on the Nanometer Scale

I n a u g u r a l - D i s s e r t a t i o n

zur

Erlangung des Doktorgrades

der Mathematisch-Naturwissenschaftlichen Fakultät

der Universität zu Köln

vorgelegt von

Dipl.-Phys. Jürgen Klinkhammer

aus Simmerath

Köln 2013

Berichterstatter:	Prof. Dr. Thomas Michely
(Gutachter)	Priv. Doz. Dr. Daniel Bürgler

Tag der mündlichen Prüfung: 28.06.2013

Abstract

This thesis deals with thin films of the ferromagnetic semiconductor EuO. These are prepared by molecular beam epitaxy under ultra high vacuum conditions and their properties are investigated *in-situ* by means of low energy electron diffraction, magneto-optical Kerr effect (MOKE), scanning tunneling microscopy (STM) and scanning tunneling spectroscopy (STS). The experiments are carried out in a low temperature STM apparatus with a base temperature of 5.3 K. The development of a highly sensitive MOKE instrument is in the technical focus of this work. EuO is grown in (100) orientation on a ferromagnetic Ni(100) single crystal as well as on single crystalline graphene on Ir(111). An antiferromagnetic coupling between the magnetic moments of the Ni(100) and the EuO(100) film turns out. The 3.3 nm thin stoichiometric films of EuO on graphene show a Curie temperature $T_C = 75$ K, which is increased with respect to films of the same thickness grown on other substrates and even with respect to bulk EuO [1–3].
Point defects in EuO films are analyzed with help of atomically resolved STM images. The defect concentration can be quantified using highly-resolved STM topography images. The mobility of the oxygen vacancies is shown by a series of topography STM images and a mobility of the vacancies along the EuO$\langle 011 \rangle$ directions is found. Investigations of the electronic structure of the EuO(100) surface are performed by STM and STS, which require a high sample quality, i.e, a topographically very well ordered and flat surface with a minimum of defects. The ultra thin films of EuO on graphene described in thesis are of such high quality. A local n-doping and an upward band bending is found at the oxygen vacancy sites. Tunneling spectroscopy maps of the ferromagnetic EuO(100) surface show standing wave patterns, which are the characteristic fingerprint of the surface state in EuO(100). The energy vs. momentum space of the surface state is explored by evaluating the surface state scattering patterns. A dispersion relation determined this way of the surface state is free electron like, with an effective mass of (1.09±0.10) times the mass of a free electron. The same measurements are performed in the paramagnetic phase of EuO at 81 K. Thereby the surface state is shifted in energy. The shift indicates indirectly the spin degeneracy of the surface state in the paramagnetic phase, which is lifted in the ferromagnetic phase of EuO. This behavior is analogous to the well known spin splitting of the EuO conduction band [4]. The spin splitting of the surface state (measured with this work) amounts to 0.66 eV.

Contents

Abstract i

Table of Contents ii

Frequently used Symbols v

1 Introduction and Motivation 1

2 Background 3

2.1 EuO Properties . . . 3

2.2 Mean Field Magnetization . . . 10

2.3 Magneto-Optics . . . 12

3 The Low Temperature Scanning Tunneling Microscopy Apparatus 15

3.1 Sample Holders and Tip Tool . . . 16

3.2 The Manipulator . . . 18

3.3 The Molecular Beam Epitaxy Station . . . 19

4 Development of a MOKE Setup 23

4.1 The Light Source . . . 24

4.2 The Magnet . . . 25

4.3 The Detector . . . 27

4.4 The Ambient Conditions MOKE Setup . . . 29

4.5 Technical Aspects of Automatization . . . 30

4.6 MOKE Test Measurements . . . 31

5 Experimental Procedures 35

5.1 Substrate Preparation . . . 35

5.2 Graphene Preparation . . . 35

5.3 EuO Growth . . . 37

5.4 LEED Measurements and Data Post Processing . . . 39

5.5 Scanning Tunneling Spectroscopy Technique . . . 40

5.6 MOKE Measurement Procedures . . . 41

6 Growth and Magnetism of EuO on Graphene **45**
6.1 From Single EuO Grains to Thin Films 45
6.2 Magnetic Reference Measurements at the LT-STM Machine 48
6.3 Magnetism of 3.3 nm Thin Films of EuO(100) on Graphene 51
6.4 Easy Magnetization Direction and Superparamagnetic Limit 54

7 Defects in EuO **57**
7.1 Strong Electronic Corrugation 57
7.2 Oxygen Vacancies 59
7.3 Defect Mobility 62
7.4 Work Function of EuO and Local Band Bending 64

8 The Spin Polarized Surface State in EuO(100) **69**
8.1 Electronic Scattering Pattern on EuO(100) 69
8.2 Spin Degeneracy of the EuO(100) Surface State 72
8.3 The Brillouin Zone of the Surface State and its Signature on Defect Sites 75

9 Magnetic Properties of EuO(100) on Ni(100) **79**
9.1 Magnetic Characterization of the Ni(100) Substrate 79
9.2 Magnetic Coupling of EuO(100) and Ni(100) Moments 82

10 Summary and Outlook **85**

References **89**

A Preparation of Tungsten Tips **105**

B Calculation of Heisenberg Magnetization Functions **111**

C Usage of MOKEsoft **113**

D Calibration of the Electromagnet **115**

E Construction Plans **123**

Publications **156**

Kurzfassung **158**

Acknowledgements **160**

Offizielle Erklärung **162**

Frequently used symbols and abbreviations

$\bar{\Phi}$	Apparent Height of Tunnel Barrier
Φ	Work Function
Θ	Coverage
Θ_{Kerr}	Kerr Angle
$\Theta_{\mathrm{Kerr}}(\mathrm{Rem})$	Remanent Kerr Angle
$\Theta_{\mathrm{Kerr}}(\mathrm{x\,mT})$	Kerr Angle at x mT
B	Magnetic Field
E_{F}	Fermi Energy
E	Energy
I	Current
M	Magnetization
T_{C}	Curie Temperature
T_{Int}	Integration Time
T_{Lat}	Latency Time
T_{Loop}	Time Per Loop
T	Temperature
U_{Bias}	Bias Voltage
z	Vertical Tip to Sample Distance
ARMCO	American Rolling Mill Company
BOP	Bipolar Operational Power
CVD	Chemical Vapor Deposition
DOS	Density of States
EDS	Electronic Defect Site
ELD	Electronic Line Defect
FM	Ferromagnetic
IF	Interference Filter
LDOS	Local Density of States
LEED	Low Energy Electron Diffraction
LT-STM	Low Temperature Scanning Tunneling Microscopy
MBE	Molecular Beam Epitaxy
MIT	Metal to Insulator Transition
ML	Monolayer
MOKE	Magneto-Optical Kerr Effect
PT	Photo Transistor
QMS	Quadrupole Mass Spectrometer
SEM	Scanning Electron Microscope
SQUID	Superconducting Quantum Interference Device
SS	Surface State
STM	Scanning Tunneling Microscopy
STS	Scanning Tunneling Spectroscopy
TPG	Temperature Programmed Growth
UHV	Ultra High Vacuum
YSZ	Yttria-Stabilized Zirconia

1 Introduction and Motivation

Since 1961 [5] scientific interest in Europium monoxide (EuO) is attracted by a variety of strong physical effects. The combination of this variety and its simple rocksalt crystal structure makes EuO a model system. EuO is famous for the strongest magneto-optical Kerr effect (MOKE) ever measured in a material, which gives rise to a Kerr rotation of of 7.1 ° for bulk samples [6]. Due to its strong coupling of light and magnetism [7], the magneto-optical Kerr effect is of importance for optical data storage media [8]. In the framework of this thesis the magneto-optical Kerr effect is utilized to *in-situ* investigate the magnetic properties of EuO samples.
Renewed interest in EuO came up with the rise of spintronics [9; 10] due to the almost 100% spin polarized bottom of the EuO conduction band [4]. Stoichiometric EuO is a ferromagnetic semiconductor, two properties not often seen in one material, with a Curie temperature $T_C = 69\,K$ [5]. T_C of bulk EuO is enhanced by n-doping [11–13], but no dopant managed to rise T_C up to room temperature. Ultra thin EuO films show a decreased Curie temperature T_C [2; 3], which is counterproductive for applications. EuO combines the properties of a semiconductor with distinct magnetic properties. Thus, it is an attractive material for information technology since it allows to store information by its charge and additionally by spin states.
Presently EuO is very prominent as spin filter barrier [10; 14–16]. The field of spintronics is intrinsically a nanotechnology and thus nanostructures of EuO are of most interest. The fabrication of EuO nanostructures requires the growth of thin epitaxial EuO films. Such high quality EuO(100) films are grown on a graphene substrate [17]. The properties of thin films can be tuned by their substrate [18]. For instance intercalation enables a tuning of the graphene's properties [19] and thus of EuO grown on top.
Further, the combination of EuO on top of graphene is attractive from the spintronic point of view. A gating of the EuO induces spin polarized charge carriers in graphene by a proximity effect [20]. The large spin relaxation times of spin polarized charge carriers in graphene [21–23] make it one of the most promising spin conductor materials.

Topic of many experiments, theories, and discussions with open questions is the metal to insulator transition (MIT) in EuO. The MIT occurs simultaneously with the ferromagnetic transition through the coupling of magnetism and electronic properties in EuO induced by n-doping [2; 24–32]. Mainly EuO n-doped by oxygen vacancies [12; 33–40] and gadolinium [12; 25; 32; 41–45] were investigated in the past. Discussions occurred, whether an oxygen off-stoichiometry alone can cause the MIT, or if the inclusion of impurities is needed [46]. The two most prominent theories explaining the MIT in EuO are the Helium-model [24] and the bound magnetic polaron (BMP)

model [26; 30]. The idea of the BMP is that the MIT is a spatial inhomogeneous percolation phase transition.
Thin films of EuO are an ideal benchmark system for the experimental techniques of surface science. The nature of the MIT can be solved by measurements which are sensible to the electronic structure with a sub-nanometer spatial resolution. Such a technique is scanning tunneling spectroscopy (STS). STS can be applied around dopant sites to map conducting areas in a semiconducting matrix at the onset of the MIT.

An autonomous motivation for spectroscopy on EuO surfaces can be gained by the present research on topological insulators [47] which exhibits two dimensional electron systems on surfaces of semiconductors. This also leads to a renewed interest in spin-polarized surface states of topologically trivial materials. Of specific interest are spin-polarized surface states in the band gap of semiconductors or insulators, as these states will contribute significantly to the transport in such systems. A prediction for an exchange-split surface state in a semiconducting oxide was made for EuO(100) more than ten years ago by R. Schiller and W. Nolting [48], but withstood experimental observation until now [45].

This thesis now looks at the electronic structure of EuO(100) on the nanometer scale with tunneling spectroscopy and its connection to ferromagnetic order. A MOKE apparatus is developed for this purpose. Tunneling spectroscopy is based on a tunneling current, and therefore requires conductive samples. EuO is grown by MBE under UHV conditions on conductive substrates and is *in-situ* investigated since it is not stable under ambient conditions. This thesis therefore continues the work initiated in the PhD project of D. F. Förster [17].

2 Background

2.1 EuO Properties

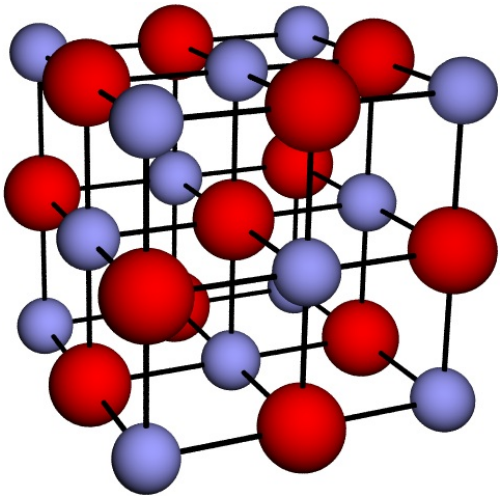

Figure 2.1: "Ball and stick model of the rock-salt crystal structure of EuO. Red balls represent O atoms and blue balls Eu atoms." [17]. Taken from reference [17].

EuO is a purely divalent ionic compound of Eu^{2+} and O^{2-} ions. The electronic configuration of the Eu^{2+} ion is $[Xe]4f^7 5d^0 6s^0$ [17], which means that the 4f orbital is half filled. It belongs to the rare class of ferromagnetic semiconductors [49; 50] with a Curie temperature T_C of about 69 K [51; 52]. It was first investigated by B. T. Matthias *et al.* in 1961 [5]. As already mentioned EuO is very interesting with its almost 100% spin polarized charge charriers in the conduction band as first shown by P. G. Steeneken and L. H. Tjeng *et al.* [4; 13]. The magneto-optical Kerr effect (MOKE) in EuO [6] is the strongest ever measured. Further strong effects observed in EuO are photoconductivity [53–55], a colossal magneto-resistance (CMR) [26; 41] and a metal to insulator transition (MIT) in n-doped EuO [2; 24–32; 48; 56].

Crystalline and Electronic Structure

EuO grows in a simple face centered cubic (fcc) rocksalt structure (see figure 2.1) with a lattice constant of 5.144 Å [57]. The EuO(100) surface exhibits a checkerboard like arrangement of europium and oxygen atoms. This surface is of considerable interest for STS and STM measurements, because both chemical species are accessible. This is not the case for EuO(111) which is an alternating stacking of oxygen and europium layers. Since the oxidation state of the oxygen is 2- and of the europium is 2+ an EuO(111) film is polar. Due to the cost of electrostatic energy it is not possible to grow polar films thicker than a few atomic monolayers without the formation of (100) facets [17].

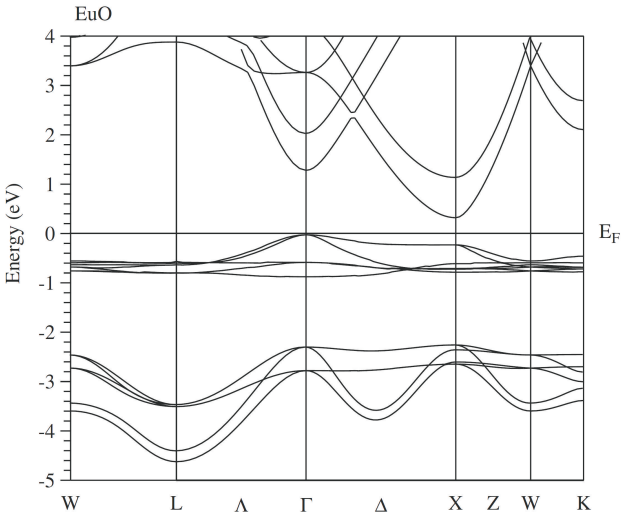

Figure 2.2: "Band structure of EuO calculated using an LSDA+U (U = 7 eV) method" [58]. Taken from reference [58].

In the 1970s the band structure of bulk EuO has been investigated by first optical absorption measurements [50]. In the paramagnetic state a band gap $E_G = 1.10\,eV$ is determined. Thereby the highest occupied valence band level belongs to the 4f level and the lowest unoccupied EuO level is at the bottom of the Eu $5d_{t2g}$ conduction band [11]. Optical measurements in the ferromagnetic state (at 20 K) reveal a red shift of the adsorption edge of 0.26 eV [33]. This effect is called the red shift, because optical light of longer wavelengths is absorbed by the band gap upon the paramagnetic to ferromagnetic transition. The red shift corresponds to an exchange splitting of the conduction band of $2 \cdot 0.26\,eV = 0.52\,eV$ [33]. In 2002 spin resolved x-ray absorption studies in the ferromagnetic state of EuO reveal an exchange splitting of the conduction band of 0.60 eV [4]. Even more important is the spin polarization that way determined of the lower conduction band edge of almost 100% [4].

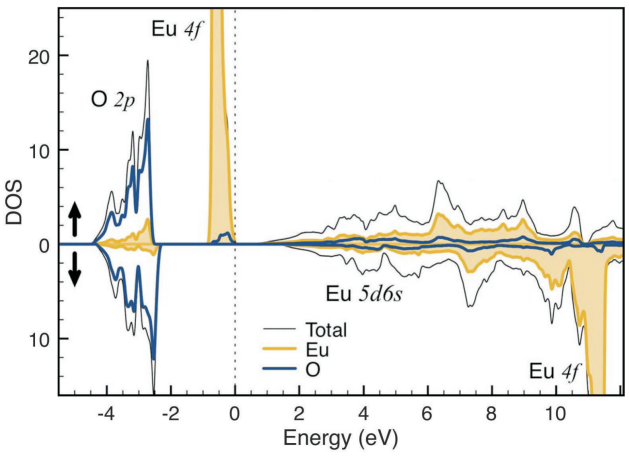

Figure 2.3: "The spin resolved density of states of bulk EuO in the FM configuration with optimized bulk lattice parameters, a=5.1578 Å. The bands are labeled and the zero of energy is at the Fermi energy" [59]. Modified from reference [59].

Early [60; 61] and later photoemission studies [62; 63] show that "the energy levels of EuO which are important for the understanding of the low energy features, i.e., those which are near the chemical potential, are the O 2p orbitals, the Eu 4f orbitals, and the Eu 5d - 6s conduction band" [62]. Band models derived from the optical $4f^7 \rightarrow 4f^6 5d$ transition [64] suggest that the 4f levels

are located directly below the Fermi energy E_F, though this is not confirmed by photoemission measurements where the peak of the one electron $4f^7 \rightarrow 4f^6$ removal spectrum is not directly below E_F [62]. "On-site correlation effects at the Eu 4f states make the existence of a 4f density of states at the Fermi level to be meaningless. Instead, one should see a $f^7 \rightarrow f^6$ peak at about 2 eV below the Fermi level, and a $f^7 \rightarrow f^8$ peak above the Fermi level at about 7 eV" [62]. Angle-resolved photoemission studies on EuO thin films in combination with density functional theory (DFT), see figure 2.2, (in the code WIEN2K [65] by H. Miyazaki *et al.*) reveal that "the Eu 4f states have sizable energy dispersion at both the G and X points" [58]. Therefore they conclude that hybridization of the Eu 4f states with other states like O 2p or Eu 5d takes place [58]. This is important for the mediation of magnetic exchange interactions, as explained in the next section 2.1.

Both band structure calculations shown in figure 2.2 and figure 2.3 are "calculated with the fullpotential linearized augmented plane-wave DFT code WIEN2K [65]" [59] and strong correleation between the 4f electrons are treated with the LSDA+U method. In both calculations the "on-site Coulomb repulsion energy U in the Eu 4f states is set to 7 eV" [58]. Figure 2.2 shows the momentum dependent band structure of bulk EuO with the 5d conduction band, the weakly dispersive 4f band at the Fermi edge and the O 2p valance band [58]. The relative energies in this plot are more reliable than the absolute values. This is the same for figure 2.3 where the spin resolved density of states (DOS) is presented for each atomic species in the EuO compound as well as for the whole compound.

Extra charge carriers are often introduced in EuO by n-doping [9; 13; 27; 33; 34; 42; 45; 66–77]. The most prominent n-doping mechanisms are the creation of oxygen vacancies and the substitution of Eu by gadolinium (Gd). Since the oxidation state of the oxygen ion in EuO is 2- the creation of an oxygen vacancy supplies two doping electrons [33; 78]. In the case of the substitution of Eu through Gd one extra electron is supplied per dopant atom, since the valence state of Gd contains one electron more as Eu [59].

Doping affects the electronic properties as well as the magnetic properties of EuO, such as the metal to insulator transition (MIT) with a drop of resistivity by 13 orders of magnitude [26] and an enhancement of T_C. T_C was increased up to 200 K by La doping [67]. The Ruderman-Kittel-Kasuya-Yosida (RKKY) coupling mediated by doping induced charge carriers is one mechanism, responsible for the T_C enhancement [11; 32]. The exact mechanisms of the MIT and T_C enhancement are not fully understood and cannot be explained with doping alone [79]. "The compression of the crystal lattice due to the incorporation of the smaller Gd^{3+} ions plays a crucial role" [79; 80].

In 2001 R. Schiller and W. Nolting performed ferromagnetic Kondo-lattice model (FKLM) band structure calculations of a 20 ML thin EuO(100) film [48]. They calculated the layer dependent band structure in the ferromagnetic phase of EuO as presented in figure 2.4. Their calculations show a band in the surface layer additional to the bands in the center layer. The obvious interpretation of this additional density of states in the surface layer is the existence of a surface state

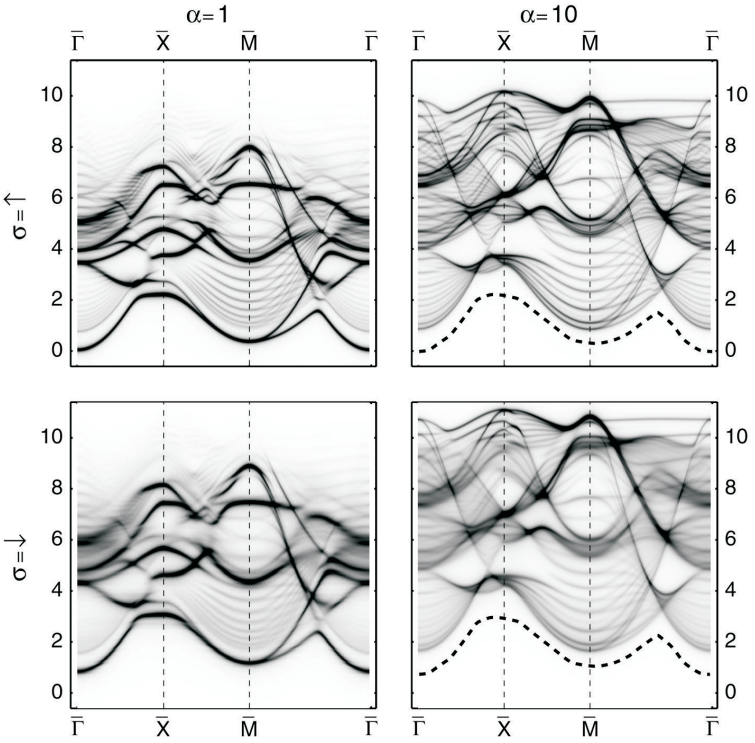

Figure 2.4: Ferromagnetic Kondo-lattice model (FKLM) calculations on 20 ML of EuO(100). The local density of states of the surface layer (α=1) is presented in the left column and of the center layer (α=10) in the right column for T=0 K. "The dashed lines in the spectral densities for the center layers (right hand side) reproduce the positions of the lower band edges of the surface state bands as given by the spectral densities of the surface layers (left hand side). The energy zero refers to the Fermi energy." [48]. Taken from reference [48].

(SS). According to the KFLM calculations the SS shows a parabola-like dispersion relation with an effective mass of $0.6 \times m_e$, whereby m_e is the mass of a free electron. The SS is spin split by 0.78 eV (extracted from figure 3 of reference [48]) and spin polarized in the ferromagnetic (FM) phase [48]. "The lower band edge of these surface state bands lies at the $\bar{\Gamma}$ point about 0.8 eV and at the $\bar{M}$ point about 0.45 eV below the lower conduction-band edge of the "bulk" bands" [48]. The $\bar{\Gamma}$ point of the spin up SS Brillouin zone is claimed to be at the Fermi energy E_{Fermi}, which leads to the idea of an MIT in the EuO(100) surface.

For a general theoretical introduction to surface states the book "Physics at Surfaces" by A. Zangwill [81] is recommended. Additional see historical important experimental work on this topic by M. F. Crommie *et al.* [82; 83].

Magnetism of Bulk EuO and Ultra Thin Films of EuO

The magnetism in EuO originates from the magnetic moment of the Eu 4f electrons. For these 4f electrons a "strong screening by other closed electron shells keeps the Hund's rules valid." [56]. According to Hund´s rules the half filled Eu 4f orbital in EuO gives rise to a pure spin angular

momentum J of J=S=7/2, with no component of an orbital angular momentum L. So with a Landé factor of g=2, the magnetic moment amounts to 7 μ_B per Eu atom. The macroscopic magnetization of an EuO crystal is gained by parallel alignment of the single atomic magnetic moments through the effective ferromagnetic exchange interaction. Because the EuO ground state is spherical symmetric $^8S_{7/2}$ the magnetic exchange interactions are isotropic and can be described by a simple Heisenberg model [11]. In this model the exchange interaction is described by the Hamiltonian in Eq. (2.1) with the exchange constant J_{ij}, between spin moments $\vec{S}_i$ and $\vec{S}_j$ at the sites i and j

$$\mathcal{H} = -\sum_{i,j} J_{ij}\vec{S}_i\vec{S}_j. \tag{2.1}$$

Since the 4f electrons are highly localized, a direct exchange mediated by overlapping 4f wave functions between neighboring Eu^{2+} ions can be neglected [79; 84] and an indirect exchange mechanism must be taken into account. Famous for the mediation of an indirect long range exchange coupling between localized magnetic moments is the Ruderman-Kittel-Kasuya-Yosida (RKKY) interaction, for example in gadolinium [85], or in heavy-fermion systems like $CeCu_{6-x}Au_x$ [86]. But since the RKKY interaction is based on the spin polarization of conduction electrons it does not hold for the semiconductor EuO. For a long time the exchange mechanism in EuO was not understood, but many models on this topic evolved [11; 29; 56; 87–91] since EuO is considered as a Heisenberg model ferromagnet and its Hamiltonian [Eq. (2.1)]is easy to treat. Nevertheless the Heisenberg model cannot be solved exactly in an analytical way, but in good approximation the exchange mechanism can be described by two indirect interactions, one between Eu^{2+} nearest neighbors (NN) and another between Eu^{2+} next nearest neighbors (NNN) [79; 92].

The exchange constant J_1 represents the NN exchange, which is a virtual transition of Eu^{2+} 4f electrons via a 5d or 6s state to an NN Eu site where it polarizes the 4f spin [11; 91]. Of course J_1 is the sum over all NN Eu atoms exchange interactions of an Eu site i. J_1 is found to be positive and therefore to mediate a ferromagnetic coupling with the coupling strength of J_1=$5.22 \cdot 10^{-5}$ eV [93; 94].

The 4f exchange coupling to an Eu^{2+} ion on site i originating from a NNN site j mediated by an oxygen p state [11], also called superexchange mechanisms, is rather complex and can be separated into three contributions as proposed by T. Kasuya [84]:

1. The Kramers-Anderson mechanism: A 4f electron is transfered to an NNN 4f state via the O p bands where it forms a pair of Eu^{3+} and Eu^{1+} ions. Just a small antiferromagnetic exchange is given by this contribution.

2. An O^{2-} p electron ion is transferred to the 5d or 6s states of the NNN Eu^{2+} site by the d-f exchange interaction. On the NNN Eu^{2+} site "it aligns the 4f spins through the d-f or s-f exchange interaction leads also to an antiferromagnetic coupling" [79].

3. The third therm is "a cross term between Kramers-Anderson mechanism and the d-f exchange interaction is considered with p-d, f-p, and d-f transitions involving an inter atomic exchange" [79].

These complex exchange mechanisms determines the exchange constant J_2, for which the sum in Eq. (2.1) over all NNN sites must be considered. J_2 has been investigated experimentally by neutron scattering and specific heat measurements and found to be ferromagnetic in total and amounts to the value of J_2=1.03 $\cdot$ 10^{-5} eV [93; 94]. Since the sum over J_1 and J_2 is positive, the magnetic coupling in EuO is effectively ferromagnetic. NMR studies found the EuO$\langle 001 \rangle$ axes to be the hard magnetization axis and the EuO$\langle 111 \rangle$ axis to be the axis of easy magnetization [95]. For films of EuO "the magnetization will always be in the film plane" [36]. Despite plenty of theoretical and experimental studies on the exchange mechanism in EuO there are still a lot of open questions [96]. The ferromagnetic character of J_2 depends strongly on the Eu-Eu distance as revealed by the other Eu chalcogenides which have a weaker ferromagnetic coupling due to the larger anion radius. For the case of EuS this results in a T_C of 40 K [11], which is lower than the T_C of EuO. For EuSe and EuTe it results in an antiferromagnetic coupling.

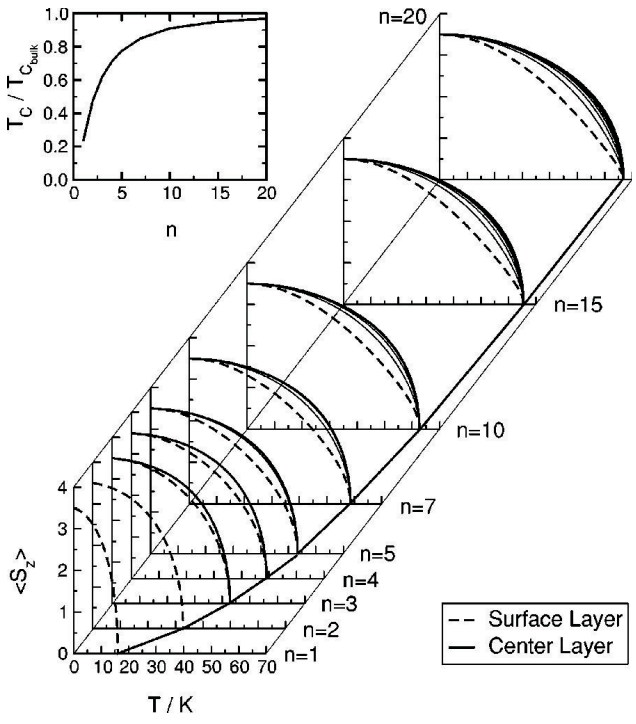

Figure 2.5: "Layer-dependent magnetizations $\langle S_\alpha^z \rangle$ of EuO(100) films as functions of temperature for various thicknesses n. $\langle S_\alpha \rangle$ always increases monotonously from the surface layer towards the film center. Inset: Curie temperature as a function of film thickness"[48]. Taken from reference [48].

Work on the magnetic properties in thin EuO films is summarized in the following. Especially the influence of the film thickness on the magnetization and therefore on the Curie temperature $T_C(n)$ of EuO is presented in this section, where n is the film thickness in atomic monolayers

(ML) of EuO(100). In 2001 R. Schiller *et al.* performed calculations on thin films of stoichiometric EuO(100) as the ideal Heisenberg ferromagnet with S=7/2 in the thickness regime from 1 ML to 25 ML [48; 56]. They treated these layers with a "combination of a multiband Kondo lattice model with first-principles tight-binding linear muffin-tin orbital band-structure calculations" [56]. The Curie temperature is T_C=15 K for a single atomic layer of EuO(100) and increases up to the bulk value with increasing film thickness, see figure 2.5. The bulk value of T_C =69 K [5] is reached at about n=25 ML, which corresponds to a thickness of 6.43 nm. Figure 2.5 also reveals a decreased magnetization of the surface layer of the film compared to the center layer of the film. This effect can be explained by the lower coordination number of the surface Eu^{2+} ions and therefore missing magnetic exchange partners compared to these of Eu^{2+} ions in the bulk. So in case of the surface layer the magnetic exchange coupling of less neighboring sites is summed up.
In 2008 T. S. Santos *et al.* [1] and in 2009 M. Müller *et al.* [2] contributed to in this field with experimental work. T. S. Santos *et al.* utilized ultra thin films of EuO as tunnel barriers. $T_C(n)$ is displayed in figure 2.6, it follows qualitatively the behavior calculated by R. Schiller *et al.*. Besides this, "a large exchange splitting of the conduction band" [1] and nearly fully spin-polarized tunneling current is found when using the films as tunnel barriers, which demonstrates the feasibility of spin filter devices based on ultra thin EuO films.

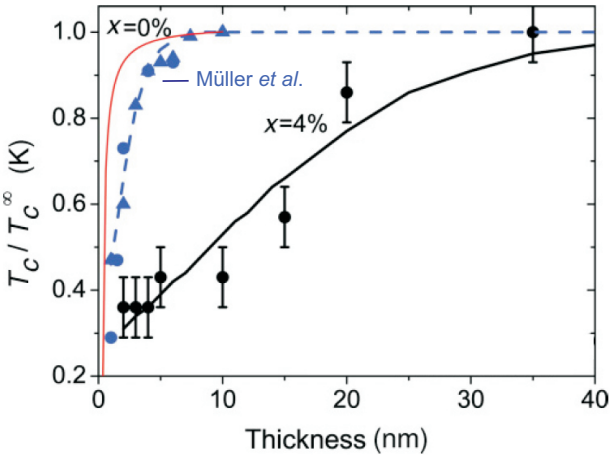

Figure 2.6: T_C vs. film thickness of different EuO samples normalized to the bulk value of T_C. The blue data originated from stoichiometric EuO samples. The data for the blue triangles is taken from reference [1] and for the blue circles are taken from reference [2]. The red curve represents a function from reference [3] fitted to the maximum value of T_C. The black data points represent the $T_C(n)$ dependence of $Eu_1O_{0.96}$ thin films. Figure modified from reference [3].

M. Müller *et al.* [2] claim that beside the major role of the reduced Eu^{2+} coordination number in the surface and interface layer a "reduced magnetic ordering at interfaces due to structural and chemical intermixing becomes particularly relevant in the low thickness regime" [2]. Therefore they take "layer-dependent magnetic moments and the effect of non-ideal interfaces" [2], into account. The magnetization is suppressed especially by the intermixing effect compared to a perfect interface to the substrate. Oxygen deficient sputtered ultra thin films of $Eu_1O_{0.96}$ are investigated by M. Barbagallo *et al.* [3]. These films also show a thickness dependent $T_C(n)$ behavior in which the Curie temperature of bulk $Eu_1O_{0.96}$ is reached at a layer thickness of about 140 ML EuO(100), see figure 2.6. The degraded magnetization is explained in terms of partially depopulated 4f states

upon band bending at the interface to a platinum capping layer [3]. Summarizing this section the Curie temperature T_C of ultra thin EuO films is lowered by finite size effects, interface effects and imperfections.

2.2 Mean Field Magnetization

This section summarizes the Weiss model of a ferromagnet and the effect of an external magnetic field on a ferromagnet as explained in the book "Magnetism in Condensed Matter" by S. Blundell [97].

What a ferromagnet and a paramagnet have in common are unpaired electrons resulting in effective magnetic moments per atom. These can be aligned in an external magnetic field resulting in a macroscopic magnetization. The character of a ferromagnet is to align those moments spontaneously without an applied external magnetic field. All magnetic moments are aligned in one direction, at least within one magnetic domain [97; 98]. This spontaneous magnetization is due to the exchange interactions J_{ij}, as discussed for the case of EuO in section 2.1. The Hamiltonian which describes a ferromagnet in an external magnetic field $\vec{B}$ (see Eq. (2.1)) expands to [97]

$$\mathcal{H} = -\sum_{i,j} J_{ij}\vec{S_i}\vec{S_j} + g\mu_B \sum_j \vec{S_j}\vec{B} \tag{2.2}$$

where g is the Landé factor and μ_B the Bohr magneton. To solve this Hamiltonian a molecular field at the i^{th} site is defined by [97]

$$\vec{B}_{mf} = -\frac{2}{g\mu_B}\sum_j J_{ij}\vec{S_j}. \tag{2.3}$$

$\vec{B}_{mf}$ is considered as a field in the material that mediates the magnetic order. Because the exchange interaction is replaced by the effective molecular field $\vec{B}_{mf}$, the effective Hamiltonian [97] can be written as

$$\mathcal{H} = g \cdot \mu_B \sum_i \vec{S_i} \cdot (\vec{B} + \vec{B}_{mf}). \tag{2.4}$$

Equation (2.4) has the form of the Hamiltonian of a paramagnet in an applied field $\vec{B} + \vec{B}_{mf}$, therefore the materials magnetization should follow the Brillouin function $B_J(y)$, whereby $y(B,T)$ is an order parameter depending on temperature and magnetic field. The Brillouin function $B_J(y)$ emerges from the quantum mechanical description of a paramagnet and can have values between 1 and -1. Therefore the magnetization M of a paramagnetic sample with saturation magnetization M_S is given by [97]

$$M = M_S \cdot B_J(y). \tag{2.5}$$

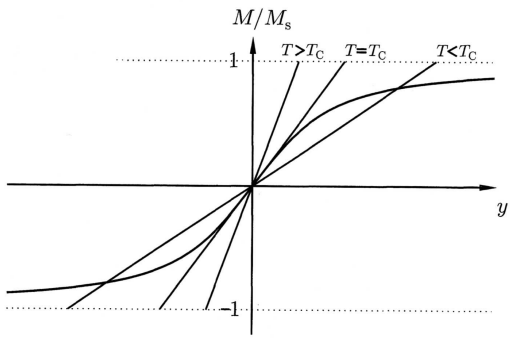

Figure 2.7: Plot of Brillouin function $B_J(y)$ (curved line) and Eq. (2.7) for different values of T and B=0. Taken from figure 5.2 of reference [97] by courtesy of Oxford University Press.

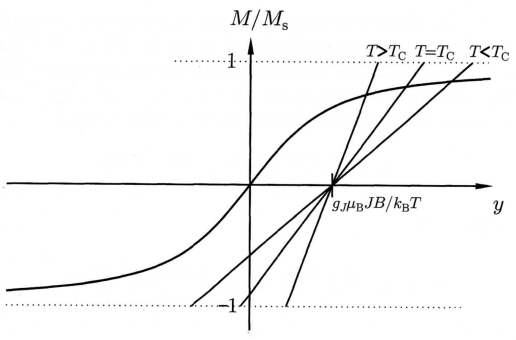

Figure 2.8: Plot of Brillouin function $B_J(y)$ (curved line) and Eq. (2.7) for different values of T and B≠0. Taken from figure 5.4 of reference [97] by courtesy of Oxford University Press.

The Brillouin function for a paramagnet should not be confused with the Heisenberg mean field magnetization for a ferromagnet. The order parameter y is [97]

$$y = \frac{g \cdot \mu_B \cdot J(B + \lambda \cdot M)}{k_B \cdot T} \tag{2.6}$$

where $\lambda \cdot M = B_{mf}$ with the positive order parameter λ, the Boltzmann constant k_B and the total angular momentum J. Equation (2.6) differs from the paramagnetic case with the λ·M term. Equation (2.6) can be transformed to

$$M = \frac{k_B \cdot T \cdot y}{g \cdot \mu_B \cdot J \cdot \lambda} - \frac{B}{\lambda}. \tag{2.7}$$

Since both equations Eq. (2.5) and Eq. (2.7) give an expression for the magnetization $M(y)$ as the function of the order parameter y the Weiss model of a ferromagnet is solved where Eq. (2.5) equals Eq. (2.7). This equation is solved graphically for each temperature T. First the graphical solution in the case of zero applied field B=0, (only the mean field $\vec{B}_{mf}$ has to be taken into account) is performed in figure 2.7.

Eq. (2.5) and Eq. (2.7) are plotted qualitatively in figure 2.7 vs. the order parameter y for some arbitrary value of the total momentum J and zero applied field B=0. The ferromagnet's magnetization is the value of M/M_S where the plots of Eq. (2.5) and Eq. (2.7) intersect, see figure 2.7. In the case of high temperatures, i.e., $T \geq T_C$, no graphical solution can be found and therefore no spontaneous magnetization occurs.

As can be seen in figure 2.8, a non-zero external magnetic field $B \neq 0$ in Eq. (2.7) results in a graphical solution of M with $M \neq 0$ for all temperatures because the plots of Eq. (2.7) are shifted to the right in figure 2.8. The larger the applied field the higher the magnetization, of course with the limit of the saturation magnetization M_S. Figure 2.9 shows the effect of an increasing applied field B on the $M(T)$ behavior qualitatively. The magnetic phase transition between the ferromagnetic

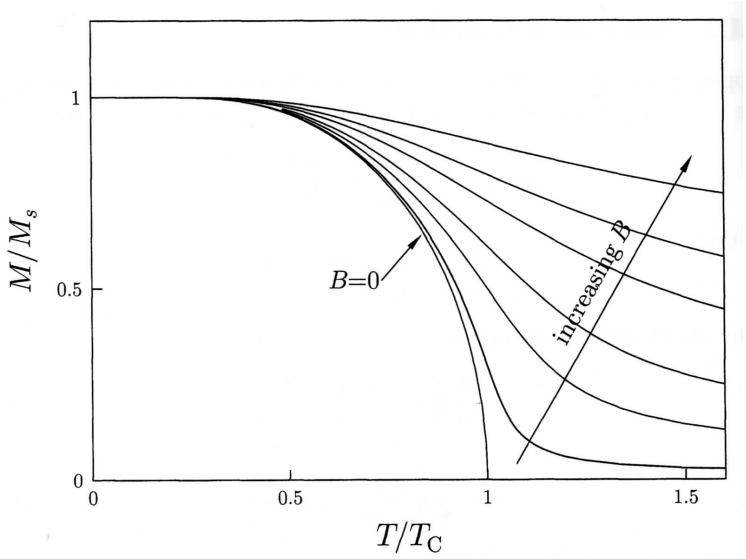

Figure 2.9: Mean field magnetization vs. temperature for various applied magnetic fields B. Taken from figure 5.5 of reference [97] by courtesy of Oxford University Press.

and paramagnetic phase does not occur for $B \neq 0$. In other words the magnetization is enhanced by the applied external field, which is important for magnetization measurements in high external fields in chapter 6. Thus experiments to determine the ferromagnetic transition temperature T_C have to be performed in zero field in an ideal case, otherwise one has to compensate for the effect of an enhanced magnetization.

2.3 Magneto-Optics

In 1877 J. Kerr first reported on the "rotation of the plane of polarization by reflection from the pole of a magnet" [7], which was the discovery of magneto-optical effects. Magneto-optical [99–105] materials manifest themself in the change of polarization of polarized light at reflection or transmission at a sample [101]. One speaks of the Faraday effect in the geometry of light transmitted through a material and of the Kerr effect in the case of reflection geometry. In this thesis only the Kerr geometry is utilized.

"On a microscopic level the Kerr effect is a consequence of the interaction between the radiation field and the electrons which under exchange lead to magnetization of the solid"[101]. This means that magneto-optical effects originate in materials from the coupling of an elastical electron motion, excited by light, to a static sample magnetization. As a macroscopic approach at optical wavelengths magneto-optical effects can be described in a dielectric tensor $\hat{\epsilon}$ [106]. The matrix elements ϵ_{ij} of $\hat{\epsilon}$ are introduced for the presence of a magnetic field $\vec{H}$ to satisfy the Onsager relations [99; 106]:

$$\hat{\epsilon}_{ij}(-\vec{H}) = \hat{\epsilon}_{ji}(\vec{H}). \tag{2.8}$$

One can expand $\hat{\epsilon}$ to a scalar term ϵ_0 and a matrix $\hat{\epsilon}_\mathrm{H}$ [99; 106] with components linear in $\vec{H}$:

$$\hat{\epsilon}_\mathrm{H} = \begin{pmatrix} 0 & \epsilon_{12} & -\epsilon_{13} \\ -\epsilon_{12} & 0 & \epsilon_{23} \\ \epsilon_{13} & -\epsilon_{23} & 0 \end{pmatrix}$$

The matrix $\hat{\epsilon}_\mathrm{H}$ is found to be antisymmetric, with non vanishing magneto-optical coefficients on its off diagonal elements. Different indices of refraction for different circular polarizations of light, of which linear polarized light is composed of, are revealed by $\hat{\epsilon}_\mathrm{H}$. This is the origin of the Kerr rotation of linear polarized light Θ_Kerr [99]. Since $\hat{\epsilon}_\mathrm{H}$ is supposed to be linear in $\vec{H}$ the Kerr rotation Θ_Kerr is proportional to the sample magnetization. Additionally a Kerr ellipticity, which is also linear in $\vec{H}$, emerges in the case of different absorption probabilities of different circular light polarizations [99].

The capability of MOKE is demonstrated in magnetic measurements on bulk samples, thin magnetic layers and even on magnetic monoatomic thin layers [105]. Due to the big magneto-optical effects in EuO, such as a Kerr rotation of 7.1° for bulk EuO [6], which is the largest known Kerr effect for any material, the magnetism of EuO has often been investigated by means of MOKE [9; 62; 70; 107–112; 112–120]. While magneto-optical effects are customarily utilized in data storage media [8] a "rotation device" device based on the Faraday effect in EuO has also been invented [117].

3 The Low Temperature Scanning Tunneling Microscopy Apparatus

The low temperature scanning tunneling microscopy (LT-STM) ultra high vacuum (UHV) setup is constructed by SPS-CreaTec GmbH [121] and consists of three UHV chambers, namely a load lock, a preparation chamber with a base pressure of 1.0×10^{-10} mbar and an STM chamber with a Cryovac helium bath cryostat. The vacuum in the UHV system is generated with turbo molecular pumps, ion getter pumps, titanium sublimation pumps and cooling traps.
Several types of sample holders are available at the LT-STM system for processing different types of samples, for instance metal single crystals and wafer samples. Details on the sample holders are presented in section 3.1. In the following the equipment and modifications of the UHV system are explained.

The load lock serves for the transfer of sample holders into / out of the preparation chamber. It has been improved by an extended sample transfer rod which now can carry two sample holders instead of one in the original design in order to allow more efficient sample transfers.

In the preparation chamber sample holders can be stored in a sample storage. The preparation chamber is equipped with the following devices for sample preparation and characterization: A four pocket electron beam (e-beam) evaporator, a quartz microbalance, an ion sputter gun, a hydrogen atomic beam source (HABS), gas supply pipes, a quadrupole mass spectrometer (QMS), and a multi channel plate low energy electron diffraction (MCP-LEED) device. Knudsen effusion cells are added to the preparation chamber within the work of this thesis. As the most important upgrade a home-built magneto-optical Kerr effect (MOKE) apparatus is added, as described in the next chapter. The samples can be moved through the UHV system with a manipulator. Details on the manipulator are explained in section 3.2.
The *in-situ* preparation of STM tips can be performed in the preparation chamber by ion bombardment and annealing. Therefore, a circular shaped filament formed from 0.18 mm tungsten wire is added at the downside of the sample storage. The STM tips are positioned in the center of the filament and annealed with it. The circular shape is established to supply the power of the filament uniformly to the tip during annealing.

The whole STM and STS measurements presented in this thesis are performed with a Besocke beetle type STM. The STM is mounted electrically isolated on three springs at the bottom side

of the helium bath cryostat and is surrounded by a radiation shield to avoid heating by thermal radiation. The STM is stabilized at 5.3 K at normal operation [122]. The whole STM, including the sample holder, can be heated up to 300 K during cooling by reverse biasing a Zener diode on the STM base plate. In thermal equilibrium of the STM a very low lateral and vertical drift of the STM tip with respect to the sample allows spectroscopy measurements for hours. Since the helium cooled cryostat acts as an effective cooling trap the sample surfaces are found to stay free from atomic adsorbates for weeks.

Nonmagnetic tungsten STM tips are used as local probes. The preparation of these STM tips is explained in great detail in section A of the appendix. STM and STS measurements are performed at 5.3 K, if not stated otherwise. The bias voltage U_{Bias} is applied to the sample via the thermocouple wires which are spot welded to the metal single crystal. The STM tip is on ground potential. By applying a positive voltage to the sample electrons tunnel from the tip into unoccupied sample states. The tunneling current is amplified by a Femto DLPCA-200 preamplifier, used at 10^9 gain in its low noise mode, and converted to a direct current (DC) signal in the range of -10 V to +10 V. The output signal of the preamplifier is adjusted to zero out of tunneling contact. STM images and STS maps are measured in constant current mode if not stated otherwise and are analyzed and post processed using WSxM [123].

An excellent vibration isolation and damping of the STM is crucial. Therefore, the whole LT-STM setup was first hung on the ceiling with large metal springs. Since the setup has to be aligned exactly horizontal, but the center of mass of the whole setup changes with the filling level of the He bath cryostat, we changed the external damping system to pneumatic laminar flow vibration isolator feet. Therefore the screed has been cut away from the lab floor and the damping feet are mounted directly on the concrete.

3.1 Sample Holders and Tip Tool

The sample holders of the LT-STM system can carry different types of samples. All kinds of sample holders have the same type of base body in common, but differ in buildups. Here we present a metal sample holder and an electron beam (e-beam) sample holder. A sample heating and a type K thermocouple are integrated in both types of sample holders. Since the utilized temperature sensor has to cover the whole temperature range from low temperatures (cooling with liquid helium) for MOKE measurements on EuO to high temperatures (1500 K) for substrate preparation a type K thermocouple is the tool of choice. The disadvantage of a type K thermocouple is its poor resolution and a small thermo voltage in the low temperature range compared to a Zener diode.

During the technical part of this work one e-beam and two metal sample holders have been build up. Some extrusions have been milled away on the sample holders base bodies (compare figure E.10) to make it fit into the slot of the MOKE-magnet (see Sec. 4.2). All parts of the sample holders, which

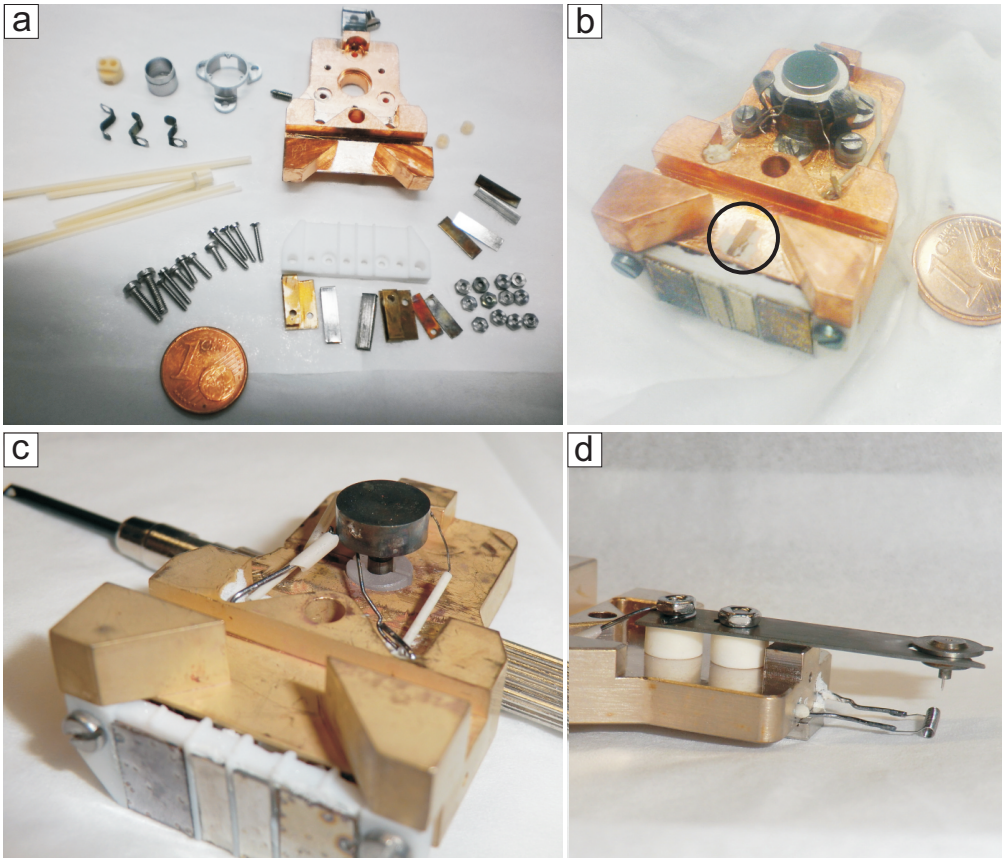

Figure 3.1: a) Photograph the home-built e-beam sample holder parts before assembly. b) Assembled e-beam sample holder with an Ir(111) single crystal mounted. An additional contact is added to the sample holder (marked by black circle). c) Picture of metal sample holder without a sample. d) Photo of tip tool with tip heating station and mounted tip holder.

get hot during sample preparation, have been degassed before assembling in UHV. Two standard metal sample holders are assembled and modified. The sample holders are optimized by home-built contact plates which allow the feeding of a type K thermocouple to the sample without cut. These metal sample holders serve for the investigation of low melting metal single crystals such as Ni(100) and Au(111). Temperatures up to 1170 K are achieved by applying 6.0 V and up to 3.0 A to the used HeatWave UHV button heater. One of such sample holders is displayed in figure 3.1 c). The sample is put directly on the button heater and attached to it with tungsten clamps. The heater is clamped to the sample holder body between two sapphire U-profiles for electrical isolation and for reasons of thermal isolation of the sample surroundings at high temperatures and a good thermal connection to the helium vaporization cryostat (of the manipulator) at low temperatures.

For preparations at higher temperatures an e-beam sample holder, as displayed in figure 3.1 a) and b), is also set up. (Parts and technical drawing for this sample holder were developed previously in our group). The e-beam sample holder design has been optimized by means of an additional contact (figure 3.1 b)) putting the sample on ground potential if the sample holder is grabbed with the manipulator, but leaves the sample isolated when it is put into the STM. This enables us to use

the e-beam heating and measure the sample temperature via the type K thermocouple at the same time as needed for the preparation of EuO films. Also the contact plate of the e-beam sample holder is supplemented by type K thermocouple contacts and optimized to fit into the slit of the MOKE-magnet yoke. A cylindrical filament is handmade out of 0.13 mm tungsten-rhenium wire. Due to its small cross section low filament currents of 1.80 A are sufficient to operate the filament in the sense of e-beam heating, which is reasonable because the supply cables on the manipulator side are only desired to carry a maximum current of 3.5 A. Sapphire balls with a diameter of 1.0 mm are used to isolate the sample for the same reasons as explained above. We achieved temperatures of 1500 K easily with this sample holder. When cooling the sample holder with the vaporization cryostat of the manipulator a sample temperature down to 50 K can be reached with the e-beam sample holder and 44 K with the metal sample holder. These lowest achievable temperatures are measured after optimization and calibration of the thermocouple the in June 2012.
A tip tool serves to transfer and exchange STM tips into or out of the STM. A special tip tool with an integrated filament allows for the annealing of the STM tips directly at the tip tool by electron beam heating, see figure 3.1 d). This serves as an alternative tip heating stage to the filament mounted on the downside of the sample storage. A typical tungsten tip after annealing with the tip tool is presented in the appendix (figure A.5 a)). The tip annealing with this tool works well even though its filament is not circular shaped.

3.2 The Manipulator

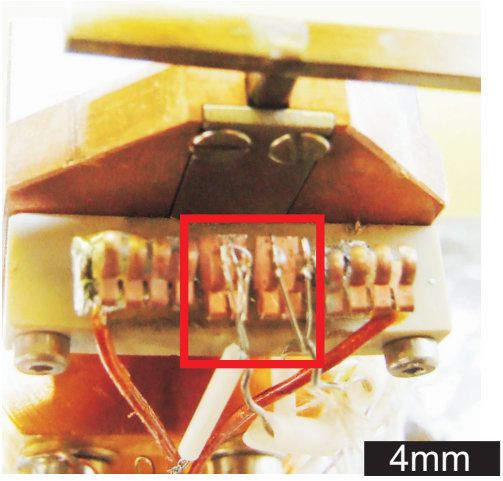

Figure 3.2: Photograph of the front of the manipulator head showing modified contact springs. The contact springs are the counter-piece to the contact plate of the sample holders. Type K thermocouple wires are spot welded onto the CuBe springs.

The sample holders (see previous section) can be used with a VAB [124] PM 25 - 500 precision manipulator, which is mounted to the preparation chamber. Cooling down can be performed with a type HVK-STM helium vaporization cryostat. The manipulator enables the transfer, movement and electrical contact of sample holders. It is delivered by SPS-CreaTec GmbH [121] with six CuBe

springs which serve as electrical contacts to the sample holder for the sample heating (integrated on each sample holder) and for measurements of the sample temperature. The middle contacts number three and number four, as marked by the box in figure 3.2, serve as contacts for the type K thermocouple. An Alumel ($Ni_{95}Mg_2Al_2Si_1$) and a Chromel ($Ni_{90}Cr_{10}$) wire was originally fed to these springs but did not go on continuously over the springs to the sample. This configuration is only suitable for temperature measurements if there is no temperature gradient at the contact springs, since otherwise also a thermovoltage occurs at the contact springs. As a consequence wrong temperature measurements occurred. This problem is technically solved in December 2010 by spot welding type K thermocouple wires onto the contact springs as visualized in figure 3.2. With this modification the thermocouple wires are fed to the sample without cut-off. As an incidental remark the Alumel wire must not be mistaken with a pure nickel wire which causes an error of 10 % in the high temperature measurements as shown in work of D. Pollock [125].
In June 2012 the contacts of the manipulator are re-designed in a mechanical and electrical more sophisticated way by S. Runte.

3.3 The Molecular Beam Epitaxy Station

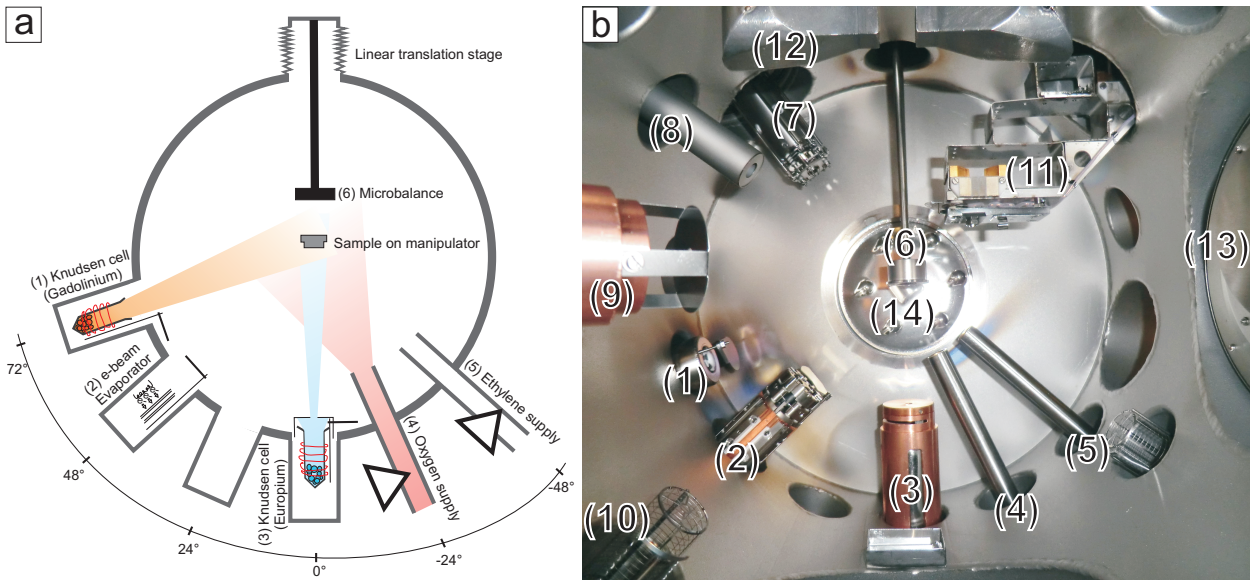

Figure 3.3: a) Sketch of the MBE station in the preparation chamber of the LT-STM system. The sketch corresponds to the A-A cut of the constructional drawing in figure E.32. b) Labeled photograph of the preparation chamber taken along the chamber's long axis. The following devices are mounted to the LT-STM preparation chamber as labeled by numbers: (1) Knudsen cell (gadolinium) WEZ40-20-16-KS, (2) e-beam evaporator Specs EBE-4, (3) Knudsen cell (europium) NTEZ40-2-16-KS, (4) oxygen supply pipe, (5) ethylene supply pipe, (6) Sycon [126] STM-100/MF quartz microbalance, (7) Prisma^{TM} QMS 200, (8) Kremer IS 10 ion sputter gun, (9) HABS-40-A, (10) Bayard Alpert gauge, (11) sample storage, (12) home-built electromagnet, (13) OCI MCP LEED BDL800IR, and (14) a VAT valve to the STM chamber.

Samples investigated in this thesis are grown *in-situ* by chemical vapor deposition (CVD) and molecular beam epitaxy (MBE) in the preparation chamber. A set of DN40CF flanges equipped with evaporators, gas inlet pipes and a quartz microbalance are arranged concentrically around the manipulator axis. This geometrical arrangement allows the simultaneous deposition of different materials as visualized in figure 3.3. For the growth of thin doped, or stoichiometric films of EuO two Knudsen effusion cells and two gas inlets are mounted to the chamber, see figure 3.3. High purity europium (Eu) from the Ames laboratory [127] is evaporated from an Al_2O_3 crucible at temperatures between T_{Knudsen}=670 K and 710 K in a low temperature effusion cell NTEZ40-2-16-KS made by the Dr. Eberl MBE Komponenten GmbH [128]. The Knudsen cell including its crucible and Eu wrapped in tantalum were degassed before at 870 K in UHV. The base pressure of the LT-STM preparation chamber does not rise above 1.0×10^{-10} mbar during evaporation of europium. The cell is mounted in a distance of 10 cm to the sample and evaporation rates around 1.0 Å Eu/min are reached at $T_{\mathrm{Knudsen}}\approx$700 K. The dopant gadolinium (Gd) is evaporated in the same way as Eu, but at evaporation temperatures from 1350 K to 1420 K from a high temperature effusion cell WEZ40-2-16-KS from an Al_2O_3 crucible. Gd doped samples are not presented in this thesis, but the evaporator is listed here for the sake of completeness. The base pressure of the preparation chamber rises up to 5.0×10^{-10} mbar at usage of the high temperature effusion cell. The distance to the sample amounts to 14 cm. The molecular beams of both Knudsen cells enclose an angle of 72°, as can be seen in the sketch. The evaporation rates of both cells are measured with a quartz microbalance STM-100/MF from Sycon instruments [126] which can be moved to the later sample position prior to film growth with help of a linear translation stage. So the evaporation rates are measured directly without further calculations. Molecular oxygen (O_2) is dosed with help of a leak valve and leaded via a gas inlet pipe to the sample, which is positioned in front of the pipe. The O_2 partial pressure p_{O_2} in the preparation chamber is checked during growth with a Pfeiffer Prisma$^{\mathrm{TM}}$ QMS 200. The QMS is always used with following settings to control p_{O_2}: a dwell time of 0.2 s, a resolution of 50 an SEM voltage of 1.4 kV and mass of 31.81 amu.

The QMS signal, in numbers of $\mathrm{I}_{\mathrm{QMS}-\mathrm{O}_2}$, has to be calibrated to the local molecular oxygen pressure p_{O_2} at the sample position. A first attempt was done by the adsorption of O_2 on Ni(100) at 400 K. Molecular oxygen dissociates at the metallic Ni(100) surface and forms oxygen adsorbate superstructures, namely a p(2 × 2) superstructure at low O_2 doses which converts to a c(2 × 2) superstructure at higher O_2 doses [129]. A more precise calibration followed by the number of oxygen atoms in an EuO film, under the assumption that all oxygen reacts (with europium) to EuO. Thereby the gas inlet pipe was found to enhance the local pressure at the sample by a factor of 85±10 compared to the background pressure. A oxygen background QMS signal of 1.5×10^{-10} $\mathrm{I}_{\mathrm{QMS}-\mathrm{O}_2}$ (always used to grow EuO) corresponds to a local oxygen pressure of $p_{O_2} = 1.6 \times 10^{-8}$ mbar at the sample.

The ethylene dosing pipe is of the same geometrical dimensions as the oxygen one and therefore also

its enhancement factor is the same. The mass spectrometer signal of the ethylene partial pressure is $I_{QMS-Ethylene}$. To utilize $I_{QMS-Ethylene}$ as a process parameter one must note that the following mass spectrometer settings are used for measuring the ethylene signal: mass of 28 amu, an SEM voltage of 1400 V, a dwell time of 0.2 s, and a resolution of 10.
The chamber pressure is decreased quickly after dosing gases by connecting an ion getter pump with an integrated liquid nitrogen filled cooling trap to the preparation chamber. The ion getter pump is never connected to the chamber during dosing gases.
Last a Specs^{TM} EBE-4 four pocket e-beam evaporator is mounted to the MBE station. It serves for the evaporation of aluminum (from a molybdenum crucible with a boron nitride liner) as a capping layer for EuO films or for the evaporation of cobalt for example.

4 Development of a MOKE Setup

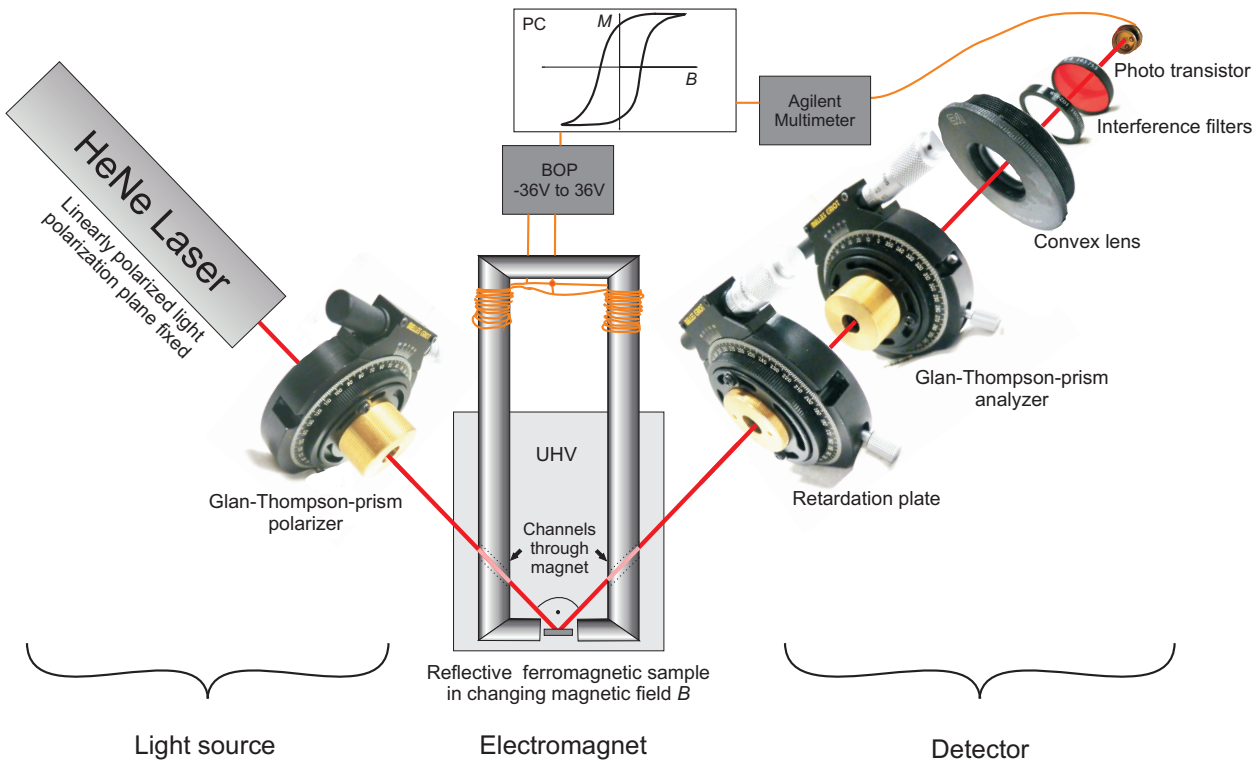

Figure 4.1: Arrangement of the longitudinal MOKE setup. The figure is assembled with drawings and with photographs of the used optical components in their mechanical mountings. The construction aims on the determination of a samples magnetic properties under UHV conditions.

The main technical project of this thesis is the construction, realization, and optimization of a magneto-optical Kerr effect (MOKE) setup. This setup investigates the magnetic properties of samples by the magneto-optical Kerr effect on linear polarized light: the change in polarization upon reflection on a sample is measured. The project contains the development of different parts: a stiff holder for a HeNe laser light source, a electromagnet for applying magnetic fields to a sample, a detector which can resolve the rotation of linear polarized light with high sensitivity and a computer software to support MOKE measurements and data logging. The global arrangement of the setup is visualized in figure 4.1. The base design of the setup is inspired by MOKE instruments of H. P. Oepen [130]. The guiding principle is to put as many components as possible outside the vacuum chamber, namely the laser, coils of the magnet and the detector with all its optical components. These components are mounted onto DN40CF view ports. Consequently the magnetic flux generated by the coils of the magnet has to be fed through into UHV with help of a yoke (see Sec. 4.2), which is welded into a flange.

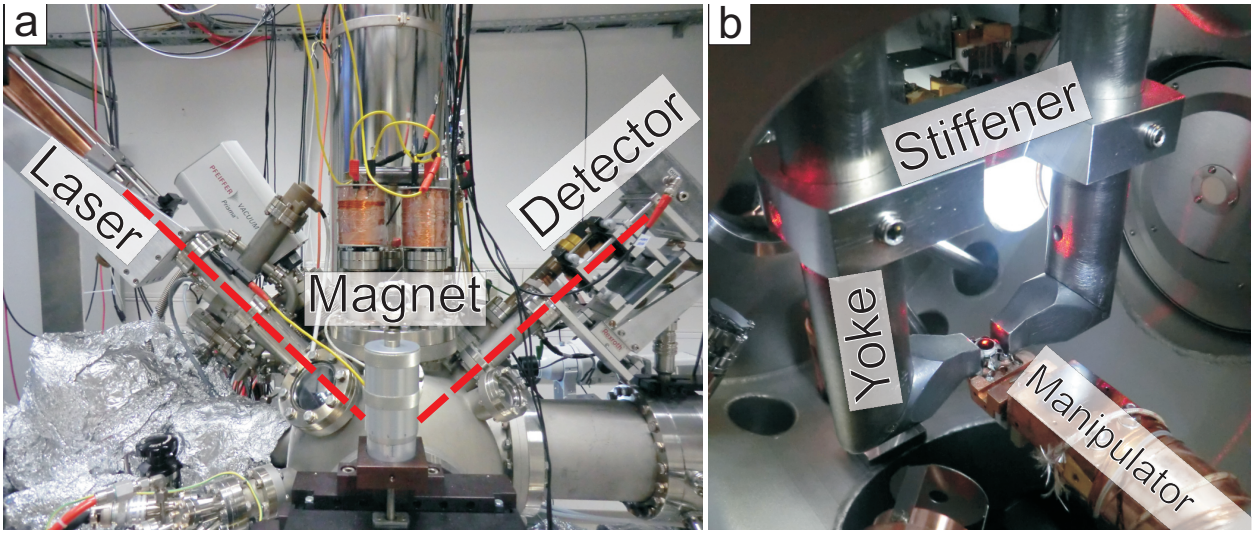

Figure 4.2: a) The LT-STM preparation chamber with the laser mounted on the left side, the magnet in the middle and the MOKE detector to the right. The lasers optical path is indicated by the red lines. b) View into the preparation chamber with a sample in the slot of the magnet and illuminated by the laser beam, which passes through the channels drilled into the yoke.

All parts of the MOKE setup, except for the yoke of the magnet, are constructed from nonmagnetic materials, i.e., aluminum or 1.4429 ESU steel. Also special non-magnetic UHV view ports with Fused Silica Spectrosil 2000® and a tantalum glass-to-metal sealing instead of a magnetic Kovar® sealing have been used for the MOKE setup. In magnetic view ports a Faraday rotation in the order of 0.1 mrad at maximum coil current superimposes the sample's Kerr signal. The improvement by nonmagnetic view ports compared to normal UHV view ports is shown experimentally in section 4.6. The MOKE setup is designed and optimized to be embedded into the preparation chamber of the LT-STM apparatus. It is mounted to the B-B cut of the design drawing in figure E.32 displayed in the appendix. The DN150CF flange in the cut is designated to host the magnet and the DN40CF flanges to host view ports for inlet and outlet of the laser beam. The geometry of the available flanges at the UHV chamber predetermine an incidence angle of 45° of the light onto the sample. The geometry of the cross section of the LT-STM chamber was replicated using a massive aluminum construction as a development and test stage, as can be seen in figure 4.5 and figure E.9. This test setup is later developed to a separate ambient conditions MOKE setup.

4.1 The Light Source

The magneto-optical Kerr effect causes a rotation of the polarization vectors of light upon reflection at a ferromagnetic sample. Therefore, a source of linear polarized light with a spatially fixed polarization plane and a constant intensity is needed. Since the magneto-optical Kerr effect in EuO is strong for red light [111] a Melles Griot [131] 25-LHP-151-230 HeNe laser is chosen as suitable the light source. This laser emits linear polarized light with an extinction ration of 1:500,

meaning that every 500^{th} emitted photon shows the wrong polarization. A high resolution and a very low noise level are desired for the MOKE measurements of this thesis. Therefore a high quality Glan-Thomson prism manufactured by Halle Nachfolger [132] with an extinction ratio of 10^6 is used to highly polarize the light of the laser, which is emitted to the sample. The emitted power of the laser amounts to 5 mW in thermal equilibrium, i.e., after warm up of the laser. Since mechanical vibrations of the laser have to be avoided a stiff mounting of the laser to a DN40CF view port is constructed. The laser holder construction allows for mechanical adjustments on the alignment of the laser and the polarizer prism at the same time. Also the laser to sample distance is kept as short as possible to reduce the influence of mechanical vibrations by a leverage effect.
Upon test measurements on a non magnetic reflective aluminum mirror measurement artifacts are found, which are caused by stray fields of the MOKE-magnet (see Sec. 4.2) on the laser. These artifacts (data not presented) are caused by a Faraday rotation which occurs in the head of the laser. The stray fields are in the order of 1.6 mT. Only stray fields of 1.0 mT are acceptable for proper operation of the laser. As a technical solution a μ-metal shielding tube is built to fully surround the laser, except for a 2 mm hole for the out coming light beam and a feed through for the power cable. Hall probe measurements reveal a shielding of magnetic fields by a factor of 20 inside the μ-metal tube, which turned out to be sufficient to eliminate stray field induced effects on the emitted laser light.
At this point it should be mentioned that the polarization plane of the laser light needs to be adjusted exactly parallel, or perpendicular to the plane of incidence, otherwise one measures some kind of ellipsometry instead of MOKE.

4.2 The Magnet

The magnet is needed to generate constant magnetic fluxes of 0.1 T. This is sufficient to drive most ferromagnets into the magnetic saturation. The magnetic fields are created by two coils. We decided to leave the coils out of the vacuum to cool them with the ambient air. The magnetic flux is carried to the sample by an ARMCO pure iron yoke as presented in figure E.1. The yoke is composed of two legs, two pole shoes and a connection part between the legs. Taking into account the available flanges on the UHV chamber for the laser path and the geometry of the manipulator leads to the realized yoke design. The sample is put in the yokes slit, whose width was first designed to put the utilized sample holders (see figure 3.1) horizontally and vertically inside to measure the longitudinal as well as the polar Kerr effect. Channels are drilled through the yoke for the optical path of the laser light (which penetrates to the sample and is reflected to the detector). Calculations taking into account the yokes susceptibility, a slit dimension of 32 mm and the length of the yoke legs are performed to determine the number of windings on each coil to reach the desired magnetic field of 0.1 T. A current of 6 A running through two coils with about

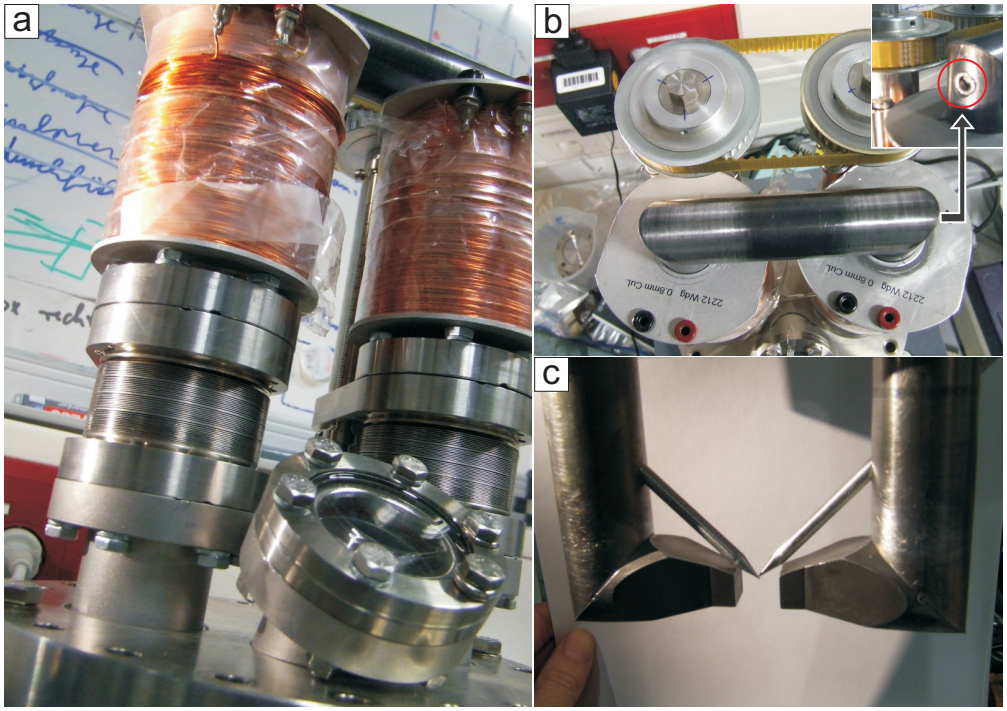

Figure 4.3: Photographs of the electromagnet of the UHV MOKE setup. a) Ambient side of the magnet. Displayed are the coils, linear translation shifts and the top side of the DN15CF host flange. b) Top view on the magnets ambient side. The drive belt which synchronizes the motion of both yoke legs is visible. Red circle in inset: Stiffening of the yoke by screw connection. c) UHV side of the magnet with the sample slot of 14 mm width. Two aluminum rods, representing the laser beam for demonstration purpose, are stuck through the channels for the laser path and demonstrate where the laser hits the sample. The pole shoes are attached by a tungsten inert gas weld spot.

1500 windings each should generate the desired magnetic flux. We decided to but as much windings as possible on the coils winding former, namely 2212. Both coils have the same winding direction. It turned out that the envisaged magnetic flux was not reached because the yoke is magnetically saturated by the coils priorly. The reached magnetic flux with a slit of 32 mm mounting the pole shoes displayed in figure E.4 just amounts to 0.043 T. To enhance the magnetic flux new pole shoes, which result in a smaller slit width of 14 mm are designed. Due to this restriction the used sample holders can only be put into the magnet horizontally, so only the longitudinal Kerr effect can be measured. More detailed considerations about the magnet are worked out in the bachelor thesis of A. Jacobi [133]. The pole shoe design, as presented in figure E.5, is rather complex to let the optical path undisturbed, but to generate spatially homogeneous magnetic fields. Finally with this configuration magnetic fluxes of 0.117 T (measured with a hall probe) are obtained. Calibration curves of the desired magnetic flux B vs. the coil current I are recorded for different maximum coil currents, as presented in figure 4.4. The magnetic flux B is found to be spatially homogeneous in the slit middle, it varies about 1 mT per millimeter.

The sample must be positioned in the center axis of the UHV chamber to utilize certain flanges for MOKE measurements, but since the flanges used for the MOKE devices are on the same UHV

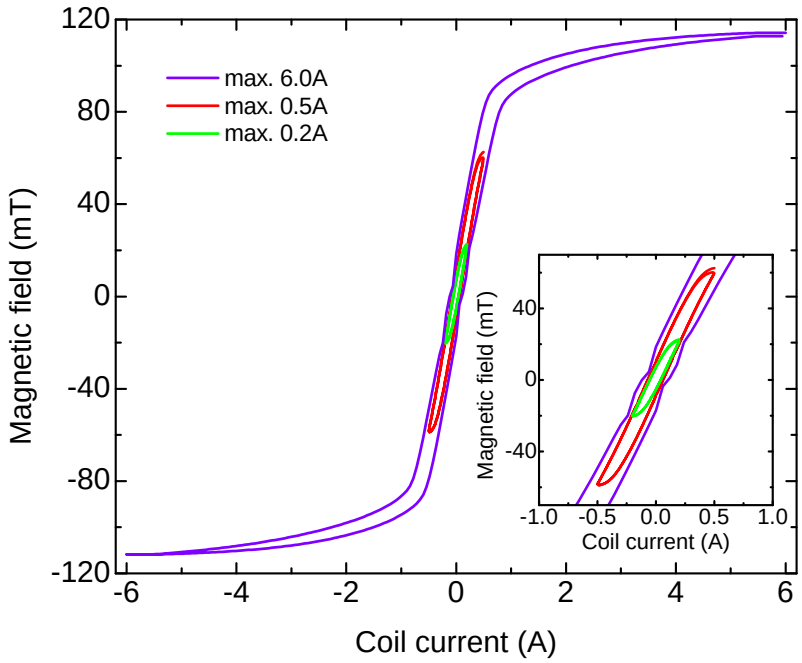

Figure 4.4: Magnetic field B vs. coil current I characteristic for the UHV-MOKE magnet and two coils with 2212 coil windings each, measured with a hall probe in the middle of the 14 mm wide magnet slot. The inset shows a zoom in.

chamber cross section as the LEED device and the load lock the magnet has to be moveable. Therefore VAB linear translation shifts LDK40-100 are used, as is visualized in figure 4.3 a). As one translation module is used for each yoke leg and the modules have some clearance against lateral twisting the yoke needed some extra stiffener. So the yoke legs are connected on the vacuum side by a thick aluminum bar, see figure 4.2 b) and the out of vacuum ARMCO iron cross part is connected with screws to the legs, see figure 4.3 b). Of course the drive of the two translation stages must be synchronized, as realized by a drive belt. The pole shoes are each connected by two welding spots to the yokes legs and adjusted previously exactly with help of installation tools. The exact alignment of all yoke components is important to let the optical path of the laser undisturbed. The right alignment is checked with help of aluminum rods which have to meet in the sample slot of the magnet, see figure 4.3 c).

4.3 The Detector

After reflection at a sample's surface the light beam shines into the detector, which consists of an active NPN silicon photo transistor (PT) BPX 38 operated with a low-noise FET input operational amplifier OPA657 and a high quality Glan-Thomson prism, with an extinction ratio of 10^6 as an analyzer. As the PT is just able to detect a signal intensity, but the aim is to detect a rotation in

the light's polarization plane there is need for a Glan-Thomson prism as analyzer. The principle of MOKE measurements is to set the polarization plane of the analyzer prism perpendicular to the laser light's polarization plane reflected at the sample in zero field and then rotate the analyzer by a small offset angle. In that configuration clockwise, or counterclockwise rotations of lights polarization plane caused by a magnetized sample appear as a decreasing or increasing intensity behind the analyzer and can be detected by the PT.

Further helpful optical components which are positioned between the analyzer prism and the PT are a narrow range interference filter (IF) and a focusing convex lens. To reduce the noise level and background intensity as far as possible only light of the wavelength of the red HeNe laser is let into the PT. The interference filter transmits light in the narrow range about 3 nm around the red HeNe laser line of 632.816 nm to the photo transistor with a high transmissivity of 85%. An additionally filter blocks light in the infrared and ultraviolet spectrum. These IF and the PT are embedded light sealed into a Teflon® bush.

As the laser beam widens upon reflection or by passing the UHV view ports a convex lens is used to focus the light on the active area of the PT which is just about 1 mm^2 large. A lens with an anti reflection coating (optimized for the red HeNe laser line) is utilized for this purpose. The previously described configuration of optical components satisfies the challenges for a high resolution MOKE detector applied at an ambient conditions MOKE setup, i.e., without view ports. Since linear polarized light is transformed upon the transmission through glasses to slightly elliptical light a $\lambda/4$ retardation plate is set in front of the analyzer prism to eliminate these effects of UHV view ports. For mounting and adjusting of the Glan-Thomson prism and the $\lambda/4$-plate high precision rotary holders manufactured by Melles Griot [131] are obstructed. One turn of the micrometer screws of the rotary holder rotates the optics by 0.725° (if the sidewards setscrew is tightened).

All optical components and the PT are mounted in holders which are beaded and mechanically fixed together to one part, namely the detector. The detector is connected to the DN40CF view port of the UHV chamber by an adjustment module, which allows linear translation in three directions and tilting around two axis, see figure E.17. This construction has the advantage of adjusting just one part with respect to the laser beam instead of many optics. To quantify the magnetization of a sample it is important to relate a measured detector voltage V to a Kerr angle Θ_{Kerr}. Therefore a calibration of the $\Theta_{\mathrm{Kerr}}(V)$ has to be performed after every adjustment of the optical path. During MOKE measurements the plane of polarization of the light rotates with respect to the analyzer plane, the calibration works the other way around. The polarization plane of the light is kept constant, while the analyzer is rotated in small angles α denoting the detector signal for each step. The detector voltage V vs. α follows the law of Malus $V \propto I_0 \cdot \sin^2(\alpha)$, whereby I_0 is the constant intensity of the laser. [134]. So a $\sin^2(\alpha)$ function is fitted to the calibration data and gives the relation $V(\alpha)$. The calibration has to be performed starting from the extinction analyzer setting. The operational amplifier of the detector runs into an overload if the detector is exposed to some

low percentage of the total laser power. So the maximum detector signal which corresponds to a Kerr rotation of 90° must be estimated by fitting the $\sin^2(\alpha)$ function to the calibration data and is a feature of the measurement automatization, as presented in the next but one section 4.5.

4.4 The Ambient Conditions MOKE Setup

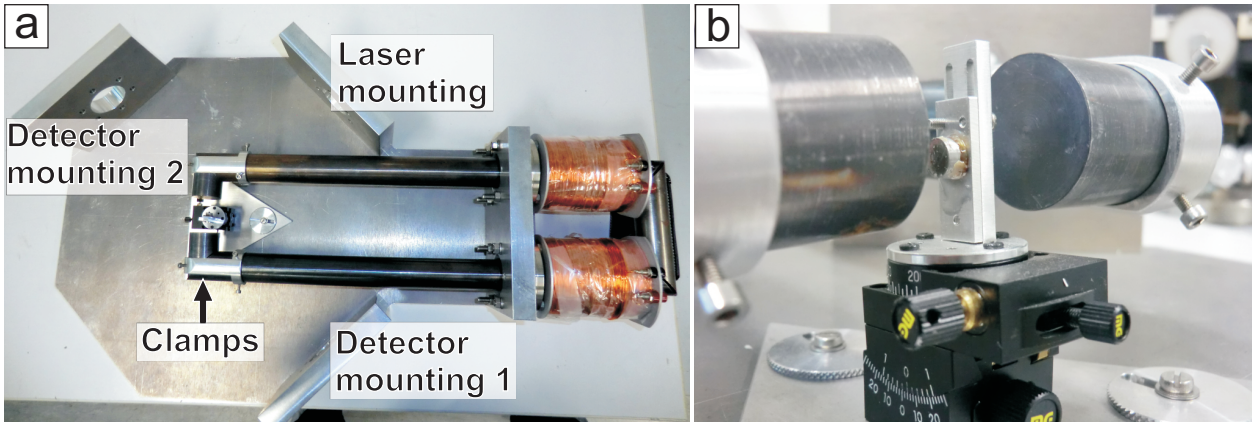

Figure 4.5: Photographs of the ambient conditions MOKE setup. a) The solid aluminum base plate with the mountings for the laser, magnet and detector is based on the flange positions and distances in the LT-STM preparation chamber and served initially as a test setup. b) Magnet slot with sample stage. The pole shoes in the ambient conditions setup are not welded to the yoke legs, but clamped and are easily permutable. The sample stage allows translations in the plane of the base plate, rotations around the samples vertical axis and tilts around the samples center.

An ambient conditions MOKE setup was first completed utilizing the completed laser, magnet and detector as described in the previous subsections. The geometry of the ambient conditions MOKE setup (see figure 4.5 a)) is adapted from the MOKE geometry determined by the LT-STM setup and therefore serves as a test setup for the single components without having to use the LT-STM setup. The development of the ambient conditions MOKE setup is documented in the bachelor thesis of A. Jacobi [133]. Test and technical characterization measurements performed with this setup are presented in section 4.6.

Later the ambient conditions MOKE is developed to a measuring station with its own magnet yoke legs, which are a copy of the UHV yoke's ones. This has the advantage of mounting different pole shoes easily by clamps instead of welding spots. A sample stage, as displayed in figure 4.5 b), is installed with two axis of translational degrees of freedom, one axis of rotation and tilting along samples horizontal middle axis via a goniometer. Thin sample holder plates allow measurements of the longitudinal as well as of the polar Kerr effect.

4.5 Technical Aspects of Automatization

The MOKE setup is operative with the completion of the mechanical and optical components. The next project is the automatization of the setup with a personal computer (PC). The tasks of driving the coil current for the generation of magnetic fields and to read out the detector signal are to be fulfilled. The data should be displayed graphically and written to data files onto hard disc drive. Desired advanced software features are a function for demagnetizing the yoke and a calibration function in which the detector signal can be calibrated vs. the rotation angle of the light's polarization plane. These software is named MOKEsoft and is realized with National Instruments LabVIEW^{TM} 2009 in the course of the bachelor thesis of F. Huttmann [135]. This thesis contains detailed information about the automatization. For the proper operation of MOKEsoft on a PC the installation of the LabVIEW^{TM} runtime environment and so called VISA driver is required.

Devices to be controlled or read out by MOKEsoft are a KEPCO® BOP 36-6M bipolar power supply with a 16 bit IEEE 488.2 plug in card to drive the coil current, an Agilent [136] 34401A multimeter to read out the detector signal and an Eurotherm 2404 [137] to log the sample temperature measured with a type K thermocouple. These devices are connected via an RS-232 serial bus to a PC. The Agilent [136] multimeter and the Eurotherm [137] can each be connected via a RS-232 to USB adapter. Inconveniently the KEPCO® BOP needs to be connected to an intrinsic RS-232 port of the PC and does not work on RS-232 extension slots and RS-232 to USB adapters, which just supply virtual RS-232 ports. The RS-232 parameter like bout rate and party must be set identical on the devices and on the ports at the PC side. Important technical details of the particular devices, which determine the limitations and capabilities of MOKE measurement are discussed hereafter.

The advantage of utilizing a KEPCO® BOP (Bipolar Operational Power supply/amplifier) as a power supply is a well defined, clear and feature free zero-crossing which is important since for measurements of magnetic hysteresis continuous loops from positive to negative magnetic fields have to be driven. The BOP output current of up to $\pm 6\,\mathrm{A}$ is controlled with a resolution of 16 bit, meaning 15 bit for every polarity. So the power can be applied in steps of 0.00183 A to the coils, respectively the magnetic flux in 0.2 mT steps to the sample (taking in account the B vs. I relation of the magnet, as discussed in section 4.2 where the current is partitioned equally on the parallel switched coils). This magnetic field resolution satisfies the needs of our measurements. According to the data sheet of the BOP there is a noise of 0.01 A, and 50 Hz on the BOP output current which is eliminated by the high impedance of the coils and by a sufficient long integration time T_{Int} over the detector signal. A further dynamic specification of the BOP is its slew rate of $0.5\,\mathrm{A}\ /\ \mu\mathrm{s}$, which means that the desired currents are available instantaneously compared with the timescales, which are desired for the measurement of a data point in the order of 0.25 s. Important technical benchmark data of the Agilent [136] 34401A multimeter are the resolution of $0.1\,\mu\mathrm{V}$ and available

integration times T_{Int} for a data point in numbers of 1/50 second, namely 0.2, 1.0, 10.0 and 100, i.e., 0.004 s, 0.02 s, 0.2 s and 5.0 s which is all quite sufficient for our tasks. As all these technical device parameters define the capabilities and limitations of the MOKE measurements ways of controlling the devices and the measurement process in the sense of minimized disturbing side effects and noise are discussed in the following.

Sources of disturbance are a drift of the emitted laser power in the order of about 5% per hour and of course background noise. Due to the laser drift one cycle of a hysteresis measurement should be recordet in the timescale of a minute. Of course the longer T_{Int} for each data point the better. We find that $T_{\mathrm{Int}} = 0.2\,\mathrm{s}$ averages out most of the noise. Due to the large inductivitiy of the coils of 0.6 H it takes some time until the applied power of the BOP is fully build up at the coils and the desired current equals the applied current. Therefore, a latency time T_{Lat} is introduced. Initially a small T_{Lat} parameter was intended just for the device communications, but it can also compensate for the coil inductivity by enlarging it. The more data points are taken for a hysteresis loop the smaller are the needed T_{Lat}. We find that measurements consisting of 120 data points per loop with $T_{\mathrm{Int}} = 0.2\,\mathrm{s}$ and T_{Lat} in the order of 0.05 s, i.e., a total measurement time of 30 s per hysteresis loop represent the samples magnetism well. The inductivity effect, which arises from to short T_{Lat} is visualized by test measurements in section 4.6. A hysteresis loop which includes reliable information of physical quantities, such as remanence, or coercive field and does not show effects of amplitude drift should be measured on a timescale between 30 s and 60 s. To eliminate rest noise and fluctuations multiple hysteresis loops are measured and the data of every single loop, as well as the averaged data is written to a data file. Before applying a magnetic flux to a sample its magnetization is undefined. To avoid an undefined sample magnetization the first data point of a MOKE hysteresis measurement is taken at the maximum desired external magnetic field. These crucial technical details are considered in the MOKE automatization software (MOKEsoft), its handling is introduced in the appendix C of this thesis.

4.6 MOKE Test Measurements

The MOKE setup is first tested on a simple and well defined sample system, namely thin Pt/Co/Pt layers. Two such samples, labeled H1 and H2, are supplied by H. P. Oepen [130]. The samples are grown by MBE on a glass substrate. First a 5 nm thick platinum layer is deposited as a seed layer, a magnetic cobalt layer as the middle layer and at last a 3 nm thick nonmagnetic platinum capping layer is grown on top. The capping layer preserves the cobalt layer against oxidation and makes the samples stable under ambient conditions. In the case of sample H1 the cobalt layer thickness amounts to 2.6 nm and in the case of H2 to 1.0 nm. The easy magnetization plane of thin cobalt layers depends on the film thickness [138; 139]. Therefore the easy magnetization

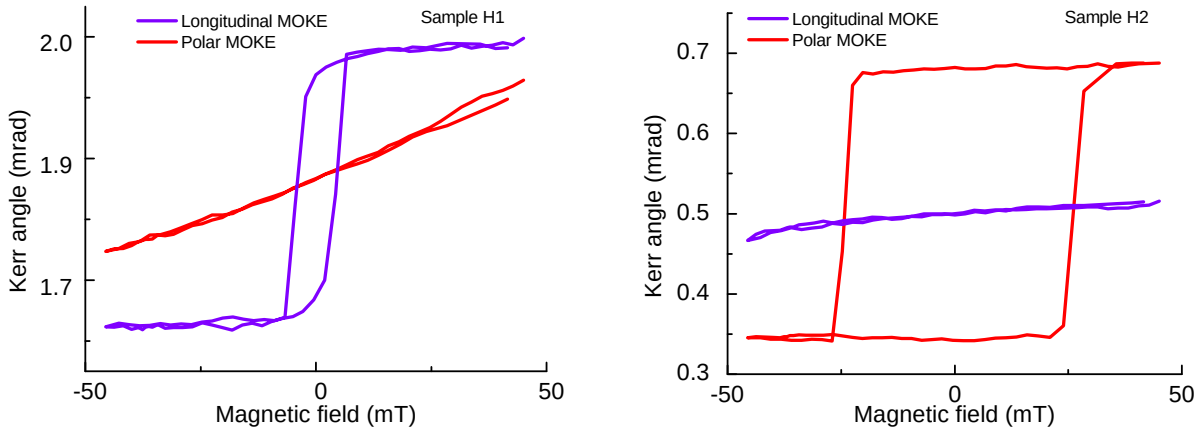

Figure 4.6: Test measurements performed at the ambient conditions MOKE setup (Sec. 4.4) on platinum capped thin cobalt films performed at room temperature. Left graph: Longitudinal and polar MOKE hysteresis measurements on a capped 2.6 nm thin cobalt film, labeled as sample H1. Right graph: Longitudinal and polar MOKE hysteresis measurements on a capped 1.0 nm thin cobalt film, labeled as sample H2.

direction of the sample H1 is in the thin film plane and the easy axis of the sample H2 out-of the cobalt film plane. So the samples H1 and H2 provide a benchmark for initial tests and characterization measurements of the MOKE setup. Hysteresis measurements on these samples are performed as explained in section 5.6. Longitudinal (sample magnetized in the sample plane and in plane of incident light) and polar (sample magnetized perpendicular to the sample plane) MOKE measurements of the sample H1 under ambient conditions are presented in the left graph of figure 4.6. The longitudinal MOKE measurement shows a ferromagnetic hysteresis while the polar measurement reveals a Kerr signal, but no hysteresis showing that the magnetizations easy axis is in the film plane. MOKE hysteresis measurements on the sample H2 show a behavior the other way around indicating an easy out-of-plane magnetization. The magnetization of the sample with the in-plane easy magnetization can also be magnetized out-of-plane by an external magnetic field and vice versa but the magnetization will show a low remanence. Characteristic numbers for a magnetic system like the remanent magnetization and coercive field can be evaluated. Here for example the sample H2 is magnetically harder than sample H1.

Since the UHV MOKE setup utilizes the longitudinal Kerr effect the sample H1 with an easy in-plane magnetization is used for further test measurements. Longitudinal MOKE hysteresis loops are measured on the sample H1 at the ambient conditions MOKE setup for different measurement times T_{Loop} per hysteresis loop as displayed in figure 4.7 and figure 4.8. The measurement time T_{Loop} per hysteresis loop can be influenced by varying the number of data points, or T_{Lat} between the setting of the magnetic field and the recording of the detector signal, or by T_{Int} per data point. Due to the strong inductivity of the electromagnet coils (of 0.6 H) the desired field needs some time to be fully built up, as explained in section 4.5. Therefore T_{Lat} must be the larger the smaller the magnetic field resolution. The way hysteresis data is determined by these measurement parameters

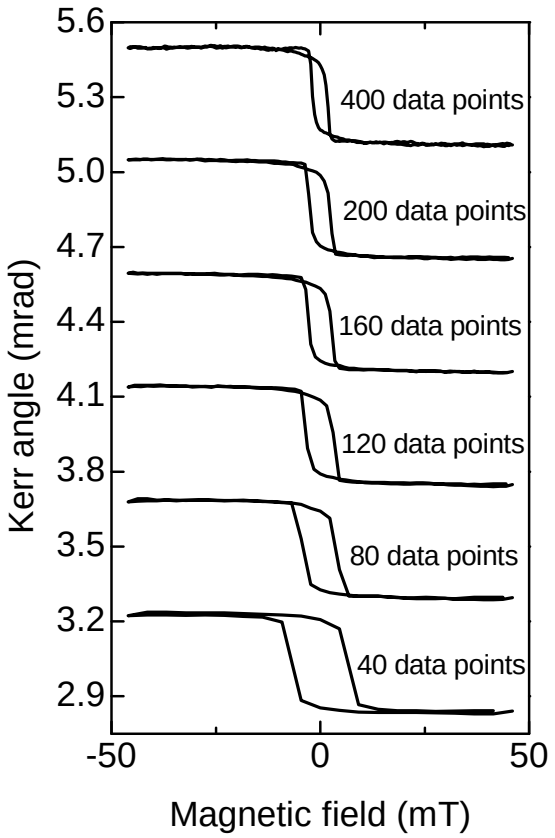

Figure 4.7: Longitudinal MOKE hysteresis loops of sample H1 with an in-plane easy axis, performed at the ambient conditions MOKE setup. The number of data points per loop is noted at the individual loops. A $T_{\mathrm{Lat}} = 0.05\,s$ passed by before recording each data point with $T_{\mathrm{Int}} = 0.2\,s$. To fast measured loops, i.e., with too less data points show a broadening, because of the coil's inductivity.

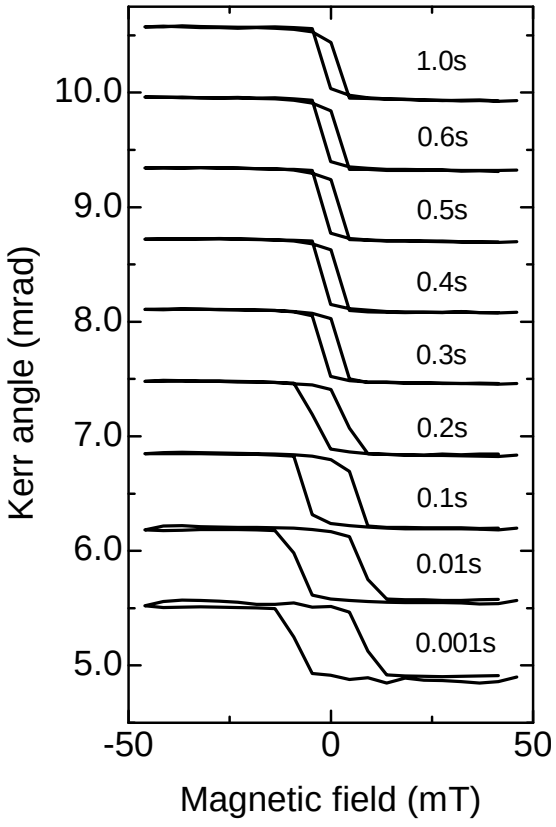

Figure 4.8: Longitudinal MOKE hysteresis loops of sample H1 with an in-plane easy axis, performed at ambient conditions MOKE setup for different latancy times, as noted at the individual loops. Every loop consists of 40 data points and $T_{\mathrm{Int}} = 0.2\,s$ for each data point. Too short T_{Lat} cause a broadening of the loops due too the high coil inductivity.

is demonstrated in figure 4.7 and figure 4.8. Too less measurement time per loop T_{Loop} leads to a broadening of the hysteresis data. Hysteresis loops measured in a loop time T_{Loop} of 30 s, e. g., 120 data points per loop, $T_{\mathrm{Lat}} = 0.05\,\mathrm{s}$ and $T_{\mathrm{Int}} = 0.2\,\mathrm{s}$ result in a hysteresis loop without broadening and without crossing, compare figure. 4.7. Therefore these parameters are defined as the standard settings for the operation of the MOKE device.

Figure 4.9 again shows MOKE measurements on the sample H1, but this time UHV view ports are put into the optical path of the laser in a distance of 30 cm to the coils. In normal magnetic, e. g., Kovar® sealed, view ports a Faraday rotation in the order of 0.1 mrad at maximum coil current superimposes the Kerr signal of the sample. The improvement gained by nonmagnetic view ports compared to normal UHV view ports is shown experimentally and illustrated in figure 4.9. Since nonmagnetic view ports improve the MOKE signal significantly these are mounted to the MOKE flanges of the LT-STM system.

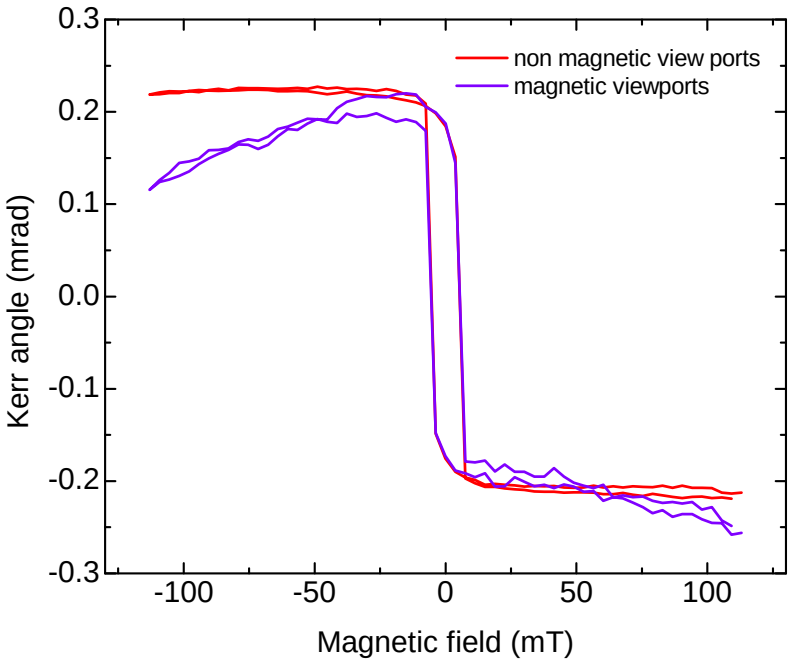

Figure 4.9: MOKE hysteresis measurement of sample H1 with magnetic, or nonmagnetic view ports in the lasers optical path recorded with the UHV MOKE at the LT-STM setup. A Faraday rotation in the order of 0.1 mrad is caused by the magnetic view ports at maximum applicable magnetic field.

The resolution of the Kerr rotation is determined to be better than 1 μrad. The noise level of the setup is determined by MOKE measurements on a reflective non ferromagnetic sample, e. g., an aluminum mirror or an Ir(111) single crystal. The noise level depends on various influences like sample roughness, transmission of the analyzer prism, misaligned plane of incidence etc.. A noise levels down to 100 nrad has been achieved by careful adjustments of the optics. Resolving magnetic features within the noise level is possible by carefully adjusting the optics.

5 Experimental Procedures

The experimental procedures of this thesis are described in this chapter. All sample preparations and measurements are performed *in-situ* under UHV conditions in the LT-STM system (see. Chap 3).

5.1 Substrate Preparation

The samples prepared in this thesis are determined to be investigated with STM and STS. These experimental techniques base on a tunneling current, and therefore, require conductive substrates. Beside the conductivity a suitable surface lattice is needed for EuO growth. Here a Ni(100) single crystal and an Ir(111) single crystal are used as substrates.
The Ni(100) single crystal is prepared with cycles of 1.5 keV Ar^+ ion bombardment and quick annealing to 1100 K on a metal sample holder as displayed in Fig. 3.1 c). The pressure in the LT-STM preparation chamber p_{prep} amounts to 6.0×10^{-7} mbar during the noble gas bombardment, whereby the preparation chamber pressure originates almost exclusively from the noble gas. The sample is grounded during sputtering to avoid charging and electrostatic screening of the sample and an ion current of 2.4 μA is measured. Due to secondary electron effects this is not the exact ion current bombarded to the sample. In the future a Faraday cup could be mounted on a sample holder body for a more precise determination of the ion current. The ion beam is focused in a way that the full sample area is bombarded by it. This is initially approved by driving the sample through the beam with help of the manipulator and measuring the ion current. The pressure in the LT-STM preparation chamber p_{prep} rises up to 2.5×10^{-9} mbar during annealing of the sample, which is a pressure sufficiently low for the aim to grow thin films onto the surface.
The Ir(111) single crystal is treated in the same way by sputtering as the Ni(100) crystal but annealed to higher temperatures of 1470 K. The sample preparation is performed on an electron beam (e-beam) sample holder as displayed in figure 3.1 b). The result of the substrate preparation is checked with LEED. The sample is treated with an annealing procedure in an oxygen atmosphere at a sample temperature of T=1170 K and a molecular oxygen pressure of p_{O_2}= 1.0×10^{-6} mbar for five minutes in the case of carbon impurities.

5.2 Graphene Preparation

Fully closed monolayers of graphene are prepared on an Ir(111) single crystal surface in a combined temperature-programmed growth (TPG) and CVD procedure [140] by using ethylene as the

precursor gas. The Ir(111) surface is put in front of the ethylene dosing pipe during this procedure. In the TPG procedure the Ir(111) substrate is exposed at room temperature for t=60 s to an ethylene atmosphere which is 1.0×10^{-11} $I_{QMS-Ethylene}$ ($p_{prep} = 5.5 \times 10^{-8}$ mbar) with a leak valve. After the step of adsorbing ethylene to the Ir(111) surface the sample is heated up quickly to T_{Flash}=1440 K for less than one second. During this step the adsorbed ethylene precursor dissociates and split-off hydrogen atoms desorb to the vacuum while the remaining carbon atoms on the Ir-surface form graphene nanoflakes with a coverage of 22% [141]. The average flake size and their epitaxial orientation to the Ir(111) surface is determined by the temperature T_{Flash} of the heating step. The graphene flakes serve as seeds for the subsequent CVD procedure. The CVD preparation step is performed for five minutes at T_{sample}=1340 K, and 4.0×10^{-10} $I_{QMS-Ethylene}$ ($p_{prep} = 2.4 \times 10^{-6}$ mbar). The special highlight of this preparation is its self limitation to exactly one atomic layer [141]. The grahene monolayer is described by the epitaxial relation of $\langle 11\bar{2}0 \rangle_C \| \langle 1\bar{1}0 \rangle_{Ir}$ [142]. The success of the graphene preparation is subsequently checked after growth with LEED, as displayed in figure 5.1.

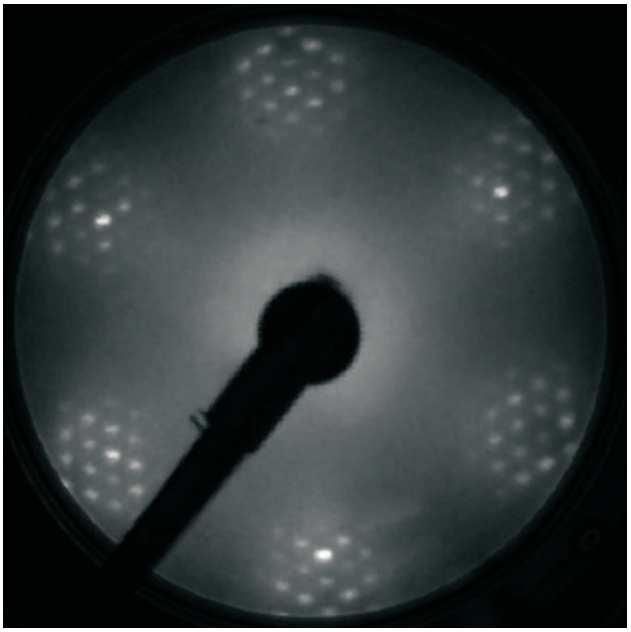

Figure 5.1: MCP-LEED diffraction pattern of a graphene monolayer prepared in a two step TPG and CVD process as described in section 5.2. Primary electron Energy E=116.5 eV. The pattern has been deskewed to compensate for the distortion due to the planar MCP of the LEED device.

As a general remark on the sample preparation the ion getter pump is shut off from the preparation chamber by a gate valve during dosing gas into the preparation chamber. During annealing the ion getter pump with the additional use of its liquid nitrogen filled cooling trap and titanium sublimation pump is connected to the preparation chamber after most gas is pumped with the turbo molecular pump to achieve clean surfaces in a low pressure of 1.0×10^{-10} mbar.

5.3 EuO Growth

The preparation of EuO is known to be delicate and strongly dependent on the growth conditions. This holds especially for EuO and other oxide compounds on chemically reactive metal surfaces. Substantiated growth procedures for EuO on Ni(100), Ir(111), and graphene on Ir(111) are established in the earlier PhD work of D. F. Förster [17] at the UHV system ATHENE in the group of T. Michely. In the current thesis the growth principles are transfered to the LT-STM system.
Thin films of EuO are grown by molecular beam epitaxy (MBE) in the preparation chamber, as explained in chapter 3.3. Eu and O_2 are deposited simultaneously in all preparations. With the aim of growing stoichiometric EuO, in the ideal case Eu and O are deposited in a flux ratio $f_{\mathrm{Eu}}/f_{\mathrm{O}}$=1 and all atoms react to EuO. An often discussed problem is the formation of the higher oxides Eu_2O_3 and Eu_3O_4 [2; 10; 12; 14; 15; 143–145] by Eu deficient growth conditions. The distillation technique [146] aims at the preparation of stoichiometric EuO. Thereby, EuO is grown under Eu excess. The re-evaporation of excess Eu to the vacuum (distillation) is enabled at enhanced sample temperatures. Thus, at T_{sample} between 570 K and 720 K there is a significant Eu re-evaporation rate [147]. In the principle of the distillation process, the effectively grown EuO coverage scales with the deposited amount of oxygen. The idea of tuning the Eu re-evaporation rate with sample temperature enables one to tune the Eu excess, or the other way around the concentration of oxygen vacancies. Current work of S. G. Altendorf exhibits not only the formation of oxygen vacancies, but also a phase separation by the inclusion of Eu-clusters [46].
Post oxidation of EuO after growth has to be prevented, therefore, the oxygen background pressure in the UHV chamber is kept as low as possible. Additionally, post oxidation of the EuO samples is prevented by turning off the oxygen flux five seconds before the europium flux. This is meaningful since the drop of the gas pressure takes some time, but the Eu molecular beam can be shut down instantaneously by the shutter of the Knudsen cell. This procedure is also reasonable in the idea of the Eu distillation process.
As the precise control of the flux ratio $f_{\mathrm{Eu}}/f_{\mathrm{O}}$ is crucial. One needs to know the relation to the quartz microbalance rate Q_{Eu} and $p_{\mathrm{O_2}}$. In the case of the gas ingredients the kinetic gas theory [148; 149] is utilized to calculate f_{O} by the following equation:

$$f_{\mathrm{O_2}} = \frac{p_{\mathrm{O_2}}}{\sqrt{2\pi m k_{\mathrm{b}} T}} = 2.69 \times 10^{24} \cdot \mathrm{m}^{-2} \cdot \mathrm{s}^{-1} \cdot \mathrm{mbar}^{-1} \cdot p_{\mathrm{O_2}} \tag{5.1}$$

whereby $p_{\mathrm{O_2}}$ is the O_2 partial pressure at the sample, m the mass of the O_2 molecule, k_{B} the Boltzmann constant and T the gas temperature. The relation between $p_{\mathrm{O_2}}$ and the QMS signal in numbers of $\mathrm{I}_{\mathrm{QMS-O_2}}$ is explained in chapter 3.3. In our experiments oxygen is supplied in molecular form to the sample where it dissociates to atomic oxygen, therefore,

$$f_{\mathrm{O}} = 2 \cdot f_{O_2}. \tag{5.2}$$

The Eu rate Q_{Eu} measured prior to the film growth with a quartz microbalance corresponds to an Eu flux f_{Eu} as shown by the following equation:

$$f_{\mathrm{Eu}} = Q_{\mathrm{Eu}} \cdot 2.08 \times 10^{18} \cdot \mathrm{m}^{-2} \cdot \mathrm{\AA}^{-1} \tag{5.3}$$

The factor of 2.08×10^{18} Eu-atoms$\cdot$m$^{-2}\cdot$ Å^{-1} is derived form the atom density in europium. In the experimental work of this thesis Eu rates of f_{Eu}= 4.16 $\times$ 10^{16} Eu-atoms m$^{-2}\cdot$s^{-1}, resulting from Knudsen cell temperatures T_{Knudsen} around 700 K, are used. One monolayer of EuO(100) with an uncompressed EuO lattice constant has an atom density of 1.51×10^{19} atoms $\cdot$ m^{-2}, whereby half of these atoms are Eu-atoms and the other half are O-atoms. In the idea of a distillation determined EuO growth process the amount of grown EuO is determined by the deposited amount of O-atoms. An EuO growth rate of Q_{EuO} = 0.15 ML EuO(100) / min. results from an O-flux of 1.88×10^{16} O-atoms m$^{-2} \cdot$ s^{-1}. The particularities on the preparation of EuO(100) on Ni(100) and of EuO (100) on graphene are pointed out in the following.

Eu and O are deposited simultaneously on the Ni(100) surface in a chemical reactive procedure. The growth is performed at T_{sample} in the range of 560 K to 720 K [150]. The flux ratio of $f_{\mathrm{Eu}}/f_{\mathrm{O}}$=1.4 has to be set precisely since the range in which mainly EuO(100) grows on Ni(100) is very narrow [17]. Growth rates of Q_{EuO} = 0.77 ML EuO / min. are used. After deposition the sample is annealed at T_{sample}=870 K for five minutes and then annealed in an europium atmosphere at T_{sample}=720 K for ten minutes [150]. EuO grown this way results in two coexisting phases of EuO(100), one pseudomorphic phase with the epitaxial relation EuO(100)[010]‖Ni(100)[011] and another phase 45° rotated to this one in the epitaxial relation of EuO(100)[011]‖Ni(100)[011] (see reference [17]). The magnetic properties of EuO on nickel are studied in chapter 9 of this thesis.

The preparation of EuO(100) on graphene on Ir(111) is less complicated than the preparation of EuO on Ni(100) [17]. The catalytically active Ir(111) metal surface is isolated from the oxide growth process by the chemically inactive carbon monolayer [151]. Therefore, the sensitive control of the flux ratio $f_{\mathrm{Eu}}/f_{\mathrm{O}}$ during the deposition of Eu and O onto graphene is less critical. Of course also in this case $f_{\mathrm{Eu}}/f_{\mathrm{O}}$ must be larger than one (i.e. europium rich) to prevent the formation of higher oxidation states than 2+ of the Eu ions. For the preparation of stoichiometric EuO(100) films Eu and O are deposited with a flux ratio of $f_{\mathrm{Eu}}/f_{\mathrm{O}}$=1.4.
The deposition of the reagents can be performed at an elevated T_{sample}=720 K, which results in three domains of EuO(100) rotated by 30 ° with respect to each other and a 4% compressed lattice constant [17]. EuO prepared this way grows epitaxially with the EuO[010] direction aligned along the C[11$\bar{2}$0] direction and coincides with the carbon lattice in a 1:2 relation [17].
The deposition of Eu and O can also be performed at room temperature (RT), crystallization to EuO(100) and re-evaporation of excess Eu is subsequently gained by annealing in an Eu flux of

f_{Eu}= 4.16 × 10^{16} Eu-atoms $\mathrm{m}^{-2}\cdot\mathrm{s}^{-1}$. The crystallization sets in at about T_{sample}=560 K, as observed with LEED, but with a poor overall sample quality in STM. EuO(100) with a crystalline quality sufficient for STM investigations is gained by annealing the EuO film at T_{sample}=720 K. EuO grown by this procedure is purely Eu(100), shows no distinct preferred in plane epitaxial relation and a bulk like EuO lattice constant [17; 152]. Additionally an Eu-intercalation layer is formed under the graphene sheet [153]. The samples consist of 3.3 nm high grains [17], or at higher amounts of deposited material a 3.3 nm thin film of of EuO(100). The advantage of the room temperature deposition and subsequent annealing process is the complete suppression of the growth of polar EuO(111) phase, which is not the case for EuO grown onto graphene in the distillation process.

5.4 LEED Measurements and Data Post Processing

Low energy electron diffraction (LEED) is a fast and powerful method to check the result of sample preparations. LEED has the capability of determining periodically ordered crystalline structures at sample surfaces (and in a few underlying layers, depending on the energy of the primary electrons) by the formation of an electron scattering pattern. Such patterns enable the determination of the crystalline surface structure, interatomic distances and the quality of crystalline order. In the case of an amorphous sample just a diffuse scattering pattern is created. In the experimental work of this thesis every preparation step is checked by this method.

Therefore, a LEED device (type OCI MCP LEED BDL800IR) is mounted to the LT-STM preparation chamber. MCP means multi channel plate, which is an electron multiplier for the diffracted electrons and allows one to operate the LEED at very low primary electron currents of 50 pA, which is an advantage for the investigation of poorly conducting samples like EuO to avoid charging of the sample, and therefore, deflection of the electron beam. The disadvantage of the MCP LEED is a distortion at the outer parts of the LEED pattern due to the non-spherical, but planar MCP geometry. This geometrical projection effect is corrected by post processing the LEED pattern images with a software set up in the group of M. Sokolowski [154]. The distance of the sample to the screen of the LEED has to be set as a parameter in the software in the number of pixel (px). Images of the LEED pattern are recorded with a sensitive camera, which is mounted outside the vacuum to the LEED-device. In the case of 640 px × 480 px LEED pattern images, as recorded in the work of this thesis, the sample to screen distance amounts to 201 px. (In the case of a fully extended LEED and a sample position at the x-axis of the manipulator of x=2.3 mm). This number is derived from the visible diameter of the screen of 75.0 mm.

5.5 Scanning Tunneling Spectroscopy Technique

Since all information gained by STM [155] and STS [156; 157] measurements is based on the tunneling current I an understanding and description of this is important. Bardeen describes the tunneling current I between a sample S and STM tip T caused by a bias voltage U_{Bias} applied to the sample, see equation (5.4) [158]

$$I \propto \int_{-\infty}^{+\infty} |M(E)|^2 \, \rho_{\mathrm{T}}(E) \rho_{\mathrm{S}}(E - e \cdot U_{\mathrm{Bias}}) \, [f(E) - f(E - e \cdot U_{\mathrm{Bias}})] \, dE. \tag{5.4}$$

In this equation $|M(E)|$ is the tunnel matrix element, E the energy, f the Fermi function, $\rho_{\mathrm{T}}(E)$ and $\rho_{\mathrm{S}}(E$ -e$\cdot U_{\mathrm{Bias}})$ the tip's respectively the sample's DOS at the applied bias $\mathrm{e} \cdot U_{\mathrm{Bias}}$. The size of the tunneling gap d and the sample's and tip's wave function mainly determine $|M(E)|$. $|M(E)|$ can be simplified to the tunneling probability $|T(U_{\mathrm{Bias}}, \Phi)|$, whereby Φ is the work function [159]. Note that the tunneling current I is determined by the applied bias voltage U_{Bias}, but also especially by the sample's and tip's DOS.

The essential dependence of the tunneling current I on the sample's and tip's DOS establishes the capability of local spectroscopy. The differential conductivity $\mathrm{d}I/\mathrm{d}U$ is proportional to either the tip's local density of states (LDOS), or the LDOS of the sample. Here only the most important relations will be given. A detailed description can be found in chapter 4.3 of D. F. Förster's PhD thesis [17]. For a positive tunneling voltage U_{Bias} applied to the sample, $\mathrm{d}I/\mathrm{d}U$ can be described by the following equation (5.5):

$$\left(\frac{dI}{dU}\right)_{U_{\mathrm{Bias}}} \propto T(d, U_{\mathrm{Bias}}) \rho_{\mathrm{S}}(E_{\mathrm{F}} + e \cdot U_{\mathrm{Bias}}) \rho_{\mathrm{T}}(E_F). \tag{5.5}$$

In the case of a positive bias voltage U_{Bias} the differential conductivity $\mathrm{d}I/\mathrm{d}U$ is dominated by electrons tunneling into sample levels at $E_{\mathrm{F}} + \mathrm{e} \cdot U_{\mathrm{Bias}}$, where E_{F} is the Fermi energy. The DOS of the tip does not depend on U_{Bias} in this equation (5.5). Therefore, $(\mathrm{d}I/\mathrm{d}U)_{U_{\mathrm{Bias}}}$ probes the unoccupied sample LDOS at an energy $E_{\mathrm{F}} + \mathrm{e} \cdot U_{\mathrm{Bias}}$. In the case of negative bias voltages U_{Bias} applied to the sample, it is the other way around as expressed by equation (5.6):

$$\left(\frac{dI}{dU}\right)_{U_{\mathrm{Bias}}} \propto T(d, U_{\mathrm{Bias}}) \rho_{\mathrm{S}}(E_F) \rho_{\mathrm{T}}(E_{\mathrm{F}} + e \cdot |U_{\mathrm{Bias}}|). \tag{5.6}$$

The differential conductivity $\mathrm{d}I/\mathrm{d}U$ in equation (5.6) is dominated by the DOS around the Fermi energy E_{F} of the tip. Therefore, the occupied DOS of the sample is difficult to measure by STS. Experimentally $\mathrm{d}I/\mathrm{d}U$ is measured with the help of a lock-in amplifier [160]. Therefore, a

small harmonic modulation voltage U_{Mod} with a defined modulation frequency f_{Mod} is superimposed to U_{Bias}. The tunneling current is analyzed on f_{Mod} by the lock-in amplifier which gives a signal directly proportional to $\mathrm{d}I/\mathrm{d}U$. For a comparison of lock-in amplifier signals the operation parameters of the lock-in have to be noted. These are the integration time constant, U_{Mod} and the sensitivity of the lock-in amplifier. For the modulation of U_{Mod} a frequency frequency f_{Mod} is chosen, which has a low amplitude in the Fourier transform of the non-modulated tunneling current I. This is important not to amplify noise consisting of this frequency. A disturbing side effect of the lock-in modulation voltage on the bias line is caused by the parasitic capacitance of the bias line. To eliminate this effect, the phase of the lock-in reference signal is shifted by 90° with respect to the response signal on the tunneling line out of tunneling contact. This adjustment minimizes the influence of the parasitic capacity on the $\mathrm{d}I/\mathrm{d}U$ signal. The physical origin of the $\mathrm{d}I/\mathrm{d}U$ signal at moving the tip into tunneling contact is then purely due to the DOS of the sample, or of the tip. In this thesis two modes of $\mathrm{d}I/\mathrm{d}U$ spectroscopy measurements are used, namely local $\mathrm{d}I/\mathrm{d}U(U_{\mathrm{Bias}})$ point spectroscopy and $\mathrm{d}I/\mathrm{d}U|_{U_{\mathrm{Bias}}}$ mapping. The lock-in output signal is set to zero out of tunneling contact in local spectroscopy mode and in tunneling contact in mapping mode. In local STS point spectroscopy mode the STM tip is stabilized over a desired sample spot. The stabilization is defined by the initially set tunneling parameters. The spectroscopy signal $\mathrm{d}I/\mathrm{d}U(U_{\mathrm{Bias}})$ is measured as a function of U_{Bias} in a constant tip to sample distance d which does not change during the measurement (feedback loop open). In contrast to this mode, in $\mathrm{d}I/\mathrm{d}U \mid_{U_{\mathrm{Bias}}}$ mapping mode the $\mathrm{d}I/\mathrm{d}U$ signal is measured at the constant bias voltage U_{Bias} while the tip scans a sample area. The spectroscopy maps are simultaneously recorded (on another channel) to the topography. In both STS modes the measurement time per data point is set to at least twice the integration time constant of the lock-in amplifier to achieve a reasonable good signal to noise ratio. In mapping mode one data point is a pixel of the STS map. The resolution of STS in energy space δE is mainly limited by temperature due to the gradual behavior of the Fermi function and due to the modulation voltage U_{Mod}. An expression for δE is given by M. Morgenstern *et al.* [161]:

$$\delta E = \sqrt{(3.3 \cdot k_{\mathrm{B}} \cdot T)^2 + (1.8 \cdot e \cdot U_{\mathrm{Mod}})^2}. \tag{5.7}$$

The most important STS measurements of this thesis are performed at 5.3 K, respectively 81 K and $U_{\mathrm{Mod}} \approx 14\,\mathrm{mV}$. Therefore, equation (5.7) gives an STS energy resolution of 25 meV at 5.3 K and 34.0 meV at 81 K.

5.6 MOKE Measurement Procedures

In this section the experimental procedures utilizing the home-built MOKE setup (section 4) are described: The HeNe laser is switched on for a heat up time of about one hour with its shutter closed before a MOKE measurement. The sample is positioned carefully in the slot of the electromagnet.

If the sample has to be cooled down the adjustment of the laser's optical path is done after cooling down. The attachment of the sample holder to the manipulator gets loose upon cooling (because the manipulator head is constructed of materials with different thermal expansion coefficients), and therefore, the optical path gets out of adjustment. MOKE measurements are usually performed with deactivated damping system of the LT-STM system and while operating the turbo molecular pumps as no significant noise is observed due to these vibrations.

In the following, the adjustment of the optical components and the laser of the MOKE setup is described. While emitting the laser light onto the sample its plane of polarization must be parallel or perpendicular to the plane of incidence. For adjusting the optical path, the laser and the manipulator can be moved, whereby, if once a suitable alignment of the laser is found it is recommendable not to change it. When the first part of the optical path is adjusted, the detector must be aligned with the aim that the laser shines straight through the optical axis and hits its photo transistor with maximum intensity. Therefore, the analyzer prism of the detector is set to transmit some light that a meaningful detector signal can be measured and the detector is moved to find the maximum signal [1]. The gain of the detector is always used in its low amplification mode. After all components are adjusted in a way that the laser is focused on the photo transistor of the detector, the analyzer prism – and in case of the UHV MOKE the $\lambda/4$ retardation plate – are set to extinguish the laser light as good as possible. The minimum achievable signal depends on sample properties like reflectivity and roughness or setup related problems like a misaligned plane of incidence. Typical minimum detector signals are in the order of 0.5 mV and correspond to a Kerr angle Θ_{Kerr} of zero. To relate the detector voltage to Θ_{Kerr} later on a calibration as explained in section 4.3 is performed. The calibration should be taken with care, because on the timescale of a few hours the laser's optical path could change possibly due to thermal expansions. A good indicator for such a misadjustment is a significantly decreased detector signal. As the last preparing step the analyzer prism is rotated by a small offset angle such, that some laser light passes through it and a clockwise rotation of the polarization plane causes a rise in signal and the other way around. For the investigation of samples with just a small Kerr angle Θ_{Kerr} also just a small offset angle is required. The resolution can be enhanced by the choice of an as small as possible offset detector angle.

The ferromagnetic hysteresis of a sample is determined by its magnetic susceptibility at a defined temperature. Thus, the response of the sample to an external magnetic field is measured. To perform such measurements the automatization software MOKEsoft is utilized as described in chapter C. Upon starting a hysteresis measurement the sample is magnetized in a stepwise changing (Sec. 4.5) constant homogeneous magnetic field and the detector signal is recorded for each value. The external magnetic field is plotted to the horizontal axis and the Θ_{Kerr}, which is proportional

[1] In the case of no meaningful operation the detector's operational amplifier (OPA657) might be broken (what happened two times during this work).

to the magnetization of the sample [99; 106], is plotted on the vertical axis. The most important parameters to set in MOKEsoft are the number of data points per quarter loop in combination with the latency time T_{Lat}. These parameters give the total time required for the measurement of a hysteresis loop. As shown by the test measurements presented in section 4.6 a loop time of 30 s gives the best results and are used for the MOKE measurements of the following chapters. If not stated otherwise the longitudinal Kerr signal is measured in an external magnetic field B, from +117 mT to -117 mT. Hysteresis loops are repeatedly measured, and the data of the single loops, as well as the data of the averaged loop are recorded. Typically averaging over five loops is sufficient.

The following lines describe the determination of the sample's ferromagnetic magnetization vs. temperature based on MOKE hysteresis measurements. The sample magnetization is accessible by these measurements since the sample's Kerr signal, recorded in a hysteresis loop, is directly proportional to its magnetization [99; 106]. A disadvantage of this method is that the magnetization is not accessible in numbers of μ_{B} per atom. A number, which is proportional to the sample magnetization is determined from a hysteresis loop automatically by MOKEsoft (section 4.5) in two different ways. As the first way, half of the difference of the maximum and minimum Kerr signal Θ_{Kerr}(+117 mT) and Θ_{Kerr}(-117 mT) of a hysteresis loop is evaluated, which normally should occur at the highest applied magnetic fields. As the second way half the difference of the remanent Kerr signal Θ_{Kerr}(Rem) at zero external magnetic field. By recording hysteresis loops permanently at various sample temperatures the Kerr signal vs. temperature is determined. In principle the maximum and minimum Kerr signal should show the same behavior, due to symmetry reasons. For unknown reasons in some measurements a deviation of these occurs, which leads to unphysical kinks, or plateaus in the $\Theta_{\mathrm{Kerr}}(T)$ data. The main goal of such measurements is the determination of the ferromagnetic transition temperature (Curie temperature) T_{C}. The individual advantages of these two methods depend on the underlying hysteresis shape. In general the disadvantage, especially of the first method, is an artificial enhancement of T_{C} by the large external magnetic field, as explained in section 2.2. The effect of an external magnetic field on T_{C} is quantified in section 6.2. In principle, this T_{C} increasing effect is less strong in remanence. Unfortunately there is a small deviation of the electromagnets real $B(I)$ characteristic (see figure 4.4) and the calibration data of those (figure D.1). This deviation is caused by the ferromagnetic behavior of the electromagnets iron yoke. There is a small residual magnetic field at the claimed zero field. This effect can be reduced by recording hysteresis loops in smaller maximum magnetic fields as displayed by figure 4.4.

6 Growth and Magnetism of EuO on Graphene

The experiments and measurements presented in this chapter were carried out by myself, except for the SQUID measurements. Sample preparations have been supported by F. Craes, D. F. Förster, S. Schumacher and C. Busse. Discussion of the data on the magnetic properties of the EuO samples took place with C. Busse, H. P. Oepen and T. Michely. Partially the contents of section 6.1 and the contend of section 6.3 are submitted to Applied Physics Letters.

This chapter shows the growth by MBE and *in-situ* measured magnetic properties of ultra thin (100) textured EuO films grown on epitaxial CVD graphene. The growth process is performed as described in the previous chapter. The topography and epitaxy of these films are investigated with constant current STM topography and LEED measurements. Large scale STM images show an overall homogeneous and well grown film quality (see next section 6.1). The magnetic properties of the thin films are investigated with MOKE in section 6.3. Thereby the magnetism of thin closed films of EuO(100) is measured as well as the magnetism of separated grains of the same thickness. A major goal of this chapter is the determination of the Curie temperature T_C of the ultra thin EuO(100) on graphene compounds. In section 6.2 two difficulties upon the determination of T_C, namely the artificial T_C enhancement in a non zero magnetic field and the imprecision of the temperature reading are explained. A way to compensate for them is worked out with help of a 45 nm thick EuO(100) on YSZ reference sample [146]. The samples discussed here are also investigated with STS and show the EuO(100) surface state, as presented in chapter 8.

6.1 From Single EuO Grains to Thin Films

The epitaxy of EuO grains on CVD graphene has first been discussed in reference [17] as (100) textured EuO with its bulk lattice constant and no preferred in plane orientation. Up to now no closed films have been prepared by this method. Here we affiliate to this work with the growth of closed EuO layers in high crystalline quality and low roughness on a mesoscopic lateral scale. Figure 6.1 shows data of two layered samples of EuO on CVD graphene on Ir(111). Both samples are grown by MBE through simultaneous deposition of Eu and O_2 under Eu excess of f_{Eu}/f_O=1.4 at room temperature and are post annealed at 720 K in an Eu-atmosphere. The data presented in figure 6.1 a)-d) come from one sample and the data shown in figure 6.1 e)-f) originate from another sample grown under the same conditions, but made with twice the deposited amount of Eu and O_2, as the sample belonging to figure 6.1 a)-d). The LEED diffraction rings in figure 6.1 a) show a (100) texture and a random in-plane orientation of the EuO. The six outer diffraction spots originate from

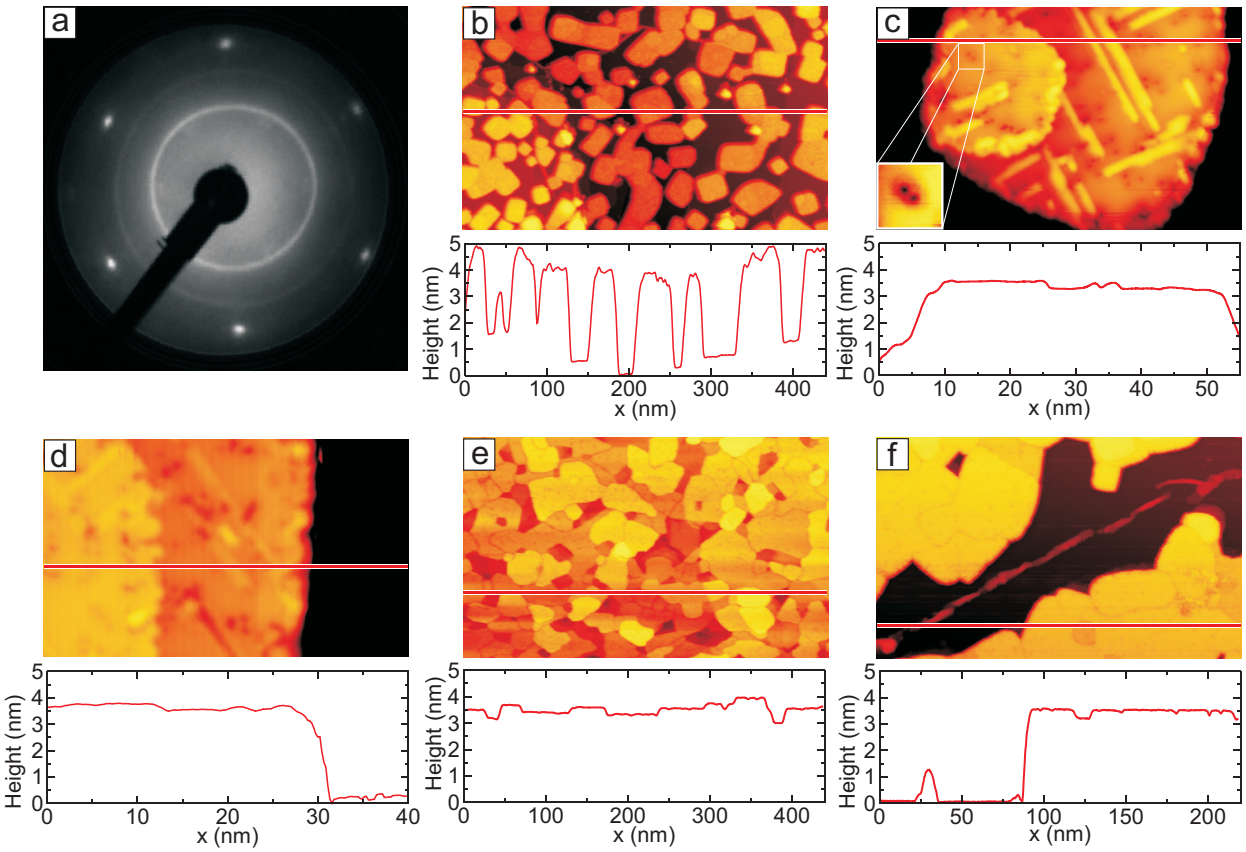

Figure 6.1: EuO on graphene on Ir(111), grown at room temperature and post annealed. a) Deskewed LEED diffraction pattern of EuO(100) grains with random in plane orientation at E=113.5 eV. b)-f) STM constant current topography images, each with height profile as indicated by red line in images. b)-d) STM images of the same sample as investigated with LEED in a). b) Large scale STM topography of (100) textured EuO grains, Θ=63 %, scan size 440 nm × 270 nm, U_{Bias} = 1.67 V, I = 50 pA, imaged at 5.3 K. c) STM topography image of an EuO(100) grain (same sample imaged in b)) scan size 55 nm × 34 nm, U_{Bias} = 1.86 V, I = 16 pA, imaged at 5.3 K. Inset: Zoom in of 5 nm × 5 nm, shows electronic defect sites (same tunneling conditions). d) STM topography image of EuO(100) grain as in c) but imaged at 81 K, scan size 41 nm × 25 nm, U_{Bias} = 1.62 V, I = 33 pA. e) STM topography of a closed (100) randomly in plane textured EuO film on graphene on Ir grown by depositing twice the amount of Eu and O as in a)-d), scan size 440 nm × 265 nm, U_{Bias} = 1.09 V, I = 77 pA, imaged at 170 K. f) STM of same sample as shown in e), a with EuO uncovered graphene wrinkle is visible, scan size 220 nm × 133 nm, U_{Bias} = 1.56 V, I = 80 pA, imaged at 5.3 K.

graphene areas which are not covered with EuO but intercalated with europium. These uncovered graphene surface area fraction amounts to 37%, as displayed in the related STM topography image figure 6.1 b). So the EuO coverage of this sample is Θ=63 %. The STM image in figure 6.1 b) shows rectangular EuO(100) grains with an average height of 3.3 nm, measured from the graphene to the lowest height level of a grain. In the margin of error the grain height corresponds to 13 ML of EuO(100). At some grains partially a height of 14 ML is measured. Consistent with the previously discussed LEED pattern a random orientation of the edges of the grains is found. The average surface area, which is covered by one EuO grain amounts to $\overline{A}$=3600 nm^2. Figure 6.1 b) faintly displays the step edges of the substrate, which run vertically through the STM image. The EuO

grains do not grow over these step edges. Therefore in the lower left part of figure 6.1 b) a small (graphene covered) Ir(111) terrace with also small EuO grains is visible. The same effect can be see at graphene wrinkles, as visible in the upper middle and left part of figure 6.1 f). Figure 6.1 c) shows one grain of the same sample, imaged at 5.3 K and at $U_{\mathrm{Bias}} = 1.86\,\mathrm{V}$. The two height levels are separated by a step height of 0.25 nm, which corresponds to the EuO(100) step height. Unfortunately due to the finite size of the STM tip the left flank of the grain is not imaged very well (compare height profile of figure 6.1 c)). Figure 6.1 c) also shows stripe features, which run parallel, or perpendicular to each other and which are characteristic in STM images of EuO(100) measured at $U_{\mathrm{Bias}} = 1.86\,\mathrm{V}$. These lines enclose an angle of 45° with the edges of the EuO grains. The borders of the grains are composed of the dense packed and electrostatic neutral EuO$\langle 010\rangle$ directions, as experimentally verified by atomic resolution STM in section 7.2. Therefore the lines visible in figure 6.1 c) follow the EuO$\langle 011\rangle$ directions. Another feature, which is typical for STM topography images is displayed in the inset of figure 6.1 c). These features are named Electronic Defect Sites (EDS) and their origin, as well as the line like features are discussed in chapter 7 of this thesis. Figure 6.1 d) again shows an STM topography image of the same sample with EuO grains, but this time imaged at an elevated temperature of 81 K. The height of the EuO grain, measured with STM height profiles, does not show a significant difference compared to the low temperature measurements of figure 6.1 b) and c). As will be demonstrated in the following section (6.3) the EuO grains are ferromagnetic at 5.3 K and paramagnetic at 81 K.
As the last issue on the growth of EuO onto CVD graphene the growth of ultra thin closed EuO layers is demonstrated in the large scale STM image of figure 6.1 e). The EuO sample presented here is prepared in the same way, as the one discussed previously, but twice the amount of Eu and O_2 are deposited. In this way grown EuO film shows grain sizes comparable to those from figure 6.1 b) and two distinct height levels. Uncovered areas are only observed close to graphene wrinkles [162]. The absolute film thickness is measured at these sample areas, as displayed in figure 6.1 f). The absolute film thickness is estimated to (3.5 ± 0.1) nm, which corresponds to 14 ML of EuO(100) in the margin of error. So both, the closed film and the separated grains show the same thickness and just differ in the covered surface are fraction.

Growth experiments with strongly enhanced Eu excess are performed with the aim to electron dope the samples by oxygen vacancies. By enhancing $f_{\mathrm{Eu}}/f_{\mathrm{O}}$ up to 6.6 and annealing at 720 K, no variations to the samples described above are found. Combining the enhanced $f_{\mathrm{Eu}}/f_{\mathrm{O}} = 6.6$ and lower annealing temperatures do not produce EuO samples in a quality sufficient for STM investigations (not presented).
Further, experiments on the growth of EuO films thicker than 14 ML are performed. Thereby, higher amounts of the reagents Eu and O are deposited (also) at room temperature and post annealed. Already enhancing the reagents amount by a factor of two (nominal coverage of 28 ML)

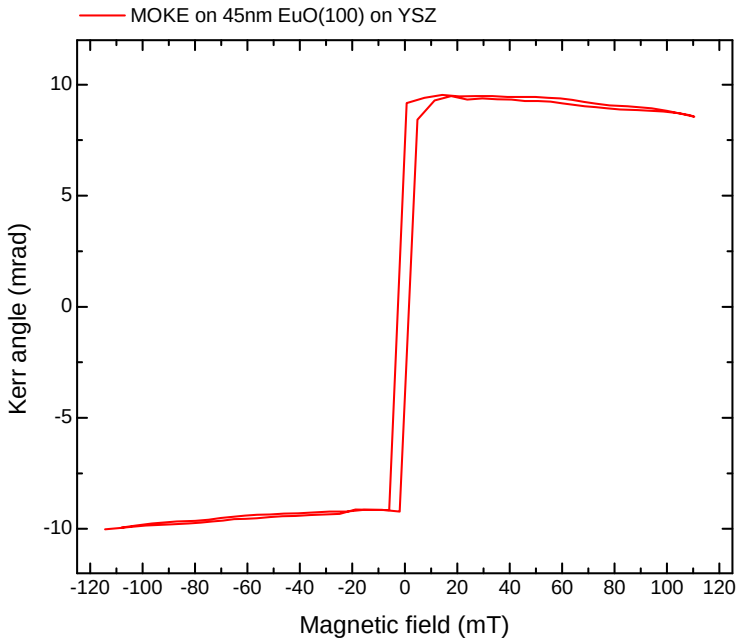

Figure 6.2: MOKE hysteresis loop of 45 nm aluminum capped single crystalline EuO(100) on YSZ (sample EuO_{Ref}) measured at 50 K.

no more leads to crystalline films, as revealed by LEED (data not presented). Also using higher annealing temperatures did not produce crystalline samples. So this growth method is limited to, and thus, ideal for the growth of 14 ML thin EuO(100) films.

6.2 Magnetic Reference Measurements at the LT-STM Machine

In the principle of MOKE measurements hysteresis loops of the Kerr angle vs. an external magnetic field $\Theta_{\mathrm{Kerr}}(B)$ are recorded and evaluated, as explained in section 5.6. T_{C} is the temperature above which Θ_{Kerr} of a sample vanishes in zero field, i.e. $\Theta_{\mathrm{Kerr}}(0\,\mathrm{mT})=0$ for $T \geq T_{\mathrm{C}}$ and $\Theta_{\mathrm{Kerr}}(0\,\mathrm{mT}) > 0$ for $T < T_{\mathrm{C}}$ (cooled in zero field). Since Θ_{Kerr} is proportional to the magnetization of the sample (see Sec. 2.3) and the spontaneous magnetization of a ferromagnet is small compared to its magnetization in an external field a measurement of $\Theta_{\mathrm{Kerr}}(T,\, 0\,\mathrm{mT})$ would lead to a poor signal to noise ratio. As a compromise between performing MOKE in zero magnetic field and an improved signal to noise ratio we evaluate the remanent Kerr angle $\Theta_{\mathrm{Kerr}}(\mathrm{Rem})$ of a hysteresis loop where B=0. In this section the effect of an external magnetic field on $\Theta_{\mathrm{Kerr}}(T,\, 117\,\mathrm{mT})$ and $\Theta_{\mathrm{Kerr}}(T,\, \mathrm{Rem})$ is quantified with help of *ex-situ* measurements on a 45 nm thick EuO(100) on YSZ reference sample [146] supplied by S. G. Altendorf. The 45 nm thick EuO(100) film on YSZ [146] reference sample is labeled as EuO_{Ref}. The sample quality is checked (not presented here) with LEED, reflection

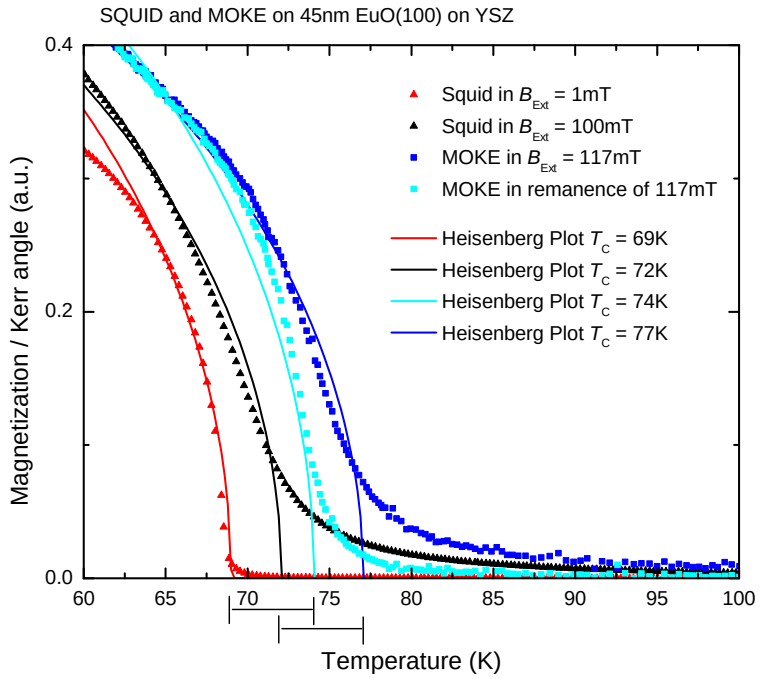

Figure 6.3: Magnetization $M(T)$ and $\Theta_{\mathrm{Kerr}}(T)$ of 45 nm aluminum capped single crystalline EuO(100) on YSZ (sample $\mathrm{EuO_{Ref}}$). $M(T)$ is determined by SQUID in an external magnetic field of 1 mT (red triangles) and 100 mT (black triangles). MOKE data of $\Theta_{\mathrm{Kerr}}(117\,\mathrm{mT})$ (dark blue squares) and $\Theta_{\mathrm{Kerr}}(\mathrm{Rem})$ (light blue squares) of the same sample, based on hysteresis measurements as presented in figure 6.2. The remanent MOKE signal is measured in a small residual field of about 10 mT due to technical complications. The temperature values are raw data. The lines show Heisenberg plots fitted to the data.

high energy electron diffraction (RHEED) and x-ray photoelectron spectroscopy (XPS) and found to be (100) textured, undoped and to contain just Eu^{2+} ions. The film is capped with 4 nm of aluminum as a protection layer against ambient conditions. Furthermore, the temperature reading is calibrated with the help of the $\mathrm{EuO_{Ref}}$ sample for temperatures around 70 K in the following part: The $\mathrm{EuO_{Ref}}$ film is first explored with MOKE hysteresis measurements (as explained in section 5.6) in s-polarization. The MOKE hysteresis of this sample is shown in the external magnetic field range of in B from -117 mT to +117 mT and at the temperature T of 50 K in figure 6.2. The data clearly show a ferromagnetic behavior and reveal the reference sample to be magnetically soft due to the low coercivity field of 3 mT and the square like shape. The sample magnetization saturates in the field of just B=5 mT. The $\mathrm{EuO_{Ref}}$ sample gives rise to a Kerr angle $\Theta_{\mathrm{Kerr}}(117\,\mathrm{mT})$ of approx. 10 mrad. Hysteresis loops are recorded vs. temperature (not shown) and analyzed for $\Theta_{\mathrm{Kerr}}(117\,\mathrm{mT})$ and $\Theta_{\mathrm{Kerr}}(\mathrm{Rem})$, as explained in section 5.6. The type K thermocouple, which has to be calibrated is pressed on top of the wafer with a clamp to guarantee a good thermal contact. Wafer and clamp are connected to the same copper body (adapter for wafer mounting on metal sample holder) part and are therefore on the same temperature. SQUID measurements on the same sample are performed in

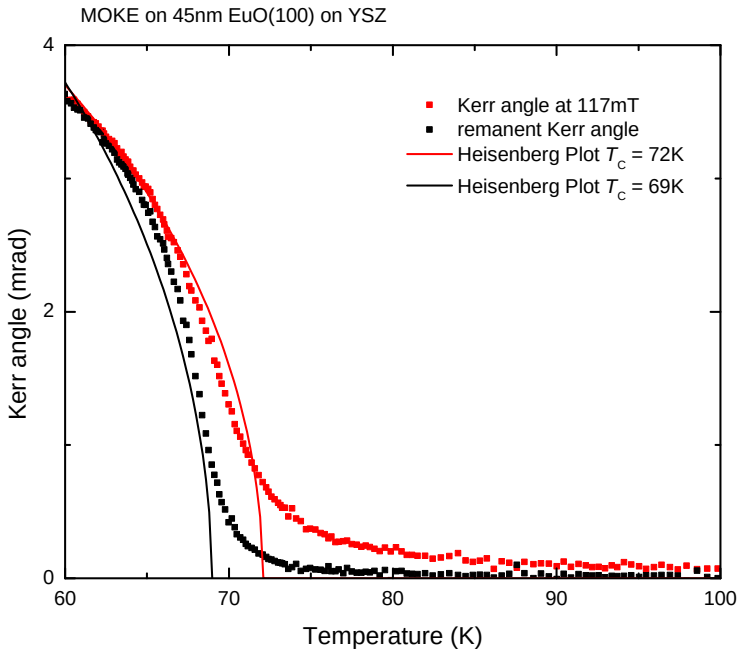

Figure 6.4: Same data as shown in Fig. 6.3 after temperature correction. The temperature values are corrected by -5 K. The lines show Heisenberg plots for T_C=69 K (black line) and T_C=72 K (red line) each fitted to the data.

B of 1 mT and 100 mT, whereby B is applied in-plane analogous to the MOKE measurements.The MOKE data of Θ_{Kerr}(117 mT) and Θ_{Kerr}(Rem) is compared to the SQUID magnetization data in B of 1 mT and 100 mT in figure 6.3. Heisenberg magnetization functions are fitted to the data. Despite the $M(T)$ data does not perfectly follow the ideal Heisenberg law the plots are still a suitable tool to determine T_C. According to the SQUID data in figure 6.3 T_C of sample EuO_{Ref} in B=1 mT is determined to 69 K, which is the overall accepted literature value of undoped EuO [51; 52], and undoped films of EuO thicker than 10 nm [3]. Measurements of Θ_{Kerr}(Rem) of the same sample in figure 6.3 show a T_C of 74 K. The remanent MOKE signal was measured in a residual magnetic field of about 10 mT for experimental reasons (hysteresis of yoke of magnet of MOKE setup, see section D). This residual field effect is corrected during data evaluation, but since the data points around B=0 mT are not measured in a very high resolution the residual field effect on the magnetization is not subtracted out completely and causes the magnetization tail on the light blue curve in figure 6.3. The SQUID measurement in B=1 mT and the MOKE measurement of Θ_{Kerr}(Rem) have to show the same T_C, since both are performed in a very small external field close to zero mT. The temperature reading of the SQUID is optimized for the low temperature range and consists of two redundant negative temperature coefficient (NTC) temperature sensors. Therefore we assume the value of T_C determined by SQUID to be correct. Hence, we include a correction value for the MOKE temperature reading of -5 K, i e., 5 K have to be subtracted from

the type K temperature reading. This is done for all data presented in the following sections.
Next the effect of an external magnetic field on T_C, as theoretically explained in section 2.2, is demonstrated in figure 6.3. Beside the SQUID measurement in B=1 mT also SQUID measurements are done in B=100 mT, as displayed in figure 6.3. The magnetization is enhanced due to the enhanced external field and thereby T_C is enhanced artificially by 3 K to T_C=72 K. Further the SQUID magnetization measurement in the high magnetic field shows a magnetization tail, which is consistent with the theoretical prediction of the magnetization (compare figure 2.9).
The T_C enhancement of 3 K by the external field in the order of B=100 mT is also visible in the MOKE data in figure 6.3, T_C determined in high field by Θ_{Kerr}(117 mT) is 3 K higher than T_C determined in remanence by Θ_{Kerr}(Rem). By taking the type K temperature reading correction (as explained in this chapter) into account in figure 6.4 Θ_{Kerr}(117 mT) gives a T_C=72 K and Θ_{Kerr}(Rem) exhibits T_C=69 K, which is the real T_C of the sample. So this chapter demonstrates that a correction of the temperature reading of -5 K (valid for the LT-STM type K thermocouple of the manipulator in the temperature range around 70 K) and an evaluation of Θ_{Kerr}(Rem) gives a meaningful value for T_C of a sample.

6.3 Magnetism of 3.3 nm Thin Films of EuO(100) on Graphene

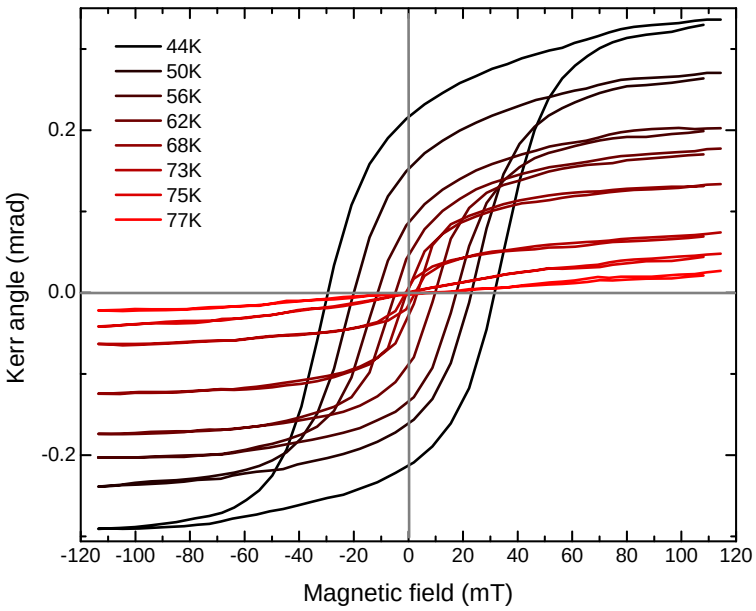

Figure 6.5: MOKE hysteresis loops $\Theta_{Kerr}(B)$, measured in p-polarization, of a 3.3 nm thin EuO(100) film as shown in figure 6.1 e) at sample temperatures from 44 K (black loop) to 77 K (red loop), as indicated in the plot.

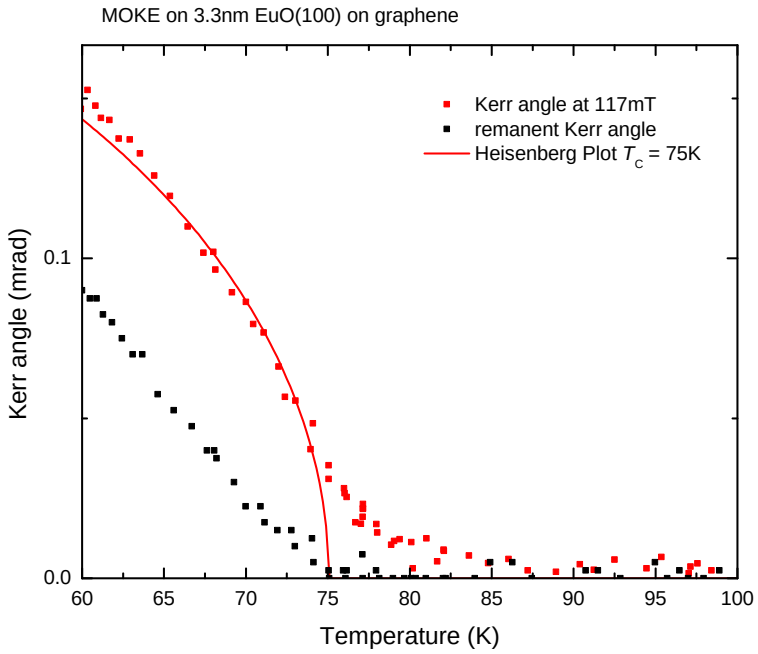

Figure 6.6: MOKE measurement of $\Theta_{\mathrm{Kerr}}(T$, 117 mT) (red data) and $\Theta_{\mathrm{Kerr}}(T$, Rem) (black data) of a 3.3 nm thin EuO(100) film as shown in figure 6.1 e). The values for Θ_{Kerr}(117 mT) and Θ_{Kerr}(Rem) are depicted from hysteresis loops at the corresponding temperature. The remanent MOKE signal is measured in a small residual field of about 10 mT. The red line shows Heisenberg fit for T_{C}=75 K fitted to the data.

In this section MOKE results on the in-plane magnetization of ultra thin *in-situ* grown EuO(100) films on CVD graphene on Ir(111) are presented. Effects of the residual magnetic field of the MOKE setups magnets are compensated for (see Sec. D).

MOKE hysteresis loops $\Theta_{\mathrm{Kerr}}(B)$ of a 3.3 nm thin EuO film (compare section 5.3 and section 6.1), are shown in figure 6.5 for sample temperatures between T=44 K and 77 K. At 44 K the hysteresis loop reveals a ferromagnetic ordered sample with a maximum Θ_{Kerr}(117 mT)=0.31 mrad and Θ_{Kerr}(Rem)=0.21 mrad caused by B=117 mT. This values of Θ_{Kerr} are small compared to those of the previously investigated sample $\mathrm{EuO_{Ref}}$, which is meaningful because of the decreased film thickness of 3.3 nm instead of 45 nm.

The investigated sample does not reach its saturation magnetization in B=117 mT and shows a coercive field of B_{Coer}=30 mT, compare figure 6.5. Therefore the thin film shows a clearly magnetically hard in plane magnetization. Since the film has a polycrystalline in plane grain distribution the value of B_{Coer} is a macroscopic average value.

In a reasonable way the MOKE signal at B=117 mT and in remanence is decreased at increasing T. Focusing on the loop at T=73 K shows a clear ferromagnetic hysteresis behavior. The MOKE data at T=75 K and T=77 K do not show a hysteresis loop, but a linear $\Theta_{\mathrm{Kerr}}(B)$ behavior with a small

$\Theta_{\mathrm{Kerr}}(117\,\mathrm{mT})$=0.05 mrad and 0.02 mrad respectively and $\Theta_{\mathrm{Kerr}}(\mathrm{Rem})$=0 mrad. So at T>75 K the MOKE signal shows no ferromagnetic behavior, but a paramagnetic magnetization caused by the external magnetic field B. Considering the $\Theta_{\mathrm{Kerr}}(B)$ loops shown in figure 6.5 T_{C} must be approximately 75 K. For a more precise determination of T_{C} $\Theta_{\mathrm{Kerr}}(T, 117\,\mathrm{mT})$ and $\Theta_{\mathrm{Kerr}}(T, \mathrm{Rem})$ are displayed in figure 6.6. $\Theta_{\mathrm{Kerr}}(T, 117\,\mathrm{mT})$ is influenced by B and gives an enhanced value of T_{C}, thus $\Theta_{\mathrm{Kerr}}(T, \mathrm{Rem})$ is decisive. For 3.3 nm thin films of stoichiometric EuO(100) on CVD graphene we find $T_{\mathrm{C}}\approx$75 K.

The literature value for undoped bulk EuO is T_{C}=69 K [51; 52], and for undoped ultra thin films of EuO with a thickness of 3.3 nm a T_{C} of about 62 K is expected [3]. So the 3.3 nm thin EuO film investigated here shows clearly an enhanced T_{C}. T_{C} is enhanced by 6 K compared to bulk EuO and remarkably by 13 K compared to films of the same thickness on an insulating support. As explained in section B of the appendix T_{C}=75 K is related to an effective ferromagnetic 4f-exchange coupling of $J_{4\mathrm{f}}$=0.530 meV [97].

As observed by M. Müller *et al.* in the ultra thin film regime the lower coordination number at the surface and interface (compared to Eu atoms in the EuO bulk) leads to a reduced T_{C} as well as intermixing of the EuO film with the substrate [2]. In the following it is discussed why T_{C} is not decreased, but increased in the system investigated here. Of course the thin EuO films of this thesis also have a lower coordination number at the surface and interface. Regarding the STM data in section 6, effects of intermixing can be ruled out, since the EuO just weakly interacts with the graphene substrate and dewets it. We also can conclude from the perfect crystalline quality, observed in the STM topography data, that T_{C} is not decreased due to structural imperfections.

Doping is also ruled out as a T_{C} increasing factor. Since our samples are prepared under UHV conditions and no co-evaporation is performed the only meaningfull kind of defects in our films are oxygen vacancies. The existence of 0.3% of oxygen vacancies is shown in chapter 7. In contrast to Gd-doping [66] 0.3% of oxygen vacancies do not cause a significant T_{C} enhancement [46]. In the ultra thin film regime oxygen vacancies even tend to cause a decrease of T_{C}, as shown by M. Barbagallo *et al.* [3].

Epitaxial biaxial strain can possibly enhance T_{C} [59]. Regarding figure 2 b) of reference [59] a biaxial lattice compression of 2% is needed for a T_{C} enhancement of 13 K. We assume our films to be uncompressed within the error margin, or even to be dilated by 0.7 % $\pm$ 1.1 % [152]. In consequence, the lattice compression of 2 % needed to explain the observed enhancement of T_{C} is far above the margin of error in our determination.

The formation of an Eu intercalation layer between the Ir(111) surface and the graphene layer takes place [153], as we know from STM. The idea of ferromagnetic order in the Eu intercalation layer and a coupling of its magnetism to the EuO film through a proximity effect comes up. XMCD measurements on the Eu intercalation layer do not show ferromagnetic order [163]. Therefore also a T_{C} enhancement caused by a proximity effect is ruled out. However one cannot rule out a mutual

amplification of EuO's and Eu's magnetic interactions.
Since the investigated EuO is undoped, no RKKY interaction in the EuO film can mediate FM order, as explained in section 2.1. But since the graphene substrate is strongly n-doped and therefore shows an increased charge carrier density at the Fermi level a ferromagnetic RKKY like 4f-exchange coupling could be mediated through it [164].
Another mechanism that could partly contribute to the increase in T_C is the image charge screening effect induced by the highly polarizable substrate, which is known to compensate finite-size phenomena [18].

6.4 Easy Magnetization Direction and Superparamagnetic Limit

Here we compare the magnetic properties of closed films whith those of separated grains of EuO(100), grown on epitaxial graphene (section 6.1). In figure 6.7 $\Theta_{\mathrm{Kerr}}(B)$ hysteresis measurements of both morphologies are presented. For an ideal comparison both measurements have been performed with the same experimental parameters. The topography of the closed film sample is presented in figure 6.1 e) and the topography of the separated grains sample is shown in figure 6.1 b). Both EuO samples are of 3.3 nm height, but of a different nominal coverage. So the separated grains sample also exhibits uncovered substrate areas.

Both samples show a ferromagnetic hysteresis $\Theta_{\mathrm{Kerr}}(B)$ behavior, see figure 6.7. For a better comparism the grain's loop has been normalized with the fraction Θ=63% of the EuO covered sample area. (Light reflected at EuO uncovered substrate areas is not affected by the Kerr effect, thus reducing the sample's avarage Kerr signal). The hysteresis loop originating from the closed film shows a Kerr angle of $\Theta_{\mathrm{Kerr}}(117\,\mathrm{mT})$=0.30 mrad, a remenant Kerr angle $\Theta_{\mathrm{Kerr}}(\mathrm{Rem})$=0.25 mrad, so $\Theta_{\mathrm{Kerr}}(\mathrm{Rem}) = 0.83 \cdot \Theta_{\mathrm{Kerr}}(117\,\mathrm{mT})$. The normalized $\Theta_{\mathrm{Kerr}}(B)$ loop of the separated grains sample shows the same $\Theta_{\mathrm{Kerr}}(117\,\mathrm{mT})$, but a $\Theta_{\mathrm{Kerr}}(\mathrm{Rem})$=0.20 mrad, so the grains $\Theta_{\mathrm{Kerr}}(\mathrm{Rem}) = 0.67 \cdot \Theta_{\mathrm{Kerr}}(117\,\mathrm{mT})$. The identical (normalized) $\Theta_{\mathrm{Kerr}}(117\,\mathrm{mT})$ of both samples is attributed to their identical thickness. Now we discuss the ratio of $\Theta_{\mathrm{Kerr}}(\mathrm{Rem})/\Theta_{\mathrm{Kerr}}(117\,\mathrm{mT})$, which is smaller than one.
Breaking a sample into domains strongly reduces its magnetization and minimizes magnetic stray fields on cost of the formation of domain walls. Since $(\Theta_{\mathrm{Kerr}}(\mathrm{Rem})/\Theta_{\mathrm{Kerr}}(117\,\mathrm{mT}))<1$ a breaking into magnetic domains in zero field is discussed. A breaking into domains would result in a very small $(\Theta_{\mathrm{Kerr}}(\mathrm{Rem})/\Theta_{\mathrm{Kerr}}(117\,\mathrm{mT}))$, which is not the case here. This does not necessarily mean that the separated grains are single domain particles, but they seem not to break into domains.
Note that the magnetic domain size in the separated EuO grains can just be as large as a grain at maximum. The magnetic domain size of the closed film can possibly be larger. Since magnetic domains in bulk materials are in the order of micrometer (which is large compared to the grain

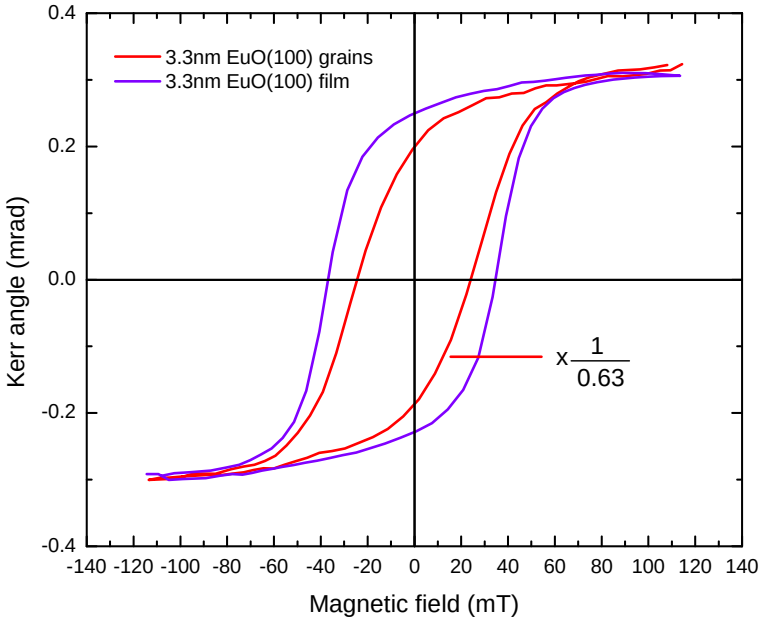

Figure 6.7: Longitudinal-MOKE hysteresis loops $\Theta_{\mathrm{Kerr}}(B)$ of a 3.3 nm thin EuO(100) closed film (purple loop) as shown in figure 6.1 e) and of the 3.3 nm thin EuO(100) separated grains (red loop) as shown in figure 6.1 b) and c). Both measurements are performed at 44 K in p-polarization. Θ_{Kerr} of the grain's loop is normalized with the EuO covered area fraction Θ=63%.

dimensions) the assumption that the separated EuO grains are single domain particles is reasonable.

Next we discuss the effect of the EuO easy axes in the hysteresis data: The EuO$\langle 111\rangle$ axes are the directions of easy magnetization in EuO, which enclose an angle of 54.7° with the EuO$\langle 100\rangle$ axes, i.e, an angle of 35.3° is enclosed by the (100) plane and the $\langle 111\rangle$ axes. The Kerr effect would gain a polar (out of plane) component, if the magnetization M rotated out of the sample's plane into the EuO[111] direction. The polar Kerr effect is about one order of magnitude higher than the longitudinal one [6; 105]. A rotation of M into the EuO easy axis would result in $(\Theta_{\mathrm{Kerr}}(\mathrm{Rem})/\Theta_{\mathrm{Kerr}}(117\,\mathrm{mT}))>1$, which is not observed here. Furthermore in the literature it is stated by J. C. Suits *et al.* that for films of EuO "the magnetization will always be in the film plane" [36]. This also holds for the separated EuO grains, since the lateral dimension of these is much larger than the vertical one. So M of the film and grains is in the sample's plane.
Notwithstanding M can be aligned along the projection of the EuO$\langle 111\rangle$ easy axes on the film plane, namely the EuO$\langle 110\rangle$ directions. The EuO samples (closed film and separated grains) show a random in plane distribution of their grains. In a high field M of all grains is aligned with the field resulting in M_{Max}, but realigns into the EuO$\langle 110\rangle$ directions in zero field. So in zero field M is randomly in plane distributed with angles φ from -45° to 45° to the direction of the previously

applied B (since the EuO(100) surface is four fold symmetric). Calculating the average projection $\bar{M}$ of the randomly aligned M on B gives

$$\bar{M} = \frac{\int_{-45°}^{45°} \cos(\varphi)\mathrm{d}\varphi}{\int_{-45°}^{45°} \mathrm{d}\varphi} = 0.90, \tag{6.1}$$

and thus, $\bar{M} = 0.90 \cdot M_{\mathrm{Max}}$. So a random in plane orientation of the individual grain's magnetizations leads to $\Theta_{\mathrm{Kerr}}(\mathrm{Rem}) = 0.90 \cdot \Theta_{\mathrm{Kerr}}(117\,\mathrm{mT})$. This decrease to 90% of the high field magnetization is in reasonable agreement with the ratio of $\Theta_{\mathrm{Kerr}}(\mathrm{Rem})/\Theta_{\mathrm{Kerr}}(117\,\mathrm{mT})$=83% for the closed film. So the hysteresis of the closed EuO film can be explained by the random in plane orientation of the EuO$\langle 110\rangle$ directions.

For the separated grains this ratio is even smaller (67%), so there must be another mechanism leading to a reduced remanence. The grain's volumes show a distribution from approx. 10 nm·10 nm·3 nm to 80 nm·80 nm·3 nm per grain (deduced from figure 6.1 b)). We calculate the in plane anisotropie energy $E_{\mathrm{Aniso}}(44\,\mathrm{K})$ of these EuO grains at the MOKE-temperature of 44 K by using the first order magnetocrystalline anisotropy constant [165]. For the smallest grains $E_{\mathrm{Aniso}} \approx 6{\cdot}10^{-22}\,\mathrm{J}$ and for the largest ones $E_{\mathrm{Aniso}} \approx 4{\cdot}10^{-20}\,\mathrm{J}$. We compare this numbers to $E_{\mathrm{Lim}} = 25{\cdot}k_{\mathrm{B}}{\cdot}44\,\mathrm{K} \approx 2{\cdot}10^{-20}\,\mathrm{J}$, which is a rule of thumb to estimate the superparamagnetic limit [166]. The anisotropie energy E_{Aniso} of the smallest grains is smaller, and E_{Aniso} of the largest grains is larger than E_{Lim}. Superparamagnetism occurs in ferromagnetic nanoparticles. In nanoparlicles below a threshold size their magnetization is flipped statistically for reasons of thermodynamics. So we conclude that the smaller separated EuO grains are superparamagnetic at 44 K and do not contribute to $\Theta_{\mathrm{Kerr}}(\mathrm{Rem})$, but to $\Theta_{\mathrm{Kerr}}(117\mathrm{mT})$. So we explain the decrease from $\Theta_{\mathrm{Kerr}}(\mathrm{Rem}) = 0.67 \cdot \Theta_{\mathrm{Kerr}}(117\,\mathrm{mT})$ by a combination of an in plane randomly distributed easy direction and superparamagnetic behaviour of the smaller EuO grains.

7 Defects in EuO

The experiments and measurements presented in this chapter were carried out by myself. S. Schumacher supported me in measurements and post processing of data on work function. Discussion of the data took place with C. Busse and T. Michely. Partially, the contents of sections 7.2 and 7.4 is included in the publication on the surface state in EuO(100), which have been submitted to Physical Review Letters.

The growth and mesoscopic texture of thin EuO films on graphene has been discussed in section 6.1. In the this chapter, we show the correlation between strong electronic features and structural defects in EuO(100).

7.1 Strong Electronic Corrugation

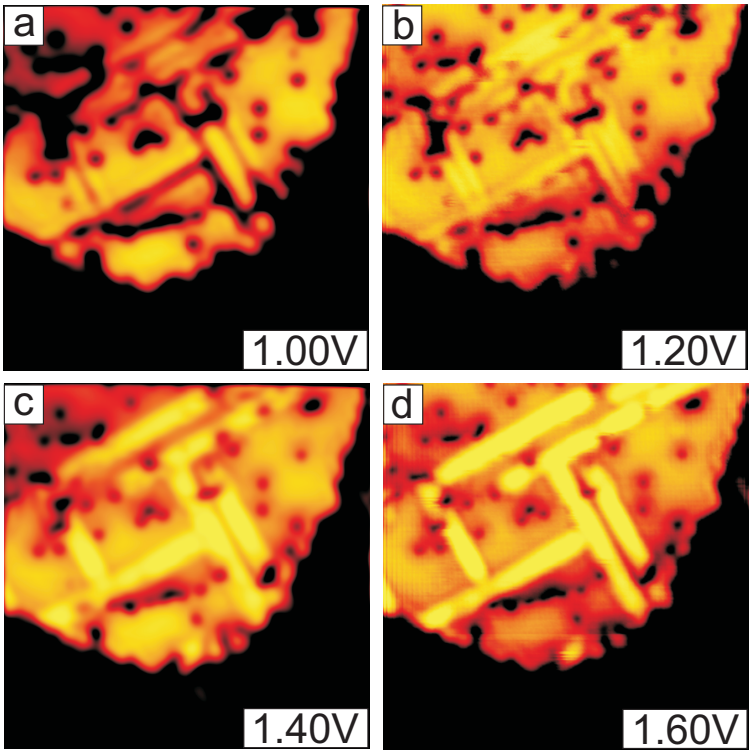

Figure 7.1: Bias dependent constant current ($I = 16\,pA$) topography STM images of an EuO(100) surface area, using the same sample as displayed in figures 6.1 a)-d). a) $U_{Bias} = 1.00\,V$, b) $U_{Bias} = 1.20\,V$, c) $U_{Bias} = 1.40\,V$, d) $U_{Bias} = 1.60\,V$. Image size $27.5\,nm \times 27.5\,nm$, measured at $5.3\,K$ and displayed in the same topography contrast.

Constant current STM images of EuO(100) surfaces show a strongly bias dependent apparent topography. In order to illustrate this, figures 7.1 a)-d) show STM topography images of the same EuO(100) surface area, measured at different bias voltages from U_{Bias}=1.00 V to U_{Bias}=1.60 V, displayed in the same contrast. A positive bias voltage probes the unoccupied DOS of the sample, (section 5.5). The EuO(100) surface exhibits line features, which enclose angles of 45° to the EuO grain edges, and dot like features (section 6.1).

The line features appear as depression at U_{Bias}=1.00 V. At a slightly enhanced U_{Bias}=1.20 V these line depressions become surrounded by a protrusion like line at each side. At even higher U_{Bias}=1.40 V and U_{Bias}=1.60 V the two lines run together to one elevated line in STM topography, where a depression was imaged at U_{Bias}=1.00 V. The height of this line is in the order of 0.15 nm at U_{Bias}=1.60 V.

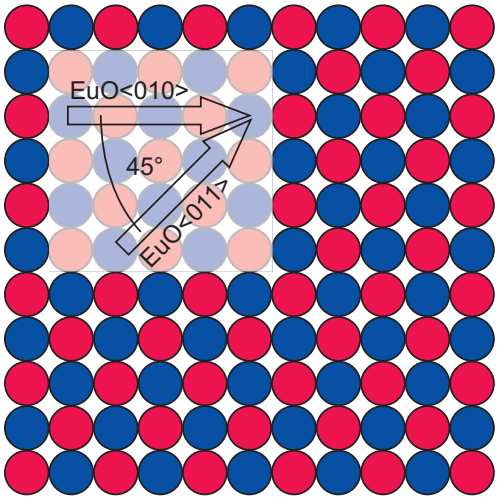

Figure 7.2: Model of the EuO(100) surface. The red dots represent O atoms and the bue ones Eu atoms. The EuO⟨011⟩ and EuO⟨010⟩ equivalent directions of high symmetry are indicated.

The EuO⟨011⟩ directions run along the dense packed rows of Eu, respectively O atoms as shown in figure 7.2. Since the lines run along the this EuO⟨011⟩ directions a relation either to Eu sites or to the O sites is reasonable. The bias dependent topography study is a promising precursor for the spectroscopy part on EuO(100) in chapter 8. Especially, the spatial dependence of the electronic line feature on the bias voltage will become clear as an effect of dispersion in chapter 8.

The dot like defects in the EuO(100) surface, here called electronic defect sites (EDS) show a similar qualitative behavior. They appear as depressions at U_{Bias}=1.00 V and show a decreasing depth upon increasing U_{Bias} up to 1.60 V. Within one image EDS of different sizes are found. Figures 7.3 a)-f) show a series of bias dependent STM constant current topography images on one electronic defect site in the range from U_{Bias}=1.20 V to U_{Bias}=2.20 V. All images are displayed in the same contrast and exhibit a strong bias dependency of the apparent topography. Figure 7.3 g) displays the radial averaged topography height profiles of the data presented in the single images.

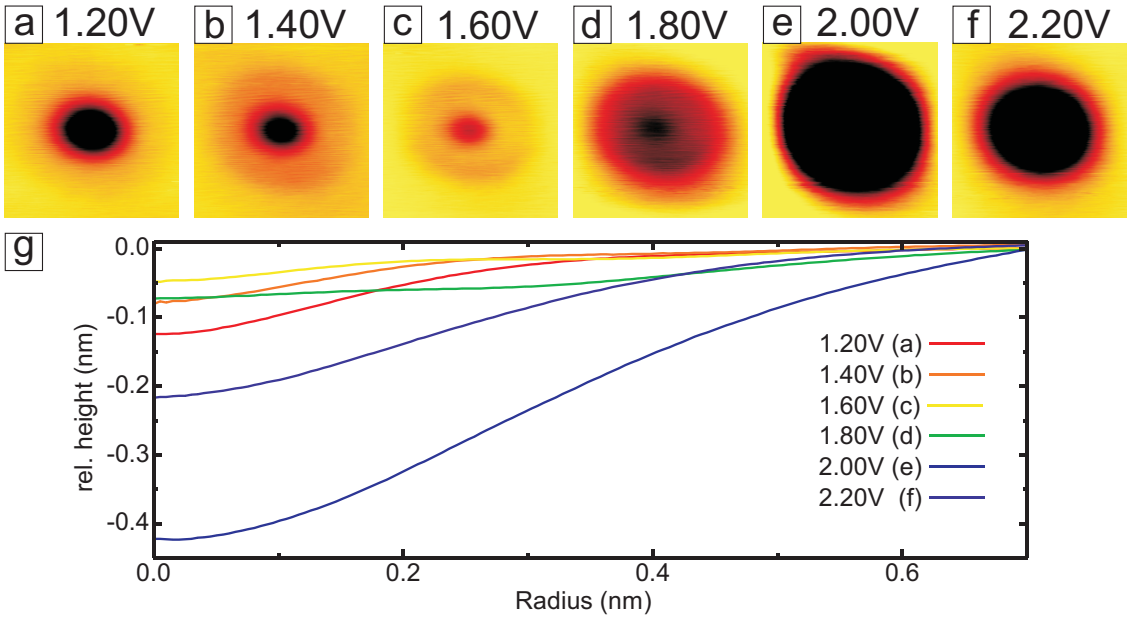

Figure 7.3: Constant current (I = 120 pA) topography STM images of an EuO(100) surface area imaged at various U_{Bias}, displayed in the same topography contrast. Measurements are performed using the same sample as displayed in figure 6.1 e)-f). a) U_{Bias} = 1.20 V, b) U_{Bias} = 1.40 V, c) U_{Bias} = 1.60 V, d) U_{Bias} = 1.80 V, e) U_{Bias} = 2.00 V, f) U_{Bias} = 2.20 V. Scan sizes 1.4 nm × 1.4 nm each, imaged at sample temperature = 100 K. g) Radial averaged heights of a)-f), whereby a radius zero means the middle of the STM images a)-f).

The measurements are consistent with the data shown in figure 7.1, since the apparent depth of the EDS decreases from U_{Bias}=1.20 V to U_{Bias}=1.60 V. Upon imaging the EDS at even higher positive bias voltages the apparent depth of the EDS again strongly increases up to 0.42 nm. Note that this electronic corrugation is extremely large compared to the structural corrugation of atomic resolution, even to monoatomic step edges.

7.2 Oxygen Vacancies

This section connects the previously demonstrated electronic corrugation to structural defects. Figures 7.4 a) and b) show STM topographies of the same EuO(100) surface area. Figure 7.4 a) is measured at U_{Bias}=1.51 V and shows an EDS with apparent depth of 0.06 nm, whereby figure 7.4 b) is imaged at U_{Bias}=-0.68 V and shows the atomically resolved EuO(100) surface. The nearest neighbors (NN) distance in the atomically resolved STM image is (0.36±0.02) nm, in good agreement with the Eu-Eu NN distance in the EuO(100) surface. STM just images the Eu atoms and not the O atoms of EuO(100). The STM measurements presented here are performed at 5.3 K in the ferromagnetic phase (FM) of EuO. The density of states (DOS) of EuO in the FM phase has to be considered in order to interpret the atomically revolved STM data. Since EuO is a semiconductor its Fermi level E_{Fermi} is located in the band gap of the EuO band structure. Reference [167] experimentally shows that the DOS below the Fermi energy is dominated by Eu-4f states. This is

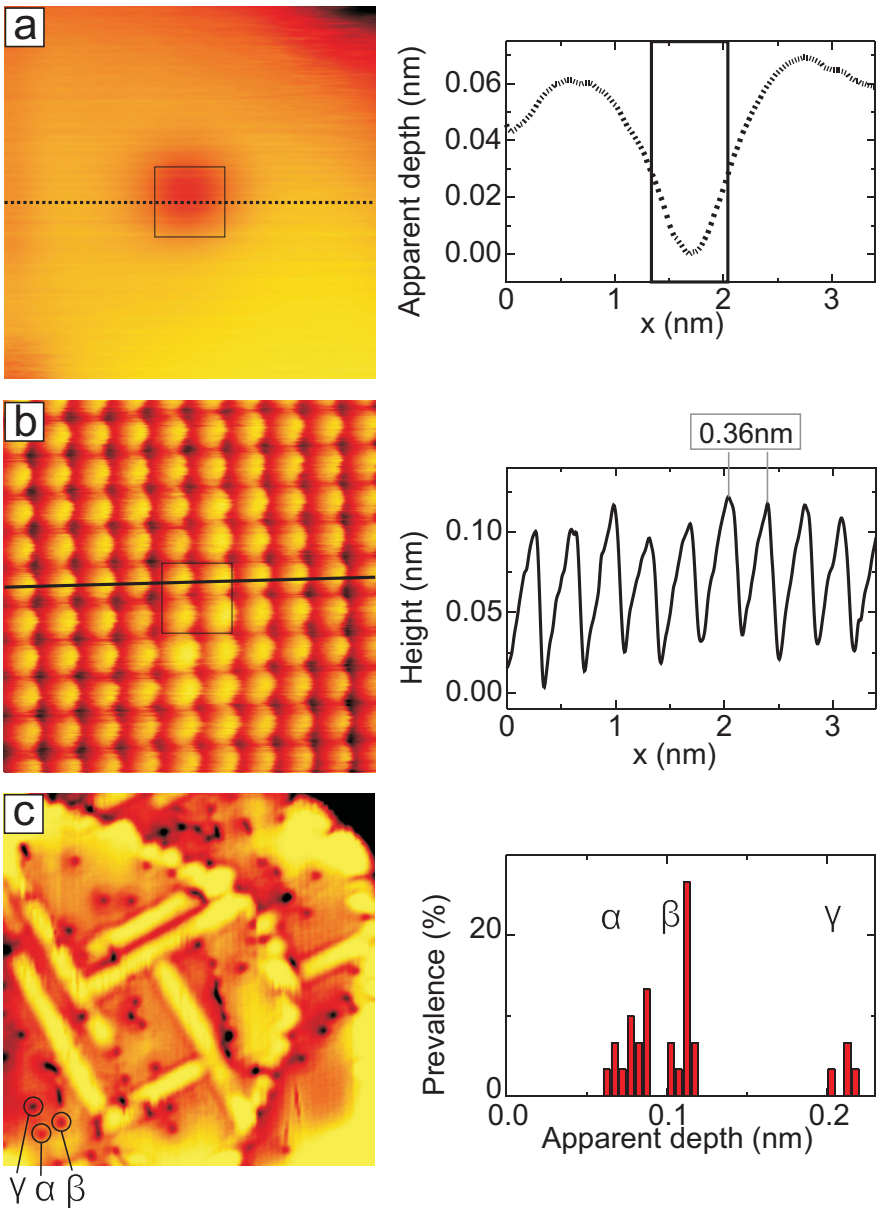

Figure 7.4: a) STM topography of an EuO(100) grain on graphene on Ir(111). Tunneling parameters: U_{Bias}=1.50 V, I=150 pA, scan width 3.4 nm, imaged at 5.3 K. A depression is measured in the center of the image. A height profile, as marked by the line in the image is shown. The two vertical lines correspond to the box in a). b) Atomically resolved STM topography image of the same sample area, as shown in a), but imaged with U_{Bias}=-0.68 V and I=100 pA, imaged at 5.3 K. The black boxes in a) and b) mark the same sample area. Also here a height profile is shown, as marked by the line in the STM image. c) STM image of an EuO(100) grain measured at U_{Bias}=1.50 V, I=16 pA and 5.3 K, scan size 27.6 nm × 27.6 nm. A statistic of the apparent depression depth within the large scale STM topography is presented.

confirmed by band structure calculations (figure 2.3). The unoccupied DOS is dominated by the bottom of the Eu 5d conduction band. Using U_{Bias}=-0.68 V the tunneling current is strongly dominated by electrons tunneling from the Eu-4f atoms into the tip and therefore only the Eu atoms of the EuO(100) surface are imaged. This is consistent with the NN distances determined by STM.

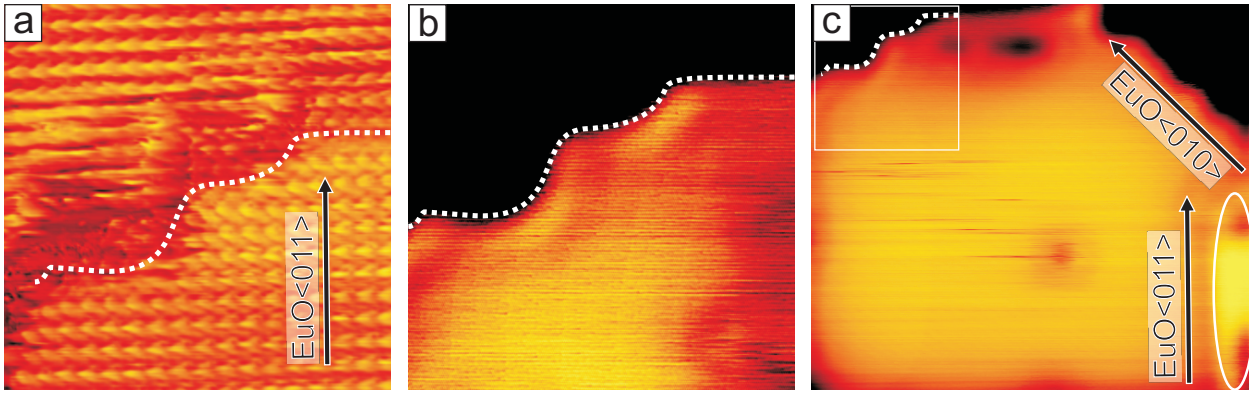

Figure 7.5: STM topography images of an EuO(100) grain on graphene on Ir(111) measured at 5.3 K. a) Atomic resolution over an EuO(100) step edge. The Eu atoms of the EuO(100) surface are imaged and the EuO⟨011⟩ directions are indicated by the black arrow. The step edge is marked by the dashed white line. Tunneling parameters: U_{Bias}=-0.69 V, I=8 pA, scan width 5.9 nm. b) Non-atomic resolution of the same sample area, as shown in a). Tunneling parameters: U_{Bias}=1.59 V, I=12 pA, scan width 5.9 nm. c) Zoom out of b), as indicated by the white box. The atomic directions are indicated. Electronic defect stripes (in the outer right part and upper part of c) marked by white ellipses) are found to be parallel to the EuO⟨011⟩ directions. The grain edges follow the EuO⟨010⟩ directions. Tunneling parameters: U_{Bias}=1.57 V, I=8 pA, scan width 13.8 nm.

Figure 7.4 b) shows an atomically well ordered and defect free surface. Defects were never observed in atomic resolution STM (also compare figure 7.5 a)). Therefore, we can exclude defects on Eu sites. The black frames plotted in figure 7.4 a) and b) mark the same surface area and connect the EDS to the atomic resolution, they show that the electronic defect site is located at an O site of the top EuO(100) layer, or an O site two monolayers below etc.

The apparent depths of the EDS are statistically evaluated in the larger scale STM image of figure 7.4 c), which is measured with the same U_{Bias} as figure 7.4 a). Therefore, the apparent depths of the EDS in figure 7.4 a) and c) are comparable. As it is visible in figure 7.4 c), there are EDS of different apparent depths, which can be classified into three characteristic classes, labeled by α, β, γ. The EDS in figure 7.4 a) with an apparent depth of 0.06 nm is classified to the EDS labeled α. A structural defect site in the topmost atomic layer of the EuO film is expected to have more influence on the electronic properties of the surface, than a defect in an underlying layer. Therefore, we consider that a defect in the topmost layer of EuO creates an EDS of maximum apparent depth (classified as γ), a defect located one monolayer below an EDS of medium apparent size (classified as β) and a defect in the third atomic layer the smallest kind of EDS (classified as α). This assumption will be supported by the spectroscopy results in the following chapter 8, where the existence of the surface state in EuO(100) is shown. A structural defect causes a scattering potential for these surface state, which decreases with the layer depth of defect.

Since the EDS in figure 7.4 a) is classified as a type α EDS it is supposed to be located on an O site in the third atomic layer. The EuO samples are grown under Eu excess and the formation of

oxygen vacancies is typical in EuO. Therefore, we consider that the EDS are connected to oxygen vacancies. By estimating the density of the EDS a vacancy concentration of 0.3% of the oxygen atoms turns out.

Next we also connect the electronic line defects (ELD) (figure 6.1 c), figure 7.1 and figure 7.4 c)) to structural defects. The ELD enclose an angle of 45° with the edges of an EuO(100) grain or terrace. Most ELD are found not to run completely through an EuO(100) grain, but to begin or start somewhere on the grain. Therefore, grain boundaries, line dislocations and slip planes are ruled out as the structural origin of the ELD. Figure 7.5 connects the ELD to the atomic directions of the EuO(100) surface. Figure 7.5 a) shows the Eu atoms of an EuO(100) surface area and figure 7.5 c) shows the alignment of an EuO(100) step edge and ELD to these atomically resolved Eu lattice. The EuO(100) step edge is found to be aligned along the EuO$\langle 010 \rangle$ directions and the ELD along the EuO$\langle 011 \rangle$ directions (dense packed Eu resp. O rows, see figure 7.2). A line up of single oxygen vacancies is often observed (for example in figure 7.1 and figure 7.4 c)). This suggests that a dense packed line up of oxygen vacancies, i.e., a missing oxygen row, leads to the formation of an ELD. But to answer the question of the ELD'S structural origin there is need for atomic resolution of these. The EDS are always depressions while the ELD are connected to protrusions. This argues against a oxygen vacancy row as the structural origin of the ELD.

In EuO a metal to insulator transition (MIT) is caused by oxygen vacancies, but there is a lower threshold vacancy concentration for the MIT [46]. The oxygen vacancy concentration determined by the EDS concentration amounts to 0.3%. Assuming that the ELD are desed packed rows of oxygen vacancies would lead to an oxygen vacancy concentration of 1%. Referring to reference [79] this oxygen vacancy concentration is not enough to cause the MIT in EuO. In the words of S. G. Altendorf, EuO samples, which show an MIT "could have oxygen deficiencies as much as several tens of percents" [79]. Therefore, an MIT is not expected in the samples presented here. Furthermore, STM shows only the oxygen vacancy concentration in the top atomic layers. Since the EuO films are post-annealed in an Eu atmosphere after growth, an increased oxygen vacancy concentration in this upper atomic layers is imaginable. So the average oxygen vacancy concentration of the whole film could be even lower.

7.3 Defect Mobility

In this section the dynamics of the defects is studied. Therefore, figures 7.6 a)-f) show STM topography images of an EuO(100) sample area, with EDSs. This sample area is repeatedly imaged by using the same tunneling conditions at a sample temperature of T=5.3 K. The time, which has passed since the first image in figure 7.6 a) is noted in the individual figures. The surface has been imaged with a rate of one image per three minutes. Some selected images are presented here. Events on the sample, which happen on a short time scale are shown by figures 7.6 a)+b) and

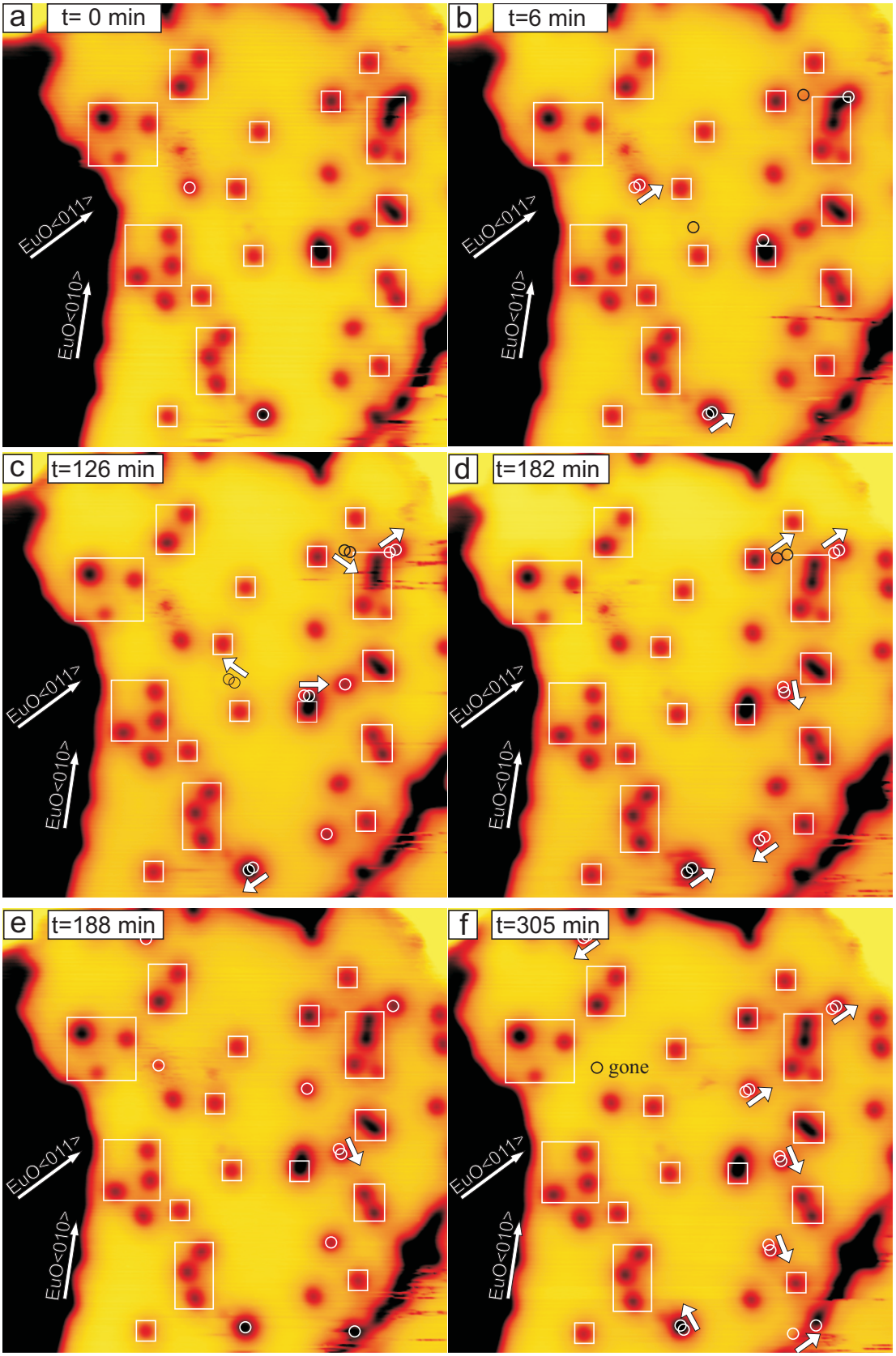

Figure 7.6: STM topography images of EuO(100), tunneling parameters: U_{Bias}=1.24 V, I=660 pA, scan width 27.7 nm, imaged at 5.3 K. The same surface area is imaged at different times, as indicated in the images. The series of images shows a defect mobility. Moves of defects are indicated by arrows and the position of defects before and after a move are indicated by circles. Defects, which do not move during the whole measurement are marked by squares.

figures 7.6 d)+e). The time interval between these events is six minutes. Longer time evolutions within about two hours are also shown. Events of spatial movements of single EDS are marked by the circles and arrows; the circles mark the initial and final spatial position and the arrows the direction of movement. Shallow EDS are marked by black colored circles, because of a lack of contrast. Three out of four of the observed EDS do not move during the complete measurement time of six hours, these are marked by the white frames. The remaining quarter of the EDS shows moves parallel to certain directions. The atomic directions in the observed EuO grain can be derived from the grain edge shown in figure 7.6. Therefore, the EDS are found to hop along the EuO$\langle 011 \rangle$ directions (with one exception), which consist of dense packed europium respectively oxygen rows. The average hopping distance of an EDS is (0.3 ± 0.1) nm, which corresponds to the O NN distance in EuO(100) within the margin of error. So during one hop of an EDS an oxygen atom changes sites with an oxygen vacancy in the EuO$\langle 011 \rangle$ direction. Furthermore, this process is the only rational one, since the move of an oxygen vacancy along the EuO$\langle 010 \rangle$ direction, i.e., over an europium site would be absurd.

In the following the EDS hopping rate is described. As already mentioned, three out of four oxygen vacancies are immobile, at least during the measurement. Since these immobile defects are of different apparent sizes, i.e., hosted in different atomic layers a layer dependency of the hopping rate cannot be found. Also in the quarter of mobile defects the hopping rate is not equally distributed. For example, the defect site in the lower part of figures 7.6 a)-f) moves frequently with a rate of approximately one hop per three minutes randomly in one of the EuO$\langle 011 \rangle$ directions. The other mobile EDS show a hopping rate from approximately one move per 100 minutes to one hop per 300 minutes. A correlation of the hopping rate and the number of the atomic layer the vacancy is hosted in cannot be found. The diffusion of oxygen vacancies in EuO was first proposed by M. Lubecka and A. Wegrzyn [168] in 1987 at temperatures from 400 K to 550 K. A diffusion of oxygen vacancies at T=5.3 K is hard to understand.

7.4 Work Function of EuO and Local Band Bending

The local work function Φ_{Sample} of a sample can be determined by STM using comparative measurements of the tunneling current $I(z)$ as a function of the vertical tip to sample distance z [17]. In this method the STM tip is stabilized over a sample spot in an arbitrary distance by a stabilization voltage $U_{\mathrm{Bias-Stab}}$ and current I_{Stab}. Then the feedback loop of the STM is opened and the tip is retracted from the surface by a certain distance. $I(z)$ decreases exponentially and the apparent height of tunneling barrier $\bar{\Phi}$ can be calculated by the following equation [169]:

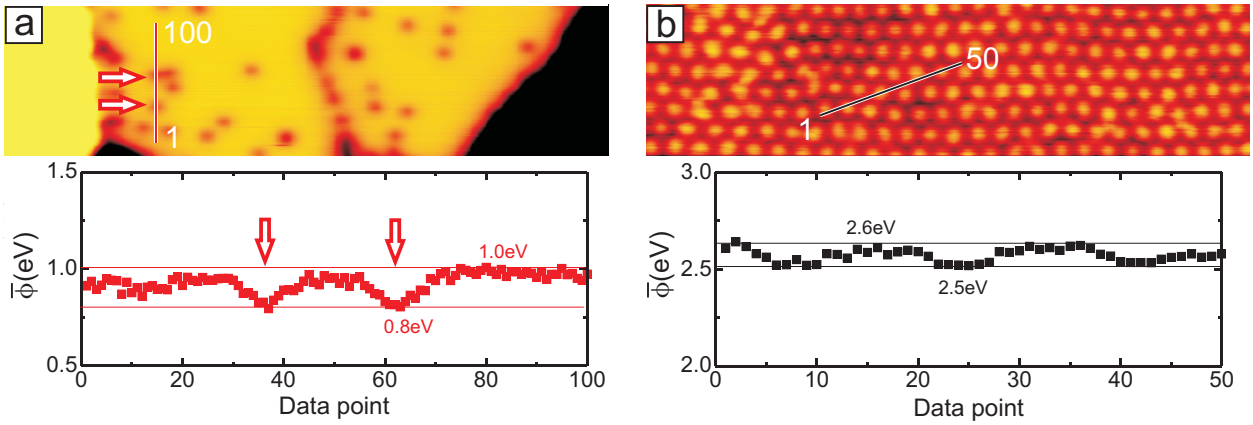

Figure 7.7: a) STM topography measurement on an EuO(100) grain, scan size 55.1 nm × 18.3 nm, U_{Bias}= 0.95 V, I = 510 pA, imaged at 5.3 K. 100 local $I(z)$ spectra are measured along the red line drawn into the STM image. The apparent barrier height $\bar{\Phi}$ of the tunneling junction on the EuO surface is determined for every spectra and plotted below the STM image. Tip stabilized for spectra at $U_{\mathrm{Bias-Stab}}$= 0.96 V and I_{Stab} = 510 pA. Spectra parameter: U_{Bias}= 0.70 V. b) STM topography of Eu intercalated graphene, scan size 55.1 nm × 18.3 nm, U_{Bias}= 0.86 V, I = 180 pA, measured between EuO grains at 5.3 K. Here also the local apparent barrier height $\bar{\Phi}$ is determined with the same tip (without any tip change in between) as used in a). Tip stabilized for spectra at $U_{\mathrm{Bias-Stab}}$= 0.70 V and I_{Stab} = 500 pA. Spectra parameter: U_{Bias}= 0.70 V.

$$\bar{\Phi} = \left(\frac{1}{k} \cdot \frac{\mathrm{d}\,\ln(I(z))}{\mathrm{d}\,z} \right)^2 \tag{7.1}$$

where k is a constant of 1.025 $\mathrm{eV}^{-0.5}$ $\mathrm{Å}^{-1}$ and (d ln($I(z)$) / d z) is determined by fitting the $I(z)$ data. The absolute work function of the tip Φ_{Tip} and of the sample Φ, and the bias voltage U_{Bias} applied during the measurement determine $\bar{\Phi}$. Comparative measurements of $\bar{\Phi}$ yield relative information of Φ. The comparative measurements must be performed with the same electronic state of the STM tip (i.e. without an atomic tip-change) and by using the same bias voltage. The work function difference of two that way measured samples (or sample areas) is calculated by the following equation [17]:

$$2 \cdot \left(\bar{\Phi}_1 - \bar{\Phi}_2 \right) = \Phi_1 - \Phi_2. \tag{7.2}$$

In figure 7.7 a) the spatially resolved $\bar{\Phi}_{\mathrm{EuO}}$ of an EuO(100) surface is plotted. 100 $I(z)$ spectra are taken along the line indicated in figure 7.7 a), which crosses two electronic defect sites in an EuO(100) area. The EDS are marked by red arrows in the STM image and in the data plot. The STM tip is stabilized over the sample for every spectrum and then retracted by 0.5 nm. The value of $\bar{\Phi}_{\mathrm{EuO}}$ determined by this method is $\bar{\Phi}_{\mathrm{EuO}}$ = (1.00±0.03) eV on the defect free EuO(100) area and drops by (0.20±0.02) eV to $\bar{\Phi}_{\mathrm{EuO}}$ = (0.80±0.02) eV at a type β oxygen vacancy site.

Figure 7.7 b) shows the comparative measurement of the apparent tunnel barrier height on europium (p(2×2)) intercalated graphene (gr) (between EuO grains). These measurements are

performed with the same STM tip (no atomic tip change) as the tip used in figure 7.7 a) and at the same $U_{\mathrm{Bias}} = 0.70\,\mathrm{V}$. A small variation of $\bar{\Phi}_{\mathrm{gr/Eu}}$ with in the moiré unit cell from $\bar{\Phi}_{\mathrm{gr/Eu}} = 2.50\,\mathrm{eV}$ to 2.60 eV is shown. For calculations the average value of $\bar{\Phi}_{\mathrm{gr/Eu}} = (2.55\pm0.10)\,\mathrm{eV}$ is taken. So the apparent barrier height difference from a defect free EuO(100) surface to an europium intercalated graphene amounts to $\bar{\Phi}_{\mathrm{gr/Eu}}$ - $\bar{\Phi}_{\mathrm{Eu0}}$ = (2.55±0.10) eV - (1.00±0.03) eV = (1.55±0.10) eV. Using equation (7.2) this results in $\Phi_{\mathrm{gr/Eu}}$ - Φ_{Eu0} = (3.10±0.20) eV. From literature we know the absolute work function of graphene on Ir(111) Φ_{gr} = (4.65±0.10) eV [170] and its difference to europium intercalated graphene on Ir(111) Φ_{gr} - $\Phi_{\mathrm{gr/Eu}}$ = (1.50±0.20) eV [17].

With this values we determine the absolute work function of EuO(100) $\Phi_{\mathrm{EuO(100)}}$ by the following equation:

$$\Phi_{\mathrm{EuO(100)}} = \Phi_{\mathrm{gr}} - \left(\Phi_{\mathrm{gr}} - \Phi_{\mathrm{gr/Eu}}\right) - \left(\Phi_{\mathrm{gr/Eu}} - \Phi_{\mathrm{EuO}}\right) \tag{7.3}$$

whereby $\Phi_{\mathrm{gr/Eu}}$ is the work function of (a p(2×2) superstructure) Eu intercalated graphene on Ir(111). Inserting the values given in the text yields:

$$\Phi_{\mathrm{EuO(100)}} = (4.65 \pm 0.10)\,\mathrm{eV} - (1.50 \pm 0.20)\,\mathrm{eV} - (3.10 \pm 0.20)\,\mathrm{eV} = (0.05 \pm 0.30)\,\mathrm{eV} \tag{7.4}$$

and a work function of $\Phi_{\mathrm{EuO(100)}}$ = (0.05±0.30) eV turns out. This value is remarkably small. In the established literature a value for $\Phi_{\mathrm{EuO(100)}}$ = (0.6±0.3) eV is measured by photoemission experiments [61]. Common values for the work function of most elements and compounds are in the range from 3.0 eV to 6.0 eV the value for EuO is comparatively small. But since the work function is determined by two independent investigations it seems to be really small. Here the determination of Φ is based on the trapezoid model of the one dimensional tunnel barrier. This model might be lacking at the here used small sample bias of 0.70 V applied to the semiconductor EuO. So the real value for Φ should be larger than 0.05 eV but probably smaller than the work function of common materials. The small work function of EuO becomes important if one considers charge transfer between EuO and its substrate. Since the work function of EuO is much smaller than the one of graphene charge is expected to flow from the EuO levels and n-dope the graphene. Thereby an upward band bending in the EuO would be the consequence. Electron doping of graphene is also gained just by intercalation with Eu [17]. So in the here investigated layer system of EuO on Eu-intercalated graphene the graphene is in contact with two n-doping sources. We can not easily conclude how the total charge transfer situation in this system is. If we just consider a Schottky contact of EuO and graphene we would expect a very strong upward band bending, which would lift the Eu-4f levels above the Fermi energy and depopulate these. This would lead to a decreased T_{C}, or even a non-magnetic sample. Since the compounds investigated here show a strong magnetism, (compare sec. 6.3) the Eu-4f levels must be occupied. So we can assume that in the three layer system of Eu/gr/EuO less electrons are transfered from the EuO levels to graphene levels

compared to the case of just a graphene/EuO junction. Note that the work function difference just gives indirect information on charge transfer. The Galvani potential is given by the chemical potentials μ of two materials [171].

Next, the local effect of oxygen vacancies on Φ is discussed. Previously, we found a local drop of $\bar{\Phi}$ at oxygen vacancy sites by $(0.20\pm0.02)\,\mathrm{eV}$ on a type β oxygen vacancy site. This directly reveals a local drop of the work function Φ by $2 \cdot (0.20\pm0.02)\,\mathrm{eV} = (0.40\pm0.04)\,\mathrm{eV}$. So the local work function is decreased by $\Delta\Phi$=0.4 eV at an oxygen vacancy site. The work function of a surface depends its surface dipole [81] and, thus is a surface sensitive quantity. Therefore the local work function is also sensitive to dipoles caused by local charge distributions. The electrostatic potential at oxygen vacancy sites in EuO constitutes F centers. This F centers can trap two (F^0), one (F^+), or zero (F^{2+}) electrons. Calculations [172] and measurements [173] have been performed on F centers in the divalent ionic compound MgO. In MgO a local surface dipole is connected to the F centers. This dipole enhances Φ on F^+ and F^0 sites, but decreases Φ at a F^{2+} site. So analogous we conclude that the oxygen vacancies in EuO are F^{2+} centers. From figure 7.7 a) we extract the radius r of the F^{2+} centers to $r = (0.8\pm0.1)\,\mathrm{nm}$.

8 The Spin Polarized Surface State in EuO(100)

The experiments and measurements presented in this chapter were carried out by myself. The measurements have been supported by C. Busse and F. Craes. Discussion of the data on the surface state took place with C. Busse, T. Michely and F. Craes. The contents of the sections 8.1 and 8.2 have been submitted to Physical Review Letters.

In this chapter the electronic structure of the EuO(100) surface is investigated by scanning tunneling spectroscopy (STS). Therefore ultra thin films of EuO(100) with a thickness of 3.3 nm grown on epitaxial graphene on Ir(111) are used. The topography, texture, magnetic properties and defects of these samples are discussed in the previous chapters 6 and 7.

8.1 Electronic Scattering Pattern on EuO(100)

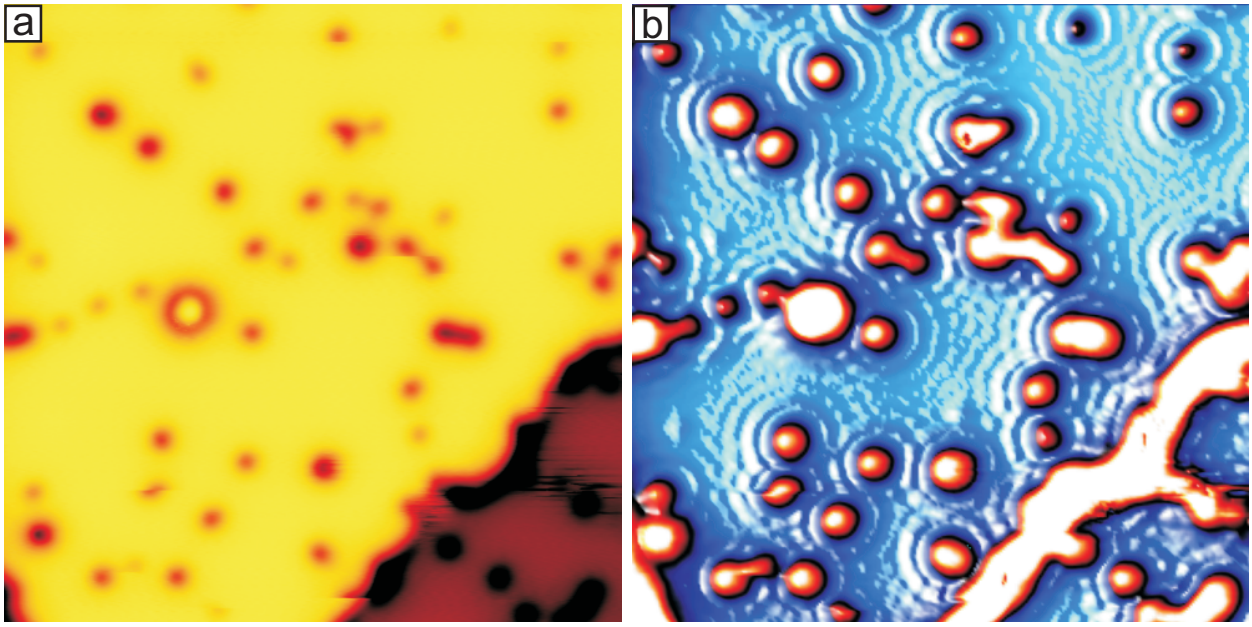

Figure 8.1: a) STM topography image of a closed EuO(100) film containing point defects and a mono atomic step edge, stabilization parameters: U_{Bias}=+1.25 V, I=77 pA, scan size 27.0 nm × 27.0 nm, imaged at 5.3 K. b) Simultaneously recorded (const. I=77 pA) differential conductivity dI/dU map at the same stabilization parameters. A spatial derivative of the spectroscopy map was added to enhance the contrast. Circular standing wave interference patterns of electrons scattered at point defects and also a high dI/dU signature at the step edge in the lower right part of the map are observed.

Figure 8.1 a) shows a medium scale STM topography image of an EuO(100) surface area containing some electronic defect sites (EDS) of different apparent depths (chapter 7) and a monoatomic

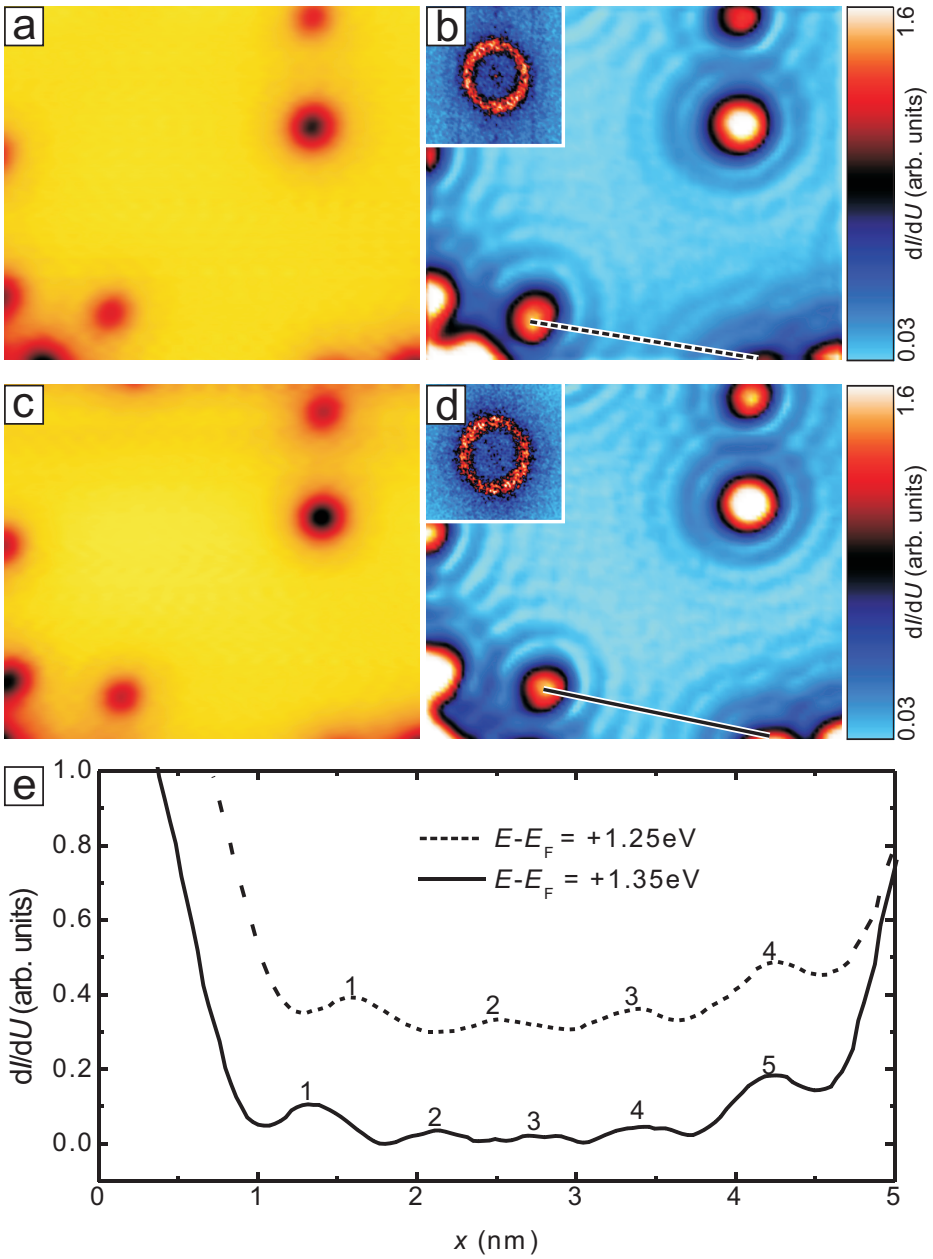

Figure 8.2: a) STM topography image of a closed EuO(100) film containing point defects, stabilization parameters: U_{Bias}=+1.25 V, I=77 pA , scan size 10.3 nm × 8.8 nm, imaged at 5.3 K. b) Simultaneously recorded (const. I) differential conductivity dI/dU map at the same stabilization parameters of the same sample area. A spatial derivative of the spectroscopy map was added to enhance the contrast. Circular standing wave interference patterns of electrons scattered at point defects are visible. Inset: Fourier transform (width 36.6 nm^{-1}) of a larger section of the Laplace-filtered dI/dU map. c) and d) same as a) and b) but measured at U_{Bias}=+1.35 V. e) Profiles of dI/dU as marked by the dashes and solid line in b) and d). The profile at 1.25 eV is shifted upwards in the plot by 0.3 arb. units for clarity. The profiles reveal an energy dependence of the scattering patterns.

step edge. We investigate the energy resolved LDOS of this sample area. Figure 8.1 b) shows the $\mathrm{d}I/\mathrm{d}U$ spectroscopy map of the unoccupied LDOS measured in constant current mode at $E - E_\mathrm{F}$=1.25 eV and 5.3 K. Concentric rings of the energy resolved LDOS are visible around the defect sites, and the scattering patterns of neighboring defects interfere with each other. This is the typical fingerprint of the scattering processes of surface state (SS) electrons. The high $\mathrm{d}I/\mathrm{d}U$ signature at the step edge in figure 8.1 b) indicates a strong scattering of the SS at this step edge. The quantitative investigation of the SS is demonstrated in figure 8.2. Figure 8.2 a) shows an STM topography cut out of figure 8.1 a) and figure 8.2 b) is the corresponding STS map displaying the concentric scattering rings around the oxygen vacancy sites. With hindsight one can see faint rings also in the topographic image (figure 8.2 a)). Right at the defect site the $\mathrm{d}I/\mathrm{d}U$ signal is very large. This is not a signature of the electrons in the surface state (SS) but an artifact of the constant current STS mode, since the tip to sample distance decreases at the topographically apparent depressions and the orbital overlap of the SS and the STM-tip's orbitals increases, leading to an enhanced STS signal. Constant height STS is the ideal tool to measure the SS directly at the defect sites and is described later in this chapter. The inset of figure 8.2 b) shows the Fourier transform (FT) of a Laplace-filtered large scale topographic image (containing figure 8.2 b)). It shows a single ring typical for a free-electron like surface state [174] and no additional features. The radius $k_\mathrm{FT}(E - E_\mathrm{F})$ of the ring is related to the wave vector of the electrons by $2 \cdot k(E - E_\mathrm{F}) = k_\mathrm{FT}(E - E_\mathrm{F})$[174]. From the data shown in figure 8.2 b) we derive $k(1.25\ \mathrm{eV}) = 3.88\ \mathrm{nm}^{-1}$ as depicted by the blue triangle in figure 8.3. The surface state is investigated in the same way at $E - E_\mathrm{F}$=1.35 eV and 5.3 K, as displayed in figure 8.1 c) (topography) and figure 8.2 d) (STS map), which also clearly displays the concentric scattering pattern. Here also the FT shows a single ring, which radius reveals $k(1.35\ \mathrm{eV}) = 4.17\ \mathrm{nm}^{-1}$. Therefore, the wave vector of the SS increases with increasing $E - E_\mathrm{F}$.

In a simplified analysis method, $k(E - E_\mathrm{F})$ can also be determined in real space by measuring the oscillation period λ of the sinusoidal modulations of the DOS patterns formed in the $\mathrm{d}I/\mathrm{d}U$ spectroscopy maps. This method is related to the FT-method by $k_\mathrm{FT} = 2\,\pi\,/\,\lambda$, so the wave vector is $k = \pi\,/\,\lambda$. In the following, we will rely on the real space evaluation method because it enables us to measure k not only at point defects, but also one-dimensional defects like step edges or grain boundaries. This is of special importance as often not enough point defects for a Fourier analysis could be found, even less one-dimensional defects, and the signal arising around line defects is much stronger. Figure 8.2 e) shows typical $\mathrm{d}I/\mathrm{d}U$-profiles between two EDS, as marked by the lines in figure 8.2 b) and d). At $E - E_\mathrm{F}$=1.25 eV four maxima of the modulated LDOS are measured between the two defects in the lower part of figure 8.2 b) and at $E - E_\mathrm{F}$=1.35 eV five maxima at the same distance. The distances between the maxima gives $k(1.25\,\mathrm{eV}) = (3.7 \pm 0.2)\,\mathrm{nm}^{-1}$ and $k(1.35\,\mathrm{eV}) = (3.9 \pm 0.2)\,\mathrm{nm}^{-1}$. The results on k from the FT and the real space method are in good agreement. We performed STS measurements over a wide range of energies (-3.0 eV to

+3.0 eV) at T=5.3 K. Scattering patterns have been observed only in the energy range 1.1 eV to 1.6 eV, the resulting relation of $k(E - E_F)$ is shown as red data points in figure 8.3 (all taken on the same film). We fit a parabolic dispersion $E = E_0 + \frac{k^2\hbar^2}{2m_{eff}}$ to the data points, see the red line in figure 8.3 and thereby determine $E_0 = 0.77$ eV and $m_{eff} = (1.09 \pm 0.10) \cdot m_e$, where m_e is the mass of the free electron. Note that this parameters represent the best fit to the red and black data points. The meaning of the black data points is discussed later in this section, but note that for physical reasons the black and red data points must result in the same m_{eff}.
Our findings are the first experimental proof of the existence of the surface state on EuO(100) predicted in reference [48]. At temperatures below T_C, the surface state is expected to be spin-split [48], following the splitting of the bulk band structure [4]. Therefore, at T=0 K a spin splitting of approx. 0.6 eV is expected, leading to a second parabola in the surface state's dispersion relation. However, in our measurement only one ring in the FT of figure 8.2 b), and thus, only one parabola for the low temperature data in figure 8.4 is visible. Note that for an exchange-split surface state it is not fundamentally forbidden to observe the spin-splitting in STM studies of standing wave patterns, in contrast to Rashba-split states [175]. In Rashba-split surface states the spin-splitting is coupled to k and the electrons would have to undergo a spin-flip for backscattering in the same branch of the surface state. In exchange-split surface states the spin-splitting originates from the exchange field (k independent) and no spin flip within one branch is needed to form scattering patterns. Therefore, scattering patterns of spin up and spin down states are formed independently.

8.2 Spin Degeneracy of the EuO(100) Surface State

In order to clarify our observations at low temperatures, we exploit the temperature dependence of the band structure of EuO [176], also known in literature as the red shift of the 5d conduction band at the ferromagnetic transition temperature T_C [177] : On approaching the Curie temperature T_C, the two spin branches are expected to converge Stoner-like. Consequently, we measured $k(E - E_F)$ clearly above T_C (T = 81.0 K). Figure 8.4 compares STS measurements on EuO(100) at b) 5.3 K and d) 81 K both performed at U_{Bias}=1.50 V. Due to the large thermal drift of the STM during heating, it is experimentally not possible to observe exactly the same sample area at different temperatures. The scattering patterns at high temperatures have a significantly larger periodicity, this is quantified in figure 8.4 c). Normalized line profiles as marked by the red and black lines in figure 8.4 b) and figure 8.4 d) show the temperature dependent wave length of the scattering patterns. The spatial distance between two minima amounts to $\lambda_{5.3K}(1.50\text{ eV}) = (0.699 \pm 0.010)$ nm and $\lambda_{81.0K}(1.50\text{ eV}) = (0.885 \pm 0.010)$ nm. The full dispersion of the surface state at high T is shown in figure 8.3 (black data points). The data at high temperatures are shifted upwards with respect to the low temperature ones. For the high temperature measurements we determined $E_0 = 1.10$ eV and m_{eff}=$(1.09 \pm 0.1) \cdot m_e$ (the fits at low and high T have been performed under the constraint of

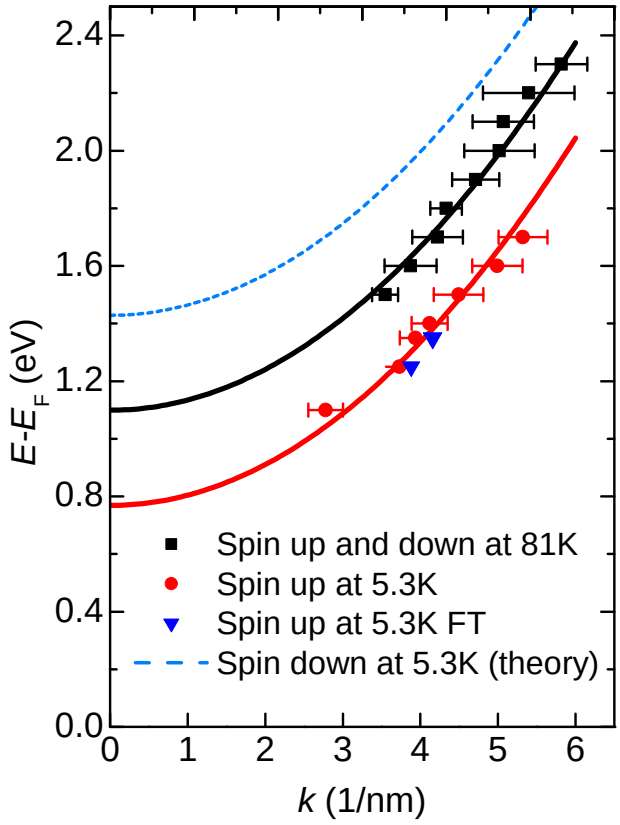

Figure 8.3: Dispersion relation $(E - E_F)(k)$. Sample temperature 5.3 K: red circles: Real-space method, blue triangle: Fourier transform method (see text). Sample temperature 81 K: Black squares: Real-space method. Lines: Parabolic fits to the data. Dashed blue line: Expected spin down branch of surface state with the same curvature as the parabolic fits.

the same m_{eff}). A comparison of the dispersion relation at high and low temperatures reveals an energy shift of (0.33 ± 0.10) eV.

We interpret the parabola found at high T as the converged surface state, i.e., both spin branches on top of each other. In turn, we propose that at low temperatures only the low energy spin branch (called spin up in the following) is visible. The expected, but unobserved surface state branch is indicated by the blue dashed line in figure 8.3, which is plotted with the same m_{eff} as both the others parabolas but shifted by twice the shift $2 \cdot 0.33\,\text{eV} = 0.66\,\text{eV}$ to higher energies with respect to the fit parabola to the 5.3 K data. The reason for the absence of the high energy branch (spin down) is unclear, however there are two possible effects: (i) The spin down surface state fully overlaps with the spin up bulk band, as visualized in figure 8.5. Consequently, a spin down surface state electron may decay into the bulk by undergoing spin-flip scattering which has a low, but finite probability. (ii) The scattering patterns of the spin down branch have a longer wavelength than the ones of the spin up branch at the same E. Such a weakly changing local density of states is difficult to observe in the presence of the short-scale pattern of the spin down state. In the model outlined above, we thus can give the spin splitting between (observed) spin up branch and the (unobserved) spin down branch as twice the splitting between the spin-down and the spin-degenerate branch, namely 0.66 eV, which is consistent with reference [48]. Thus, the comparison of the data above and below T_C is an indirect proof the exchange-split surface state.

A more direct proof of the surface state's exchange splitting could be done with analogous mea-

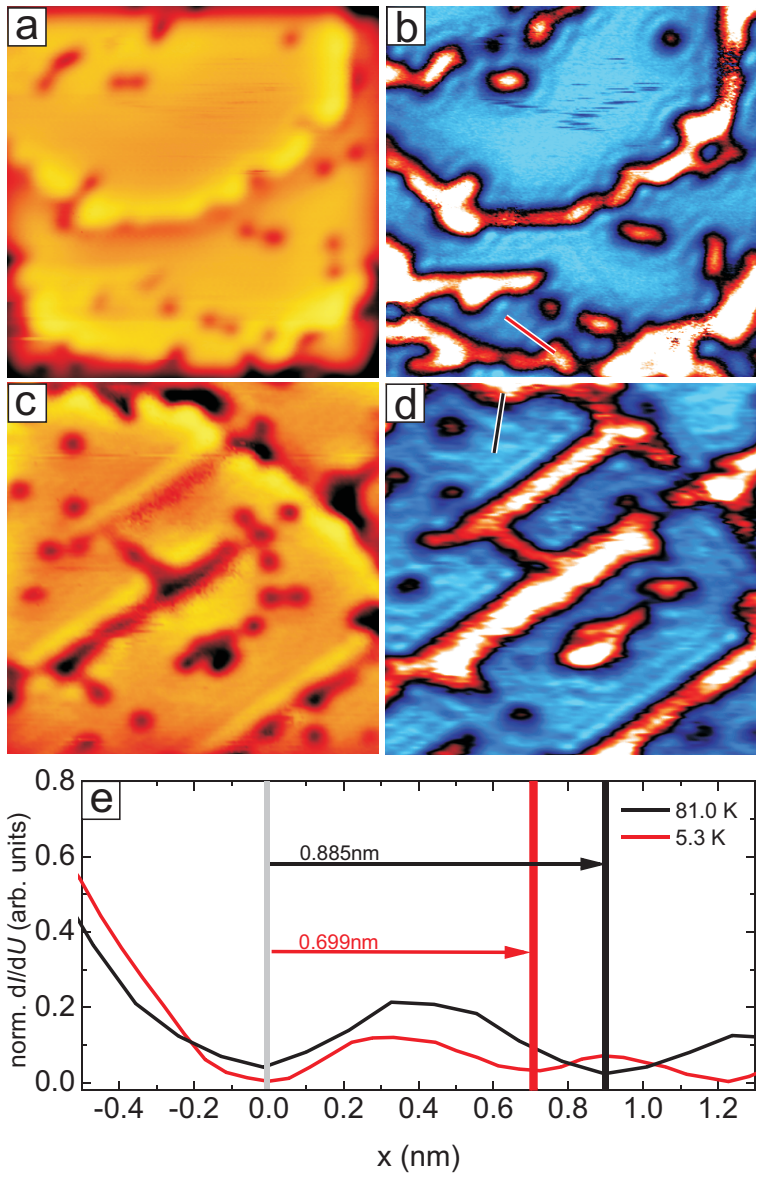

Figure 8.4: a) STM topography and b) same area (const. I) differential conductivity dI/dU map at 5.3 K measured on 3.3 nm thick EuO(100). Scattering is observed at step edges (stabilization parameters: U_{Bias}=1.50 V, I=73 pA) scan width 16.5 nm. c) STM topography and d) same area (const. I) dI/dU map of the same sample, but different area at 81.0 K. Scattering is observed at line defects (stabilization parameters: U_{Bias}=1.50 V, I=33 pA), scan width 16.5 nm. e) Line profiles of dI/dU as indicated by the red and black line in b) and d).

surements close below T_{C}, for instance at $0.9 \cdot T_{\mathrm{C}}$. At that temperatures like this the surface state should show a large exchange splitting, but should not overlap with bulk band bands. Thus, both bands of the surface state should be observable by STS.

The surface states in our experiment are up-shifted in energy with respect to the calculations in Ref [48]: The bottom of the spin down branch does not touch E_{F} but is situated 0.77 eV above it. There are several possible reasons for this discrepancy: (i) Regarding theory, there is the common difficulty to correctly treat the on-site Coulomb interaction which significantly influences the width

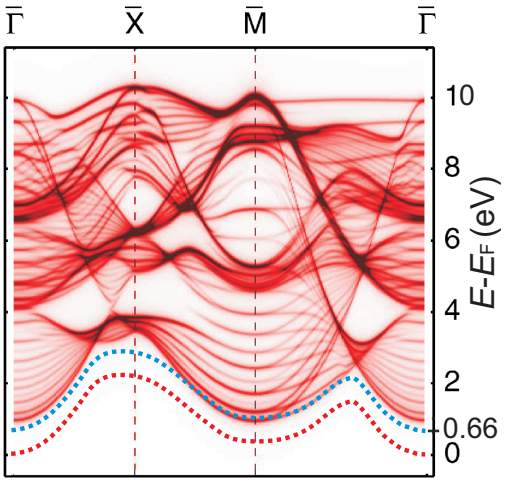

Figure 8.5: Unoccupied spin up (colored red) band structure of spectral densities of states of the top layer of EuO(100) at T=0 K calculated in the ferromagnetic Kondo-lattice model (FKLM). The dashed lines represent the surface state (spin up branch is red colored and spin down branch is blue colored) and the solid bands are bulk bands. The measured spin splitting of 0.66 eV is indicated. An overlap of the SS spin down branch with the spin up bulk conduction band is shown. The figure is modified from reference [48].

of the band gap. (ii) As the work function of EuO is much lower than the one of Eu-intercalated graphene (section 7.4), a charge transfer from EuO to it substrate seems feasible, which would cause an up-shift of all EuO-bands. However, it is very unlikely that such an effect is responsible for the full shift of 0.77 eV we observe here, as such a shift would already push the Eu 4f levels above the Fermi level [59]. (iii) Experimentally, also the tip could induce a band bending and thus shift the states in energy [178; 179]. However, we consider this effect to be insignificant as we could not observe any change in the dispersion relation upon varying the tunneling current by a factor of four.

The effective mass determined by our experiments is larger than predicted by calculations in reference [48]. The origin of this deviation is unclear, but could be due to correlation effects or the surface crystal potential. The local band bending, as discussed in section 7.4, does not influence the dispersion relation of the surface state, presented in figure 8.3, because we evaluated the SS scattering patterns in real space not at the defect sites, but in some distance of at least 1.5 nm.

8.3 The Brillouin Zone of the Surface State and its Signature on Defect Sites

Up to now we did not take the full two-dimensional band-structure of the EuO(100) surface state (SS) into account. To compare our results on the surface state with the calculations of R. Schiller and W. Nolting we transform the calculated SS spin up band (see figure 2.4) into equipotential cuts of its two-dimensional first Brillouin zone, see figure 8.6. It exhibits concentric equipotential contours around the $\bar{\Gamma}$-point, oval ones around the $\bar{X}$-point and square like ones around the $\bar{M}$-point. Elastic scattering of the SS can take place between all equipotential DOS in the Brillouin zone, particularly nesting prefers scattering between parallel regions (figure 8.6).
Our measurements exhibit circular scattering patterns in STS (displayed by figure 8.2 b) and d)).

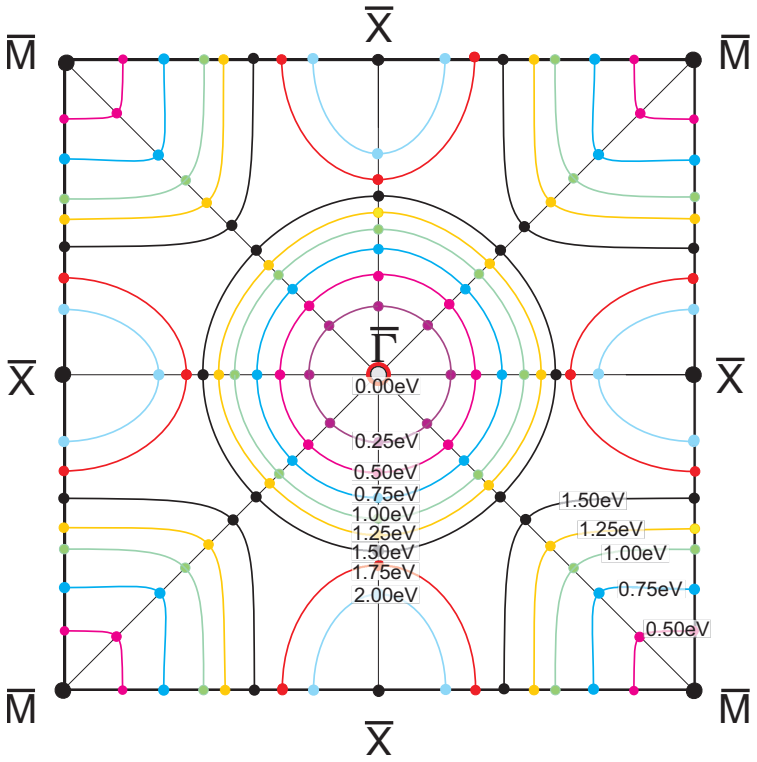

Figure 8.6: Equipotential cuts of the two-dimensional first Brillouin zone of the spin up surface state in EuO(100) at $(E - E_F)$=0.0 eV to 2.0 eV (as indicated in the figure). The solid points between the high symmetry directions are deduced from figure 3 of reference [48] and have been connected by the lines in a meaningful way considering the periodicity of the Brillouin zone and by avoiding kinks. The dispersion of the SS around the $\bar{\Gamma}$-point is free electron like and isotropic.

This suggests that we just observe the patterns of elastically scattered surface states around the $\bar{\Gamma}$-point. The tunneling current in STM and STS is strongly dominated by states from the $\bar{\Gamma}$-point [180]. So due the high k-selectivity of STS we only measure the elastically scattered surface state around the $\bar{\Gamma}$-point. The experimentally determined parabolic dispersion and circular scattering patterns fit nicely to the dispersion relation at the $\bar{\Gamma}$-point theoretically determined by R. Schiller and W. Nolting.

As the next issue the scattering patterns of the surface state right at the oxygen defect sites are discussed. As mentioned above in constant current STS mode right at the defect sites the $\mathrm{d}I/\mathrm{d}U$ signal is very large (compare figure 8.1 b), figure 8.2 b) + d) and figure 8.4 b) + d)). Scattering patterns of the SS are just evaluated in some distance to defects up to now. The center column of figure 8.7 shows energy resolved constant height STS maps of the surface state scattered at a single defect site, measured in the ferromagnetic phase of EuO. The constant height maps do not show a large $\mathrm{d}I/\mathrm{d}U$ signal at the defect site in general, but an energy dependent signature. The constant height STS maps the $\mathrm{d}I/\mathrm{d}U$ signatures in a constant height over the sample, while the constant current mode maps it on contours of equal integral DOS. The STS maps in figure 8.7 a) and i)

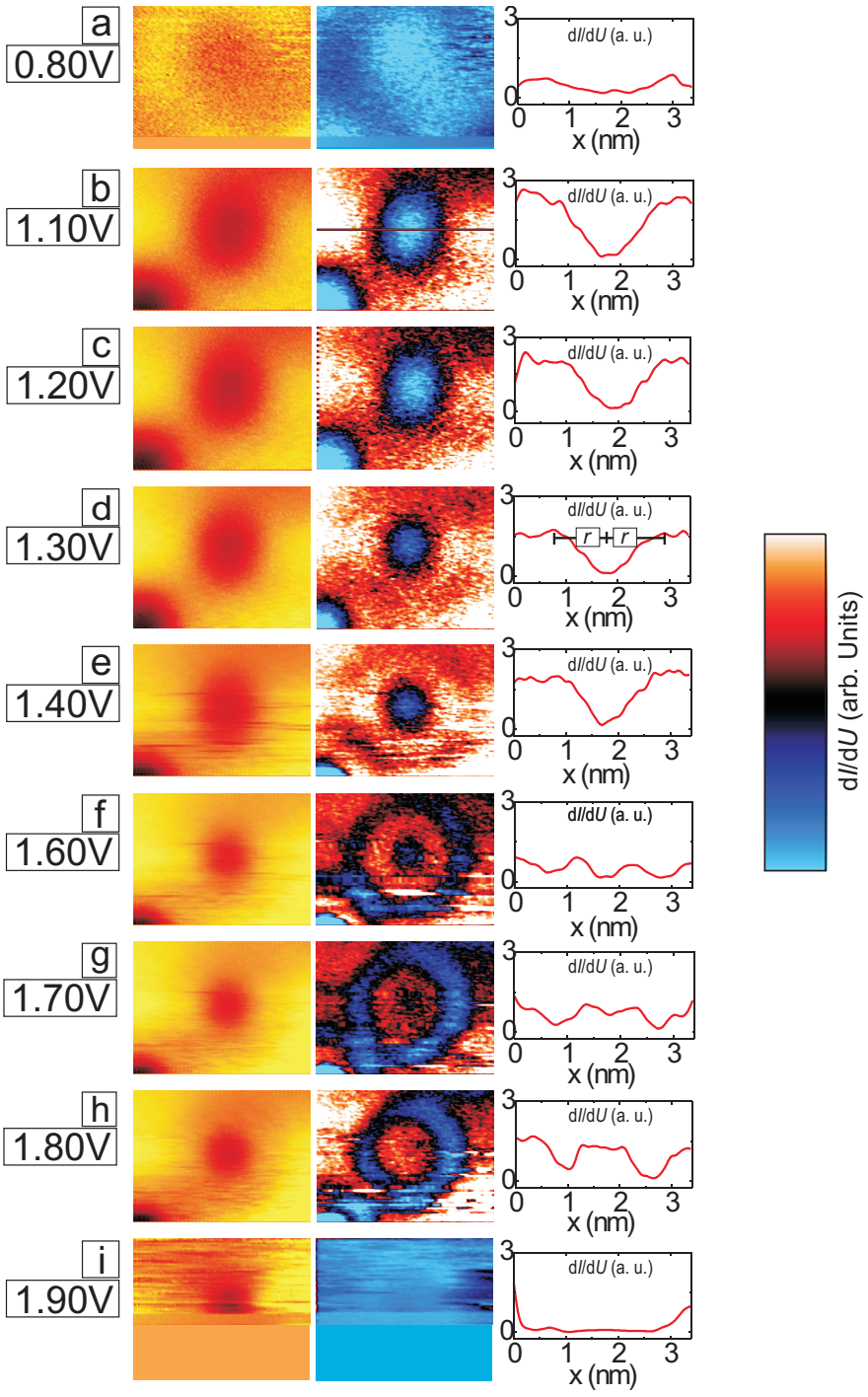

Figure 8.7: Bias dependent constant height STM and STS maps of a single electronic defect site in EuO(100). Scan size 3.4 nm × 2.6 nm for b) to h). The STM tip is stabilized at $U_{\mathrm{Bias}} = 1.63\,\mathrm{V}$, $I = 46\,\mathrm{pA}$ each and measurements are performed at 5.3 K. The first column shows the color coded STM tunneling current I at a) $U_{\mathrm{Bias}} = 0.80\,\mathrm{V}$ - scan size 3.4 nm × 2.5 nm, b) $U_{\mathrm{Bias}} = 1.10\,\mathrm{V}$, c) $U_{\mathrm{Bias}} = 1.20\,\mathrm{V}$, d) $U_{\mathrm{Bias}} = 1.30\,\mathrm{V}$, e) $U_{\mathrm{Bias}} = 1.40\,\mathrm{V}$, f) $U_{\mathrm{Bias}} = 1.60\,\mathrm{V}$, g) $U_{\mathrm{Bias}} = 1.70\,\mathrm{V}$, h) $U_{\mathrm{Bias}} = 1.80\,\mathrm{V}$, i) $U_{\mathrm{Bias}} = 1.90\,\mathrm{V}$ - scan size 3.4 nm × 1.3 nm. The middle column shows the related dI/dU spectroscopy maps, all displayed in the same color scale (displayed to the far right). The right column shows dI/dU profiles horizontally through the middle of the electronic defect site, as generically illustrated in b).

measured at the lowest $(E - E_F)$=0.80 eV and highest energy $(E - E_F)$=1.90 eV just exhibit a very weak dI/dU signal, but a strong dI/dU signature at energies in between. Therefore figure 8.7 nicely shows that the SS is just observable in a limited energy range. Following the discussion of the spin splitting, it is noted that at $(E - E_F)$=1.90 eV the spin down SS branch of the surface state is also not observed in the constant height STS measurements, supporting the interpretation mentioned above.

To summarize the most important results of this chapter, we have investigated the electronic structure of the EuO(100) surface via the analysis of scattering patterns of surface electrons. Thereby, we have experimentally verified the prediction of a spin-split surface state on stoichiometric EuO with a spin splitting as large as 0.66 eV. We could observe the Stoner-like convergence of the spin-split branches indirectly by heating above T_C. The proposed surface metal to insulator transition is absent.

9 Magnetic Properties of EuO(100) on Ni(100)

The experiments and measurements presented in this chapter were carried out by myself, as well as the data evaluation and final interpretation. The MOKE data have been discussed with D. Bürgler, H. P. Oepen, T. Michely and C. Busse.

In this chapter we treat the magnetic properties of EuO on Ni(100). Nickel, our substrate, is a ferromagnetic 4d transition metal with a face centered cubic (fcc) lattice and a T_C=627 K [98]. EuO is integrated on the Ni(100) surface by MBE (as explained in Sec. 5.3), the growth is checked with LEED and STM, and the magnetic properties of this system are studied *in-situ* with MOKE. Since the magnetic properties of this system are not purely determined by EuO, but also by its substrate the Ni(100) crystal is first characterized by MOKE. These measurements of our substrate show a rather complex character.

9.1 Magnetic Characterization of the Ni(100) Substrate

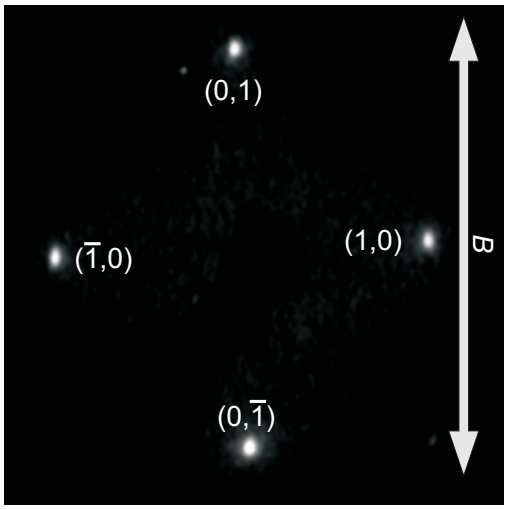

Figure 9.1: LEED pattern of a Ni(100) single crystal at a primary electron energy of E=132.5 eV and a temperature. The arrow shows the direction of the external magnetic field B used for subsequent MOKE measurements.

A Ni(100) single crystal is prepared, as explained in section 5.1. The result of the sample preparation is checked with the LEED. Figure 9.1 displays the LEED pattern of the clean prepared Ni(100) crystal surface. During MOKE measurements (in longitudinal MOKE geometry and p-polarization) on this crystal the external magnetic field is applied along a Ni⟨011⟩ direction. Figure 9.2 shows MOKE $\Theta_{\mathrm{Kerr}}(B)$ loops of this Ni(100) single crystal in the temperature range from T=413 K to T=44 K. The different loops are stacked with respect to each other by adding a constant offset Θ_{Kerr} to the individual loops. The $\Theta_{\mathrm{Kerr}}(B)$ data at T=413 K show a hysteresis loop of typical shape for a ferromagnet without special features and with the expected direction of

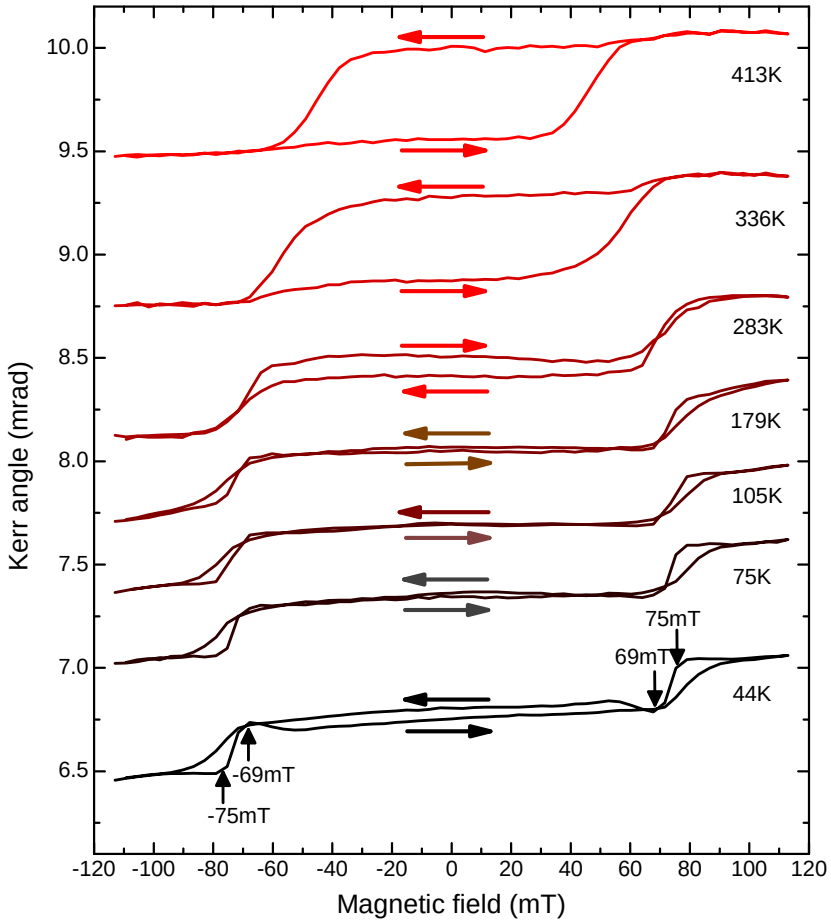

Figure 9.2: Temperature dependent MOKE hysteresis measurements on a Ni(100) single crystal measured in longitudinal MOKE geometry with red HeNe laser light in p-polarization for sample temperatures from 413 K to 44 K. The individual hysteresis loops are stacked in the plot with respect to each other. The loop directions are indicated by the arrows.

the loop (indicated by the arrows). The magnetization is saturated at B=±61 mT. The remanent magnetization equals the saturation magnetization.

The hysteresis data becomes more complex upon decreased sample temperatures: At T=336 K steps emerge in the loops at B=±69 mT and the remanent magnetization is decreased by 34% compared to the saturation magnetization at this temperature. This behavior becomes more distinct at decreasing temperatures. Complex stepped hysteresis loops are found below room temperature. The hysteresis loop measured at the lowest temperature T = 44 K shows distinct features: At high positive field B=+117 mT Θ_{Kerr} shows a high value, indicating magnetic saturation, followed by a steep drop at B=+75 mT, and a local minimum at B=+69 mT. Then Θ_{Kerr} follows a plateau with Θ_{Kerr}(0 mT)=0.03 mrad and just a small slope and drops smoothly at B=-69 mT until the magnetic saturation sets in. $\Theta_{\mathrm{Kerr}}(B)$ is symmetric with respect to the central point of the loop and the direction of the loop is counterclockwise. Most remarkable beside the stepped shape of the loops is the strongly decreased Θ_{Kerr} of the 44 K loop in the range from B=-69 mT to B=+69 mT.

In the following possible explanations for the complicated hysteresis behavior at low temperatures described above are discussed:

The magnetic anisotropy energy in nickel is described by C. Zener [181]. The "magnetization energy of a ferromagnetic crystal is usually dependent to some extent upon the relative orientation of the magnetization vector with respect to the crystalline axes" [181]. The physical origin of this magneto crystalline anisotropy, i. e. axes of hard and of easy magnetization is the spin orbit coupling. The anisotropy energy is mainly determined by the temperature dependent anisotropy constants K_1 and K_2. For nickel at $0.57 \cdot T_C = 357\,\mathrm{K}$ the magnetic anisotropy sets in. Above this temperature no preferred magnetization axis exists, and below it the Ni$\langle 111 \rangle$ directions are the easy magnetization axes [182]. This temperature fits to the featureless $\Theta_{\mathrm{Kerr}}(B)$ loop at 413 K and to the onset of the steps at 336 K.

Next, we discuss the formation of closure domains [183] as a reason for the MOKE hysteresis behavior of a Ni(100) crystal. In ferromagnets energy associated to dipolar fields can be saved by breaking the sample into domains. Closure domain structures minimize the dipolar energy, but introduce a number of domain walls [97]. First investigations with the Bitter technique on Ni(111) surfaces showed complex domain patterns [184]. This research was extended to Ni single crystals with an $\langle 110 \rangle$ axis (including Ni(100)) by H. Spreen [185]. Later the domain structures on Ni(100) have been experimentally observed with Kerr-microscopy by D. Krause and H. Frey [186]. They found an echelon pattern at 293 K on the Ni(100) surface, which is a domain stripe pattern along a Ni$\langle 011 \rangle$ direction, with a stripe separation in the order of 70 μm. Magnetic stray fields are not fully depleted by the domain pattern at room temperature, but this is expected at low temperatures [186]. This leads to a zero net magnetization of the surface domains. In our measurements the penetration depth of the red probing light into the Ni(100) metal is in the order of 10 nm. Therefore, the MOKE signal is dominated by the closure domain pattern and not by the bulk domains of the nickel crystal, which explains the low Θ_{Kerr} in a low magnetic field. At higher magnetic fields above B=+69 mT and below B=-69 mT the closure domain pattern is broken up and the sample is fully magnetized.
So we conclude that the complex $\Theta_{\mathrm{Kerr}}(B)$ behavior is due to nickel's magnetic anisotropy in combination with the formation of closure domains. Although the complex $\Theta_{\mathrm{Kerr}}(B)$ loops of the Ni(100) surface are interesting, this data just serves as a substrate characterization. The main topic of this chapter are the magnetic properties of EuO/Ni(100), as presented in the following section.

A flip of the magnetization into a Ni$\langle 111 \rangle$ direction would cause a polar (out of plane) component of the Kerr signal. Since the polar Kerr effect is generally about one order of magnitude larger than the longitudinal one [105; 187; 188] an increased $\Theta_{\mathrm{Kerr}}(0\,\mathrm{mT})$ would be expected. This is not

the case here, and thus, the magnetic anisotropy does not explain the low $\Theta_{\mathrm{Kerr}}(0\,\mathrm{mT})$. So there is another effect visible in the $\Theta_{\mathrm{Kerr}}(B)$ data.

Nonlinear magneto-optical effects on a nickel surface have been described by W. Hübner and K. H. Bennemann [189]. It is stated that in linear optical reflection measurements the bulk contributions are dominant, but the surface magnetism of a material can be investigated by nonlinear magneto-optics. Second order effects can be measured with second-harmonic generation (SHG). Nonlinear magneto-optical effects are measured by frequency-doubled light [189]. Since we use an interference filter in our MOKE detector (compare Sec. 4.3) just the light of the red HeNe laser and not its frequency-doubled light is measured. So we exclude nonlinear effects for experimental reasons.

9.2 Magnetic Coupling of EuO(100) and Ni(100) Moments

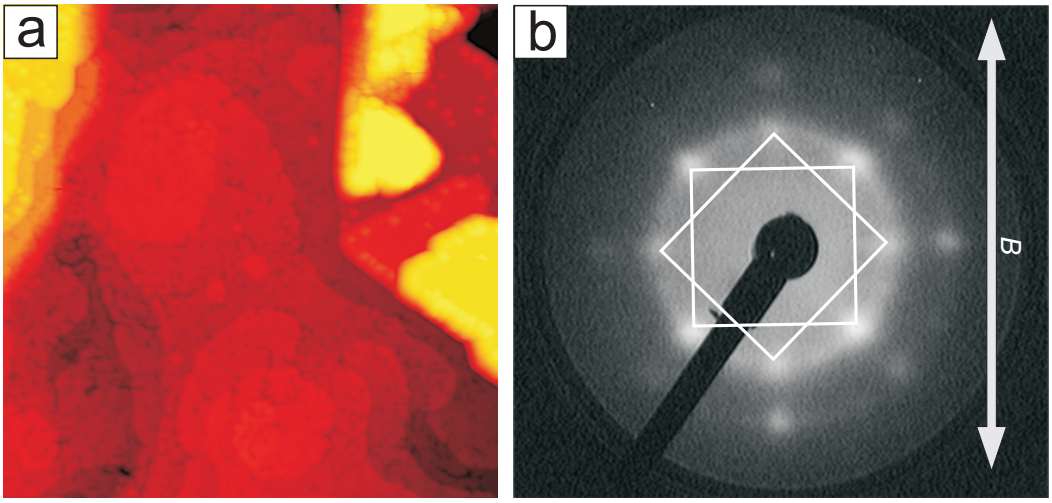

Figure 9.3: A 5.7 nm thin EuO(100) film on Ni(100). a) STM constant current topography image at $I = 320\,pA$, $U_{\mathrm{Bias}} = +1.12\,V$, scan size of $71.5\,nm \times 71.5\,nm$. b) LEED pattern at E=92 eV and T=300 K. LEED spots of two EuO(100) phases are visible. (1,0) LEED spots originating from one EuO phase are marked with a white square.

Europium monoxide is grown by MBE on the Ni(100) metal surface. The typical structural and epitaxial details of such samples are discussed in section 5.3 and reference [109]. Figure 9.3 shows *in-situ* STM and LEED data of a 5.7 nm thin EuO film. The LEED diffraction pattern reveals the existence of two domains of EuO(100). Beside EuO(100) STM shows triangular shaped grains, which represents the coexisting polar EuO(111) phase. The majority of the sample surface is covered with EuO(100). The EuO film is analyzed by means of MOKE analogously to the previously MOKE measurements on Ni(100). This $\Theta_{\mathrm{Kerr}}(B)$ loops, measured in the temperature range from 290 K to 44 K, are presented in figure 9.4. The direction of the loops is indicated by

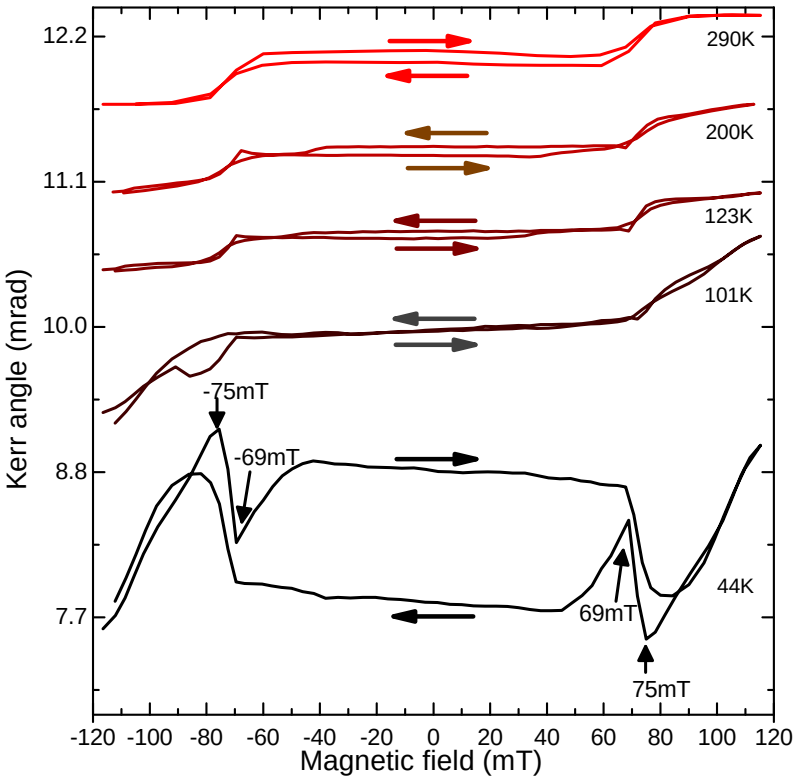

Figure 9.4: Temperature dependent MOKE hysteresis measurements on the 5.7 nm thin EuO film on Ni(100), as shown in figure 9.3. The hysteresis data is measured in longitudinal MOKE geometry with red HeNe laser light in p-polarization, sample temperatures from 290 K to 44 K. The individual hysteresis loops are stacked in the plot with respect to each other. The loop directions are indicated by the arrows.

the arrows. Since the probing depth of the red light in EuO is in the order of 100 nm (which is larger than the thickness of the investigated EuO film) and the Curie temperature $T_{\mathrm{C-EuO}}$ of EuO is much smaller than of the Ni(100) substrate, the Θ_{Kerr} of loops measured at $T > T_{\mathrm{C-EuO}}$ originates just from the Ni(100). In other words, the EuO film is transparent for MOKE above its Curie temperature, and thus only the magnetism of the Ni(100) crystal is decisive. By comparing the hysteresis loops measured at T=290 K, 200 K and 123 K to those measured on pure Ni(100) at similar temperatures (compare figure 9.2) loops with identical shapes and directions are found. The hysteresis loop measured at 101 K on EuO/Ni(100) exhibits some differences compared to the loop measured at 105 K on Ni(100). The direction of this loop and the hysteresis in the range from -70 mT to +70 mT is identical with the one of the pure Ni(100) substrate. But in higher fields, i.e., from -117 mT to -70 mT and from +117 mT to +70 mT a stronger Kerr effect sets in.

Measuring the MOKE hysteresis at the lowest accessible temperature of 44 K results in a loop, which strongly differs from those of Ni(100) at this temperature. The direction of the loop changes from counterclockwise to clockwise. Now $\Theta_{\mathrm{Kerr}}(0\,\mathrm{mT}) = 0.5\,\mathrm{mrad}$, which is about seventeen times higher than on Ni(100). Remarkable are the kinks at fields of B=-75 mT, -69 mT, 69 mT and 75 mT (as indicated in figure 9.4). These are the same fields at which strong magnetization changes in the

Ni(100) MOKE hysteresis occur. By comparing the Θ_{Kerr} at the kinks one finds an inverse Kerr effect. For instance at B=-75 mT a low Θ_{Kerr} is measured Ni(100), while the EuO sample exhibits a high Θ_{Kerr}. The kinks seem to be imprinted by the Ni(100). The correlation between the kinks in the hysteresis loop of the EuO and those of the Ni(100) suggests that the magnetic moments of the EuO film and the Ni(100) couple to each other.

In 1969 K. Ahn and G. Almasi measured MOKE hysteresis loops of Fe and of EuO/Fe. They found reversed loop directions of this two samples. Here we observe the same. They attributed this effect to an antiferromagnetic coupling between the magnetic moments of EuO and of its iron substrate [120].

The inverse Kerr angles of the EuO/Ni(100) and Ni(100) and the change of the loop direction from counterclockwise to clockwise also show that the magnetic moments of the EuO film are oppositely aligned to the Ni(100) ones. So there is an antiferromagnetic coupling between the magnetic moments of the EuO film and the Ni(100) surface domains.

10 Summary and Outlook

This thesis deals with the electronic structure and magnetism of europium monoxide (EuO) films. These EuO films are ultra thin, stoichiometric, ferromagnetic, semiconducting, and of high crystalline quality. Such films of EuO are integrated in (100) texture by reactive molecular beam epitaxy (MBE) onto the zero band gap semiconductor graphene on Ir(111) and onto a ferromagnetic Ni(100) single crystal. The EuO films are grown with europium excess to avoid the formation of europium oxides with higher valence of the Eu-ions. A graphene substrate enables the growth of separated EuO(100) grains with a preferred thickness of 3.3 nm and of closed epitaxial EuO(100) films with the same thickness. The in plane orientation of the EuO(100) grains is randomly distributed. This samples show an uncompressed EuO bulk-like lattice constant, and contain an oxygen vacancy concentration of 0.3 % (of the total oxygen sites in EuO). Ultrathin EuO(100) films of just a few nm thickness on epitaxial graphene are the subject of most measurements of this thesis, especially on magnetic and electronic properties. The EuO on Ni(100) systems are of interest for magnetic measurements in the last chapter of this thesis.
All sample preparations and measurements are performed *in-situ* in a low temperature ultra high vacuum (UHV) system, which consists of two UHV chambers. The preparation chamber is equipped with heat- and coolable sample holders, a MBE station and a low energy electron diffraction (LEED) device. A low temperature scanning tunneling microscope (LT-STM) is mounted to a separate chamber, which is connected to the preparation chamber.

For the *in-situ* determination of magnetic properties an instrument utilizing the longitudinal magneto-optical Kerr effect (MOKE) was developed as the main technical project of this work. The MOKE setup consists of a HeNe laser as light source, an electromagnet, and a detector composed of optical components and a photo transistor. It is designed to be integrated into the preparation chamber of the UHV system and aims on resolving small Kerr signals from ferromagnetic submonolayers. Therefore high quality optical components are used for the detector. The electromagnet generates magnetic fields B by driving a current I through coils. All components of the MOKE setup, except for the yoke of the electromagnet, are mounted to the ambient side of the UHV system, facilitating both design and maintenance of the instrument. The laser light of MOKE setup is highly linear polarized with a polarization ratio of $5{\cdot}10^8$, and a spatially fixed polarization plane. The UHV electromagnet generates constant magnetic fields B up to 117 mT in a sample slot with a width of 14 mm. The generated magnetic fields show a homogeneity of 1 mT per millimeter. The magnet shows a nonlinear $B(I)$ characteristic due to the used iron yoke. Therefore a complex $B(I)$ calibration has to be performed and one has to compensate for the hysteresis of the iron yoke. The

detector of the MOKE setup is designed to resolve rotations of the polarization plane of the HeNe laser light. The resolution of the detector turns out to be better than 1 μrad and the noise level to be of the order of 0.1 μrad (depending on the investigated sample). The measurement and data acquisition process is automized with a LabVIEW software. Test measurements are performed on thin cobalt layers. Measuring parameters such as the speed of a measurement and the integration time T_{Int} per data point are optimized. Disturbing side effects resulting from magnetic stray fields on the laser and on the UHV view ports are eliminated.

MOKE hysteresis measurements are performed on 3.3 nm thin closed EuO(100) films and separated EuO(100) grains, both on epitaxial graphene. The MOKE hysteresis loops reveal ferromagnetic (FM) order at low temperatures. The Curie temperature T_{C} amounts to 75 K. In literature, the Curie temperature T_{C} of (undoped) bulk EuO is 69 K [51; 52] and the T_{C} for (undoped) 3.3 nm thin films is about 62 K [3]. Therefore we find a by 13 K increased T_{C}. Epitaxial strain, n-doping and a proximity effect are ruled out as the origin for the T_{C} enhancement. We explain the enhanced T_{C} by an RKKY like mediation of ferromagnetic order through the graphene substrate. The magnetization of EuO grains aligns along their easy directions in the film plane. Very small separated EuO grains below the superparamagnetic limit are found.

The electronic properties of ultra thin EuO(100) layers are further investigated on the nanometer scale by STM and scanning tunneling spectroscopy (STS). If not stated otherwise the measurements are performed at a base temperature of 5.3 K, i.e., in the ferromagnetic phase of the EuO samples. A strong electronic corrugation of the EuO(100) is found in constant current STM. This corrugation depends strongly on the bias voltage U_{Bias} at which STM is performed. The electronic features found by STM appear as point features, electronic defect sites (EDS) and in line form, electronic line defects (ELD). The EDS are structural oxygen vacancy sites and the ELD are oxygen vacancies arranged along the EuO$\langle 011\rangle$ directions. The EuO(100) grain's borders follow the EuO$\langle 010\rangle$ directions, which are composed of oxygen and europium atoms. The dynamics of the oxygen vacancies are observed by repetitive imaging an EuO(100) sample area at 5.3 K. Surprisingly even at this low temperature a mobility of some defects is observed. The vacancies are found to hop along the EuO$\langle 011\rangle$ directions, i.e., along the closed packed oxygen rows in an EuO(100) layer.

Since the structural defects in EuO(100) are connected to strong electronic features we perform tunneling spectroscopy on these surfaces. The local work function Φ is determined by $I(z)$ spectroscopy, whereby the n-charged character of the oxygen vacancies turns out. A local upward band banding of (0.2$\pm$0.1) eV is also found at the vacancies. Further, the energy resolved local density of states (LDOS) is measured by differential conductivity $\mathrm{d}I/\mathrm{d}U$ maps on ferromagnetically ordered

EuO(100) surfaces. Concentric standing wave interference patterns are observed around defect sites. With this measurements the surface state (SS) in EuO(100) is discovered experimentally for the first time.
The energy dependence of these scattering patterns is related to the dispersion of the surface state. This dispersion relation $E(k)$ is found the be free-electron like with an effective mass of $m_{\mathrm{eff}} = (1.09 \pm 0.1) \cdot m_{\mathrm{e}}$, whereby k is the wave vector of the surface state and m_{e} the free electron mass. The bottom of the surface state band is at k=0 and E_0=0.77 eV, i.e., in the unoccupied part of the EuO band structure. The EuO band structure is known to be spin split in the ferromagnetic phase [4] and band structure calculations of the EuO(100) surface state also predict a spin splitting of approx. 0.6 eV of the surface states spin up and spin down branch [48]. We do not measure two branches of the surface state. We assume the spin down surface state band to fully overlap with the spin up bulk band and therefore being a surface resonance. A surface resonance is not confined in a surface and therefore not observable by two dimensional scattering patterns at defects. An indirect proof of the spin splitting in the ferromagnetic phase is given by comparable spectroscopy measurements in the paramagnetic phase. Thereby an upward shift of 0.33 eV of the surface states dispersion relation is found. Since we measure the integral surface state of the converged spin up and the spin down branch in the paramagnetic phase a total spin splitting of $2 \cdot 0.33\,\mathrm{eV} = 0.66\,\mathrm{eV}$ is revealed for the ferromagnetic phase. This number is consistent with Kondo lattice model calculations [48]. So the unobserved spin down surface state band is 0.66 eV above the spin up one. Comparing the calculated band structure of the surface state with our experimental data shows that we only observe the elastically scattered surface state around the $\bar{\Gamma}$-point. This is not surprising since the tunneling current in STM and STS is strongly dominated by electrons with a momentum $k_\perp$ perpendicular to the surface and vanishing momentum parallel $k_\parallel$=0 to the surface [180], i.e., tunneling is dominated by states around the Γ-point ($k_\parallel$=0). To relate the observed surface state to the EuO bulk band structure we investigate the EuO band gap and find the surface state in the direct band gap.
During $\mathrm{d}I/\mathrm{d}U$ spectroscopy no DOS is observed at the Fermi level at any temperature and therefore, no metallic behavior is found. So the samples do not show the metal to insulator transition.

As the last issue of this work the magnetic properties of EuO on Ni(100) are characterized by means of variable temperature MOKE $\Theta_{\mathrm{Kerr}}(B)$ measurements. A Ni(100) single crystal is first characterized and shows a normal ferromagnetic hysteresis loop at T=413 K. At lower temperatures complex shaped $\Theta_{\mathrm{Kerr}}(B)$ loops with kinks and a decreased Kerr signal in low fields form. We attributed this $\Theta_{\mathrm{Kerr}}(B)$ behavior to nickel's magnetic anisotropy [181] and to the formation of closure domains [183].
Identical MOKE hysteresis measurements are performed on a 5.7 nm thin EuO film on the nickel crystal. These hysteresis loops are identical to the ones measured on the pure nickel for temperatures

above T=123 K since the EuO is not ferromagnetic at this temperatures. At lower temperatures also the hysteresis loops of the EuO/Ni system show kinks at the same magnetic fields, as the pure nickel substrate ones do, but the Kerr signal at this fields and the direction of the hysteresis loop are oppositely to the pure nickel ones. So we conclude that the magnetic moments of the EuO and nickel couple antiferromagnetically.

For the further progress at the LT-STM apparatus another optimization of the MOKE automatization software MOKEsoft is recommended: The calibration files of the electromagnets field $B(I)$ do not compensate for the hysteresis of the iron yoke. Up to now this compensation is performed manually after the MOKE measurements (compare section D). This issue can easily be optimized by separate $B(I)$ calibration files for increasing and decreasing currents I.
The scientific results of this thesis on the magnetic and electronic properties of EuO can stimulate further investigations. Questions arising directly from the presented results concern the domains of separated EuO grains. The domain structure can be imaged with spin polarized (SP)-STS. In general the further adaption of SP-STS techniques at the LT-STM apparatus with antiferromagnetic Cr-tips will be a subject.
In this thesis local $\mathrm{d}I/\mathrm{d}U$ STS shows irreproducible spectra. In general a defined and constant electronic structure of STM tips is crucial for systematic local $\mathrm{d}I/\mathrm{d}U$ spectroscopy. Therefore, the *in-situ* tip preparation on silver will be established.
Interestingly we found a magnetic coupling of the magnetic moments of EuO and nickel. We did not determine the Curie temperature of this compound due to experimental complications during this period. The Curie temperature of this system is expected to be increased due to the proximity to the underlying nickel crystal.
The origin of the metal to insulator transition (MIT) in n-doped EuO has not been solved by STS, despite several attempts (not presented). Although the resistivity of EuO decreases by several orders of magnitude upon the MIT this should be hard to observe in STS. The reason behind this is the sensitivity of STS on the samples LDOS and not the conductivity. Only a small doping DOS is related to the MIT.
The system of the spin injector EuO integrated onto the spin conductor graphene is of fundamental interest for spintronics. Up to now there is no experimental proof on the unaffected electronic structure of graphene in touch with EuO. We suggest to estimate the doping level and band structure of graphene in this layer system by hard x-ray photoelectron spectroscopy (HAXPES).
Beyond this issues of fundamental research it would be easy and attractive to put a gate electrode on top of the EuO/graphene system to induce spin polarized charge carriers into the graphene [20]. By this the system becomes accessible for applications.

References

[1] T. S. Santos, J. S. Moodera, K. V. Raman, E. Negusse, J. Holroyd, J. Dvorak, M. Liberati, Y. U. Idzerda, and E. Arenholz. Phys. Rev. Lett. **101**, 147201 (2008). *Determining exchange splitting in a magnetic semiconductor by spin-filter tunneling.* doi:10.1103/PhysRevLett.101.147201, [link]. i, 9, 159

[2] M. Müller, G.-X. Miao, and J. S. Moodera. J. Appl. Phys. **105**, 07C917 (2009). *Thickness dependence of ferromagnetic- and metal-insulator transition in thin EuO films.* doi:10.1063/1.3063673, [link]. 1, 3, 9, 37, 53

[3] M. Barbagallo, T. Stollenwerk, J. Kroha, N.-J. Steinke, N. D. M. Hine, J. F. K. Cooper, C. H. W. Barnes, A. Ionescu, P. M. D. S. Monteiro, J.-Y. Kim, K. R. A. Ziebeck, C. J. Kinane, R. M. Dalgliesh, T. R. Charlton, and S. Langridge. Phys. Rev. B **84**, 075219 (2011). *Thickness-dependent magnetic properties of oxygen-deficient EuO.* doi:10.1103/PhysRevB.84.075219, [link]. i, 1, 9, 10, 50, 53, 86, 159

[4] P. G. Steeneken, L. H. Tjeng, I. Elfimov, G. A. Sawatzky, G. Ghiringhelli, N. B. Brookes, and D.-J. Huang. Phys. Rev. Lett. **88**, 047201 (2002). *Exchange splitting and charge carrier spin polarization in EuO.* doi:10.1103/PhysRevLett.88.047201. i, 1, 3, 4, 72, 87, 159

[5] B. T. Matthias, R. M. Bozorth, and J. H. Van Vleck. Phys. Rev. Lett. **7**, 160 (1961). *Ferromagnetic interaction in EuO.* doi:10.1103/PhysRevLett.7.160. 1, 3, 9

[6] H.-Y. Wang, J. Schoenes, and E. Kaldis. Helv. Phys. Acta **59** (1986). *Magnetooptical polar Kerr effect of EuO.* 1, 3, 13, 55

[7] J. Kerr. The London, Edinburgh, and Dublin Philosophical Magazine and Journal of Science **3**, 321 (1877). *XLIII. On rotation of the plane of polarization by reflection from the pole of a magnet.* 1, 12

[8] T. Chen, Magneto-optic storage media, US Patent 4,556,291, 1985. 1, 13

[9] A. Schmehl, V. Vaithyanathan, A. Herrnberger, S. Thiel, C. Richter, M. Liberati, T. Heeg, M. Röckerath, L. F. Kourkoutis, S. Mühlbauer, P. Böni, D. A. Muller, Y. Barash, J. Schubert, Y. Idzerda, J. Mannhart, and D. G. Schlom. Nat. Mater. **6**, 882 (2007). *Epitaxial integration of the highly spin-polarized ferromagnetic semiconductor EuO with silicon and GaN.* doi:10.1038/nmat2012. 1, 5, 13

[10] T. S. Santos and J. S. Moodera. Phys. Rev. B **69**, 241203 (2004). *Observation of spin filtering with a ferromagnetic EuO tunnel barrier.* doi:10.1103/PhysRevB.69.241203. 1, 37

[11] A. Mauger and C. Godart. Phys. Rep. **141**, 51 (1986). *The magnetic, optical, and transport properties of representatives of a class of magnetic semiconductors: The europium chalcogenides.* doi:10.1016/0370-1573(86)90139-0, [link]. 1, 4, 5, 7, 8

[12] T. Matsumoto, K. Yamaguchi, M. Yuri, K. Kawaguchi, N. Koshizaki, and K. Yamada. J. Phys.: Condens. Matter **16**, 6017 (2004). *Preparation of Gd-doped EuO_{1-x} thin films and the magnetic and magneto-transport properties.* doi:10.1088/0953-8984/16/34/003, [link]. 1, 37

[13] H. Ott, S. J. Heise, R. Sutarto, Z. Hu, C. F. Chang, H. H. Hsieh, H.-J. Lin, C. T. Chen, and L. H. Tjeng. Phys. Rev. B **73**, 094407 (2006). *Soft x-ray magnetic circular dichroism study on Gd-doped EuO thin films.* doi:10.1103/PhysRevB.73.094407. 1, 3, 5

[14] M. Müller, G.-X. Miao, and J. S. Moodera. Europhys. Lett. **88**, 47006 (2009). *Exchange splitting and bias-dependent transport in EuO spin filter tunnel barriers.* doi:10.1209/0295-5075/88/47006, [link]. 1, 37

[15] E. Negusse, J. Holroyd, M. Liberati, J. Dvorak, Y. U. Idzerda, T. S. Santos, J. S. Moodera, and E. Arenholz. J. Appl. Phys. **99**, 08E507 (2006). *Effect of electrode and EuO thickness on EuO-electrode interface in tunneling spin filter.* doi:10.1063/1.2176590, [link]. 37

[16] D. DiVincenzo. J. Appl. Phys. **85**, 4785 (1999). *Quantum computing and single-qubit measurements using the spin-filter effect.* 1

[17] D. F. Förster. PhD thesis, Universität zu Köln (2011). *EuO and Eu on metal crystals and graphene: interface effects and epitaxial films.* [link]. 1, 2, 3, 37, 38, 39, 40, 45, 64, 65, 66

[18] S. Altieri, M. Finazzi, H. H. Hsieh, M. W. Haverkort, H.-J. Lin, C. T. Chen, S. Frabboni, G. C. Gazzadi, A. Rota, S. Valeri, and L. H. Tjeng. Phys. Rev. B **79**, 174431 (2009). *Image charge screening: A new approach to enhance magnetic ordering temperatures in ultrathin correlated oxide films.* doi:10.1103/PhysRevB.79.174431. 1, 54

[19] J. Coraux, L. Marty, N. Bendiab, and V. Bouchiat. Acc. Chem. Res. (2012). *Functional Hybrid Systems Based on Large-Area High-Quality Graphene.* 1

[20] H. Haugen, D. Huertas-Hernando, and A. Brataas. Phys. Rev. B **77**, 115406 (2008). *Spin transport in proximity-induced ferromagnetic graphene.* doi:10.1103/PhysRevB.77.115406. 1, 88

[21] H. Min, J. E. Hill, N. A. Sinitsyn, B. R. Sahu, L. Kleinman, and A. H. MacDonald. Phys. Rev. B **74**, 165310 (2006). *Intrinsic and Rashba spin-orbit interactions in graphene sheets.* doi:10.1103/PhysRevB.74.165310. 1

[22] M. Dragoman, D. Dragoman, G. Deligiorgis, G. Konstantinidis, D. Neculoiu, A. Cismaru, and R. Plana. J. Appl. Phys. **106**, 044312 (2009). *Current oscillations in a wide graphene sheet.* doi:10.1063/1.3208061, [link].

[23] P. Seneor, B. Dlubak, M. Martin, A. Anane, H. Jaffres, and A. Fert. MRS Bull. **37**, 1245 (2012). *Spintronics with graphene.* 1

[24] M. R. Oliver, J. A. Kafalas, J. O. Dimmock, and T. B. Reed. Phys. Rev. Lett. **24**, 1064 (1970). *Pressure dependence of the electrical resistivity of EuO.* doi:10.1103/PhysRevLett.24.1064. 1, 3

[25] S. von Molnar and M. W. Shafer. J. Appl. Phys. **41**, 1093 (1970). *Transport in Gd-doped EuO.* doi:10.1063/1.1658826, [link]. 1

[26] J. B. Torrance, M. W. Shafer, and T. R. McGuire. Phys. Rev. Lett. **29**, 1168 (1972). *Bound magnetic polarons and the insulator-metal transition in EuO.* doi:10.1103/PhysRevLett.29.1168. 2, 3, 5

[27] H. Rho, C. S. Snow, S. L. Cooper, Z. Fisk, A. Comment, and J.-P. Ansermet. Phys. Rev. Lett. **88**, 127401 (2002). *Evolution of magnetic polarons and spin-carrier interactions through the metal-insulator transition in* $Eu_{1-x}Gd_xO$. doi:10.1103/PhysRevLett.88.127401. 5

[28] P. Sinjukow and W. Nolting. Phys. Rev. B **68**, 125107 (2003). *Metal-insulator transition in EuO.* doi:10.1103/PhysRevB.68.125107.

[29] P. Sinjukow and W. Nolting. Phys. Rev. B **69**, 214432 (2004). *Fully self-consistent determination of transport properties in Eu-rich EuO.* doi:10.1103/PhysRevB.69.214432. 7

[30] U. Yu and B. I. Min. Phys. Rev. B **74**, 094413 (2006). *Magnetic-phase transition in the magnetic-polaron system studied with the Monte Carlo method: Anomalous specific heat of* EuB_6. doi:10.1103/PhysRevB.74.094413. 2

[31] M. Arnold and J. Kroha. Physica C **460-462**, 1137 (2007). *Simultaneous ferromagnetic and semiconductor-metal transition in EuO.* doi:10.1016/j.physc.2007.03.240, [link].

[32] M. Arnold and J. Kroha. Phys. Rev. Lett. **100**, 046404 (2008). *Simultaneous ferromagnetic metal-semiconductor transition in electron-doped EuO.* doi:10.1103/PhysRevLett.100.046404. 1, 3, 5

[33] J. Schoenes and P. Wachter. Phys. Rev. B **9**, 3097 (1974). *Exchange optics in Gd-doped EuO.* doi:10.1103/PhysRevB.9.3097. 1, 4, 5, 159

[34] M. Barbagallo, N. Hine, J. Cooper, N. Steinke, A. Ionescu, C. Barnes, C. Kinane, R. Dalgliesh, T. Charlton, and S. Langridge. Phys. Rev. B **81**, 235216 (2010). *Experimental and theoretical analysis of magnetic moment enhancement in oxygen-deficient EuO.* 5

[35] T. Yamasaki, K. Ueno, A. Tsukazaki, T. Fukumura, and M. Kawasaki. Appl. Phys. Lett. **98**, 082116 (2011). *Observation of anomalous Hall effect in EuO epitaxial thin films grown by a pulse laser deposition.*

[36] J. C. Suits and K. Lee. J. Appl. Phys. **42**, 3258 (1971). *Giant magneto-optical Kerr effect in EuO.* doi:10.1063/1.1660721, [link]. 8, 55

[37] O. Massenet, Y. Capiomont, and N. V. Dang. J. Appl. Phys. **45**, 3593 (1974). *Effects of high nonstoichiometry on EuO properties.* doi:10.1063/1.1663822, [link].

[38] A. Samokhvalov, A. Gunichev, B. Gizhevskii, N. Loshkareva, N. Chebotaev, and N. Viglin. Sov. Phys. (Engl. Transl.) **20** (1978). *Nonstoichiometric EuO films with an elevated Curie temperature.*

[39] A. Borukhovich, V. Bamburov, and A. Sidorov. J. Magn. Magn. Mater. **73**, 106 (1988). *Magnetic heterogeneity effects in EuO-based phases.*

[40] T. Konno, N. Ogawa, K. Wakoh, K. Sumiyama, and K. Suzuki. Jpn. J. Appl. Phys. **35**, 6052 (1996). *Synthesis and magnetic properties of non-equilibrium Eu-rich EuO thin films.* 1

[41] Y. Shapira, S. Foner, and T. B. Reed. Phys. Rev. B **8**, 2299 (1973). *EuO. I. Resistivity and Hall Effect in fields up to 150 kOe.* doi:10.1103/PhysRevB.8.2299. 1, 3

[42] T. Mairoser, A. Schmehl, A. Melville, T. Heeg, L. Canella, P. Böni, W. Zander, J. Schubert, D. E. Shai, E. J. Monkman, K. M. Shen, D. G. Schlom, and J. Mannhart. Phys. Rev. Lett. **105**, 257206 (2010). *Is there an intrinsic limit to the charge-carrier-induced increase of the Curie temperature of EuO?* 5

[43] M. R. Oliver, J. O. Dimmock, A. L. McWhorter, and T. B. Reed. Phys. Rev. B **5**, 1078 (1972). *Conductivity studies in europium oxide.* doi:10.1103/PhysRevB.5.1078.

[44] A. Mauger, C. Godart, M. Escorne, J. Achard, and J. Desfours. J. Phys. **39**, 1125 (1978). *Magnetic properties and instability phenomena in doped Euo.*

[45] D. Shai, A. Melville, J. Harter, E. Monkman, D. Shen, A. Schmehl, D. Schlom, and K. Shen. Phys. Rev. Lett. **108**, 267003 (2012). *Temperature dependence of the electronic structure and fermi-surface reconstruction of $Eu_{1-x}Gd_xO$ through the ferromagnetic metal-insulator transition.* 1, 2, 5

[46] S. G. Altendorf, A. Efimenko, V. Oliana, H. Kierspel, A. D. Rata, and L. H. Tjeng. Phys. Rev. B **84**, 155442 (2011). *Oxygen off-stoichiometry and phase separation in EuO thin films.* doi:10.1103/PhysRevB.84.155442, [link]. 1, 37, 53, 62

[47] M. Z. Hasan and C. L. Kane. Rev. Mod. Phys. **82**, 3045 (2010). *Colloquium: Topological insulators.* doi:10.1103/RevModPhys.82.3045, [link]. 2

[48] R. Schiller and W. Nolting. Phys. Rev. Lett. **86**, 3847 (2001). *Prediction of a surface state and a related surface insulator-metal transition for the (100) surface of stochiometric EuO.* doi:10.1103/PhysRevLett.86.3847. 2, 3, 5, 6, 8, 9, 72, 73, 74, 75, 76, 87

[49] F. Matsukura and H. Ohno. Handbook of Magnetism and Advanced Magnetic Materials (2007). *Ferromagnetic semiconductors.* 3

[50] P. Wachter. Crit. Rev. Solid State Mater. Sci. **3**, 189 (1972). *The optical electrical and magnetic properties of the europium chalcogenides and the rare earth pnictides.* 3, 4

[51] E. L. Boyd. Phys. Rev. **145**, 174 (1966). *Nuclear magnetic resonance studies of some materials containing divalent europium.* doi:10.1103/PhysRev.145.174, [link]. 3, 50, 53, 86

[52] A. Kornblit and G. Ahlers. Phys. Rev. B **11**, 2678 (1975). *Heat capacity of EuO near the Curie temperature.* 3, 50, 53, 86

[53] C. Llinares, E. Monteil, G. Bordure, and C. Paparoditis. Solid State Commun. **13**, 205 (1973). *Magnetic order effect on optical absorption and photoconductivity in EuO thin films.* 3

[54] R. Bachmann and P. Wachter. Solid State Commun. **6**, 711 (1968). *Magnetic effects on the low temperature photoconductivity of EuO and EuS.* doi:10.1016/0038-1098(68)90570-X, [link].

[55] C. Llinares, L. Gouskov, C. Duchemin, and G. Bordure. J. Phys. Chem. Solids **36**, 567 (1975). *Photoconductivity on europium oxyde single crystals and thin films.* 3

[56] R. Schiller, W. Müller, and W. Nolting. Phys. Rev. B **64**, 134409 (2001). *Kondo lattice model: Application to the temperature-dependent electronic structure of EuO(100) films.* doi:10.1103/PhysRevB.64.134409. 3, 6, 7, 9

[57] F. Lévy. Z. Phys. B: Condens. Matter **10**, 85 (1969). *Spontaneous magnetoelastic effects in some rare earth compounds.* 3

[58] H. Miyazaki, T. Ito, S. Ota, H. Im, S. Yagi, M. Kato, K. Soda, and S. I. Kimura. Physica B **403**, 917 (2008). *Angle-resolved photoemission study on EuO thin films.* 4, 5

[59] N. J. C. Ingle and I. S. Elfimov. Phys. Rev. B **77**, 121202 (2008). *Influence of epitaxial strain on the ferromagnetic semiconductor EuO: First-principles calculations.* doi:10.1103/PhysRevB.77.121202. 4, 5, 53, 75

[60] G. Busch, P. Cotti, and P. Munz. Solid State Commun. **7**, 795 (1969). *Photoemission from europium chalcogenides.* 4

[61] D. E. Eastman, F. Holtzberg, and S. Methfessel. Phys. Rev. Lett. **23**, 226 (1969). *Photoemission studies of the electronic structure of EuO, EuS, EuSe, and GdS.* doi:10.1103/PhysRevLett.23.226. 4, 66

[62] P. G. Steeneken. PhD thesis, Groningen (2002). *New light on EuO thin films: Preparation, transport, magnetism and spectroscopy of a ferromagnetic semiconductor.* 4, 5, 13

[63] J. Beukers, J. Kleibeuker, G. Koster, D. Blank, G. Rijnders, H. Hilgenkamp, and A. Brinkman. Thin Solid Films **518**, 5173 (2010). *Epitaxial EuO thin films by pulsed laser deposition monitored by in situ x-ray photoelectron spectroscopy.* doi:10.1016/j.tsf.2010.04.071, [link]. 4

[64] G. Güntherodt, P. Wachter, and D. Imboden. Z. Phys. B: Condens. Matter **12**, 292 (1971). *Energy level scheme and the effect of magnetic order on the optical transitions in europium chalcogenides.* 4

[65] P. Blaha, K. Schwarz, and J. Luitz. Comput. Phys. Commun. 59, 399 (1990). *WIEN2k.* 5

[66] R. Sutarto, S. G. Altendorf, B. Coloru, M. Moretti Sala, T. Haupricht, C. F. Chang, Z. Hu, C. Schüßler-Langeheine, N. Hollmann, H. Kierspel, J. A. Mydosh, H. H. Hsieh, H.-J. Lin, C. T. Chen, and L. H. Tjeng. Phys. Rev. B **80**, 085308 (2009). *Epitaxy, stoichiometry, and magnetic properties of Gd-doped EuO films on YSZ(001).* doi:10.1103/PhysRevB.80.085308. 5, 53

[67] H. Miyazaki, H. J. Im, K. Terashima, S. Yagi, M. Kato, K. Soda, T. Ito, and S. Kimura. Appl. Phys. Lett. **96**, 232503 (2010). *La-doped EuO: A rare earth ferromagnetic semiconductor with the highest Curie temperature.* doi:10.1063/1.3416911, [link]. 5

[68] T. Matsumoto, K. Yamaguchi, M. Yuri, K. Kawaguchi, N. Koshizaki, and K. Yamada. J. Phys. Condens. Matter **16**, 6017 (2004). *Preparation of Gd-doped EuO_{1-x} thin films and the magnetic and magneto-transport properties.*

[69] P. Liu, J. Tang, J. Colón Santana, K. Belashchenko, and P. Dowben. J. Appl. Phys. **109**, 07C311 (2011). *Ce-doped EuO: Magnetic properties and the indirect band gap.*

[70] K. Y. Ahn and T. R. McGuire. J. Appl. Phys. **39**, 5061 (1968). *Magnetic and magneto-optic properties of EuO films doped with trivalent rare-earth oxide.* doi:10.1063/1.1655924, [link]. 13

[71] K. Ahn. Appl. Phys. Lett. **17**, 347 (1970). *Increase of Curie temperature in EuO films by Fe doping.*

[72] K. Ahn, K. Tu, and W. Reuter. J. Appl. Phys. **42**, 1769 (1971). *Preparation and structure of Fe-doped EuO films.*

[73] T. R. McGuire, G. F. Petrich, B. L. Olson, V. L. Moruzzi, and K. Y. Ahn. J. Appl. Phys. **42**, 1775 (1971). *Magnetic and magneto-optical properties of Fe-doped EuO films.* doi:10.1063/1.1660428, [link].

[74] K. Lee and J. Suits. Phys. Lett. A **34**, 141 (1971). *Enhanced ferromagnetic exchange in EuO films doped with Eu and non-magnetic ions.*

[75] M. Shafer and T. McGuire. J. Appl. Phys. **39**, 588 (1968). *Studies of Curie-point increases in EuO.*

[76] A. Samokhvalov, T. Arbuzova, V. Babushkin, B. Gizhevskii, N. Efremova, M. Simonova, and N. Chebotaev. Sov. Phys. (Engl. Transl.) **18** (1976). *Ferromagnetic semiconductors of $Eu_{1-x}Sm_xO$ composition with elevated Curie temperatures.*

[77] A. Mauger, M. Escorne, C. Godart, J. Desfours, and J. Achard. J. de Phys. **41**, 5 (1980). *Magnetic properties of Gd doped EuO single crystals.* 5

[78] G. Petrich, S. von Molnar, and T. Penney. Phys. Rev. Lett. **26**, 885 (1971). *Exchange-induced autoionization in Eu-rich EuO.* 5

[79] S. G. Altendorf, PhD thesis, Universität zu Köln (2011), *Growth, electronic structure, and properties of electron-doped EuO thin films.* 5, 7, 8, 62

[80] S. G. Altendorf, N. Hollmann, R. Sutarto, C. Caspers, R. C. Wicks, Y.-Y. Chin, Z. Hu, H. Kierspel, I. S. Elfimov, H. H. Hsieh, H.-J. Lin, C. T. Chen, and L. H. Tjeng. Phys. Rev. B **85**, 081201 (2012). *Spectroscopic observation of strain-assisted T_C enhancement in EuO upon Gd doping.* doi:10.1103/PhysRevB.85.081201, [link]. 5

[81] A. Zangwill, *Physics at surfaces*, Cambridge University Press, 1988. 6, 67

[82] M. F. Crommie, C. P. Lutz, and D. M. Eigler. Nature **363**, 69 (1993). *Imaging standing waves in a two-dimensional electron gas.* doi:10.1038/363524a0. 6

[83] M. Crommie, C. Lutz, and D. Eigler. Science **262**, 218 (1993). *Confinement of electrons to quantum corrals on a metal surface.* 6

[84] T. Kasuya. IBM J. Res. Dev. **14**, 214 (1970). *Exchange mechanisms in europium chalcogenides.* 7

[85] T. McGuire, R. Gambino, S. Pickart, and H. Alperin. J. Appl. Phys. **40**, 1009 (1969). *Magnetic structure and exchange interactions in cubic gadolinium compounds.* 7

[86] H. von Loehneysen, A. Neubert, T. Pietrus, A. Schröder, O. Stockert, U. Tutsch, M. Loewenhaupt, A. Rosch, and P. Wölfle. Eur. Phys. J. B **5**, 447 (1998). *Magnetic order and transport in the heavy-fermion system CeCuAu.* 7

[87] J. Kuneš, W. Ku, and W. E. Pickett. J. Phys. Soc. Jpn. **74**, 1408 (2005). *Exchange coupling in Eu monochalcogenides from first principles.* doi:10.1143/JPSJ.74.1408. 7

[88] S. Q. Shi, C. Y. Ouyang, Q. Fang, J. Q. Shen, W. H. Tang, and C. R. Li. Europhys. Lett. **83**, 69001 (2008). *Electronic structure and magnetism of EuX (X = O, S, Se and Te): A first-principles investigation.* doi:10.1209/0295-5075/83/69001, [link].

[89] R. Rausch and W. Nolting. J. Phys.: Condens. Matter **21**, 376002 (6pp) (2009). *The Curie temperature of thin ferromagnetic films.* doi:10.1088/0953-8984/21/37/376002, [link].

[90] W. Söllinger, W. Heiss, R. T. Lechner, K. Rumpf, P. Granitzer, H. Krenn, and G. Springholz. Phys. Rev. B **81**, 155213 (2010). *Exchange interactions in europium monochalcogenide magnetic semiconductors and their dependence on hydrostatic strain.* doi:10.1103/PhysRevB.81.155213.

[91] X. Wan, J. Dong, and S. Y. Savrasov. Phys. Rev. B **83**, 205201 (2011). *Mechanism of magnetic exchange interactions in europium monochalcogenides.* doi:10.1103/PhysRevB.83.205201. 7

[92] W. Nolting. Phys. Status Solidi B **96**, 11 (1979). *Theory of ferromagnetic semiconductors.* 7

[93] O. Dietrich, A. Henderson Jr, and H. Meyer. Phys. Rev. B **12**, 2844 (1975). *Spin-wave analysis of specific heat and magnetization in EuO and EuS.* 7, 8

[94] L. Passell, O. Dietrich, and J. Als-Nielsen. Phys. Rev. B **14**, 4897 (1976). *Neutron scattering from the Heisenberg ferromagnets EuO and EuS. I. The exchange interactions.* 7, 8

[95] M. W. Pieper, D. Bätjer, and K. Fischer. Z. Phys. B: Condens. Matter **98**, 1 (1995). *Magnetic anisotropies in the nuclear magnetic resonance of the Heisenberg-ferromagnet EuO.* doi:10.1007/BF01318271. 8

[96] S. Burg, V. Stukalov, and E. Kogan. Phys. Status Solidi B (2012). *On the theory of indirect exchange in EuO.* 8

[97] S. Blundell. Oxford Master Series in Condensed Matter Physics, Oxford University Press, New York (2001). *Magnetism in condensed matter.* 10, 11, 12, 53, 81, 111

[98] C. Kittel, *Introduction to solid state physics*, Wiley & Sons, New York, 1995, ISBN 0471111813. 10, 79

[99] E. Moog, C. Liu, S. Bader, and J. Zak. Phys. Rev. B **39**, 6949 (1989). *Thickness and polarization dependence of the magnetooptic signal from ultrathin ferromagnetic films.* 12, 13, 43, 114

[100] J. Zak, E. Moog, C. Liu, and S. Bader. Phys. Rev. B **43**, 6423 (1991). *Magneto-optics of multilayers with arbitrary magnetization directions.*

[101] J. Zak, E. Moog, C. Liu, and S. Bader. J. Magn. Magn. Mater. **89**, 107 (1990). *Universal approach to magneto-optics.* 12

[102] J. Zak, E. Moog, C. Liu, and S. Bader. J. Appl. Phys. **68**, 4203 (1990). *Fundamental magneto-optics.*

[103] J. Zak, E. Moog, C. Liu, and S. Bader. J. Magn. Magn. Mater. **88**, L261 (1990). *Additivity of the Kerr effect in thin-film magnetic systems.*

[104] E. Moog, S. Bader, and J. Zak. Appl. Phys. Lett. **56**, 2687 (1990). *Role of the substrate in enhancing the magneto-optic response of ultrathin films: Fe on Au.*

[105] S. Bader. J. Magn. Magn. Mater. **100**, 440 (1991). *Smoke.* 12, 13, 55, 81

[106] L. Landau, E. Lifšic, J. Sykes, J. Bell, M. Kearsley, and L. Pitaevskii, *Electrodynamics of continuous media*, Vol. 364, Pergamon press Oxford, 1960. 12, 13, 43, 114

[107] J. Suits and K. Lee. J. Appl. Phys. **42**, 3258 (1971). *Giant magneto-optical Kerr effect in EuO.* 13

[108] A. G. Swartz, J. Ciraldo, J. J. I. Wong, Y. Li, W. Han, T. Lin, S. Mack, J. Shi, D. D. Awschalom, and R. K. Kawakami. Appl. Phys. Lett. **97**, 112509 (2010). *Epitaxial EuO thin films on GaAs.* doi:10.1063/1.3490649, [link].

[109] D. F. Förster, J. Klinkhammer, C. Busse, S. G. Altendorf, T. Michely, Z. Hu, Y.-Y. Chin, L. H. Tjeng, J. Coraux, and D. Bourgault. Phys. Rev. B **83**, 045424 (2011). *Epitaxial europium oxide on Ni(100) with single-crystal quality.* doi:10.1103/PhysRevB.83.045424. 82

[110] A. G. Swartz, P. M. Odenthal, Y. Hao, R. S. Ruoff, and R. K. Kawakami. ACS Nano **6**, 10063 (2012). *Integration of the ferromagnetic insulator EuO onto graphene.*

[111] K. Ahn and J. Suits. IEEE Trans. Magn. **3**, 453 (1967). *Preparation and properties of EuO films.* doi:10.1109/TMAG.1967.1066089. 24

[112] J. H. Greiner and G. J. Fan. Appl. Phys. Lett. **9**, 27 (1966). *Longitudinal magneto-optical Kerr effect in EuO and EuS.* doi:10.1063/1.1754584, [link]. 13

[113] P. Grünberg and B. Schwarz. J. de Phys. **41**, 5 (1980). *Light scattering from spinwaves and magnetooptic hysteresis measurements on EuO and EuS.*

[114] J. Lettieri, V. Vaithyanathan, S. K. Eah, J. Stephens, V. Sih, D. D. Awschalom, J. Levy, and D. G. Schlom. Appl. Phys. Lett. **83**, 975 (2003). *Epitaxial growth and magnetic properties of EuO on (001) Si by molecular-beam epitaxy.* doi:10.1063/1.1593832, [link].

[115] T. McGuire and M. Shafer. J. Appl. Phys. **35**, 984 (1964). *Ferromagnetic europium compounds.*

[116] D. Ghosh, M. De, and S. De. Phys. Rev. B **70**, 115211 (2004). *Electronic structure and magneto-optical properties of magnetic semiconductors: Europium monochalcogenides.*

[117] F. Holtzberg, Faraday rotation, US Patent 3,418,036, 1968. 13

[118] K. Ahn. IEEE Trans. Magn. **4**, 408 (1968). *Kerr effects in thin EuO films on mirror substrates.*

[119] M. Matsubara, A. Schmehl, J. Mannhart, D. G. Schlom, and M. Fiebig. Phys. Rev. B **81**, 214447 (2010). *Large nonlinear magneto-optical effect in the centrosymmetric ferromagnetic semiconductor EuO.* doi:10.1103/PhysRevB.81.214447.

[120] K. Ahn and G. Almasi. IEEE Trans. Magn. **5**, 944 (1969). *Coupling effects between films of Fe and EuO.* 13, 84

[121] *SPS-CreaTec GmbH, Magnusstr. 11, 12489 Berlin, Germany*
www.sps-createc.com. 15, 18, 108, 123, 154, 155

[122] S. Zöphel. PhD Thesis, FU Berlin (2000). *Der Aufbau eines Tieftemperatur-Rastertunnelmikroskops und Strukturuntersuchungen auf vicinalen Kupferoberflächen.* 16

[123] I. Horcas, R. Fernández, J. M. Gómez-Rodríguez, J. Colchero, J. Gómez-Herrero, and A. M. Baro. Rev. Sci. Instrum. **78**, 013705 (2007). *WSXM: A software for scanning probe microscopy and a tool for nanotechnology.* doi:10.1063/1.2432410. 16

[124] Manufacturer of the precission manipulator *VAb Vakuum-Anlagenbau GmbH, Marie-Curie-Str. 11, 25337 Elmshorn.* www.vab-vakuum.de. 18

[125] D. Pollock, *The theory and properties of thermocouple elements*, no. 492, ASTM International, 1971. 19

[126] Thickness rate monitor from the manufacturer *Sycon instruments, 6757 Kinne Street, East Syracuse, New York 13057 USA.* www.sycon.com. 19, 20

[127] Ames Laboratory (Materials Preparation Center) of the US DOE, Iowa State University, Ames, Iowa 50011-3020, USA. 20

[128] *Dr. Eberl MBE-Komponenten GmbH, Gutenbergstrasse 8, D-71263 Weil der Stadt.* www.mbe-components.com. 20

[129] W. D. Wang, N. J. Wu, and P. A. Thiel. J. Chem. Phys. **92**, 2025 (1990). *Structural steps to oxidation of Ni(100).* doi:10.1063/1.458036. 20

[130] H. P. Oepen, Private communications, 2009. 23, 31, 123, 153

[131] Konvex lens, Laser and precision rotary holder from the manufacturer *CVI Melles Griot GmbH, Lilienthalstraße 30-32 64625 Bensheim.* www.cvimellesgriot.com. 24, 28

[132] Glan Thompson prism and retardation plate from the manufacturer *Bernhard Halle Nachfl. GmbH, Hubertusstraße 10, D - 12163 Berlin.* www.b-halle.de. 25

[133] A. Jacobi. Bachelor thesis Universität zu Köln (2010). *Aufbau und Test eines Messplatzes für den Magneto-Optischen Kerr-Effekt (MOKE).* 26, 29

[134] F. Jenkins and H. White, Fundamentals of optics—fourth edition; 1976; isbn: 0-07-032330-5. 28

[135] F. Huttmann. Bachelor thesis Universität zu Köln (2010). *Automatisierung, Fehler- und Rauschanalyse für einen Messaufbau zum magneto-optischen Kerr-Effekt (MOKE).* 30, 113, 114

[136] Manufacturer of the multimeter for the MOKE detector *Agilent Technologies Deutschland GmbH, Herrenberger Str. 130, 71034 Böblingen.* www.home.agilent.com. 30

[137] Temperature controller from the manufacturer *Eurotherm UK, Faraday Close, Durrington, Worthing, West Sussex BN13 3PL.* www.eurotherm.co.uk. 30

[138] J. Lee, J. Jeong, S. Shin, J. Kim, and S. Kim. Phys. Rev. B **66**, 172409 (2002). *Spin-reorientation transitions in ultrathin Co films on Pt(111) and Pd(111) single-crystal substrates.* 31

[139] R. Sellmann, H. Fritzsche, H. Maletta, V. Leiner, and R. Siebrecht. Phys. Rev. B **64**, 054418 (2001). *Spin-reorientation transition and magnetic phase diagrams of thin epitaxial Au(111)/Co films with W and Au overlayers.* 31

[140] J. Coraux, A. T. N'Diaye, M. Engler, C. Busse, D. Wall, N. Buckanie, F.-J. Meyer zu Heringdorf, R. van Gastel, B. Poelsema, and T. Michely. New J. Phys. **11**, 023006 (2009). *Growth of graphene on Ir(111).* doi:10.1088/1367-2630/11/2/023006, [link]. 35

[141] A. T. N'Diaye, J. Coraux, T. N. Plasa, C. Busse, and T. Michely. New J. Phys. **10**, 043033 (2008). *Structure of epitaxial graphene on Ir(111).* doi:10.1088/1367-2630/10/4/043033, [link]. 36

[142] R. van Gastel, A. T. N'Diaye, D. Wall, J. Coraux, C. Busse, N. M. Buckanie, F.-J. Meyer zu Heringdorf, M. Horn-von Hoegen, T. Michely, and B. Poelsema. Appl.Phys. Lett. **95**, 121901 (2009). *Selecting a single orientation for millimeter sized graphene sheets.* doi:10.1063/1.3225554, [link]. 36

[143] N. Iwata, G. Pindoria, T. Morishita, and K. Kohn. J. Phys. Soc. Jpn. **69**, 230 (2000). *Preparation and magnetic properties of EuO thin films epitaxially grown on MgO and $SrTiO_3$ substrates.* doi:10.1143/JPSJ.69.230. 37

[144] R. P. Panguluri, T. S. Santos, E. Negusse, J. Dvorak, Y. Idzerda, J. S. Moodera, and B. Nadgorny. Phys. Rev. B **78**, 125307 (2008). *Half-metallicity in europium oxide conductively matched with silicon.* doi:10.1103/PhysRevB.78.125307.

[145] E. Negusse, J. Dvorak, J. S. Holroyd, M. Liberati, T. S. Santos, J. S. Moodera, E. Arenholz, and Y. U. Idzerda. J. Appl. Phys. **105**, 07C930 (2009). *Magnetic characterization of ultrathin EuO films with XMCD.* doi:10.1063/1.3076044, [link]. 37

[146] R. Sutarto, S. G. Altendorf, B. Coloru, M. Moretti Sala, T. Haupricht, C. F. Chang, Z. Hu, C. Schüßler-Langeheine, N. Hollmann, H. Kierspel, H. H. Hsieh, H.-J. Lin, C. T. Chen, and L. H. Tjeng. Phys. Rev. B **79**, 205318 (2009). *Epitaxial and layer-by-layer growth of EuO thin films on yttria-stabilized cubic zirconia(001) using MBE distillation.* doi:10.1103/PhysRevB.79.205318. 37, 45, 48

[147] J. M. Haschke and H. A. Eick. J. Phys. Chem. **73**, 374 (1969). *Vaporization thermodynamics of europium monoxide.* 37

[148] M. Herman and H. Sitter, *Molecular beam epitaxy: fundamentals and current status*, Springer-Verlag Berlin, 1989. 37

[149] H. Lüth, *Surfaces and interfaces of solids*, Vol. 15, Springer, 1993. 37

[150] D. F. Förster, J. Klinkhammer, and T. Michely. Surf. Sci. , (2012). *Eu oxides on Ni(100): Polar surfaces, magic clusters and structures with large lattice dilation.* doi:10.1016/j.susc.2012.02.021, [link]. 38

[151] A. Kane, T. Sheps, E. Branigan, V. Apkarian, M. Cheng, J. Hemminger, S. Hunt, and P. Collins. Nano Lett. **9**, 3586 (2009). *Graphitic electrical contacts to metallic single-walled carbon nanotubes using Pt electrodes.* 38

[152] J. Klinkhammer, D. F. Förster, S. Schumacher, H. P. Oepen, T. Michely, and C. Busse. submitted to Appl. Phys. Lett. (2013). *Enhanced curie temperature of ultra thin textured EuO films on graphene.* 39, 53

[153] S. Schumacher, D. F. Förster, M. Rösner, T. O. Wehling, and T. Michely. Phys. Rev. Lett. **110**, 086111 (2013). *Strain in epitaxial graphene visualized by intercalation.* doi:10.1103/PhysRevLett.110.086111, [link]. 39, 53

[154] M. Sokolowski, Private communications, 2012. 39

[155] G. Binnig, H. Rohrer, C. Gerber, and E. Weibel. Phys. Rev. Lett. **49**, 57 (1982). *Surface studies by scanning tunneling microscopy.* doi:10.1103/PhysRevLett.49.57, [link]. 40

[156] M. Passoni, F. Donati, A. Li Bassi, C. S. Casari, and C. E. Bottani. Phys. Rev. B **79**, 045404 (2009). *Recovery of local density of states using scanning tunneling spectroscopy.* doi:10.1103/PhysRevB.79.045404. 40

[157] H. Zandvliet and A. van Houselt. Annu. Rev. Anal. Chem. **2**, 37 (2009). *Scanning tunneling spectroscopy.* 40

[158] J. Bardeen. Phys. Rev. Lett. **6**, 57 (1961). *Tunnelling from a many-particle point of view.* doi:10.1103/PhysRevLett.6.57, [link]. 40

[159] V. A. Ukraintsev. Phys. Rev. B **53**, 11176 (1996). *Data evaluation technique for electron-tunneling spectroscopy.* doi:10.1103/PhysRevB.53.11176. 40

[160] J. Tersoff and D. Hamann. Phys. Rev. B **31**, 805 (1985). *Theory of the scanning tunneling microscope.* 40

[161] M. Morgenstern. Surf. Rev. Lett. **10**, 933 (2003). *Probing the local density of states of dilute electron systems in different dimensions.* 41

[162] A. T. N'Diaye, R. van Gastel, A. J. Martínez-Galera, J. Coraux, H. Hattab, D. Wall, F.-J. Meyer zu Heringdorf, M. Horn-von Hoegen, J. M. Gómez-Rodríguez, B. Poelsema, C. Busse, and T. Michely. New J. Phys. **11**, 113056 (2009). *In situ observation of stress relaxation in epitaxial graphene.* doi:10.1088/1367-2630/11/11/113056, [link]. 47

[163] S. Schumacher, Private communications, 2009. 53

[164] M. A. H. Vozmediano, M. P. López-Sancho, T. Stauber, and F. Guinea. Phys. Rev. B **72**, 155121 (2005). *Local defects and ferromagnetism in graphene layers.* doi:10.1103/PhysRevB.72.155121, [link]. 54

[165] N. Miyata and B. E. Argyle. Phys. Rev. **157**, 448 (1967). *Magnetocrystalline Anisotropy of Single-Crystal Europium Oxide.* doi:10.1103/PhysRev.157.448, [link]. 56

[166] C. P. Bean and J. D. Livingston. J. Appl. Phys. **30**, S120 (1959). *Superparamagnetism.* 56

[167] J. A. Colón Santana, J. M. An, N. Wu, K. D. Belashchenko, X. Wang, P. Liu, J. Tang, Y. Losovyj, I. N. Yakovkin, and P. A. Dowben. Phys. Rev. B **85**, 014406 (2012). *Effect of gadolinium doping on the electronic band structure of europium oxide.* doi:10.1103/PhysRevB.85.014406, [link]. 59

[168] M. Lubecka and A. Wegrzyn. Vacuum **37**, 111 (1987). *The diffusion of oxygen vacancies and electrical properties of EuO thin films doped with Eu.* 64

[169] L. Olesen, M. Brandbyge, M. R. Sørensen, K. W. Jacobsen, E. Lægsgaard, I. Stensgaard, and F. Besenbacher. Phys. Rev. Lett. **76**, 1485 (1996). *Apparent barrier height in scanning tunneling microscopy revisited.* doi:10.1103/PhysRevLett.76.1485. 64

[170] D. Niesner, T. Fauster, J. I. Dadap, N. Zaki, K. R. Knox, P.-C. Yeh, R. Bhandari, R. M. Osgood, M. Petrović, and M. Kralj. Phys. Rev. B **85**, 081402 (2012). *Trapping surface electrons on graphene layers and islands.* doi:10.1103/PhysRevB.85.081402, [link]. 66

[171] V. S. Bagotsky, *Fundamentals of electrochemistry*, Vol. 44, Wiley-Interscience, 2005. 67

[172] L. Giordano, U. Martinez, G. Pacchioni, M. Watkins, and A. L. Shluger. J. Phys. Chem. C **112**, 3857 (2008). *F and F+ Centers on MgO/Ag (100) or MgO/Mo (100) ultrathin films: Are they stable?* 67

[173] T. Konig, G. Simon, H.-P. Rust, G. Pacchioni, M. Heyde, and H.-J. Freund. J. Am. Chem. Soc. **131**, 17544 (2009). *Measuring the charge state of point defects on MgO/Ag (001).* 67

[174] L. Petersen, P. Sprunger, P. Hofmann, E. Lægsgaard, B. Briner, M. Doering, H. Rust, A. Bradshaw, F. Besenbacher, and E. Plummer. Phys. Rev. B **57**, 6858 (1998). *Direct imaging of the two-dimensional Fermi contour: Fourier-transform STM.* 71

[175] L. Petersen and P. Hedegård. Surf. Sci. **459**, 49 (2000). *A simple tight-binding model of spin-orbit splitting of sp-derived surface states.* 72

[176] G. Busch, P. Junod, and P. Wachter. Phys. Lett. **12**, 11 (1964). *Optical absorption of ferro-and antiferromagnetic europium chalcogenides.* 72

[177] J. Schoenes and P. Wachter. Phys. Rev. B **9**, 3097 (1974). *Exchange optics in Gd-doped EuO.* 72

[178] R. M. Feenstra and J. A. Stroscio. J. Vac. Sci. Technol. B **5**, 923 (1987). *Tunneling spectroscopy of the GaAs(110) surface.* 75

[179] S. Modesti, H. Gutzmann, J. Wiebe, and R. Wiesendanger. Phys. Rev. B **80**, 125326 (2009). *Correction of systematic errors in scanning tunneling spectra on semiconductor surfaces: The energy gap of Si(111)-7 × 7 at 0.3 K.* doi:10.1103/PhysRevB.80.125326, [link]. 75

[180] V. A. Ukraintsev. Phys. Rev. B **53**, 11176 (1996). *Data evaluation technique for electron-tunneling spectroscopy.* 76, 87

[181] C. Zener. Phys. Rev. **96**, 1335 (1954). *Classical theory of the temperature dependence of magnetic anisotropy energy.* doi:10.1103/PhysRev.96.1335, [link]. 81, 87

[182] W. L. O'Brien and B. P. Tonner. Phys. Rev. B **49**, 15370 (1994). *Transition to the perpendicular easy axis of magnetization in Ni ultrathin films found by x-ray magnetic circular dichroism.* doi:10.1103/PhysRevB.49.15370, [link]. 81

[183] A. Hubert and R. Schäfer, *Magnetic domains: the analysis of magnetic microstructures*, Springer, (2008). 81, 87

[184] L. Bates and G. Wilson. Proc. Phys. Soc. (London), Sect. A **64**, 691 (2002). *Some new Bitter patterns on a single crystal of nickel.* 81

[185] H. Spreen. Phys. Status Solidi B **24**, 413 (1967). *Untersuchungen der Bereichstruktur von Nickeleinkristallen III. Die Abschlußstruktur in zylindrischen Kristallen mit <110> als Achse.* 81

[186] D. Krause and H. Frey. Z Physik A **224**, 257 (1969). *Untersuchungen zur Temperaturabhängigkeit der Bereichstrukturen stabförmiger Nickel-Einkristalle.* 81

[187] R. Hicken and J. Wu. J. Appl. Phys. **85**, 4580 (1999). *Observation of ferromagnetic resonance in the time domain.* 81

[188] C. S. Arnold, D. P. Pappas, and A. P. Popov. Phys. Rev. Lett. **83**, 3305 (1999). *Second- and first-order phase transitions in the magnetic reorientation of ultrathin Fe on Gd.* doi:10.1103/PhysRevLett.83.3305, [link]. 81

[189] W. Hübner and K.-H. Bennemann. Phys. Rev. B **40**, 5973 (1989). *Nonlinear magneto-optical Kerr effect on a nickel surface.* doi:10.1103/PhysRevB.40.5973, [link]. 82

[190] R. Wiesendanger. Rev. Mod. Phys. **81**, 1495 (2009). *Spin mapping at the nanoscale and atomic scale.* 105

[191] T. Michely. Diploma thesis - Universität Bonn (1988). *Eine Kombination von Rastertunnel- und Feldionenmikroskop.* 105

[192] D. Szynka. Diploma thesis - RWTH AAchen (1990). *Untersuchung von Grenzflächen und Gitterbaufehlern in Halbleitern mit Hilfe der Ratertunnelmikroskopie.* 105

[193] T. Michely, K. Besocke, and M. Teske. J. Microsc. **152**, 77 (1988). *A combined scanning tunnelling and field ion microscope.* 105

[194] T. Stollenwerk, Private communications. 111

A Preparation of Tungsten Tips

A necessary prerequisite for STM is the preparation of well-defined tips. The idea is to prepare STM tips which can obtain magnetic STM contrast, for example non magnetic tips with magnetic coating, tips of ferromagnetic, or antiferromagnetic materials [190]. First attempts were performed with non magnetic tungsten (W) tips. The tips were etched electrochemically by the lamella-method [191] (figure A.1 a)) and by the dip-in method (figure A.1 b)). At first etching experiments were performed with the aim to create atomically sharp STM tips and afterwards tips with an apex diameter in the range of a micrometer. Atomically sharp tips are probes of choice for scanning probe experiments with atomic resolution and the possibility to image steep sample flanks, whereas rounded tips allow the deposition of ferromagnetic materials (as cobalt) onto the tip. Such coated tips and can gain magnetic contrast for spin polarized STM/STS measurements. In this chapter the preparation of STM tips is explained.

The Lamella-Method

The lamella method, as displayed in figure A.1 a), uses a ring-electrode of a noble material, in our case platinum. A lamella of a NaOH electrolyte is produced by dipping the ring-electrode into a glass with a 5% NaOH solution. A polycrystalline tungsten wire of 0.25 mm diameter is dipped perpendicular through the lamella by a linear motion drive. The alignment of the ring-electrode should be horizontal. The tungsten wire is etched electrochemically by applying a voltage between it and the platinum ring-electrode. The following chemical reaction sets in during the etching process [192]:

$$2 \cdot \mathrm{W} + 2 \cdot \mathrm{NaOH_{aq}} + 6 \cdot \mathrm{H_2O} \leftrightarrow 2 \cdot \mathrm{NaWO_{4aq}} + 7 \cdot \mathrm{H_2}$$

With this process STM tips with an apex radius of less than 10 nm can be achieved [193]. Most etching on the wire takes place at the height of the ring-electrode. The tip will be the lower part of the tungsten wire, which falls down when the wire is etched into two parts. The tip apex results from severing the tungsten wire into two parts by a combination of etching and of plastic tearing. A glass filled with shaving foam is put below it to catch the falling tip carefully. Since the etching on the tip stops just in the moment when it is etched off from the upper part of the wire (due to the missing electrical connection of the etching voltage) it is very probably monoatomicly sharp at its apex. The formation of crystalline facets at the apex is expected, as discussed in the thesis of D. Szynka [192].

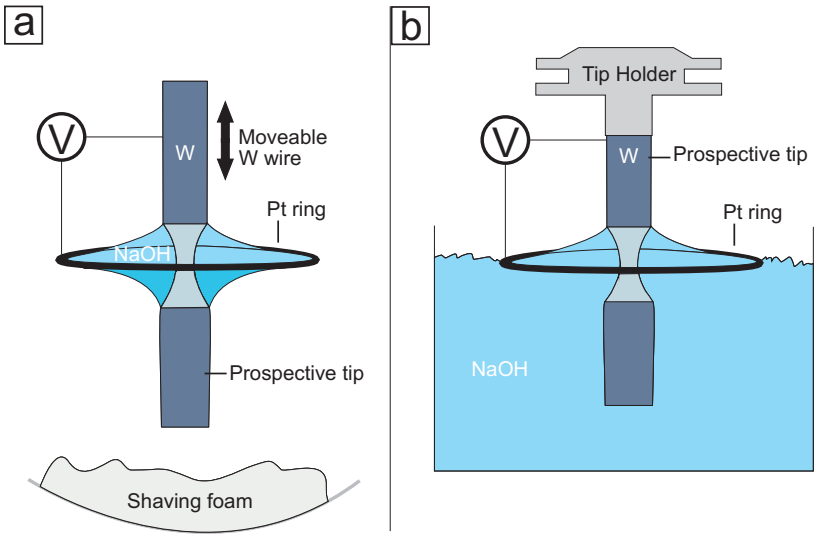

Figure A.1: Sketch of the two setups for the electrochemical etching of tungsten STM tips in NaOH. a) In the lamella-method setup a tungsten wire is dipped perpendicular through a lamella of NaOH solution within a platinum ring-electrode. The tungsten wire is etched into two parts, the lower part falls softly into the shaving foam and is used as an STM tip. b) In the dip-in method setup, the ring-electrode and wire is dipped into the surface of a NaOH solution bath. The wire is also etched into two parts, but the upper wire part is used as an STM tip.

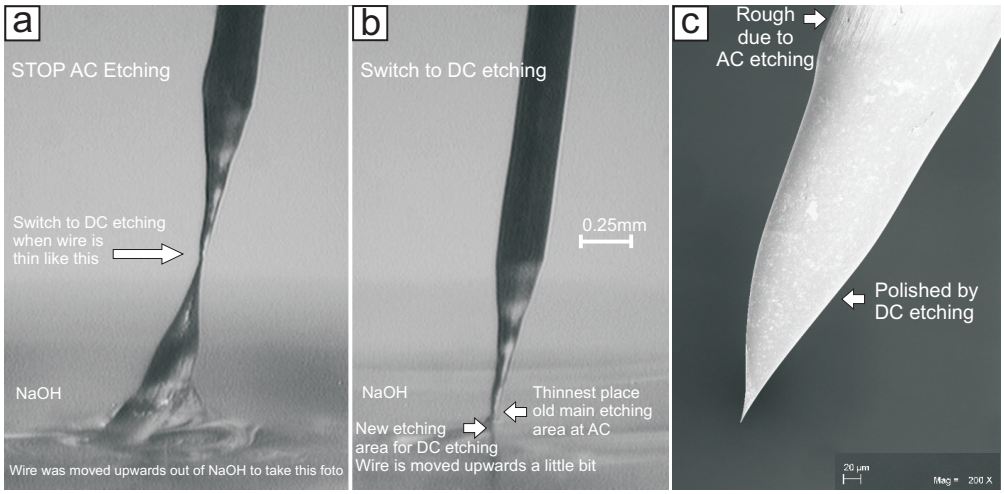

Figure A.2: a) and b) Optical microscope photographs of a tungsten wire used in the lamella-method etching procedure. The state where one should switch from AC to DC etching is described in the images. c) An SEM image of a finished STM tip produced by the lamella-method.

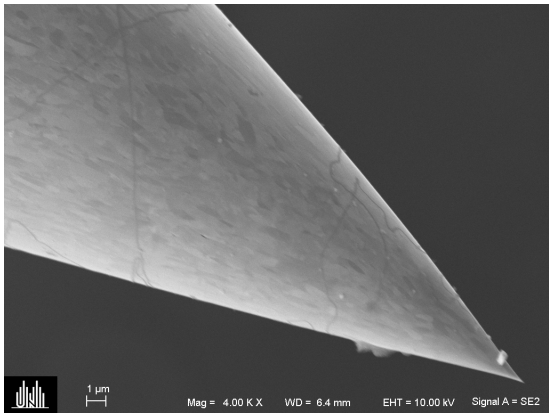

Figure A.3: High magnification SEM image of a tungsten STM tip etched by the lamella-method. The front of the tip is sharp, even, symmetric and clean with no long thin, antenna like end.

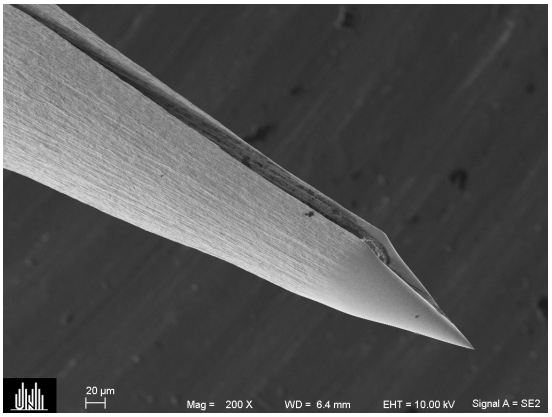

Figure A.4: Large scale SEM image of a tungsten STM tip etched by the lamella-method. A crack along the brittle tungsten wire is visible. The crack is a result of a cut with the wire side cutter.

The handling of the etching procedure is described in the following paragraph, as visualized by optical microscopy images in figure A.2 a) and b). First an AC voltage of 3 V is applied to the electrodes until the tungsten wire is nearly separated (see figure A.2 a)), which takes about five minutes. At this stadium the thinnest part of the wire has a diameter of about 0.01 mm. The wire is then displaced upwards by about 0.03 mm, see figure A.2 b). The formation of a long thin, antenna like end of the tip is thereby prevented. The thinnest part of the tip should be as short as possible to avoid mechanical vibrations during later STM measurements. Now a DC voltage of +5 V is applied to the wire (ring-electrode on negative potential) until the wire is etched into two parts which takes about fifteen minutes unless the remaining wire is already very thin. The tip is electro polished by the DC voltage, since the etching products are guided away from it uniformly to the ring-electrode. (During AC etching there is no constant electric field in the NaOH solution which can guide solved ions into a certain direction and small hydrogen gas bubbles originate at the tungsten wire, which make it rough.) The tip is picked out of the shaving foam carefully with tweezers and cleaned by cycles of swiveling it into hot isopropyl and distilled water. An atomically sharp STM tip produced in this way is displayed in the SEM image A.2 c). The SEM image shows the difference of the AC and DC etching steps on the tip. A shiny front of the tip in an optical microscope image is an indication for a successful tip preparation. A high magnification SEM image of such a tip is presented in figure A.3. The front of the tip is sharp, even, symmetric and clean with no long thin, antenna like end. The finished tip has to be put in a tip holder carefully with help of very small tools. In principle it would be easier to mount the sample holder on the lower wire part before etching, but it turned out that the lower part becomes too heavy so that the tip breaks off to early with a frayed end.

Tungsten wire tends to form cracks, as displayed in figure A.4. As tungsten itself is a brittle

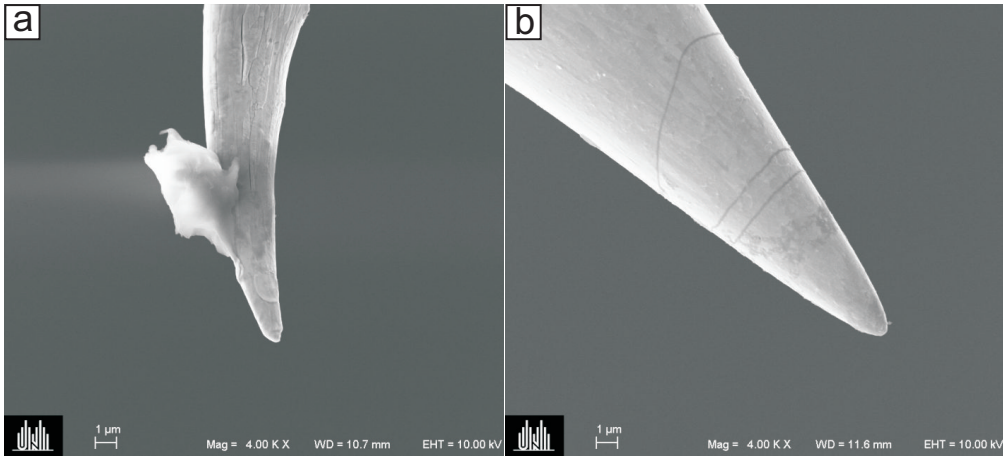

Figure A.5: Round apex tungsten tips. a) Tip etched by the lamella-method and post annealed under UHV conditions. b) Tip etched by dip-in method and post etched for another second to achieve a round apex.

material it is not recommendable to cut a tungsten wire. It is better to etch the wire without applying too much mechanical force on the wire or bending it in small radii.

The Dip-In Method

The dip-in method, as illustrated in figure A.1 b) also works by electrochemical etching the tungsten wire in a NaOH electrolyte. An AC voltage in the range from 5 V to 10 V is applied to the tungsten wire. The wire is dipped into a glass of NaOH solution and the platinum ring-electrode is put onto the surface of the solution. Contrary to the lamella-method the upper part of the etched wire is used as a tip. The advantage is that the tip holder can be mounted to the tip before etching. The challenge is to stop the etching process exactly at the time the lower wire part falls off. If the etching voltage is not switched off exactly at this moment the tip will not be as sharp as possible. A tool of SPS-CreaTec GmbH [121] is utilized to switch the etching voltage, which is connected to the STM control unit as described in the LT-STM manual. The etching current is measured with the SPS-CreaTec GmbH [121] software. Upon the fall of the lower wire part there is less material in the NaOH solution which is etched so the etching current will drop. Upon this drop the voltage is switched off. Tips gained by this method turned out to be less perfect than the ones gained with the lamella-method, especially if etching voltages above 10 V were applied.

Round Apex Tips

STM tips with an apex diameter of about one micrometer are produced for the purpose of depositing some magnetic coating on them. Two methods were used to make these tips. First by annealing atomically sharp tips, and second by etching an atomically sharp STM tip with the setup of the dip-in method for about one second. The tips are thereby rounded nicely.

Figure A.5 a) shows an SEM image of a round apex tip, gained by annealing a sharp tip by electron beam heating at a temperature of about 1470 K. The annealing step is performed under UHV conditions in the preparation chamber of the LT-STM system. Therefore the modified tip tool, as displayed in figure 3.1 d), was used. Indications of grain grooving during annealing and some brittle areas can be seen.
Tips can also be rounded by etching: Figure A.5 b) shows an STM tip which is dipped it into the NaOH electrolyte bath of figure A.1 b) and etched for one second. The apex of this tip shows a nice sphere-like shape with a radius of one μm. It is clean, even and free of cracks. So the dip-in method is recommended to achieving a round apex tip, because it does not require UHV conditions.

Experiments of depositing cobalt on round apex tips were performed and tested with spin polarized STS on magnetic films (not presented in this thesis). Since these coatings are very fragile a tip crash has to be avoided to protect the thin cobalt layer, therefore we did not persist this way.

B Calculation of Heisenberg Magnetization Functions

Heisenberg magnetization functions $M(T)$ are fitted to some magnetization data of this thesis. These functions are not simple analytical functions of the temperature T. The Mean-Field-Magnetization can only be calculated by numerical approximation, as explained in section 2.2. A C-program is programmed and friendly provided by T. Stollenwerk [194]. It solves the Heisenberg model of localized magnetic moments in the Mean-Field-Theory for a given integral 4f-coupling J_{4f}. A solution for $M(T)$ is calculated for every T with help of the program. The Curie temperature T_C of the calculated magnetization function is determined through the integral 4f-coupling $J_{4f} = \sum_{ij} J_{ij}$ by the following relationship: $T_C = 2/3\ J(J+1) \cdot J_{4f}/k_B$ [97], whereby J is the total spin in numbers of μ_B.
A Linux environment is necessary to run the program. Cygdrive can be used to run the program also within an MS operating system. Plugins which have to be installed with Cygdrive are "gcc", "binutils" and "make". To execute the program start Cygdrive, go to the directory which hosts the following files: makefile, main.cpp, main.o and heisenbergMF.out. Execute heisenbergMF.out with the following four parameters:

1. The external magnetic field
2. The 4f-coupling (in eV)
3. The 4f-moment in numbers of μ_B
4. The name of the output file

For example the magnetization function of a sample in zero external magnetic field with a spin of 7/2 μ_B and a T_C of 69 K (J_{4f}=0.00050883358666 eV) and the output file name mag69.dat can be calculated by the command:

./heisenbergMF.out 0.0 0.00050883358666 3.5 magj3.5.dat

The output file is generated in the program folder and contains a column for the temperature values in Kelvin and a column for the spin magnetization in numbers of μ_B per europium atom.

The C-program is stored in network of the II. Physikalische Institut of the Universität zu Köln and accessible for the workgroup of Prof. Dr. Michely.

C Usage of MOKEsoft

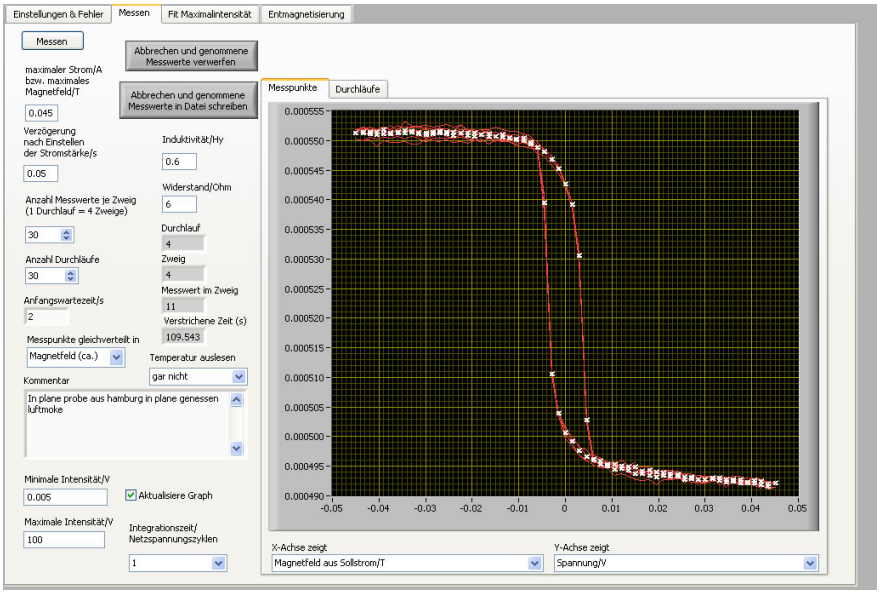

Figure C.1: Screenshot of the MOKEsoft measurement screen. Measurements are controlled via this control panel and the recorded data is displayed.

This chapter is a kind of manual for the usage of the MOKE measuring arrangements automatization software MOKEsoft. The chapter is written from the users point of view. For a better understanding of this chapter one should keep MOKEsoft in sight. The user starts by executing the MOKEsoft.exe win32 file. On the starting tab one has to choose the serial ports on which the BOP power supply, Agilent multimeter and the Eurotherm are plugged to. As the second step the $B(I)$ calibration curve of the magnet has to be read in as a .lvm file. So with this calibration the software has the capability of applying defined magnetic fluxes to a sample. The software fits the $B(I)$ calibration data with a spline fit (for details it is referred to the bachelor thesis of F. Huttmann [135]).

The second tab, as displayed in figure C.1, serves for the measurement control. One has to set the following measuring parameter in this tab: The integration time (of the Agilent multimeter) in numbers of 1/50 seconds, the number of data points in each quarter of a hysteresis loop, the number of loops to be measured and whether the data points should be distributed in equal steps of magnetic fields, or coil currents. When the option “magnetic flux” is chosen on has to type in the maximum applicable magnetic flux in numbers of mT into the provided box, otherwise the desired maximum coil current in ampere. The graphical presentation of data also takes place in the measuring tab, once for hysteresis loops and once for data directly evaluated from these loops. This evaluated data is half the difference of a loops amplitude ΔA at maximum field and in remanence.

Since A is directly proportional to the samples magnetization [99; 106] we utilized it to perform magnetization vs. temperature measurements by recording multiple loops and slowly varying the sample temperature T. The signal plotted on the y axis, namely the Kerr signal can be displayed in numbers of the detector voltage or as Kerr angle plus a offset angle. But for the determination of the Kerr signal in numbers of rad the minimum detector voltage (analyzer prism extinguishes laser beam) and maximum detector voltage (analyzer fully opened) have to be typed into the provided boxes in numbers of volts. Since the detector voltage with a fully opened analyzer cannot be measured (due to an occurring overload of the detector) this number has to be estimated by a fit. The fit is done with the third tab of MOKEsoft as described later in this chapter.
The measured MOKE data is written to a hard disc drive after all hysteresis cycles are finished. Thereby the data is written to four files. Here just some essential issues are noted, for details is is also referred to the bachelor thesis of F. Huttmann [135]. The first file contains the measuring parameters. The second file contains the lab time, sample temperatures, set and real coil currents, set and real magnetic fields, the detector voltage and the Kerr angle in numbers of rad for every single data point. The third file contains the same columns, but with values averaged over the single loops. The fourth file stores the lab time, sample temperature and the sample magnetization at high fields and in remanence, both in numbers of the detector voltage and in numbers of rad.
The third tab of MOKEsoft offers a tool to fit the maximum detector voltage. This tool is handled as follows: Some defined analyzer angles have first to be set at the detector with help of the precision rotary holder (first setting in extinction of the laser) and second typed to the fitting tool and lastly the detector voltage for the set angles is read out (automatically). Doing so for five angles leads to a reliable fitted value of the maximum detector voltage. Typical numbers for detector voltages are in the order of 0.5 mV in extinction and 160 V for fully transmitted light. It should be noted that these numbers depend on the physical properties of the investigated samples like its reflectivity.
The last feature of MOKEsoft, which is available in the fourth tab is a demagnetizing tool. It works by driving the magnet with loops of magnetic fluxes with decreasing amplitudes and thus driving down the remanence of the sample and the yoke by each cycle.

MOKEsoft and the utilized .lvm file is stored in the network of the II. Physikalische Institut of the Universität zu Köln and accessible for the workgroup of Prof. Dr. Michely.

D Calibration of the Electromagnet

This appendix includes the magnetic field B vs. coil current I calibration of the MOKE apparatus electromagnet for assemblies with different pole shoes. Two coils with 2212 windings each have always been used. The descending branch of the $B(I)$ characteristic serves as the calibration file, which is read into MOKEsoft, as described in the manual in appendix C. By this calibration the hysteresis of the iron yoke of the MOKE-magnet itself is not considered.

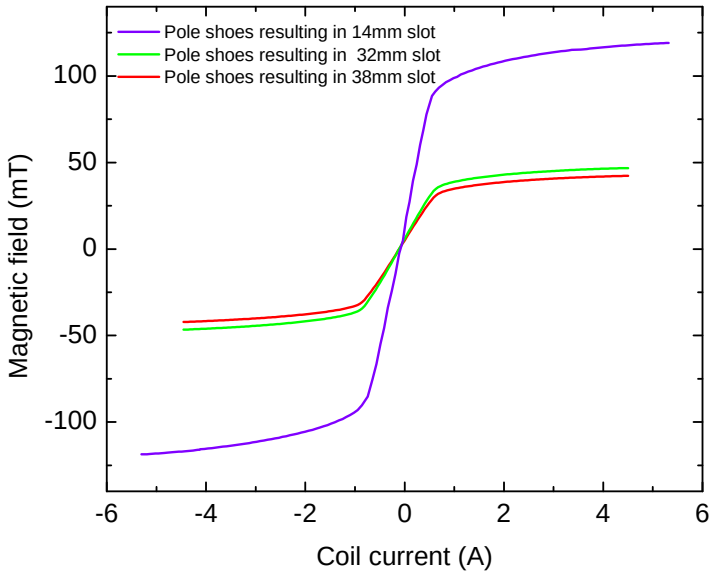

Figure D.1: Plot of .lmv pair of values for different magnet assemblies. Plot of figure D.2 for magnet as used in the UHV MOKE, see figure E.1, resulting in a 14 mm magnet slot. Plot of figure D.5 achieved with pole shoes displayed in figure E.4 resulting in a 32 mm magnet slot. Plot of figure D.6 recorded with pole shoes displayed in figure E.6 resulting in a magnet slot of 38 mm. The magnetic field is produced by two coils with 2212 windings each on the magnets upper side.

I (A)	B(mT)		I (A)	B(mT)		I (A)	B(mT)
5.320	119.103		1.805	107.163		-2.081	-106.120
5.270	119.030		1.730	106.650		-2.158	-106.599
5.210	118.968		1.655	105.971		-2.232	-107.167
5.160	118.851		1.581	105.421		-2.309	-107.591
5.100	118.776		1.505	104.664		-2.383	-108.120
5.040	118.672		1.431	104.049		-2.459	-108.556
4.980	118.595		1.356	103.216		-2.533	-109.035
4.920	118.478		1.281	102.534		-2.610	-109.419
4.860	118.393		1.206	101.576		-2.684	-109.881
4.800	118.280		1.131	100.800		-2.760	-110.228
4.740	118.203		1.057	99.491		-2.833	-110.656
4.680	118.065		0.982	98.767		-2.910	-111.008
4.620	117.968		0.908	97.501		-2.984	-111.406
4.560	117.838		0.834	96.373		-3.060	-111.734
4.500	117.722		0.761	94.760		-3.134	-112.101
4.440	117.573		0.688	93.274		-3.210	-112.404
4.380	117.479		0.618	90.954		-3.284	-112.760
4.320	117.353		0.553	88.404		-3.360	-113.045
4.260	117.202		0.496	83.487		-3.434	-113.371
4.200	117.064		0.438	77.730		-3.510	-113.638
4.150	116.885		0.377	68.591		-3.584	-113.958
4.090	116.769		0.310	60.242		-3.660	-114.210
4.030	116.595		0.241	48.909		-3.734	-114.498
3.970	116.455		0.168	39.398		-3.810	-114.734
3.910	116.274		0.096	27.291		-3.883	-115.014
3.850	116.129		0.032	18.517		-3.959	-115.238
3.790	115.939		-0.037	4.870		-4.033	-115.512
3.730	115.786		-0.110	-2.540		-4.120	-115.706
3.670	115.577		-0.184	-14.295		-4.130	-115.918
3.610	115.428		-0.260	-24.248		-4.160	-116.058
3.550	115.219		-0.336	-33.850		-4.200	-116.209
3.366	115.040		-0.412	-45.686		-4.260	-116.388
3.306	114.816		-0.489	-55.006		-4.320	-116.536
3.232	114.521		-0.567	-66.459		-4.380	-116.718
3.155	114.265		-0.646	-75.264		-4.440	-116.841
3.082	113.965		-0.743	-85.315		-4.490	-117.018
3.005	113.687		-0.861	-90.249		-4.550	-117.132
2.931	113.364		-0.946	-93.114		-4.610	-117.288
2.855	113.067		-1.023	-94.556		-4.670	-117.414
2.781	112.720		-1.100	-96.029		-4.730	-117.574
2.705	112.423		-1.175	-97.072		-4.790	-117.687
2.631	112.036		-1.252	-98.222		-4.840	-117.836
2.554	111.690		-1.327	-99.082		-4.900	-117.961
2.480	111.278		-1.403	-100.069		-4.960	-118.088
2.404	110.930		-1.478	-100.805		-5.020	-118.206
2.330	110.489		-1.555	-101.695		-5.080	-118.315
2.254	110.103		-1.629	-102.351		-5.140	-118.423
2.180	109.724		-1.706	-103.143		-5.190	-118.547
2.105	109.205		-1.780	-103.727		-5.250	-118.644
2.030	108.777		-1.857	-104.446		-5.290	-118.626
1.955	108.232		-1.931	-104.979		-5.300	-118.555
1.880	107.777		-2.007	-105.626			

Figure D.2: Pair of values to be read into MOKEsoft as a .lmv file for the calibration for the UHV magnet at usage of maximum coil current of 6 A. The .lmv file consists of the descending branch of the magnets B(I) characteristic figure 4.4.

I (A)	B(mT)		I (A)	B(mT)
0.500	0.625		-0.020	0.074
0.490	0.624		-0.030	0.060
0.480	0.622		-0.040	0.046
0.470	0.620		-0.050	0.031
0.460	0.617		-0.060	0.016
0.450	0.614		-0.070	0.002
0.440	0.610		-0.080	-0.013
0.430	0.606		-0.090	-0.028
0.420	0.601		-0.100	-0.043
0.410	0.595		-0.110	-0.058
0.400	0.589		-0.120	-0.073
0.390	0.583		-0.130	-0.087
0.380	0.575		-0.140	-0.102
0.370	0.568		-0.150	-0.116
0.360	0.559		-0.160	-0.139
0.350	0.550		-0.170	-0.148
0.340	0.541		-0.180	-0.161
0.330	0.532		-0.190	-0.175
0.320	0.522		-0.200	-0.189
0.310	0.512		-0.210	-0.203
0.300	0.501		-0.220	-0.218
0.290	0.490		-0.230	-0.232
0.280	0.479		-0.240	-0.246
0.270	0.468		-0.250	-0.260
0.260	0.456		-0.260	-0.274
0.250	0.445		-0.270	-0.288
0.240	0.433		-0.280	-0.302
0.230	0.420		-0.290	-0.315
0.220	0.408		-0.300	-0.329
0.210	0.396		-0.310	-0.342
0.200	0.383		-0.320	-0.356
0.190	0.370		-0.330	-0.369
0.180	0.357		-0.340	-0.382
0.170	0.344		-0.350	-0.395
0.160	0.331		-0.360	-0.408
0.150	0.318		-0.370	-0.421
0.140	0.304		-0.380	-0.434
0.130	0.290		-0.390	-0.447
0.120	0.276		-0.400	-0.460
0.110	0.263		-0.410	-0.472
0.100	0.249		-0.420	-0.485
0.090	0.234		-0.430	-0.497
0.080	0.220		-0.440	-0.510
0.070	0.206		-0.450	-0.522
0.060	0.192		-0.460	-0.535
0.050	0.177		-0.470	-0.547
0.040	0.163		-0.480	-0.559
0.030	0.149		-0.490	-0.571
0.020	0.134		-0.500	-0.583
0.010	0.120			
0.000	0.105			
-0.010	0.083			

Figure D.3: Pair of values to be read into MOKEsoft as a .lmv file for the calibration for the UHV magnet at usage of maximum coil current of 0.5 A. The .lmv file consists of the descending branch of the magnets B(I) characteristic figure 4.4.

I (A)	B(mT)		I (A)	B(mT)
0.200	22.137		-0.008	6.059
0.196	22.241		-0.012	5.545
0.192	22.193		-0.016	5.025
0.188	22.116		-0.020	4.502
0.184	22.029		-0.024	3.976
0.180	21.940		-0.028	3.439
0.176	21.842		-0.032	2.908
0.172	21.732		-0.036	2.375
0.168	21.608		-0.040	1.833
0.164	21.477		-0.044	1.297
0.160	21.334		-0.048	0.746
0.156	21.178		-0.052	0.199
0.152	21.011		-0.056	-0.339
0.148	20.839		-0.060	-0.894
0.144	20.648		-0.064	-1.444
0.140	20.442		-0.068	-1.992
0.136	20.232		-0.072	-2.545
0.132	19.998		-0.076	-3.092
0.128	19.754		-0.080	-3.649
0.124	19.499		-0.084	-4.192
0.120	19.236		-0.088	-4.743
0.116	18.956		-0.092	-5.293
0.112	18.666		-0.096	-5.844
0.108	18.367		-0.100	-6.397
0.104	18.058		-0.104	-6.948
0.100	17.725		-0.108	-7.496
0.096	17.390		-0.112	-8.050
0.092	17.047		-0.116	-8.593
0.088	16.694		-0.120	-9.152
0.084	16.328		-0.124	-9.699
0.080	15.951		-0.128	-10.251
0.076	15.567		-0.132	-10.796
0.072	15.176		-0.136	-11.341
0.068	14.775		-0.140	-12.078
0.064	14.353		-0.144	-12.642
0.060	13.956		-0.148	-13.043
0.056	13.538		-0.152	-13.552
0.052	13.103		-0.156	-14.082
0.048	12.670		-0.160	-14.623
0.044	12.229		-0.164	-15.158
0.040	11.788		-0.168	-15.702
0.036	11.336		-0.172	-16.242
0.032	10.873		-0.176	-16.776
0.028	10.416		-0.180	-17.320
0.024	9.825		-0.184	-17.853
0.020	9.319		-0.188	-18.388
0.016	8.950		-0.192	-18.925
0.012	8.508		-0.196	-19.459
0.008	8.032		-0.200	-19.989
0.004	7.547			
0.000	7.051			
-0.004	6.562			

Figure D.4: Pair of values to be read into MOKEsoft as a .lmv file for the calibration for the UHV magnet at usage of maximum coil current of 0.2 A. The .lmv file consists of the descending branch of the magnets B(I) characteristic figure 4.4.

I (A)	B(mT)		I (A)	B(mT)		I (A)	B(mT)		I (A)	B(mT)
4.500	46.770		2.160	43.361		-0.180	-3.579		-2.520	-43.287
4.455	46.762		2.115	43.248		-0.225	-5.936		-2.565	-43.404
4.410	46.737		2.070	43.125		-0.270	-8.265		-2.610	-43.512
4.365	46.692		2.025	43.004		-0.315	-10.552		-2.655	-43.619
4.320	46.662		1.980	42.871		-0.360	-12.804		-2.700	-43.720
4.275	46.634		1.935	42.747		-0.405	-15.033		-2.745	-43.827
4.230	46.589		1.890	42.607		-0.450	-17.225		-2.790	-43.922
4.185	46.553		1.845	42.477		-0.495	-19.373		-2.835	-44.028
4.140	46.507		1.800	42.331		-0.540	-21.485		-2.880	-44.113
4.095	46.465		1.755	42.187		-0.585	-23.554		-2.925	-44.211
4.050	46.425		1.710	42.030		-0.630	-25.575		-2.970	-44.309
4.005	46.382		1.665	41.880		-0.675	-27.524		-3.015	-44.396
3.960	46.343		1.620	41.722		-0.720	-29.423		-3.060	-44.486
3.915	46.289		1.575	41.554		-0.765	-31.236		-3.105	-44.578
3.870	46.241		1.530	41.385		-0.810	-32.918		-3.150	-44.666
3.825	46.195		1.485	41.212		-0.855	-34.288		-3.195	-44.749
3.780	46.148		1.440	41.029		-0.900	-35.262		-3.240	-44.830
3.735	46.094		1.395	40.841		-0.945	-35.957		-3.285	-44.913
3.690	46.042		1.350	40.641		-0.990	-36.492		-3.330	-44.992
3.645	45.988		1.305	40.439		-1.035	-36.946		-3.375	-45.074
3.600	45.936		1.260	40.227		-1.080	-37.346		-3.420	-45.152
3.555	45.880		1.215	40.010		-1.125	-37.698		-3.465	-45.223
3.510	45.813		1.170	39.776		-1.170	-38.025		-3.510	-45.304
3.465	45.765		1.125	39.531		-1.215	-38.328		-3.555	-45.374
3.420	45.702		1.080	39.282		-1.260	-38.599		-3.600	-45.447
3.375	45.641		1.035	39.022		-1.305	-38.863		-3.645	-45.519
3.330	45.581		0.990	38.730		-1.350	-39.107		-3.690	-45.590
3.285	45.510		0.945	38.423		-1.395	-39.342		-3.735	-45.657
3.240	45.452		0.900	38.102		-1.440	-39.569		-3.780	-45.720
3.195	45.386		0.855	37.743		-1.485	-39.785		-3.825	-45.788
3.150	45.323		0.810	37.337		-1.530	-39.993		-3.870	-45.858
3.105	45.241		0.765	36.882		-1.575	-40.196		-3.915	-45.916
3.060	45.172		0.720	36.343		-1.620	-40.400		-3.960	-45.978
3.015	45.105		0.675	35.665		-1.665	-40.575		-4.005	-46.040
2.970	45.028		0.630	34.756		-1.710	-40.760		-4.050	-46.102
2.925	44.948		0.585	33.512		-1.755	-40.939		-4.095	-46.165
2.880	44.871		0.540	31.932		-1.800	-41.103		-4.140	-46.216
2.835	44.794		0.495	30.124		-1.845	-41.265		-4.185	-46.273
2.790	44.716		0.450	28.184		-1.890	-41.433		-4.230	-46.327
2.745	44.629		0.405	26.134		-1.935	-41.580		-4.275	-46.383
2.700	44.543		0.360	24.005		-1.980	-41.739		-4.320	-46.445
2.655	44.456		0.315	21.826		-2.025	-41.882		-4.365	-46.495
2.610	44.366		0.270	19.596		-2.070	-42.026		-4.410	-46.545
2.565	44.276		0.225	17.358		-2.115	-42.172		-4.455	-46.598
2.520	44.187		0.180	15.093		-2.160	-42.308		-2.520	-43.287
2.475	44.085		0.135	12.812		-2.205	-42.441		-2.565	-43.404
2.430	43.999		0.090	10.506		-2.250	-42.568		-2.610	-43.512
2.385	43.891		0.045	8.202		-2.295	-42.701		-2.655	-43.619
2.340	43.797		0.000	5.864		-2.340	-42.818		-2.700	-43.720
2.295	43.695		-0.045	3.623		-2.385	-42.938			
2.250	43.582		-0.090	1.217		-2.430	-43.056			
2.205	43.470		-0.135	-1.179		-2.475	-43.167			

Figure D.5: MOKEsoft .lmv file calibration pair of values for usage of the yoke assembled with the pole shoes displayed in figure E.4 resulting in a 32 mm large magnet slot.

I (A)	B(mT)		I (A)	B(mT)		I (A)	B(mT)		I (A)	B(mT)
4.500	42.240		2.160	39.069		-0.180	-3.297		-2.520	-39.100
4.455	42.242		2.115	38.963		-0.225	-5.378		-2.565	-39.200
4.410	42.212		2.070	38.849		-0.270	-7.426		-2.610	-39.302
4.365	42.186		2.025	38.740		-0.315	-9.454		-2.655	-39.404
4.320	42.155		1.980	38.618		-0.360	-11.454		-2.700	-39.493
4.275	42.121		1.935	38.499		-0.405	-13.424		-2.745	-39.591
4.230	42.087		1.890	38.376		-0.450	-15.361		-2.790	-39.686
4.185	42.055		1.845	38.240		-0.495	-17.261		-2.835	-39.774
4.140	42.015		1.800	38.114		-0.540	-19.139		-2.880	-39.862
4.095	41.975		1.755	37.981		-0.585	-20.973		-2.925	-39.952
4.050	41.935		1.710	37.837		-0.630	-22.765		-2.970	-40.041
4.005	41.885		1.665	37.699		-0.675	-24.515		-3.015	-40.126
3.960	41.852		1.620	37.542		-0.720	-26.204		-3.060	-40.202
3.915	41.804		1.575	37.391		-0.765	-27.830		-3.105	-40.285
3.870	41.761		1.530	37.238		-0.810	-29.366		-3.150	-40.373
3.825	41.711		1.485	37.067		-0.855	-30.660		-3.195	-40.445
3.780	41.667		1.440	36.893		-0.900	-31.616		-3.240	-40.518
3.735	41.619		1.395	36.721		-0.945	-32.305		-3.285	-40.604
3.690	41.581		1.350	36.541		-0.990	-32.817		-3.330	-40.670
3.645	41.522		1.305	36.358		-1.035	-33.238		-3.375	-40.745
3.600	41.475		1.260	36.167		-1.080	-33.611		-3.420	-40.824
3.555	41.417		1.215	35.964		-1.125	-33.944		-3.465	-40.894
3.510	41.368		1.170	35.745		-1.170	-34.236		-3.510	-40.956
3.465	41.315		1.125	35.519		-1.215	-34.510		-3.555	-41.025
3.420	41.262		1.080	35.289		-1.260	-34.779		-3.600	-41.089
3.375	41.199		1.035	35.036		-1.305	-35.020		-3.645	-41.158
3.330	41.140		0.990	34.768		-1.350	-35.245		-3.690	-41.223
3.285	41.077		0.945	34.490		-1.395	-35.465		-3.735	-41.288
3.240	41.021		0.900	34.177		-1.440	-35.670		-3.780	-41.343
3.195	40.958		0.855	33.841		-1.485	-35.872		-3.825	-41.408
3.150	40.897		0.810	33.470		-1.530	-36.064		-3.870	-41.467
3.105	40.834		0.765	33.034		-1.575	-36.251		-3.915	-41.529
3.060	40.764		0.720	32.507		-1.620	-36.430		-3.960	-41.585
3.015	40.702		0.675	31.832		-1.665	-36.599		-4.005	-41.646
2.970	40.625		0.630	30.913		-1.710	-36.766		-4.050	-41.702
2.925	40.556		0.585	29.680		-1.755	-36.928		-4.095	-41.757
2.880	40.481		0.540	28.211		-1.800	-37.090		-4.140	-41.819
2.835	40.408		0.495	26.562		-1.845	-37.238		-4.185	-41.859
2.790	40.331		0.450	24.808		-1.890	-37.383		-4.230	-41.919
2.745	40.257		0.405	22.979		-1.930	-37.529		-4.275	-41.969
2.700	40.182		0.360	21.085		-1.980	-37.663		-4.320	-42.020
2.655	40.097		0.315	19.152		-2.025	-37.803		-4.365	-42.064
2.610	40.017		0.270	17.182		-2.070	-37.930		-4.410	-42.119
2.565	39.928		0.225	15.198		-2.115	-38.065		-4.455	-42.164
2.520	39.842		0.180	13.197		-2.160	-38.182			
2.475	39.752		0.135	11.170		-2.205	-38.307			
2.430	39.662		0.090	9.140		-2.250	-38.425			
2.385	39.564		0.045	7.103		-2.295	-38.545			
2.340	39.477		0.000	5.039		-2.340	-38.660			
2.295	39.373		-0.045	3.049		-2.385	-38.771			
2.250	39.275		-0.090	0.932		-2.430	-38.884			
2.205	39.168		-0.135	-1.184		-2.475	-38.985			

Figure D.6: Same issue as previous figure, but with magnet assembled with the pole shoes displayed in figure E.6 resulting in a magnet slot of 38 mm.

Compensation for Hysteresis of the Electromagnet

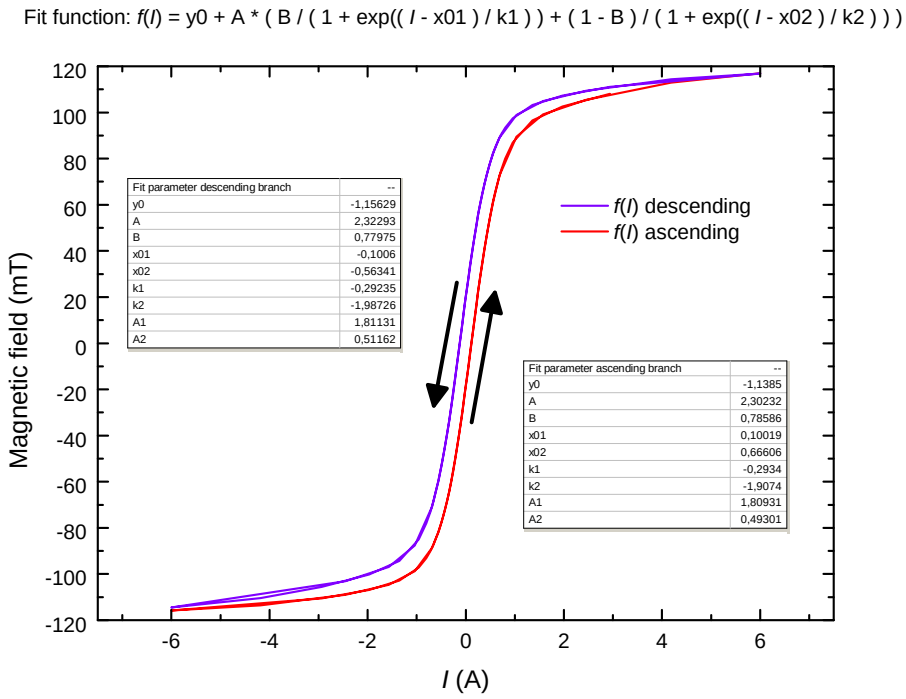

Figure D.7: Magnetic field B vs. coil current I of MOKE magnet reproduced by the double Boltzmann function f(I) for a max. current of I=6 A. The ascending and descending branch are reproduced by the parameters of f, as each indicated in the plot. These functions are used to calculate the magnetic field of the MOKE magnet considering the hysteresis of the yoke of the magnet.

As shown in figure 4.4 the magnet of the MOKE setup shows a $B(I)$ hysteresis behavior itself, due to the used iron yoke. For this hysteresis of the yoke it is not compensated for automatically, neither in the automatization software MOKEsoft (see Sec. 4.5), nor in the .lmv calibration files for MOKEsoft (see previous section D). If no such compensation takes place an artificially hysteresis splitting, or a shear of a hysteresis is observed. So the compensation is performed manually upon data evaluation. Therefore the magnetic fields of the MOKE magnet are calculated from the coil currents I with different formulas for increasing and decreasing I. The conversion formula have been achieved by fitting the ascending and the descending $B(I)$ branches of figure 4.4. This procedure is only performed for the curve with the maximum I of 6 A, since in all measurements of this thesis the maximum obtainable magnetic field is used. A fit with a double Boltzmann function $f(I)$ is

found to fit this curve best. The fit (fit function, fit parameter, and plot) is presented in figure D.7. The MOKE data shown in chapter 6 and chapter 9 is corrected with help of this formulas.

E Construction Plans

This chapter hosts the construction plans of components for the MOKE setup, namely the magnet, detector parts and laser stage. Yoke parts are constructed out of American Rolling Mill Company (ARMCO) pure iron and post processed by vacuum annealing to enhance the irons susceptibility. Annealing of the ARMCO iron parts is performed at 1100 K under vacuum conditions for three hours and then slowly cooled down with a rate of 1 K per minute. Thereby the permeability of the iron is raised by a factor of three, as verified with a practical course setup. All other parts are constructed of nonmagnetic stainless steel, or aluminum, Teflon®, or PVC. The dimensions of the magnets yoke are optimized to fit into the LT-STM preparation chamber and to be compatible with the utilized sample holders. The design of the MOKE detector is realized following a design of a MOKE setup from H. P. Oepen [130].
All plans presented here have been handed to the mechanical workshop of the II. Physikalisches Institut, who constructed the mechanical components.

Last drawings of the LT-STM UHV system have been included by courtesy of Sven Zöphel from SPS-CreaTec GmbH [121]. The MOKE components are mounted at the B-B cut of figure E.32 to the LT-STM system.

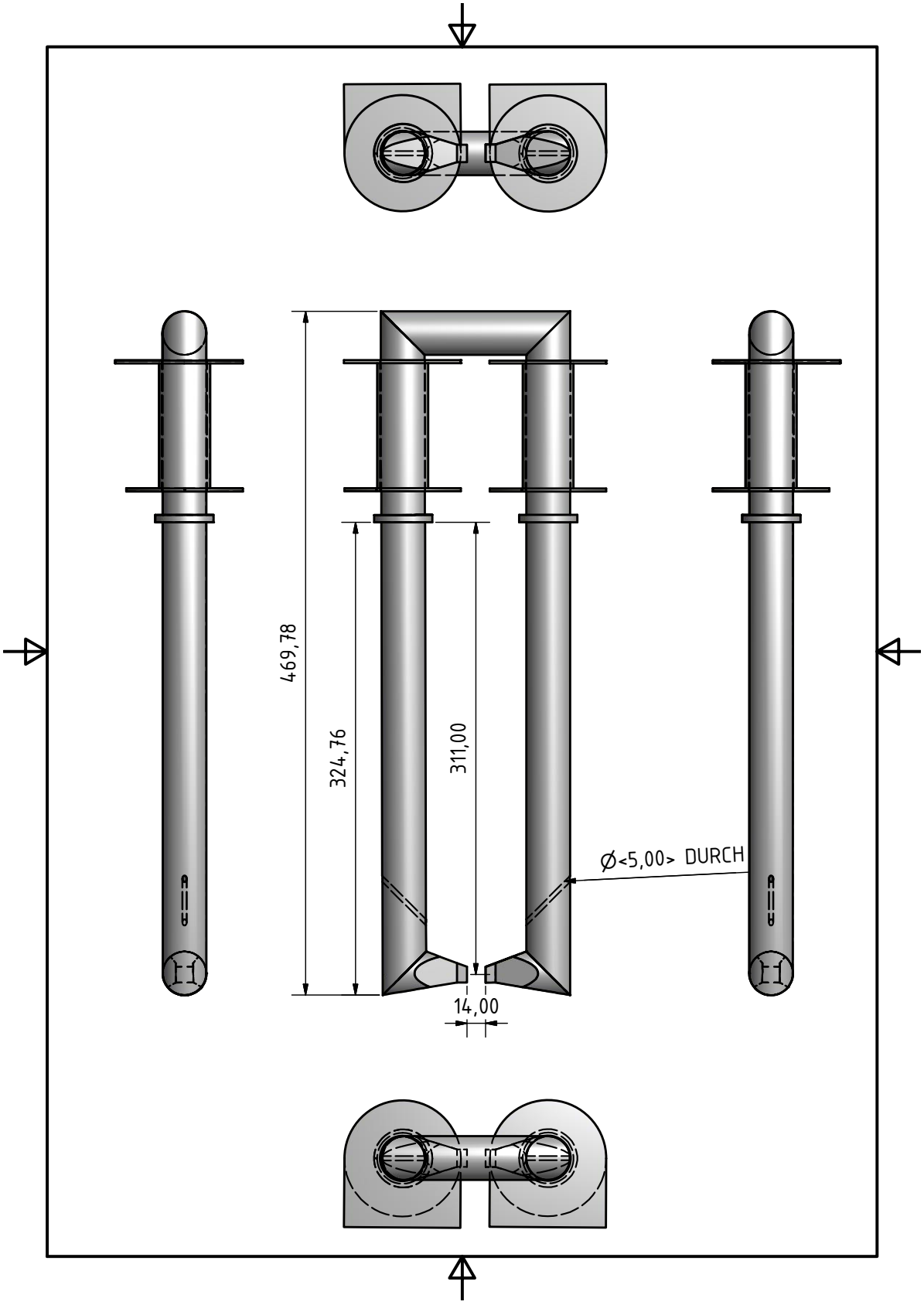

Figure E.1: CAD sketch of the yoke of electromagnet assembly composed of two legs, two pole shoes, connection part and coil winding former. The displayed configuration results in a sample holder slot of 14 mm. The this way assembled magnet is mounted to the preparation chamber of the LT-STM system.

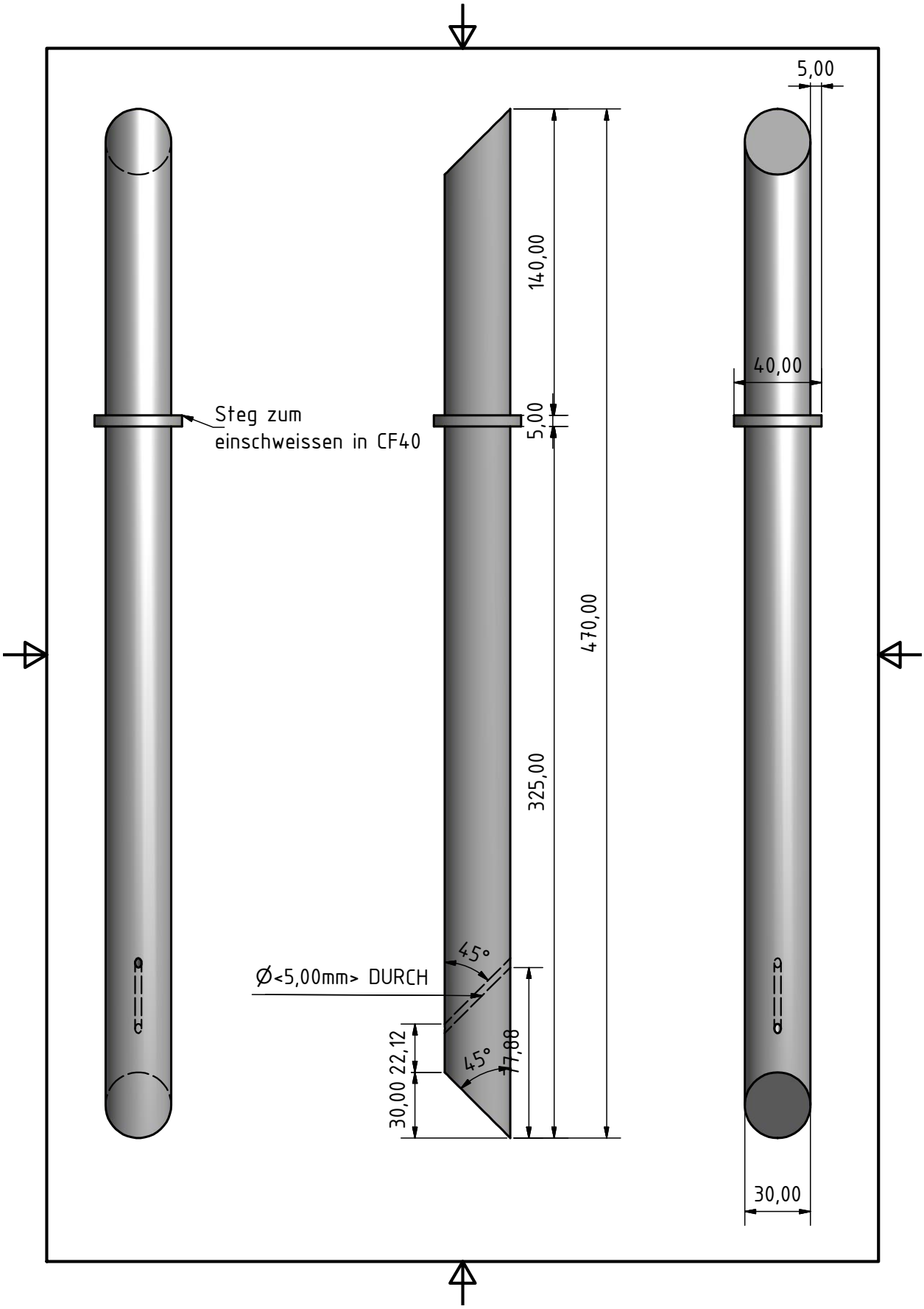

Figure E.2: CAD sketch of yoke legs of electromagnet. Holes of 5 mm diameter for the optical path of the laser are visible.

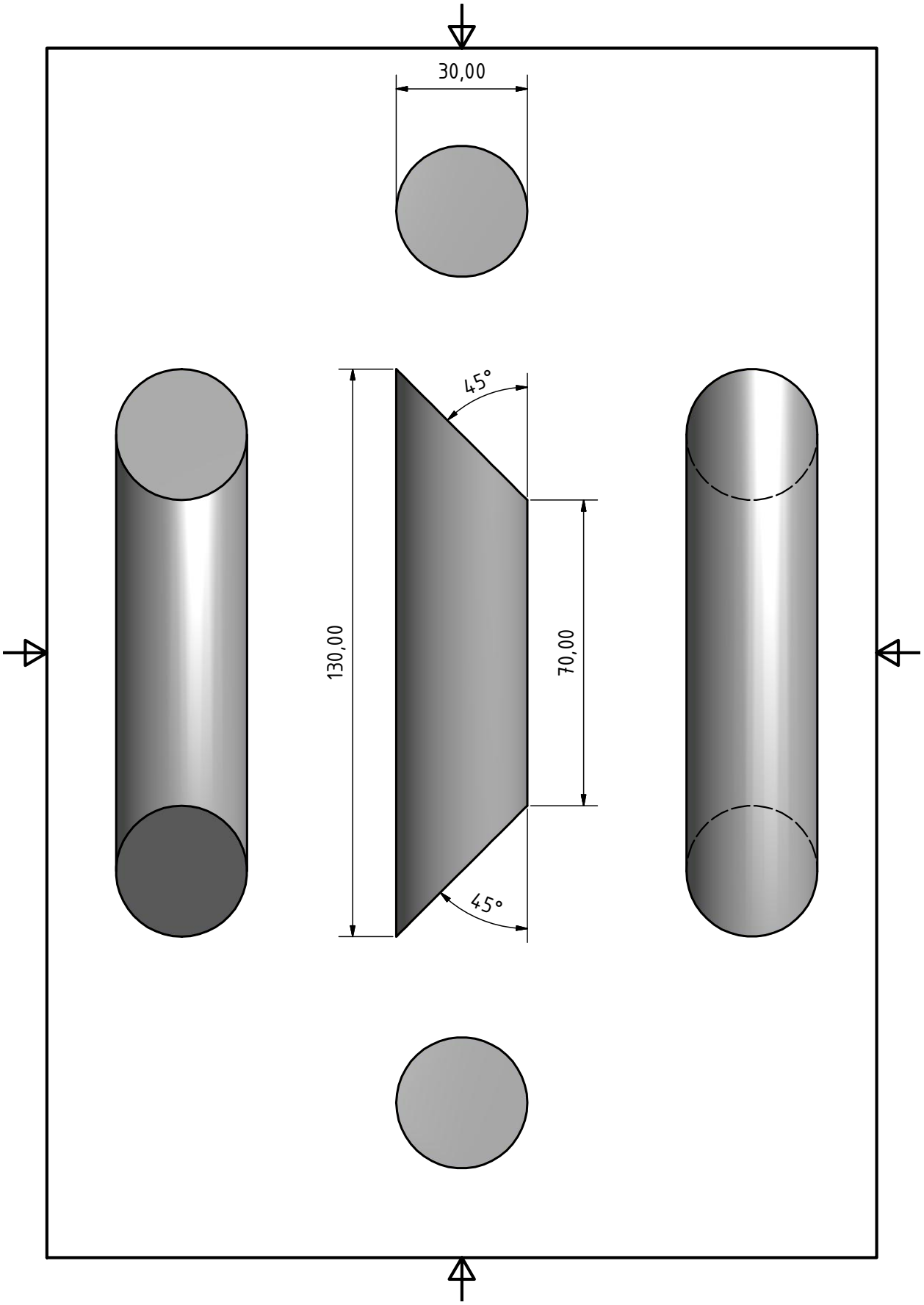

Figure E.3: CAD sketch of yoke connection part.

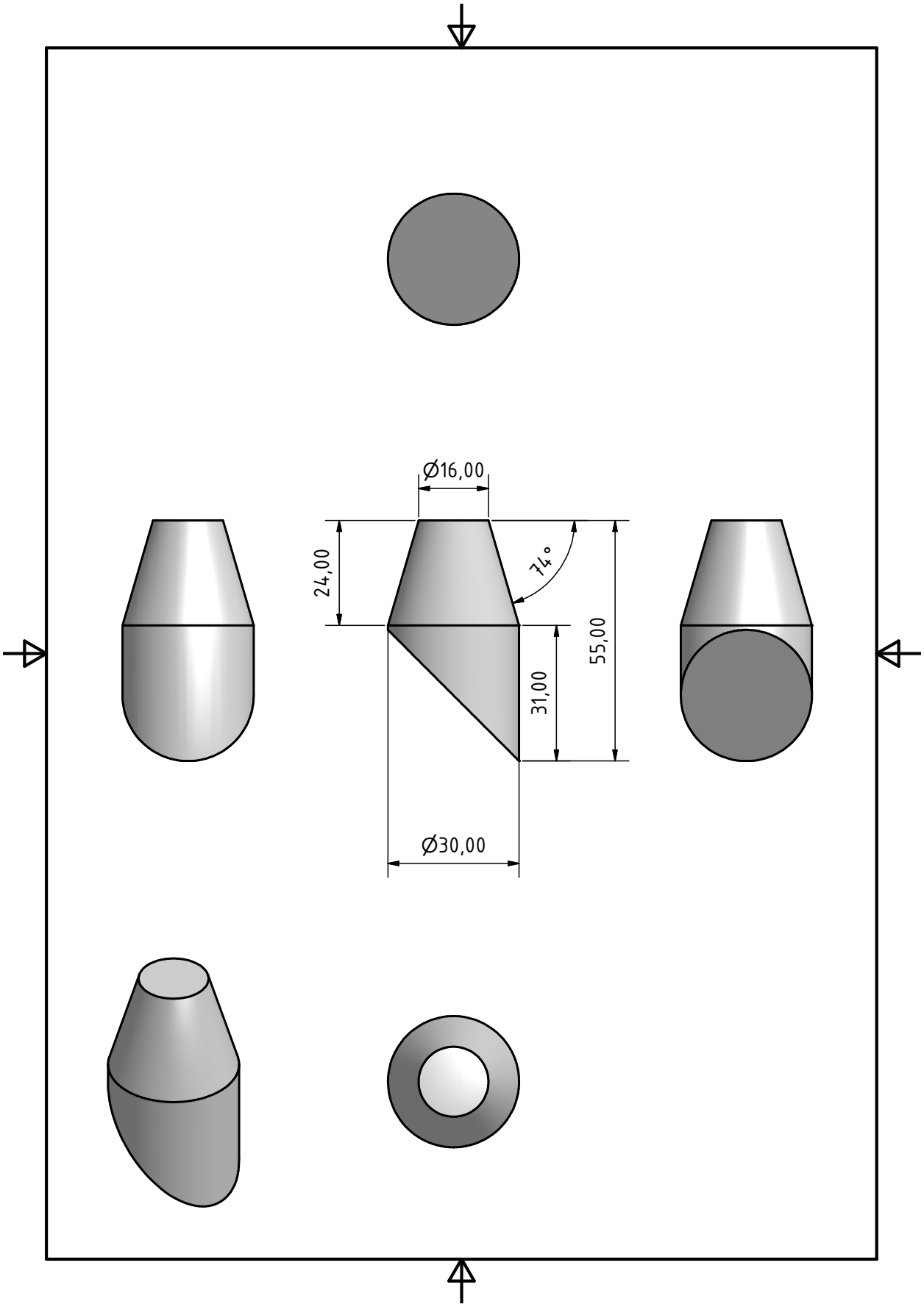

Figure E.4: CAD sketch of yokes pole shoes (first edition). A sample slot with a width of 32 mm in the electromagnet is gained by usage of this pole shoes.

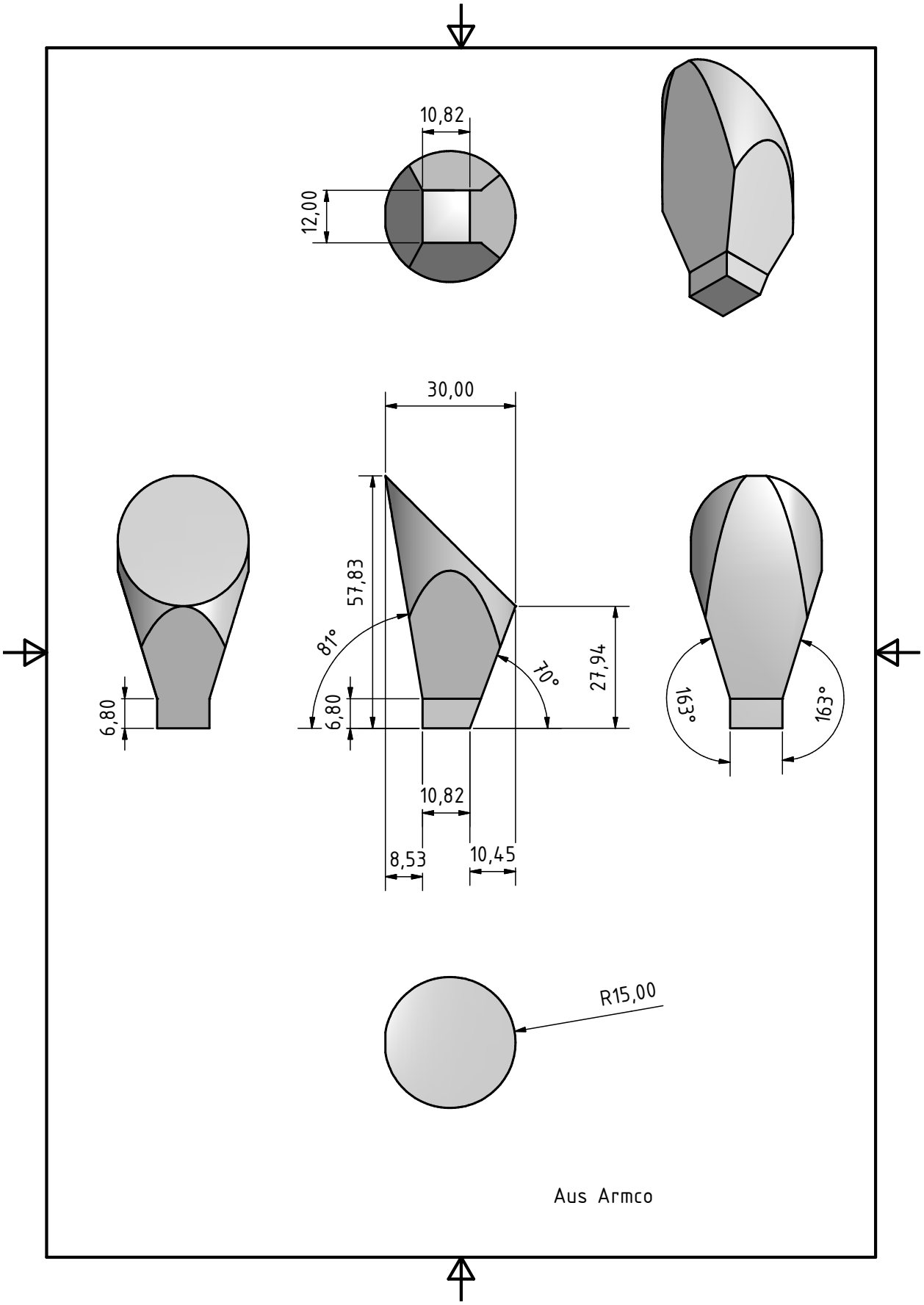

Figure E.5: CAD sketch of yoke pole shoe (second edition). Results in the complete magnet assembly as shown in figure E.1 with a sample slot width of 14 mm, as used on the magnet mounted to the LT-STM chamber.

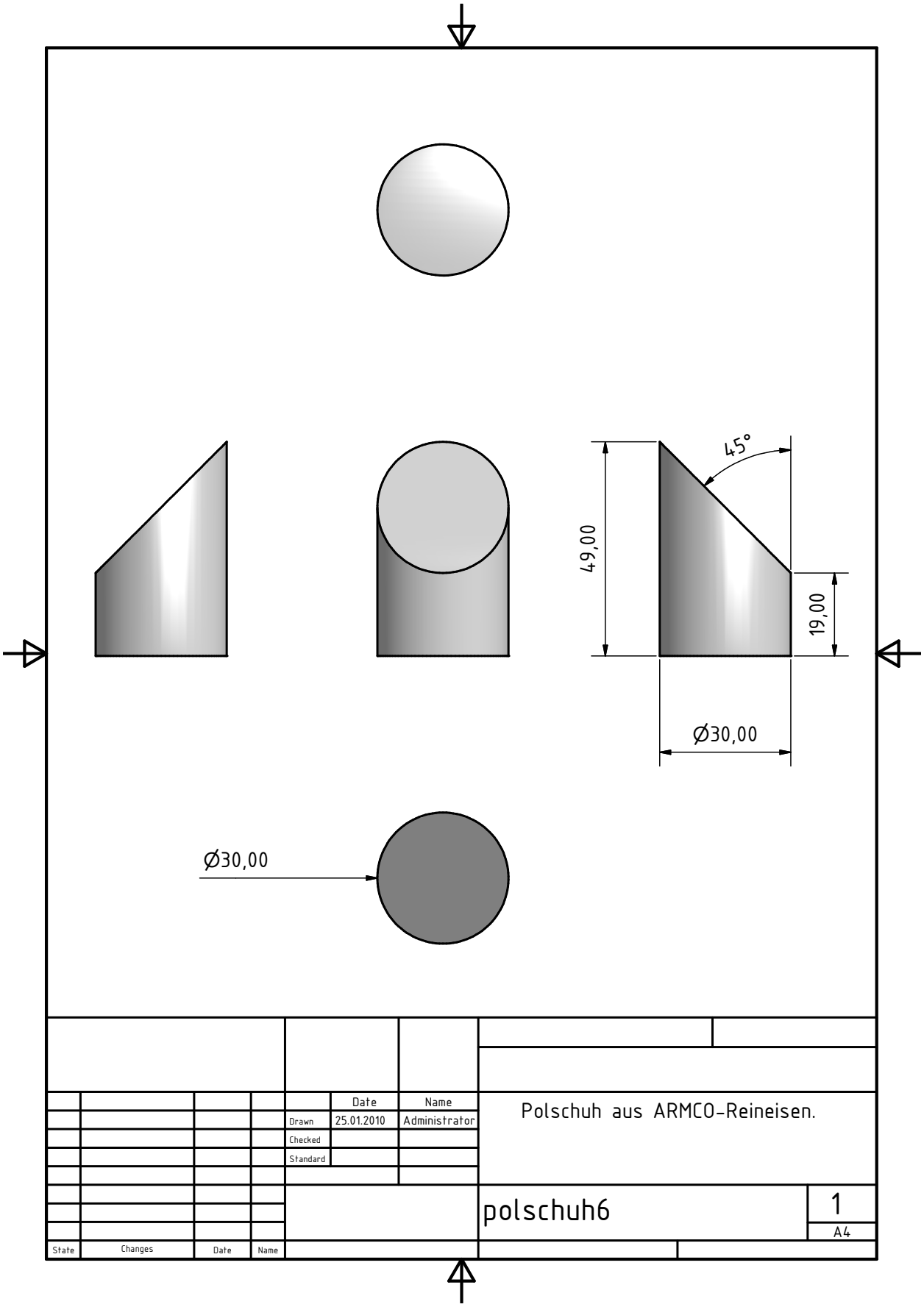

Figure E.6: CAD sketch of yoke pole shoe (third edition), resulting in a magnet slot of 38 mm. The designed is optimized to generate very homogenous magnetic fields.

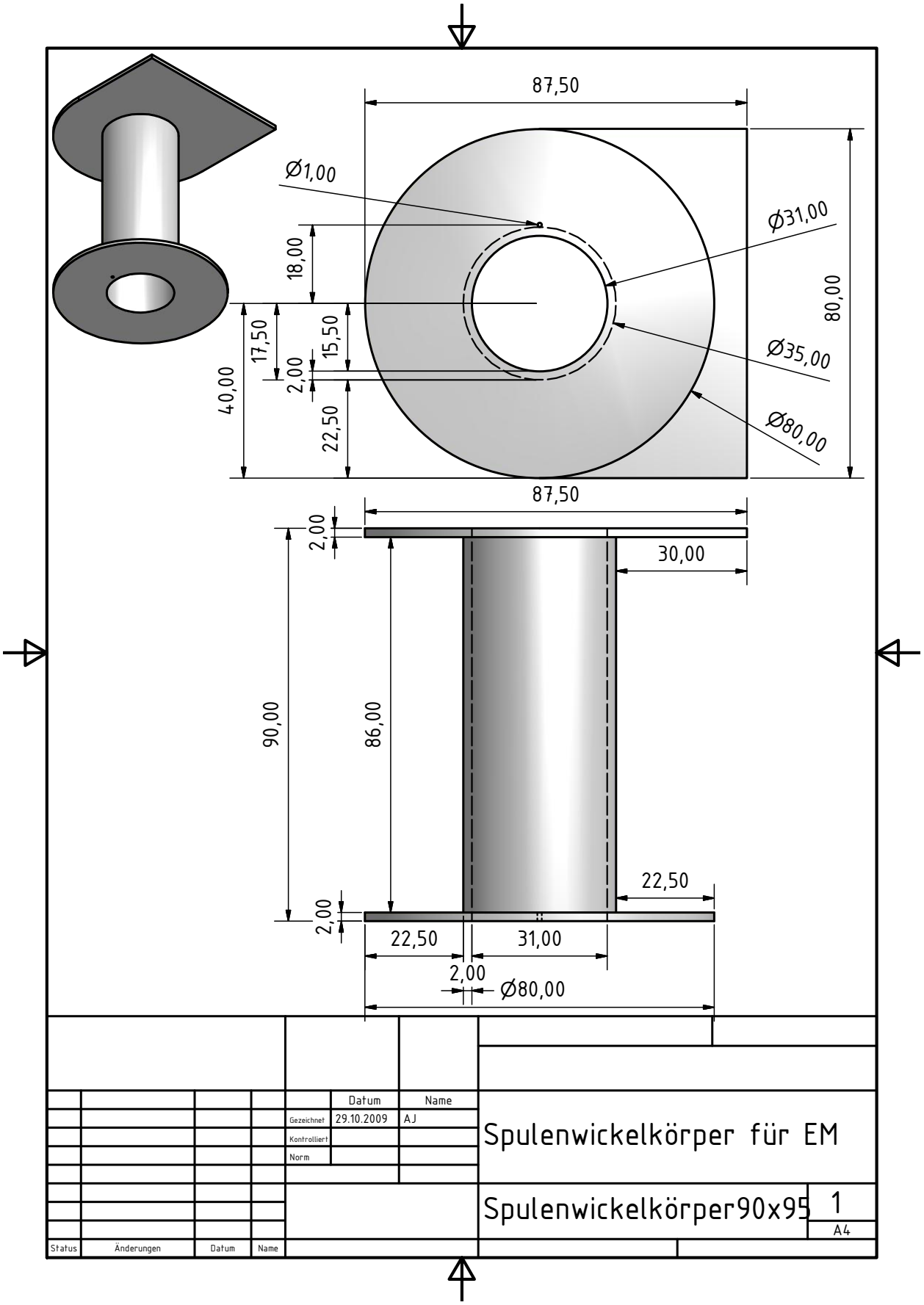

Figure E.7: CAD sketch of coil base part made out of aluminum. Designed to be plugged onto the legs of the yoke and to be compatible with VAT linear translation stages LDK40-100.

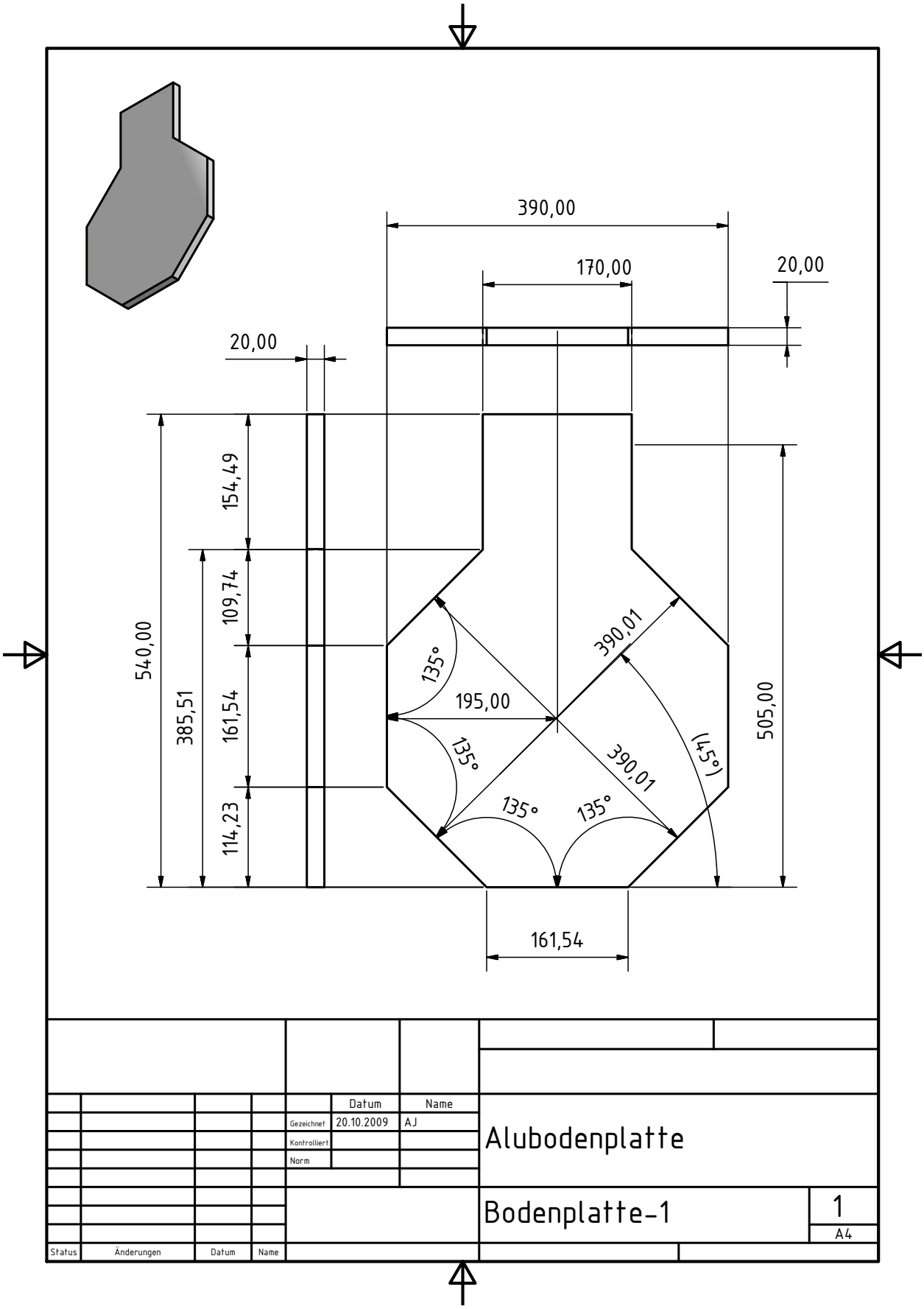

Figure E.8: CAD sketch of the aluminium base plate of MOKE ambient conditions construction.

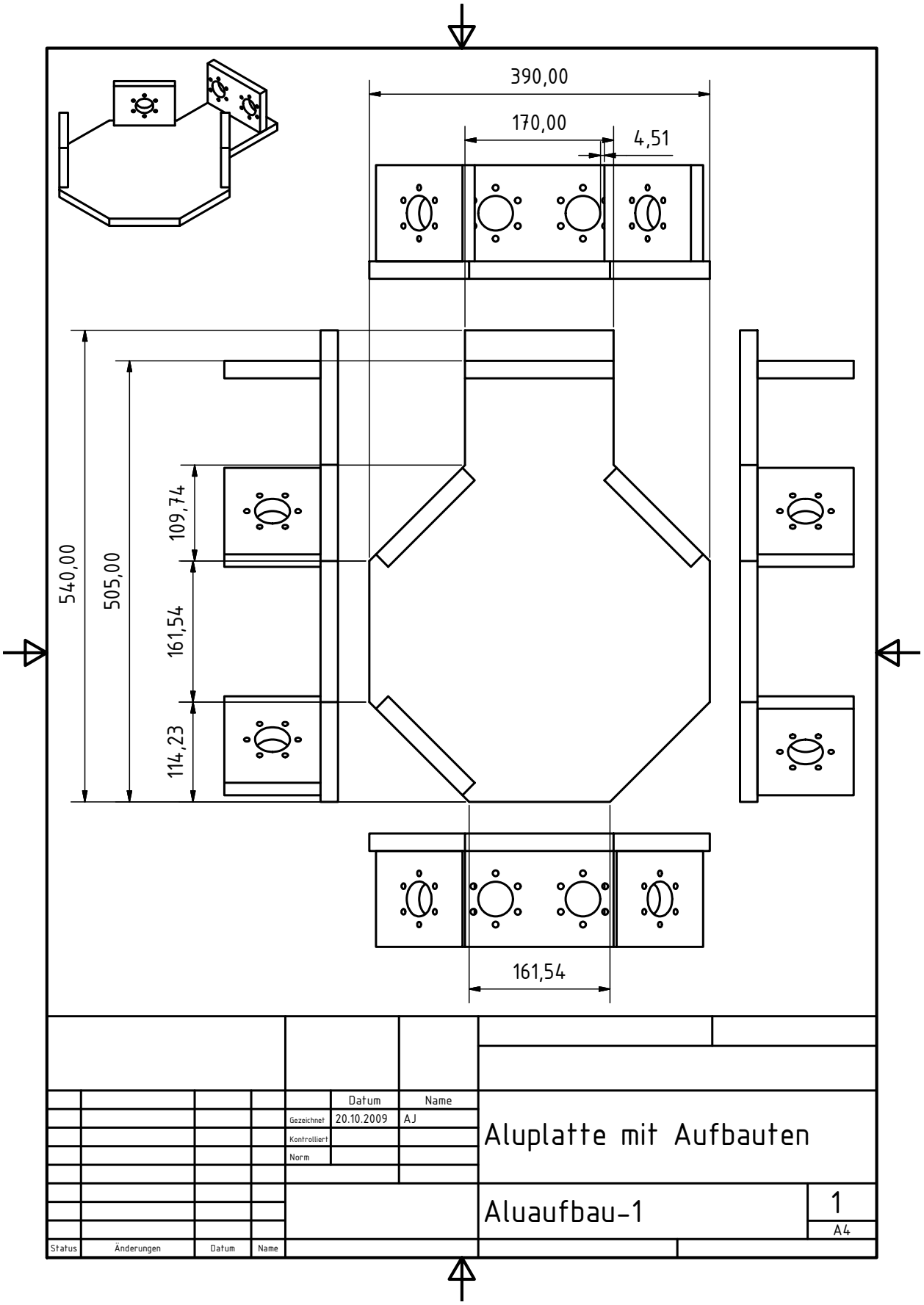

Figure E.9: CAD sketch of aluminium base plate for MOKE ambient conditions setup representing. It represents a cross section of the LT-STM system, compare the B-B cut of figure. E.32. The attached build-ups represent DN40CF flanges.

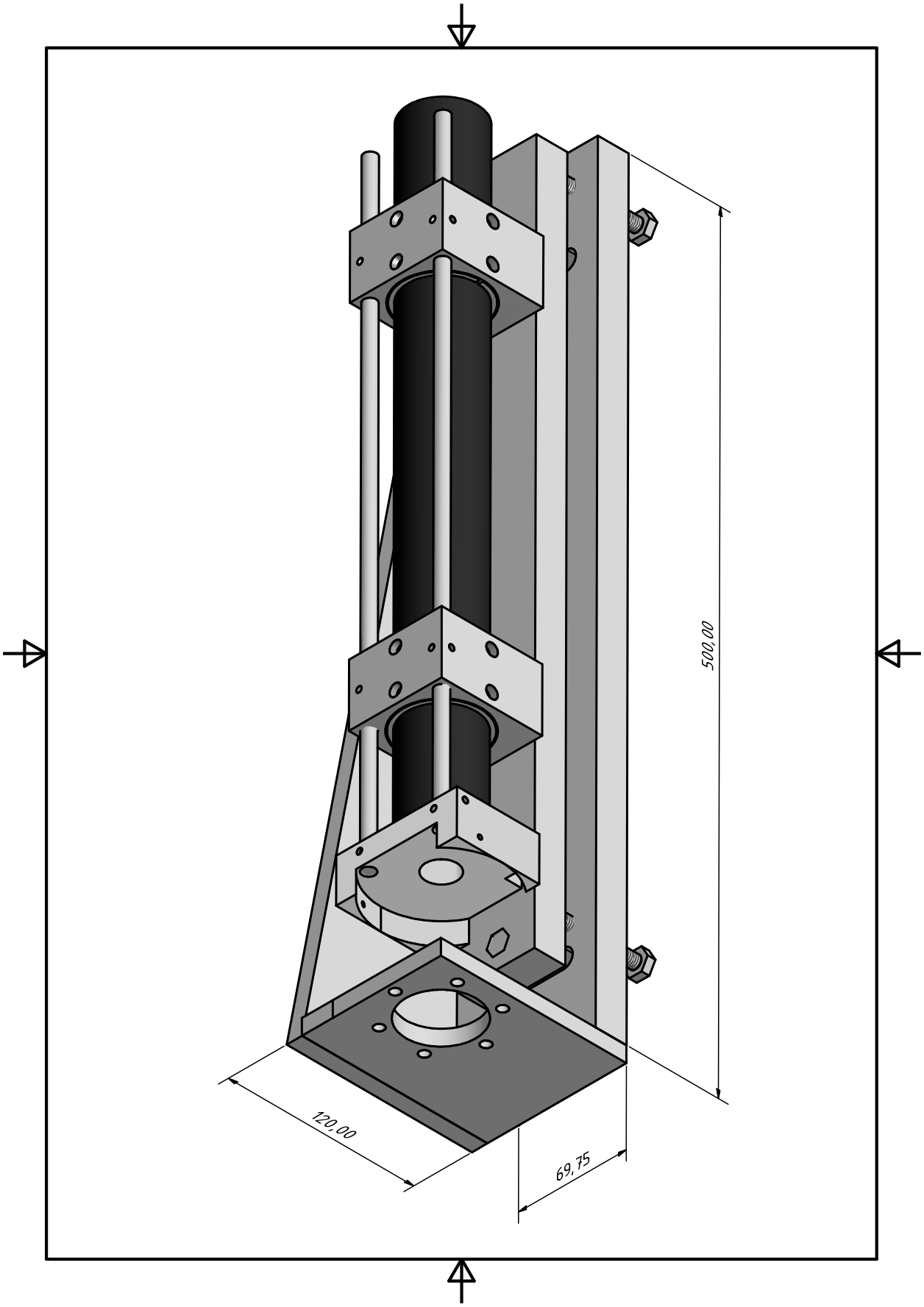

Figure E.10: Laser holder assembly with adjustment elements 3D representation. The technical drawings of the single parts are shown on the next pages.

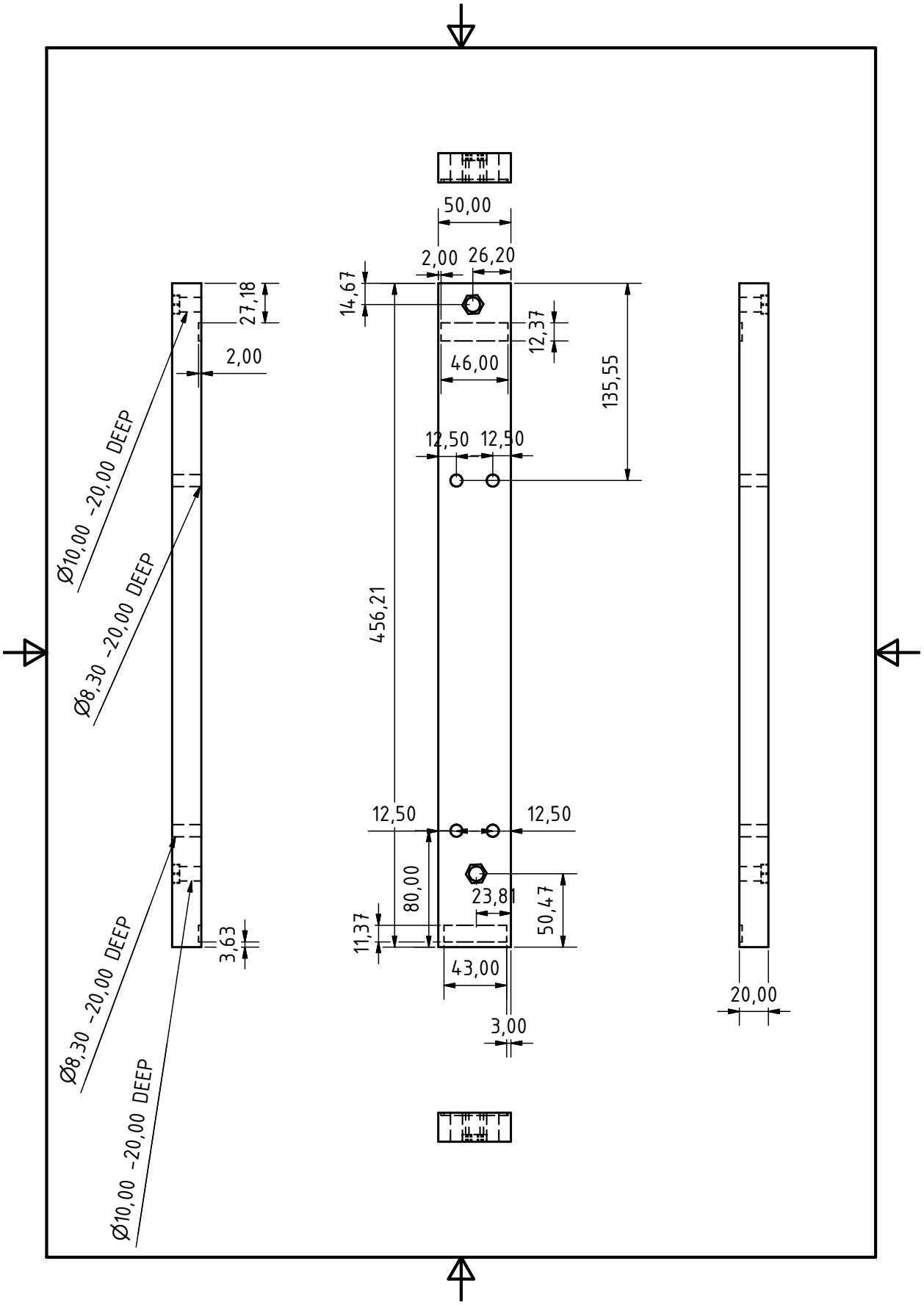

Figure E.11: CAD sketch of laser carrier plate.

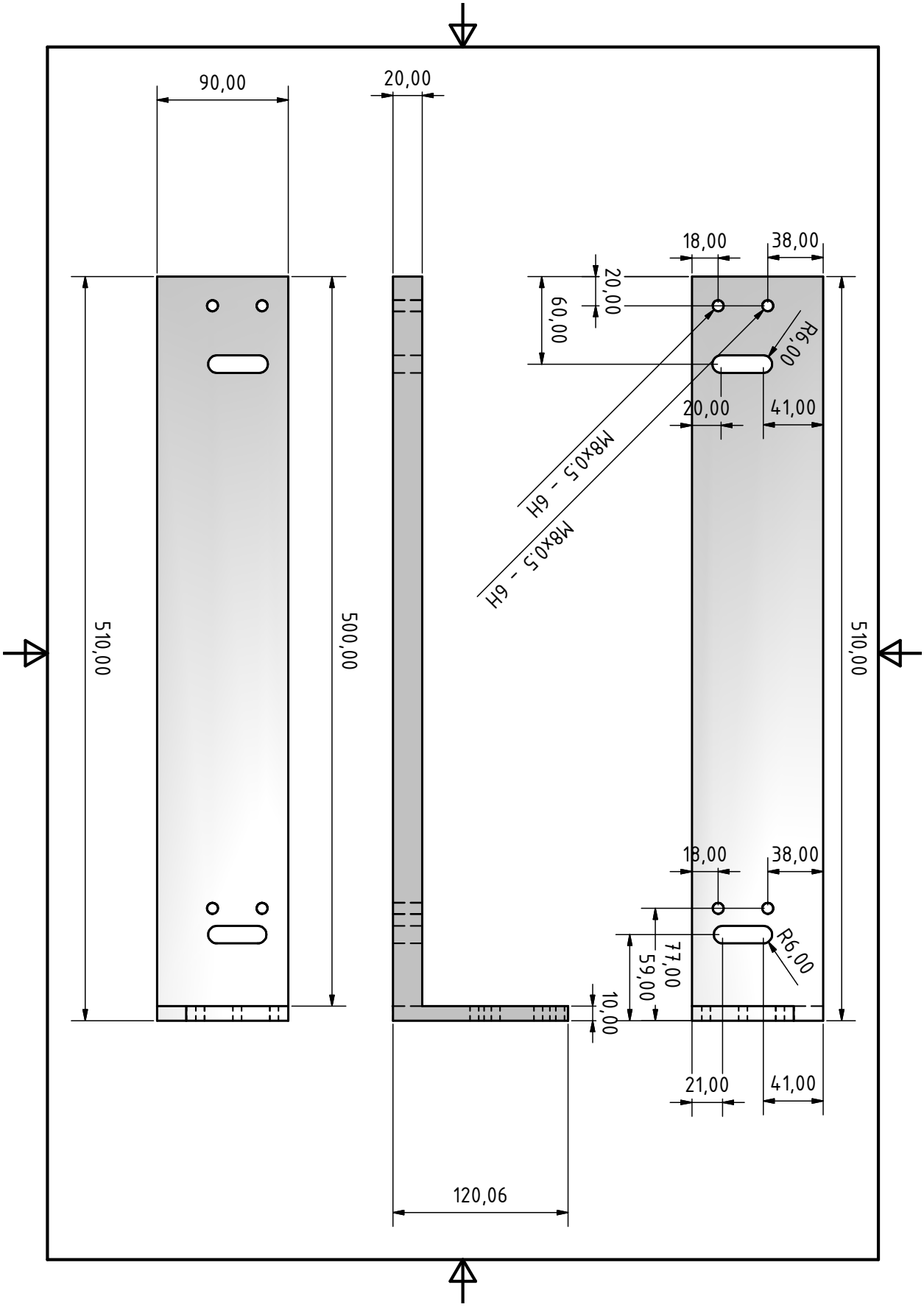

Figure E.12: CAD sketch of laser holder base plate with mounting station to CF40 flange.

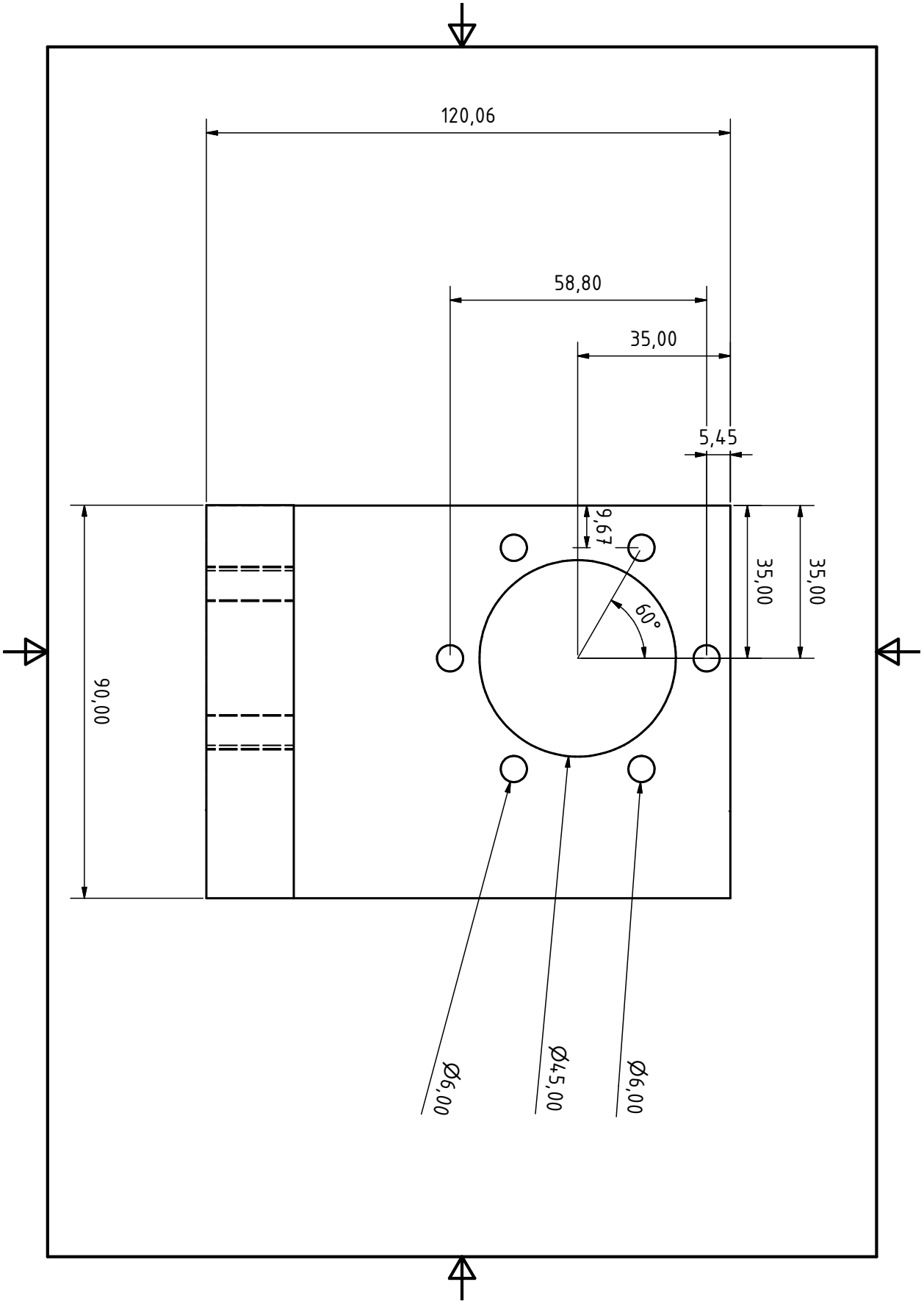

Figure E.13: CAD sketch of mounting to CF40 flange part.

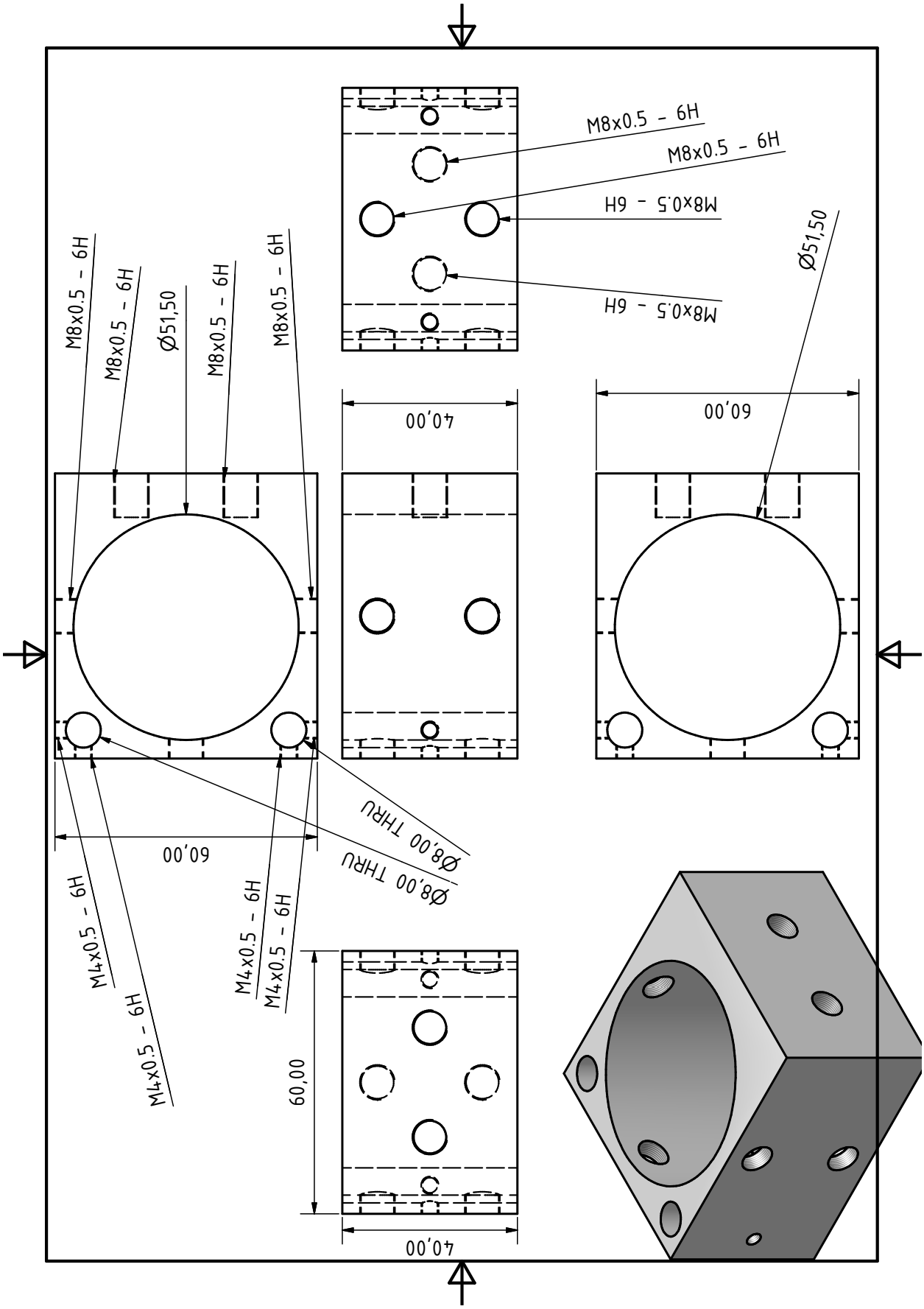

Figure E.14: CAD sketch of laser to carrier plate connection cube.

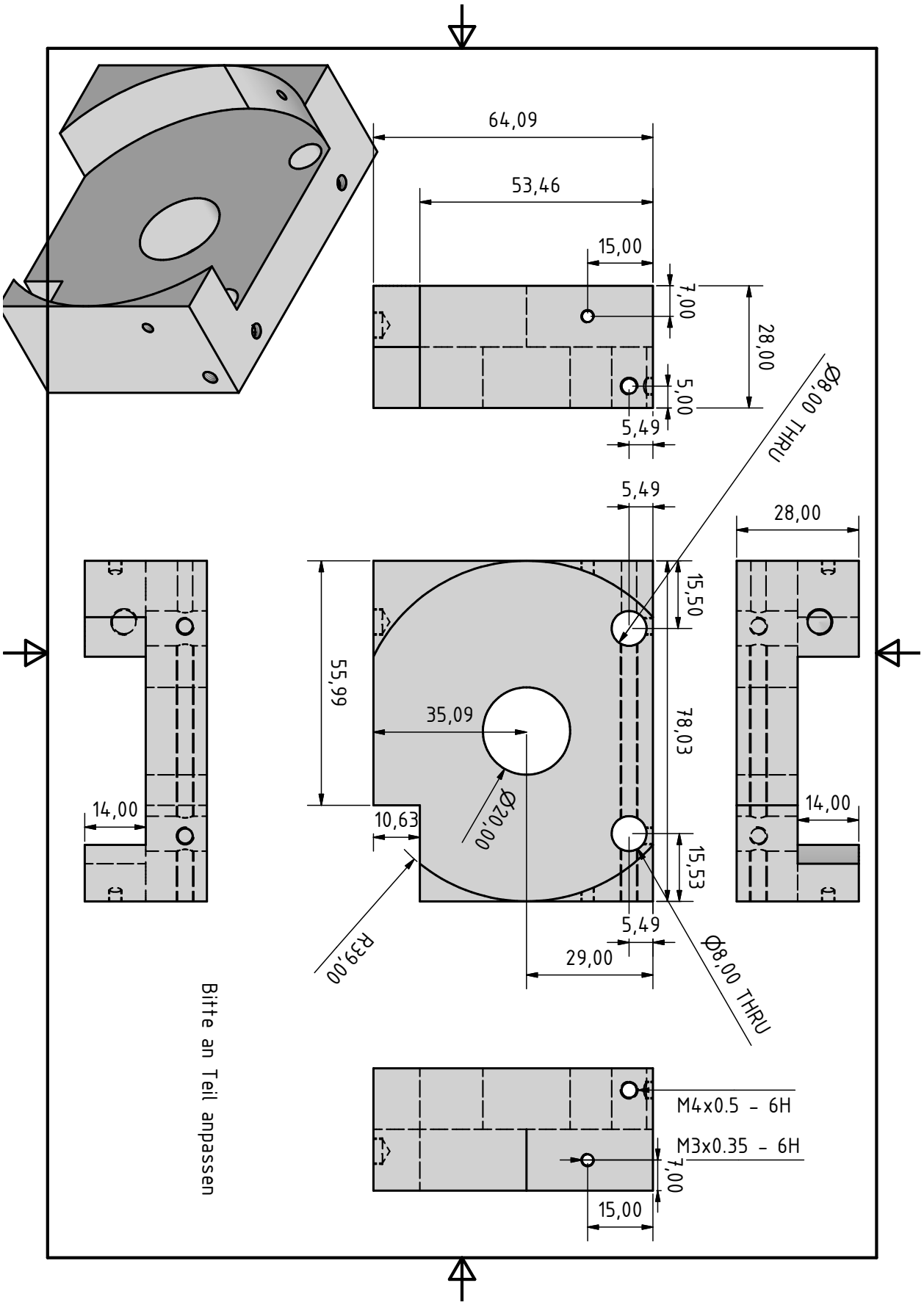

Figure E.15: CAD sketch of socket for high precision rotation optic holder.

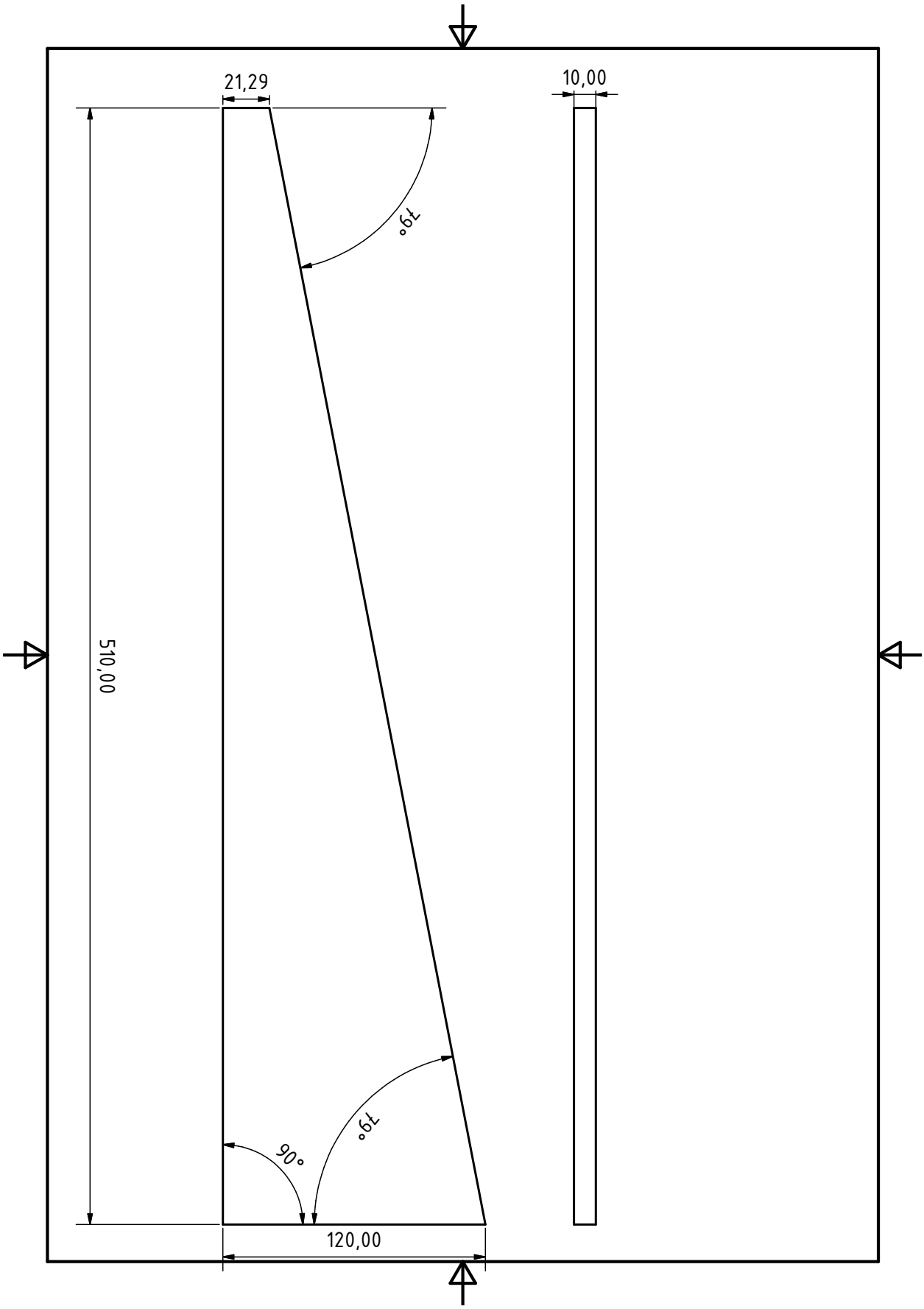

Figure E.16: CAD sketch of stiffener side part of the laser holder.

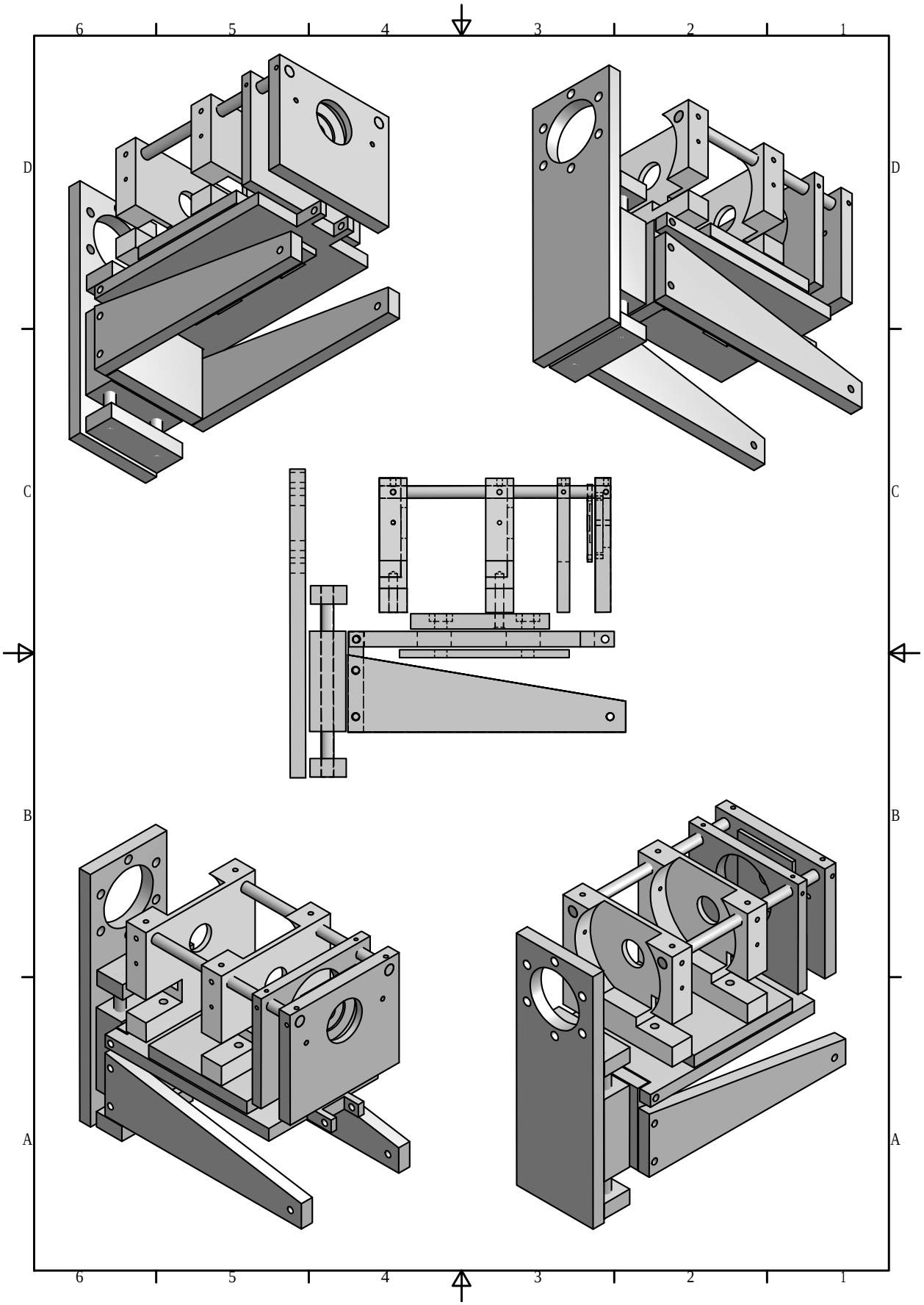

Figure E.17: Detector assembly. The technical drawings of the single parts are presented on the following pages.

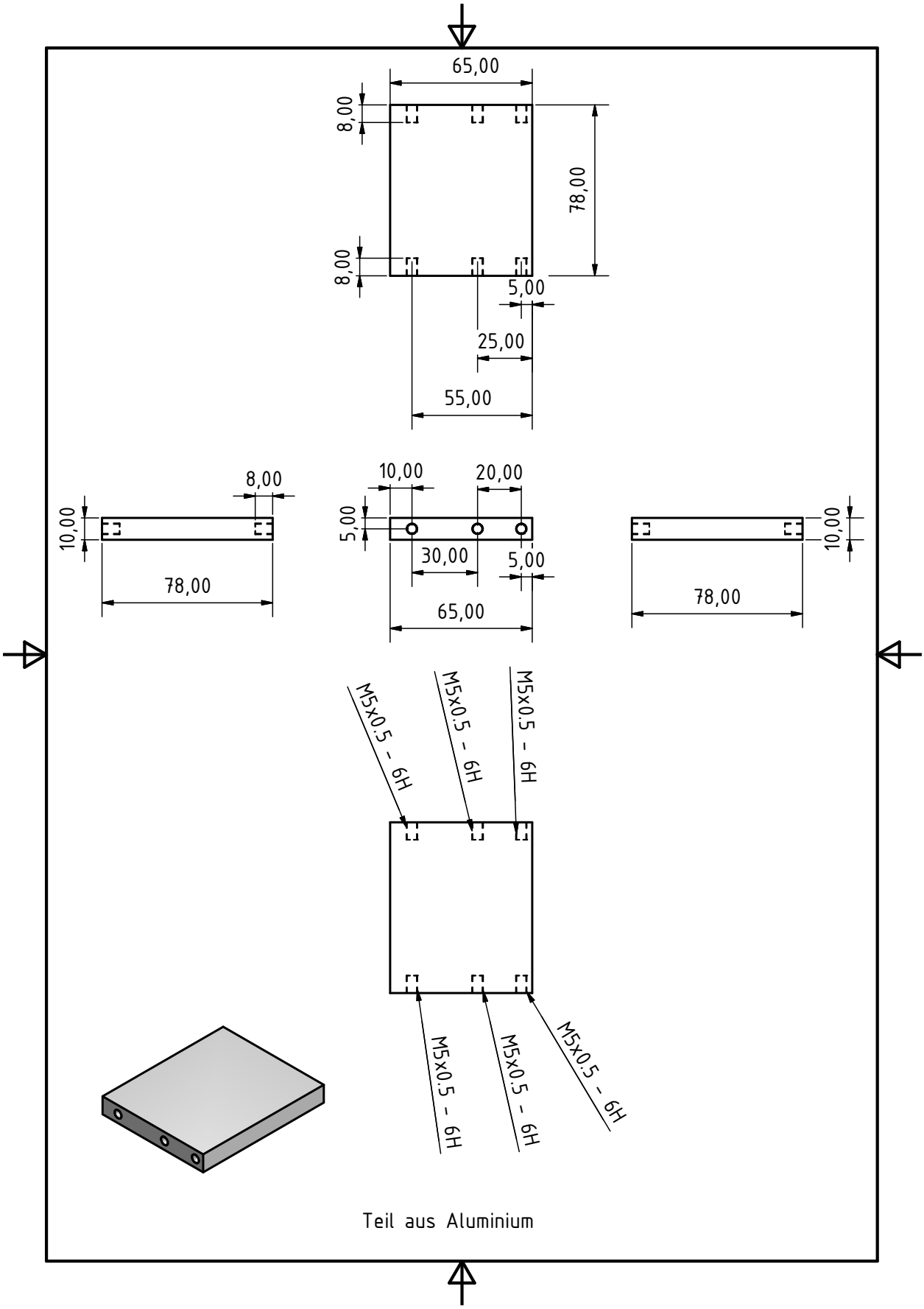

Figure E.18: CAD sketch of detector tilting component.

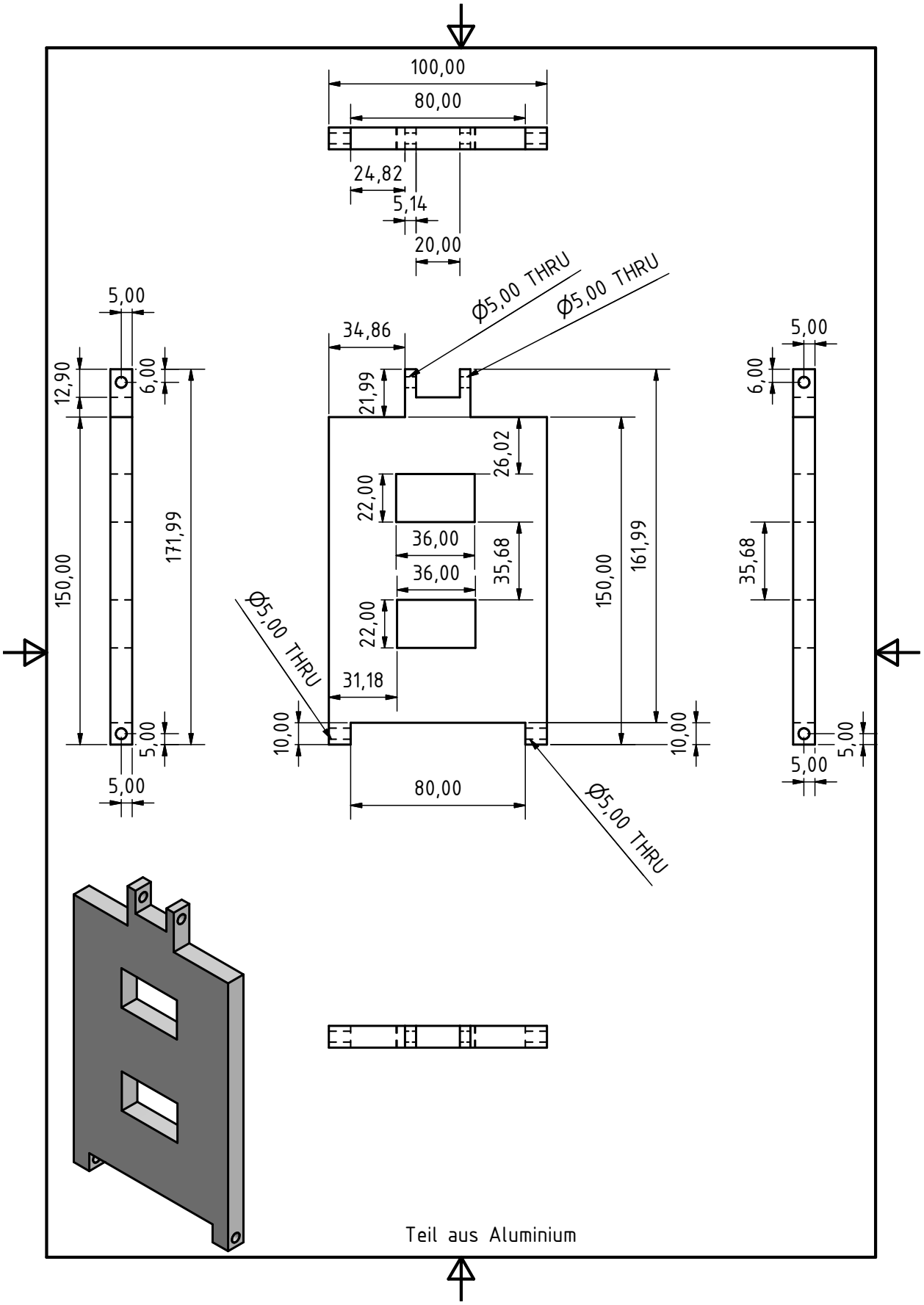

Figure E.19: CAD sketch of detector second tilting component

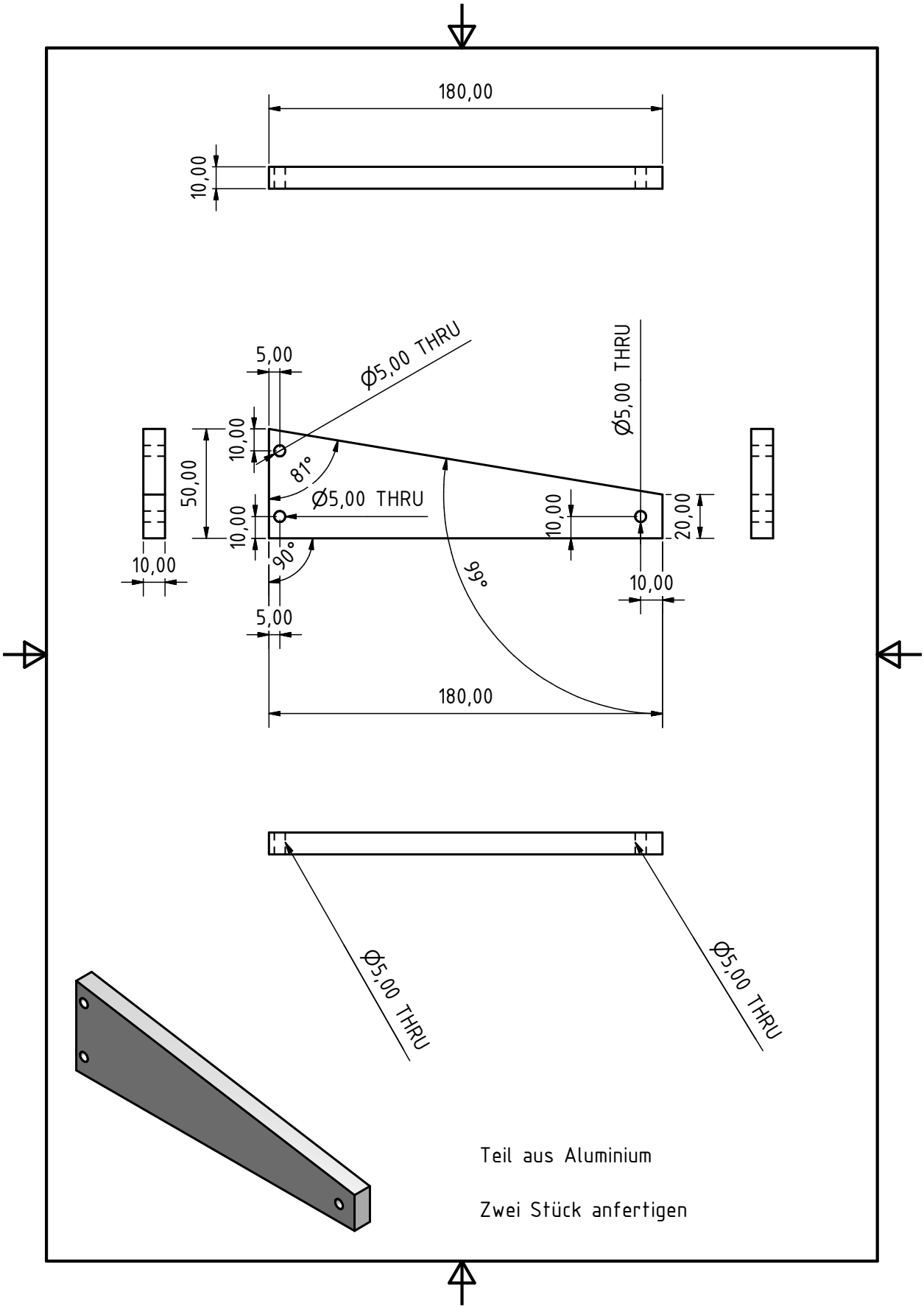

Figure E.20: CAD sketch of third part of detector tilting mechanism. Connection parts between these three parts, such as bushes are not sketched, but have been placed in by the workshop.

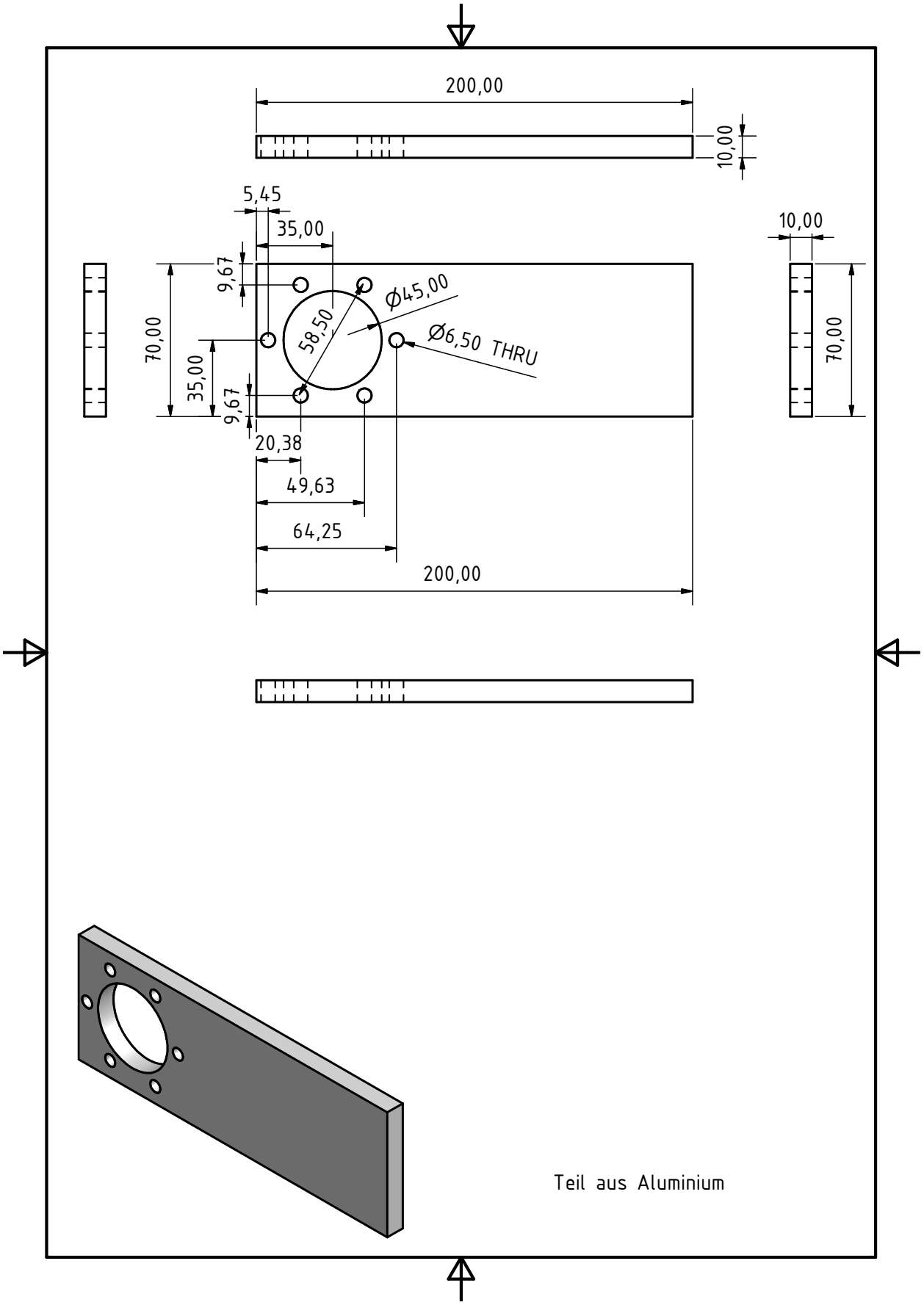

Figure E.21: CAD sketch of detector to CF40 flange mounting part.

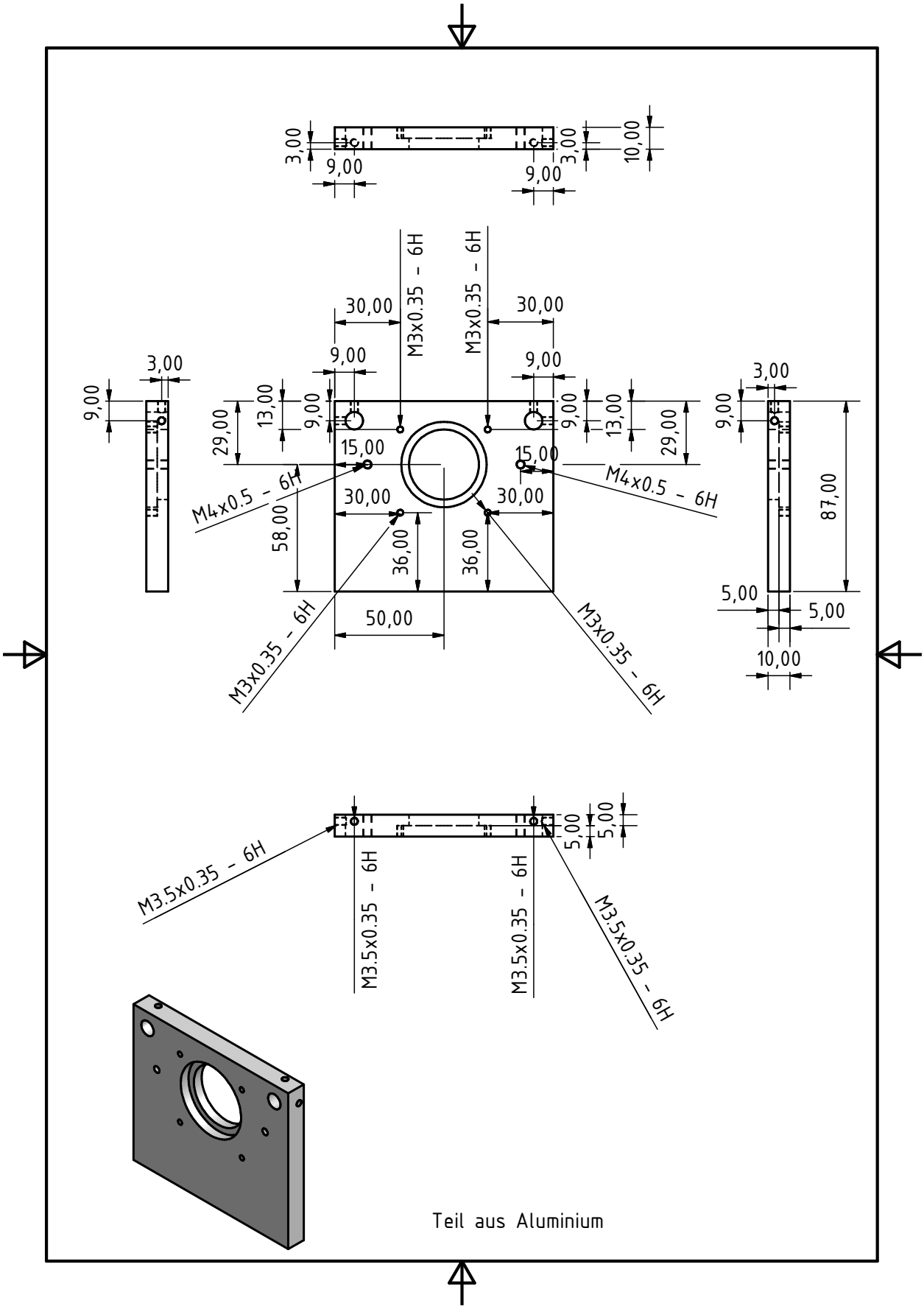

Figure E.22: CAD sketch of detector interference filter holder part and socket for teflon inset. A box with the detector electronics is fixed with two screws to the back side of this part.

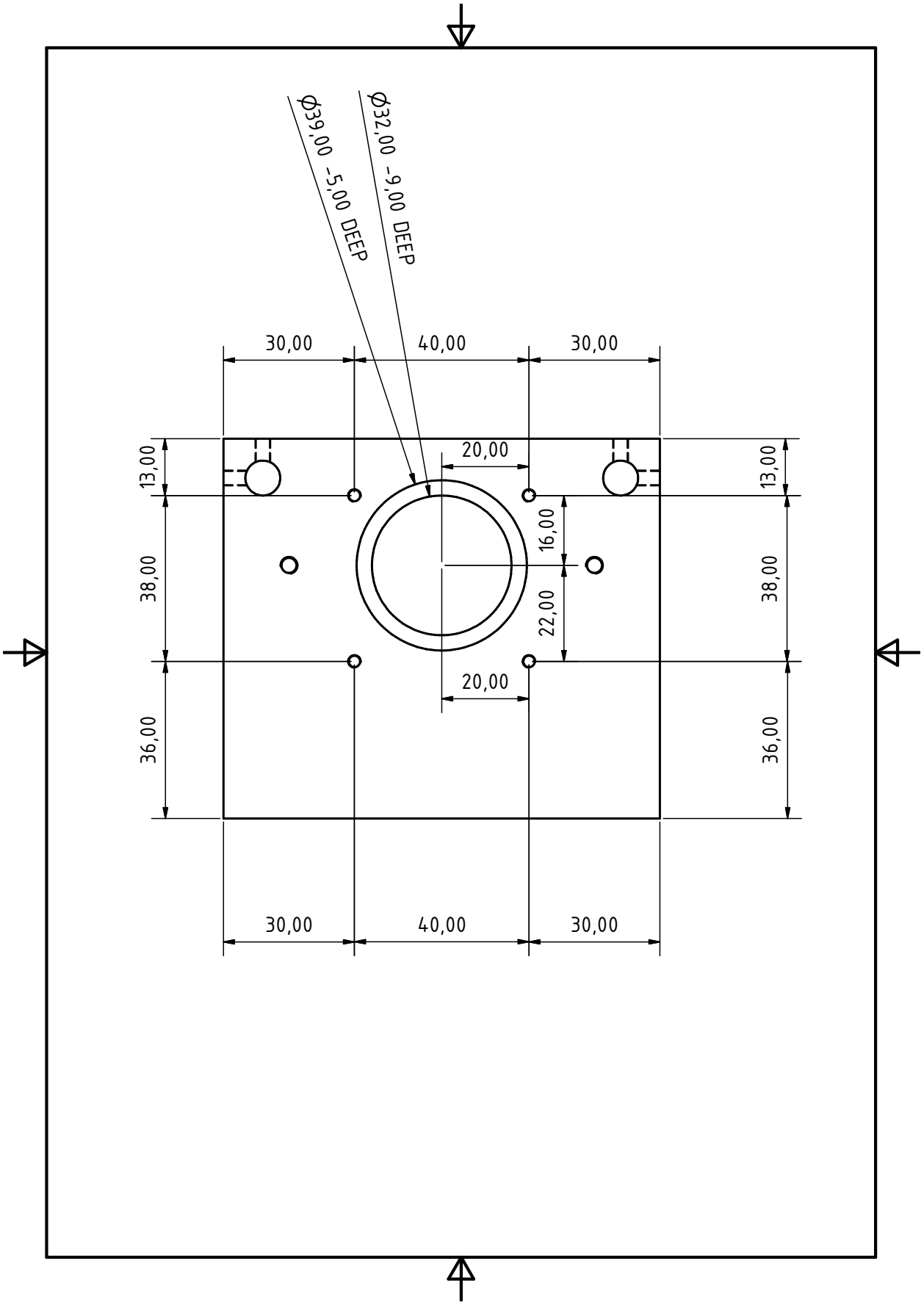

Figure E.23: Additional CAD sketch of part E.22.

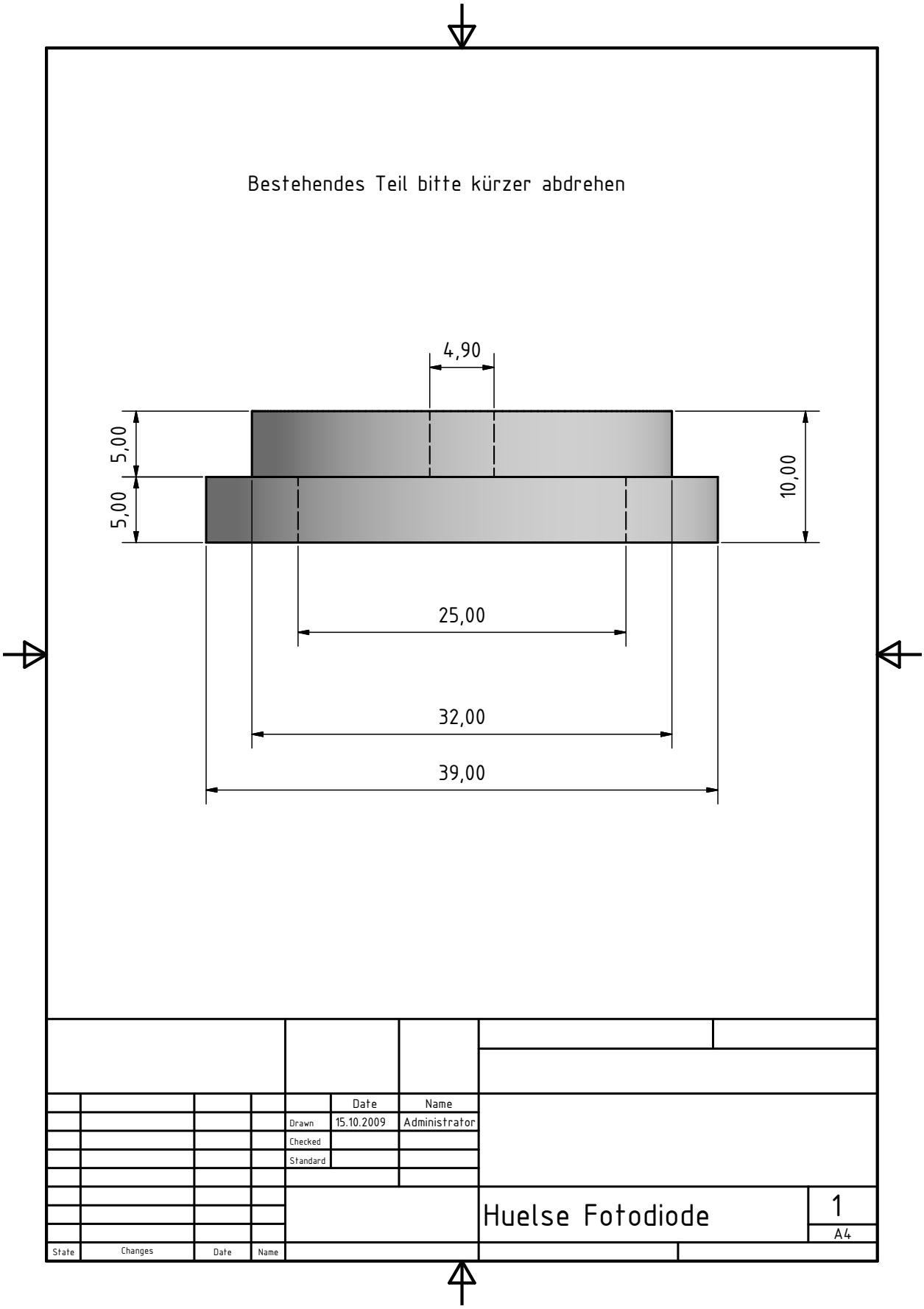

Figure E.24: CAD sketch of Teflon® bush, which is set into the part displayed in figure E.22 as socket for interference filter and photo transistor as essential part of the detektor.

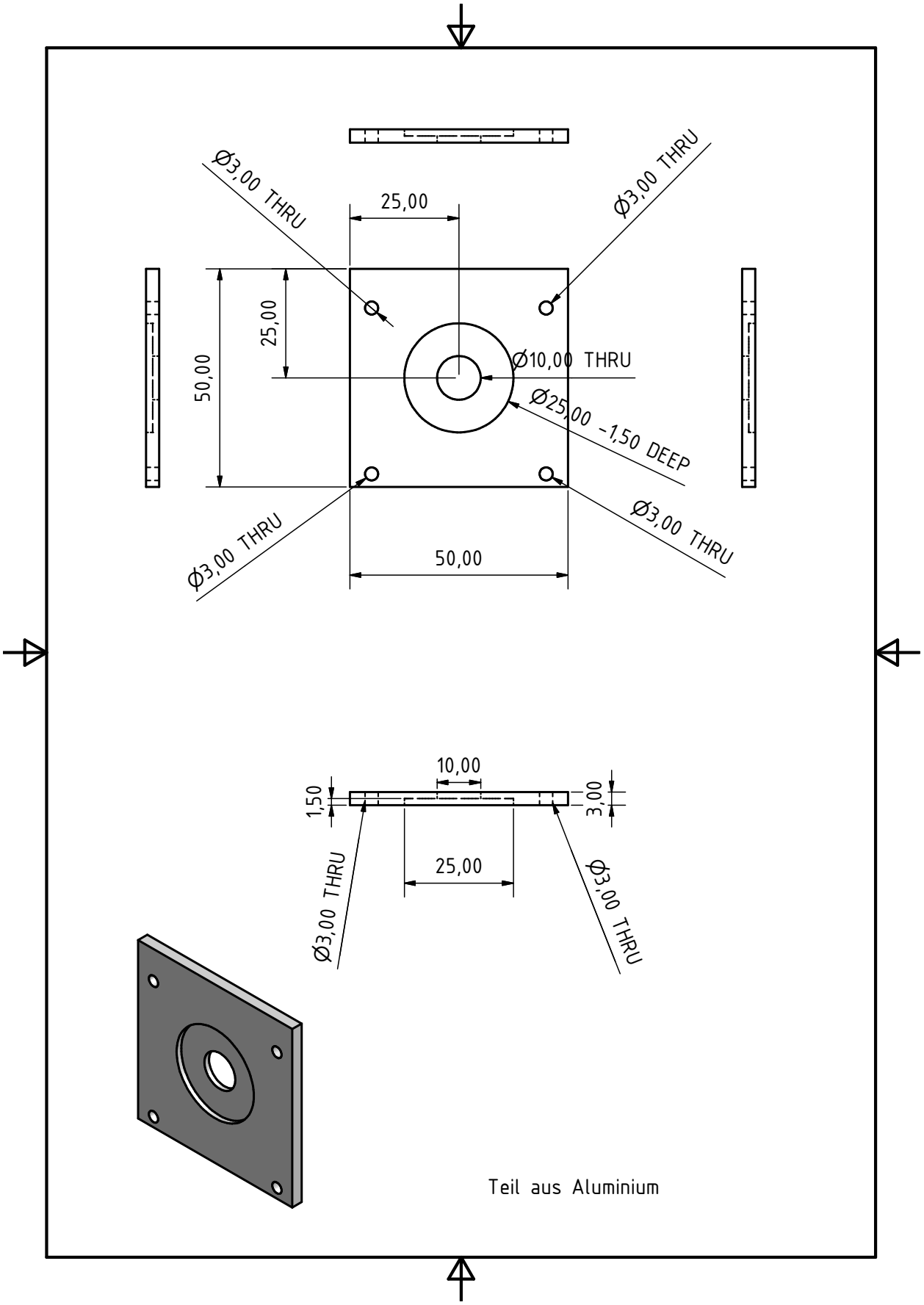

Figure E.25: CAD sketch of a plate that fixes the interference filter on the part shown in figure E.22.

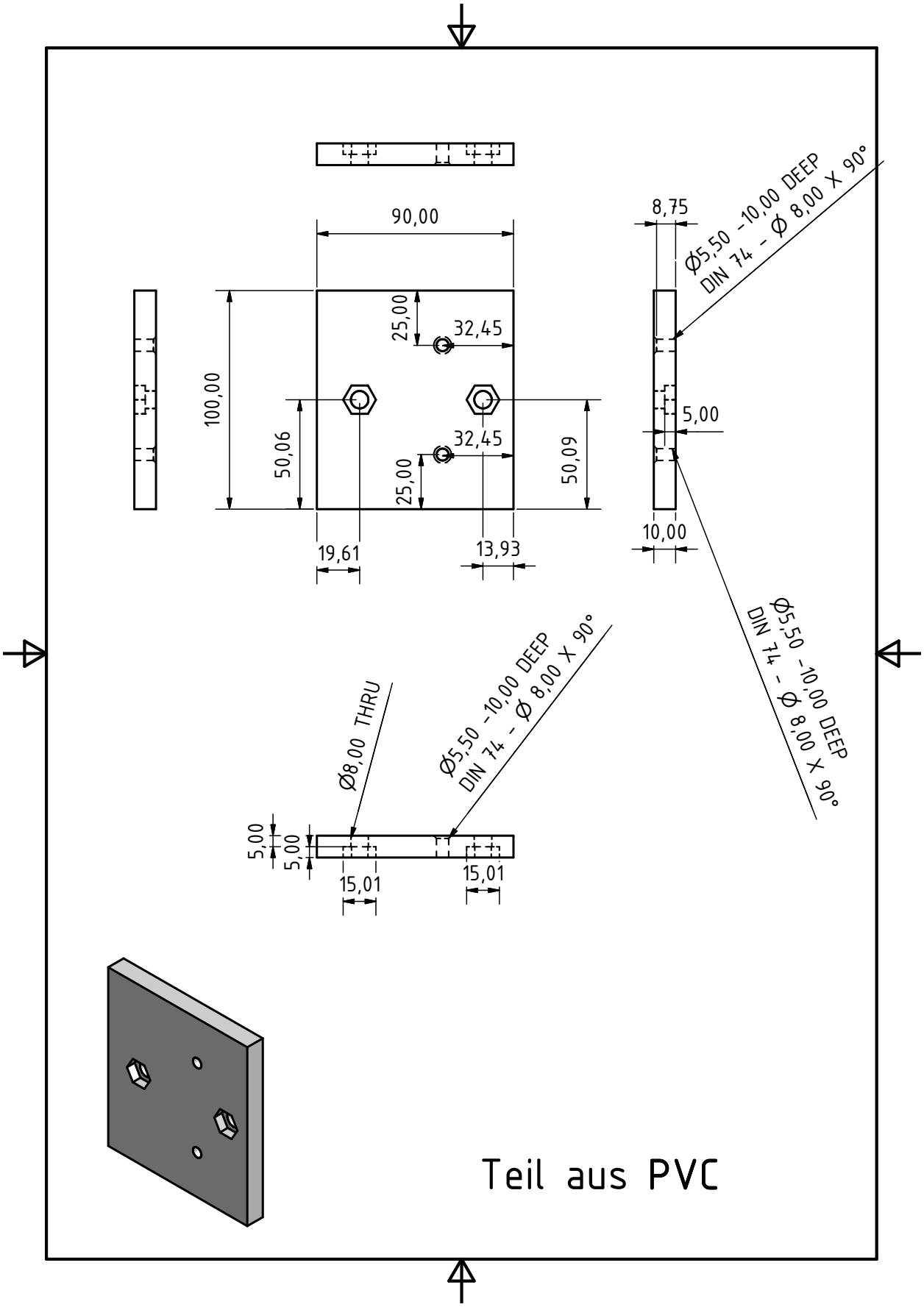

Figure E.26: CAD sketch of detector basis part that carries the optics part on the adustment elements.

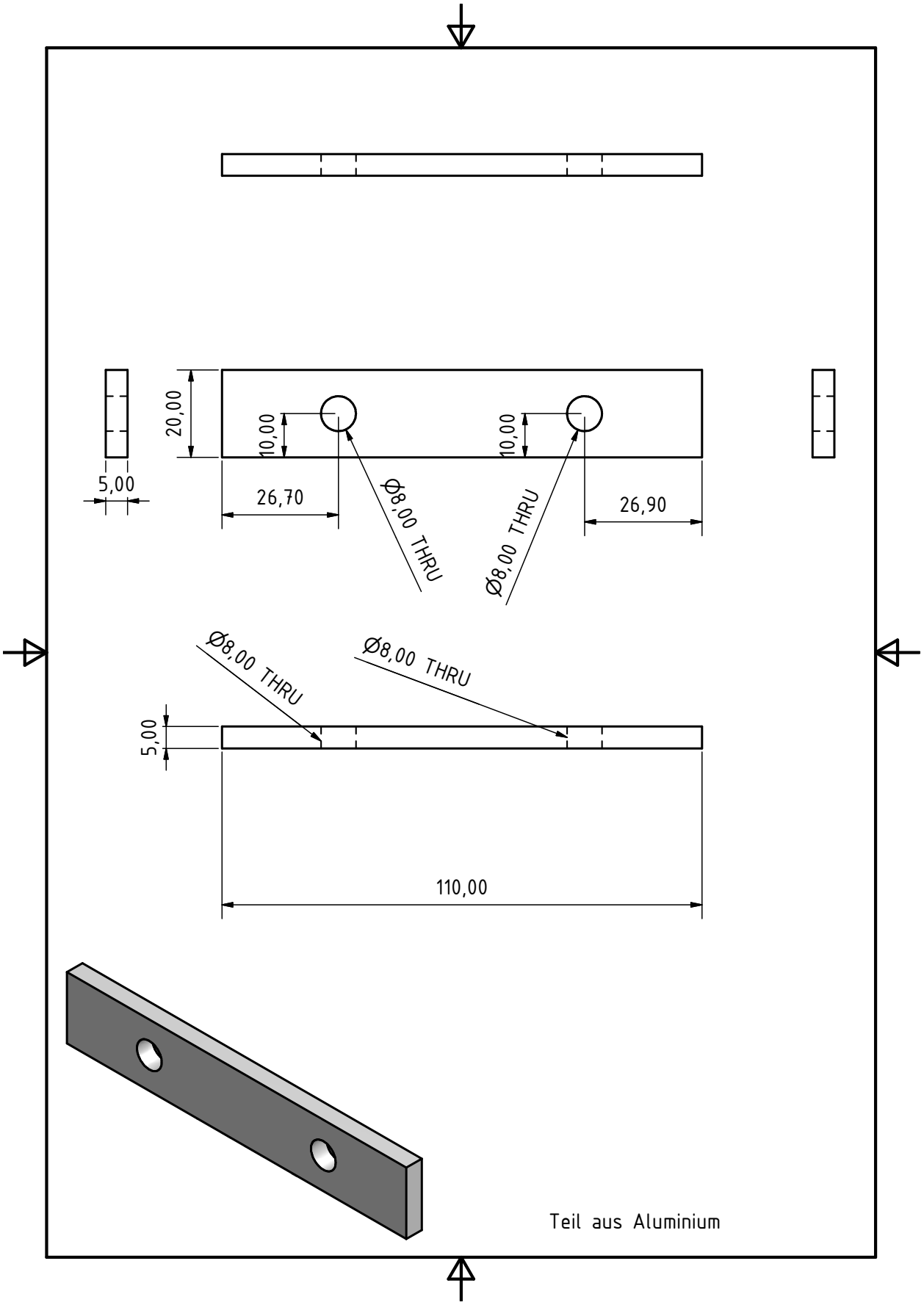

Figure E.27: CAD sketch of detector locking bar to fix the part shown in figure E.26 in the horizontal plane.

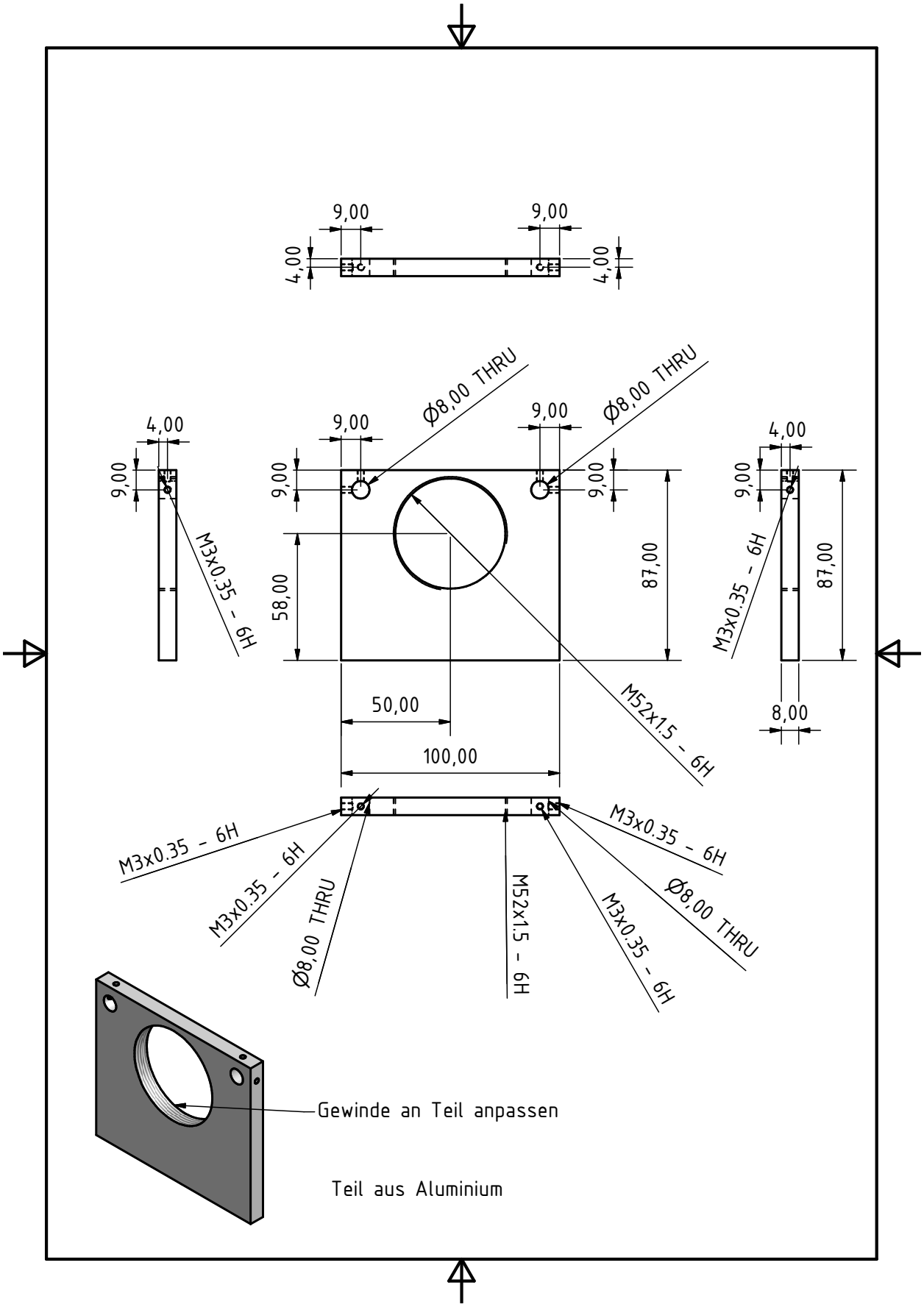

Figure E.28: CAD sketch of detector slot with female thread fitting to holder of convex lens.

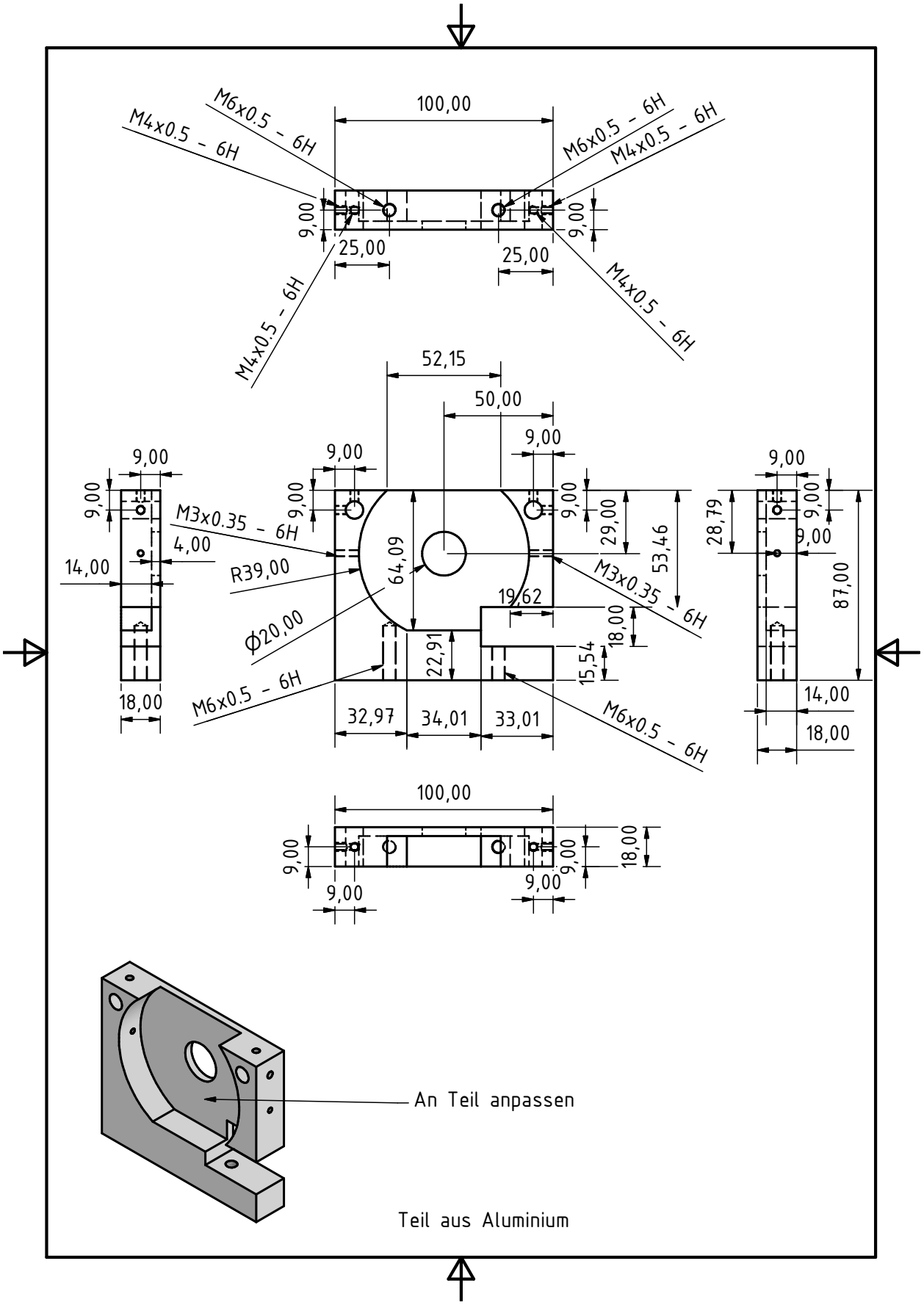

Figure E.29: CAD sketch of detector holder for high precision ratation optics stage for optics.

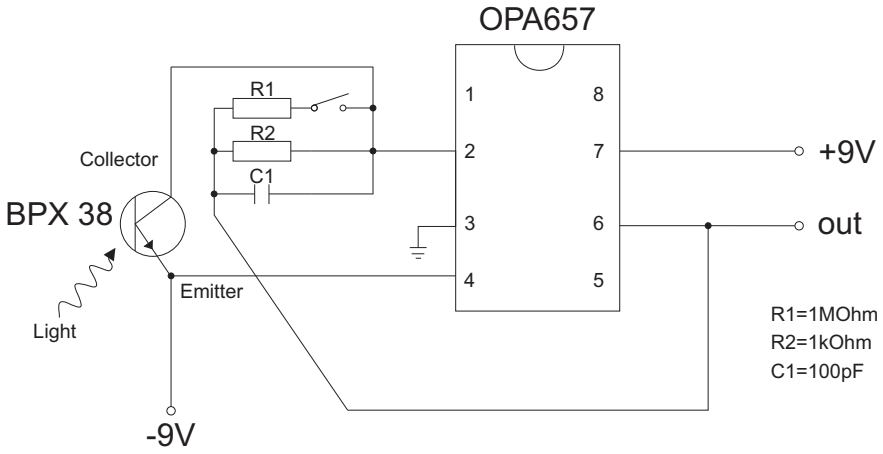

Figure E.30: Schematic circuit diagram of the MOKE detector electronic mainly consisting of a photo transistor and an operational amplifier. The DV output signal is read out with an Agilent multimeter, which is connected to a PC. The figure is modified from [130].

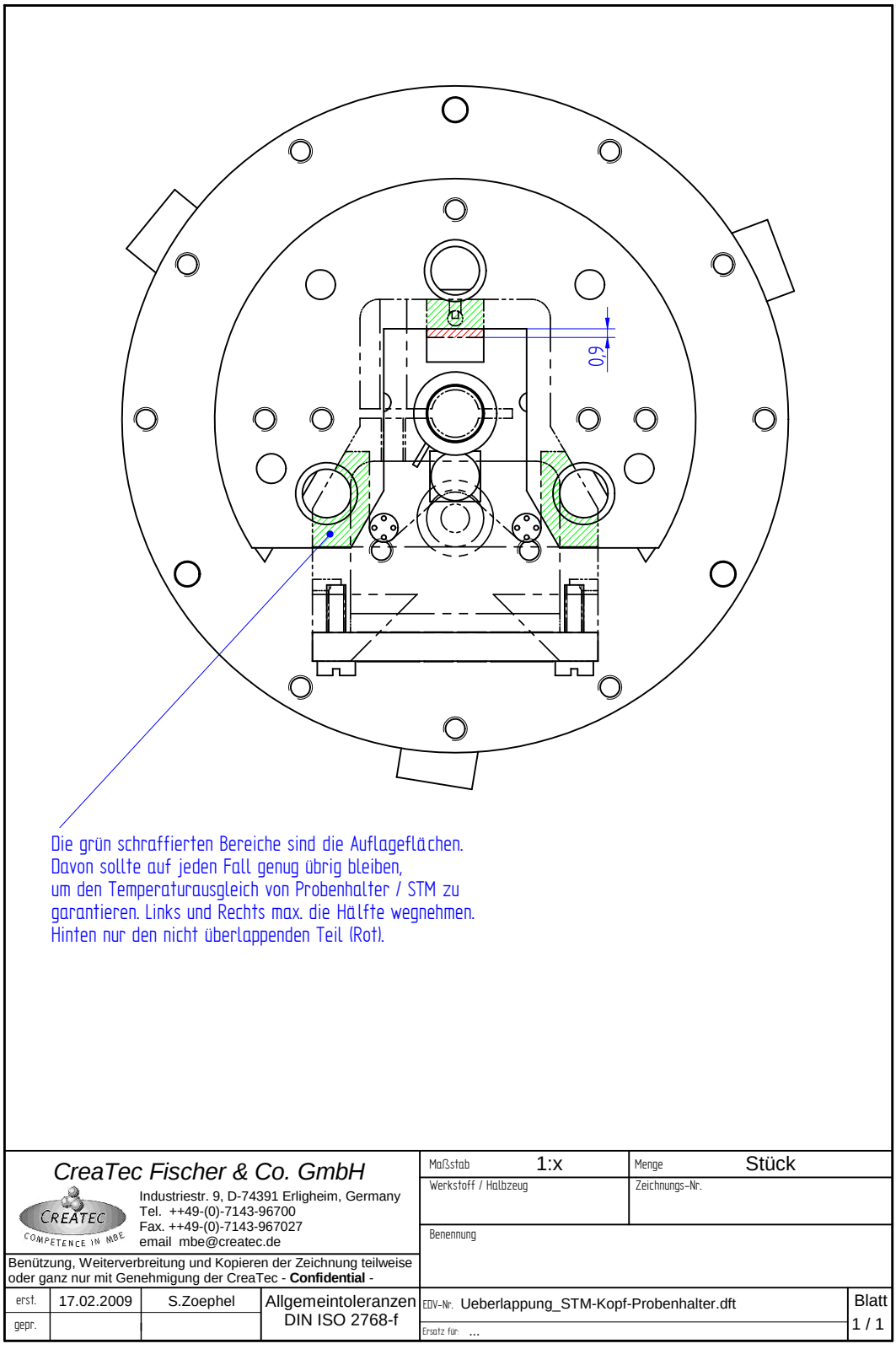

Figure E.31: Sketch of the contact areas of the sample holder with the downside of the STM piezo plate [121]. The upper third of the lower two green marked areas have been milled away at our sample holder bodies to make them fit into magnet of the MOKE setup. Courtesy of Sven Zöphel from SPS-CreaTec GmbH [121].

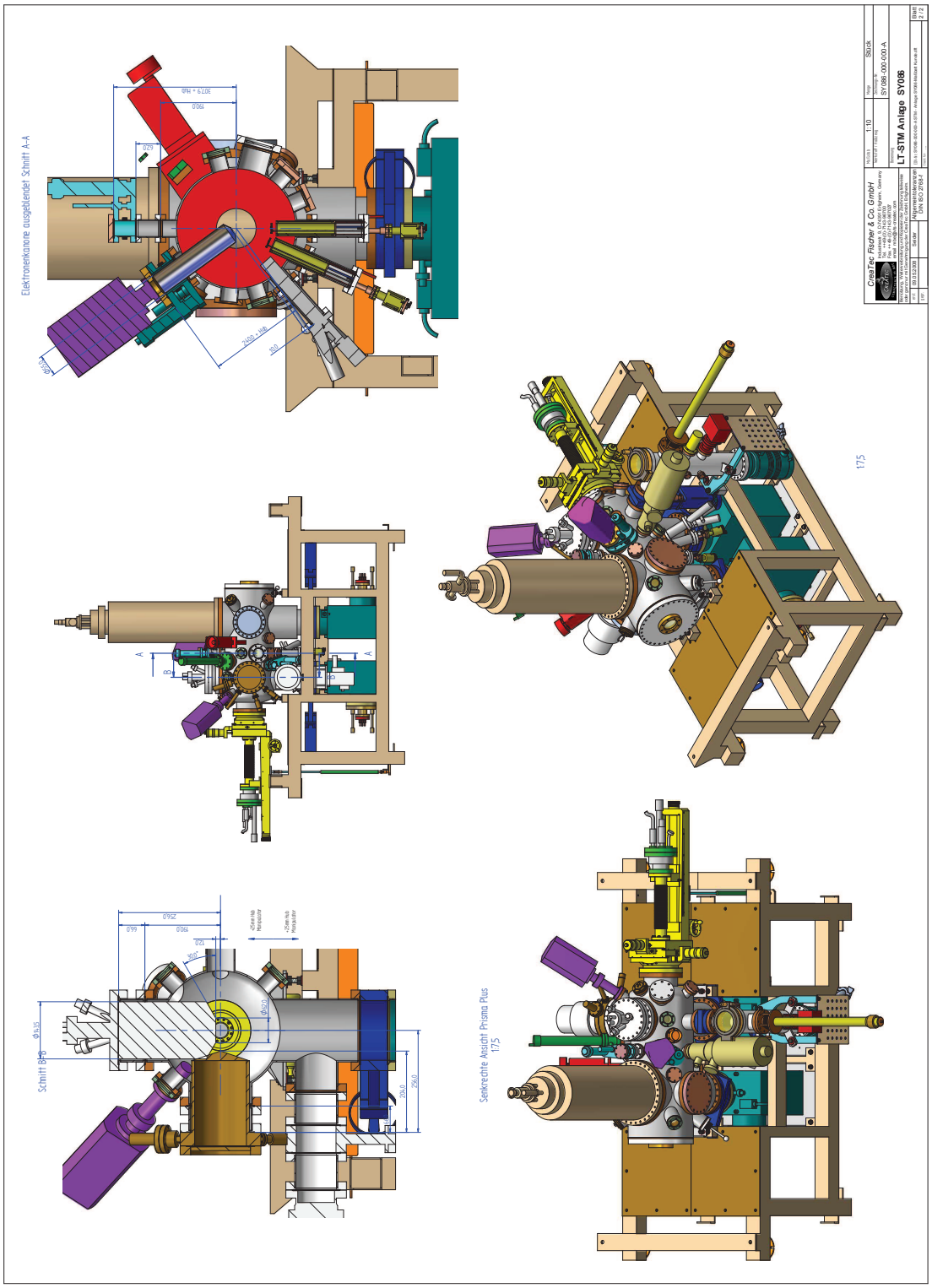

Figure E.32: Sketch of the LT-STM UHV setup [121]. The UHV system consists of an STM chamber with a He bath cryostat on top, a preparation chamber and a load lock. Sample preparations of this thesis are performed in the B-B cut of the preparation chamber and MOKE measurements are performed in the A-A cut of the chamber. The configuration of single devices mounted to the chamber differs from the CAD sketch. Courtesy of Sven Zöphel from SPS-CreaTec GmbH [121].

Publications

The main findings of this thesis, namely an enhanced Curie temperature in thin EuO films on graphene and the spin polarized surface state in EuO(100) are submitted for publication in international peer-reviewed journals:

- Jürgen Klinkhammer, Daniel F. Förster, Stefan Schumacher, Hans P. Oepen, Thomas Michely, and Carsten Busse. *Enhanced Curie temperature of ultra thin textured EuO films on graphene.* Submitted to Appl. Phys Lett. (Feb. 2013).
- Jürgen Klinkhammer, Fabian Craes, Sven Runte, Stefan Schumacher, Thomas Michely, and Carsten Busse. *Spin-polarized surface state in EuO(100) investigated with scanning tunneling spectroscopy.* Submitted to Phys. Rev. Lett. (May 2013).

My research work also contributed to the following articles which do not form a part of this thesis:

- D. F. Förster, J. Klinkhammer, C. Busse, S. G. Altendorf, T. Michely, Z. Hu, Y.-Y. Chin, L. H. Tjeng, J. Coraux, and D. Bourgault. Phys. Rev. B **83**, 045424 (2011). *Epitaxial europium oxide on Ni(100) with single-crystal quality.* doi:10.1103/PhysRevB.83.045424.
- D. F. Förster, J. Klinkhammer, and T. Michely. Surf. Sci. 606, 13–14 (2012). *Eu oxides on Ni (100): Polar surfaces, magic clusters and structures with large lattice dilation.* http://dx.doi.org/10.1016/j.susc.2012.02.021.
- Fabian Craes, Sven Runte, Jürgen Klinkhammer, Marko Kralj, Thomas Michely, and Carsten Busse. *Mapping Image Potential States on Graphene Quantum Dots.* Submitted to Phys. Rev. Lett. (2013). http://arxiv.org/abs/1303.1800.

Deutsche Kurzzusammenfassung

Diese Arbeit befasst sich mit dünnen Schichten des ferromagnetischen Halbleiters EuO. Diese werden mit Molekularstrahlepitaxie im Ultrahochvakuum gewachsen und ihre Eigenschaften *in-situ* mit niederenergetischer Elektronenbeugung, magneto-optischem Kerr-Effekt (MOKE), Rastertunnelmikroskopie (RTM) und Rastertunnelspektroskopie (RTS) untersucht. Die Experimente werden in einer Tieftemperatur RTM Apparatur mit einer Basistemperatur von 5,3 K ausgeführt. Die Entwicklung eines hochempfindlichen MOKE-Instruments steht im technischen Fokus dieser Arbeit. EuO wird in (100) Orientierung sowohl auf einem ferromagnetischen Ni(100) Einkristall, als auch auf einkristallinem Graphen auf Ir(111) gewachsen. Eine antiferromagnetische Kopplung zwischen den magnetischen Momenten von Ni(100) und EuO(100) stellte sich heraus. Die ultradünnen stöchiometrischen EuO Schichten auf Graphen zeigen eine Curie Temperatur T_C von ca. 75 K, was eine Erhöhung im Vergleich mit EuO Volumenproben und besonders dünnen EuO Schichten auf anderen Substraten darstellt [1–3].

Die Analyse von Punktdefekten in EuO Schichten auf Graphen wurden mittels atomar aufgelösten Mikroskopieaufnahmen durchgeführt. Die Defektstellen wurden als Sauerstoffleerstellen in einer Konzentration von 0,3% aller Sauerstoffatome in EuO identifiziert. Die Dynamik dieser Sauerstoffleerstellen wird mit einer Folge von RTM Topographie-Abbildungen gezeigt und ein Hüpfen entlang der EuO$\langle 011\rangle$ Richtungen wird entdeckt. Untersuchungen der elektronischen Struktur der EuO(100) Oberfläche werden mit RTM und RTS durchgeführt, was eine hohe Probenqualität erfordert, d.h. eine topographisch sehr gut geordnete und ebene Oberfläche mit einer geringen Defektzahl. Die ultra dünnen EuO Schichten auf Graphen dieser Arbeit sind von solch einer hohen Qualität. Eine lokale Bandverbiegung zu höheren Energien wurde an den Sauerstofffehlstellen gemessen, was eine lokale n-Dotierung der EuO Filme zeigt. Tunnelspektroskopiekarten der ferromagnetischen EuO(100) Oberfläche zeigen stehende Wellenmuster, welche der charakteristische Fingerabdruck des Oberflächenzustands in EuO(100) sind. Die Dispersionsrelation $E(k)$ des Oberflächenzustandes wurde systematisch durch die Auswertung seiner Streumuster erforscht. Die auf diese Weise ermittelte Dispersionsrelation des Oberflächenzustandes stellt sich als die eines freien Elektrons heraus, mit einer effektiven Masse von $m_{\text{eff}}=(1{,}09\pm0{,}10)\cdot m_e$, wobei m_e die Masse eines freien Elektrons ist. Analoge Messungen wurden bei 81 K in der paramagnetischen Phase von EuO ausgeführt. Dabei wird der Oberflächenzustand energetisch verschoben. Diese Verschiebung ist ein indirektes Indiz für die Spin-Entartung des Oberflächenzustandes in der paramagnetischen Phase, welche in der ferromagnetischen Phase aufgehoben wird. Dieses Verhalten ist analog zur wohlbekannten Rotverschiebung [33] durch die Spin-Aufspaltung des EuO Leitungsbandes [4]. Die in dieser Arbeit gemessene Spin-Aufspaltung des Oberflächenzustandes beträgt 0,66 eV.

Acknowledgements

With this acknowledgements I gratefully would like to thank many people who supported this thesis.

- First I would like to thank Thomas Michely. He gave me the opportunity to be part of his workgroup and believed in me to lead this thesis to a success. I benefited a lot of his experience.
- I thank Daniel Bürgler for evaluating this thesis as a referee and for his wide interest in the physics of EuO. I also want to thank him for inviting me to the Jülich research center and for discussion of the MOKE on Ni(100) measurements.
- Many thanks Ladislav Bohatý for being the chairman of my disputation.
- A special thanks goes to Carsten Busse for supervising the LT-STM laboratory, discussing my results, working on our publications, proofreading, and for being that smart person.
- I am very thankful to Hans Peter Oepen who shared his knowledge about MOKE devices with me.
- Many thanks go to Hans Kroha and Tobias Stollenwerk for discussion and for the program to calculate Heisenberg magnetization functions.
- Simone Altendorf is gratefully acknowledged for the preparation of an EuO reference sample.
- I have to thank Andreas Jacobi and Felix Huttmann a lot. They supported me within their bachelor theses. Andreas contributed to the mechanical construction of the MOKE setup and Felix set up MOKEsoft with LabVIEW ^{TM}.
- I also want to thank Fabian Craes, Sven Runte, Ulrike Schröder, Stefan Schumacher, Sven Macko, Rabia Djemour and Anna Djemour for proofreading.
- Many thanks go to Ruth Bruker who imaged etched STM tips with SEM.
- Very special thanks go to Nobert Henn and Lucie Hamdan for being great technicians and for supporting all of us whenever there is need for.
- Susanne Heijligen is gratefully acknowledged for doing a SQUID measurement of an EuO film.

- Many thanks go to the mechanical and electrical workshop of the II. Physikalisches Institut. They put a lot of work in the construction of the MOKE setup and helped me with their experience.
- I thank all members of our workgroup and also the former ones for being such nice people and for helping each other. I especially want to mention my close friends Fabian Craes, Sven Runte and Sebastian Standop for having good times in the Kegel-club.
- I am very thankful to Daniel Förster, who introduced me to may issues of our workgroup and to EuO already in my diploma thesis. He also performed scientific work on which this thesis is based on. And I also thank him for proofreading.
- I like to thank my parents Marianne Klinkhammer and Maximilian Klinkhammer for paving my way and supporting me during my whole study.
- Finally I would like to thank my girlfriend Anna-Lena for always supporting me and being there for me, also in the future. I enjoy every single moment with you.

Offizielle Erklärung

Ich versichere, dass ich die von mir vorgelegte Dissertation selbständig angefertigt, die benutzten Quellen und Hilfsmittel vollständig angegeben und die Stellen der Arbeit - einschließlich Tabellen, Karten und Abbildungen -, die anderen Werken im Wortlaut oder dem Sinn nach entnommen sind, in jedem Einzelfall als Entlehnung kenntlich gemacht habe; dass diese Dissertation noch keiner anderen Fakultät oder Universität zur Prüfung vorgelegen hat; dass sie - abgesehen von den angegebenen Teilpublikationen - noch nicht veröffentlicht worden ist, sowie, dass ich eine solche Veröffentlichung vor Abschluss des Promotionsverfahrens nicht vornehmen werde. Die Bestimmungen der Promotionsordnung sind mir bekannt. Die von mir vorgelegte Dissertation ist von Prof. Dr. Thomas Michely betreut worden.

Köln, den 03. Mai 2013

Jürgen Klinkhammer